

The Determination of Chemical Concentrations in Nano-scaled Phases by Use of Quantitative Anomalous Small-Angle X-ray Scattering

Kumulative Habilitationsschrift zur Erlangung der Venia legendi im
Fach Physikalische Chemie

Vorgelegt der Fakultät für Naturwissenschaften
der Universität Paderborn

Günter Johannes Goerigk
Institut für Weiche Materie und Funktionale Materialien
des Helmholtz-Zentrum Berlin

Berlin 2012

Table of Contents

1. Introduction.....	2
2. Anomalous Small-Angle X-ray Scattering.....	4
3. Experimental.....	8
4. ASAXS measurements on the distribution of Sr ²⁺ counter ions around polyacrylate chains in highly diluted aqueous solution.....	10
4.1. Sample preparation and ASAXS measurements.....	10
4.2. Quantitative results from ASAXS measurements on diluted polyelectrolyte solutions.....	12
5. Temperature induced differences in the nanostructure of hot-wire deposited silicon-germanium alloys analyzed by Anomalous Small-Angle X-ray Scattering.....	15
5.1. Sample preparation and ASAXS measurements.....	15
5.2. Quantitative results from ASAXS measurements on hot-wire deposited silicon-germanium alloys – A combined invariant analysis.....	16
6. Spinodal decomposition of Ni-Nb-Y metallic glasses probed by quantitative Anomalous Small-Angle X-ray Scattering.....	18
6.1. Sample preparation and ASAXS measurements.....	18
6.2. The determination of the chemical concentrations located in the thermal fluctuations caused by spinodal decomposition in ternary Ni-Nb-Y metallic glasses.....	19
7. Discussion.....	22
8. Summary and future perspectives.....	27
9. References.....	29
9.1. Contributions by the author establishing the habilitation.....	29
9.2. Other references.....	30

The Determination of Chemical Concentrations in Nano-scaled Phases by Use of Quantitative Anomalous Small-Angle X-ray Scattering

Synopsis From Anomalous Small-Angle X-ray Scattering experiments precise quantitative information about the different chemical constituents in multi-component systems can be correlated with structural analysis.

Abstract In the last years Anomalous Small-Angle X-ray Scattering became a precise quantitative method resolving scattering contributions two or three orders of magnitude smaller compared to the overall small-angle scattering, which are related to the so-called pure-resonant scattering contribution. Additionally to the structural information precise quantitative information about the different chemical constituents of multi-component systems like the fraction of the chemical components localized in the nanostructure of the materials are obtained from these scattering contributions. The application of the Gauss elimination algorithm to the vector equation established by ASAXS measurements at three X-ray energies is demonstrated for three examples from chemistry and solid state physics. All examples deal with the quantitative analysis of the Resonant Invariant (RI-analysis). From the integrals of the pure-resonant scattering contribution the chemical concentrations in nano-scaled phases are determined. In one example the correlated analysis of the Resonant Invariant and the Non-resonant Invariant (NI-analysis) is employed. The structural and quantitative informations are correlated to the macroscopic properties respectively to the properties of the phase diagrams of the analyzed materials.

1. Introduction

Small-Angle X-ray Scattering (SAXS) experiments average over a large sample volume and give structural and quantitative information of high statistical significance on a mesoscopic length scale between 1 and hundreds of nanometers, which can be correlated to the macroscopic physical and chemical parameters of the analyzed materials. Detailed descriptions of the experimental and theoretical aspects of Small-Angle Scattering can be found under [1-3]. By use of synchrotron radiation at suitable storage rings the so-called Anomalous Small-Angle X-ray Scattering (ASAXS) can be employed, which is an excellent tool for the chemical selective structural analysis of multi-component systems. In the last

three decades numerous ASAXS studies on very different systems such as alloys, ceramics, magnetic systems, catalysts, semiconductors, glasses, polymers, membranes and other soft matter systems have been performed. A review can be found under [4]. These materials show strong differences, when analyzed by ASAXS. For instance metal nanoparticles prepared on porous support structures show a strong small-angle X-ray scattering predominantly related to the small-angle X-ray scattering of the pores, while the scattering of the metal nanoparticles is a minor contribution due to their small volume fraction [5,6]. Glasses and alloys especially when dealing with metallic glasses show a different behaviour i.e. only a weak SAXS signal is originating from small concentration fluctuations of the different constituents [7,S1]. The situation is similar for diluted chemical solutions like polyelectrolytes surrounded by counter ions, where the overall SAXS signal is weak due to the dilution and small changes occur, which are related to specifically interacting counter ions [8].

This habilitation thesis summarizes the scientific results obtained from the method of quantitative Anomalous Small-Angle X-ray Scattering. It outlines more generally the context between required accuracies of the measurement techniques and a proper mathematical description and is based on the use of the special matrix inversion of Eqs.6-7. The thesis was developed in a series of publications documented in a separate list (page 29).

In more detail this thesis addresses the quantitative analysis of nano-scaled phases and their correlation with structural parameters in three different systems: (1) the conformation of macromolecules under the influence of counter ions in a highly diluted aqueous solution (2) the inhomogeneous distribution of germanium and hydrogen in semiconductor alloys and (3) the spinodal decomposition in metallic Ni-Nb-Y glasses. The different systems have in common a high degree of dilution and/or homogeneity and thus are weak scattering systems. The related scientific problems cannot be addressed by a classical Small-Angle X-ray Scattering (SAXS) experiment, because the specific scattering contributions of the different chemical components need to be separated. As outlined below an outstanding experimental accuracy is needed in order to separate the so-called pure-resonant (element specific) scattering contribution. Additionally a suitable mathematical algorithm is employed (the Gauss elimination algorithm), which turned out to provide the best results when inverting the vector equation introduced by ASAXS measurements. The latter is demonstrated by calculations of the so-called Turing numbers of the different systems.

In the 2nd chapter a short summary of the related mathematics is given i.e. the inversion of the vector equations stated by an ASAXS experiment performed at in minimum three X-ray energies with the aim to obtain the so-called basic scattering functions. Moreover a concept is explained, which quantifies the errors of the basic scattering functions obtained by matrix inversion based on the Turing condition (see below). Special attention will be given to the Gauss elimination procedure. The 3rd chapter summarizes the experimental aspects including the required measurement accuracies and experimental resolution demands of synchrotron radiation based ASAXS measurements followed by some explicit descriptions of the accuracies, which have been achieved for the three scientific examples outlined in the chapters 4 to 6. Finally in the 7th chapter a detailed discussion of the results will be given in the light of the Turing condition. Chapter 8 will summarize and give a short outlook of ASAXS experiments at 3rd generation sources.

2. Anomalous Small-Angle X-ray Scattering

The remarkable possibilities of the ASAXS technique are based on the energy dependence of the atomic scattering factors giving selective access to the specific SAXS contributions of nano-scaled phases, which are built up by different chemical constituents in composites like for instance alloys or chemical solutions. In general the atomic scattering factors are energy dependent complex quantities:

$$f_Z(E) = f_{0,Z} + f'_Z(E) + if''_Z(E) \quad (1)$$

where Z represents the atomic number. When performing ASAXS measurements on multi-component systems in the vicinity of the absorption edge of one of the sample constituents the scattering amplitude is:

$$A(\vec{q}, E) = \int_{V_p} \Delta\rho_0(\vec{r}) \cdot \exp(-i\vec{q}\vec{r}) d^3r + \int_{V_p} \Delta\rho_R(\vec{r}, E) \cdot \exp(-i\vec{q}\vec{r}) d^3r, \quad (2)$$

where q is the magnitude of the scattering vector $[= (4\pi/\lambda)\sin\Theta]$, 2Θ is the scattering angle, λ the X-ray wavelength and V_p is the irradiated sample volume. $\Delta\rho_0, \Delta\rho_R$ are the differences of electron densities of the non-resonant and the resonant scattering atoms,

$$\begin{aligned}\Delta\rho_0(\vec{r}) &= \Delta f_0 \cdot u(\vec{r}) = (f_0 - \rho_m V_0) \cdot u(\vec{r}) \\ \Delta\rho_R(\vec{r}, E) &= \Delta f_R(E) \cdot v(\vec{r}) = ((f_{0,R} - \rho_m V_R) + f'_R(E) + if''_R(E)) \cdot v(\vec{r})\end{aligned}\quad (3)$$

calculated from the electron density, ρ_m , and the atomic (molecular) volumes V_0 and V_R , respectively. In the two cases of an alloy or a diluted solution ρ_m is the electron density of the entire alloy or of the solvent respectively. The volume V_0 represents the atomic (molecular) volume of the non-resonant scattering atoms or building groups for instance the volume of a monomer in a polymer chain in the case of the diluted solutions. V_R corresponds to the atomic volumes of the resonant scattering atoms. The functions $u(\vec{r}), v(\vec{r})$ are the number densities of the non-resonant and the resonant scattering units, respectively and represent their spatial distribution in the sample. The atomic (molecular) scattering factor, $f_0(E) \approx \text{const}$, is nearly energy independent, while the atomic scattering factor, $f_R(E) = f_{0,R} + f'_R(E) + if''_R(E)$, shows strong variation with the energy in the vicinity of the absorption edge of the resonant scattering atoms due to the so-called anomalous dispersion corrections $f'_R(E), f''_R(E)$. Calculating the scattering intensity $I(\vec{q}, E) = |A(\vec{q}, E)|^2 = A(\vec{q}, E) \cdot A^*(\vec{q}, E)$ by means of Eqs.2-3 and averaging over all orientations yields a sum of three contributions $I(q, E) = S_0(q) + S_{0R}(q) + S_R(q)$, with the convolution integrals [9]:

$$\begin{aligned}S_0(q) &= \Delta f_0^2 \iint_{V_p} u(\vec{r})u(\vec{r}') \frac{\sin(q|\vec{r} - \vec{r}'|)}{q|\vec{r} - \vec{r}'|} d^3 r d^3 r' = \Delta f_0^2 |A_0(q)|^2 \\ S_{0R}(q, E) &= 2\Delta f_0 \cdot (f_{0,R} - \rho_m V_R + f'_R(E)) \iint_{V_p} u(\vec{r})v(\vec{r}') \frac{\sin(q|\vec{r} - \vec{r}'|)}{q|\vec{r} - \vec{r}'|} d^3 r d^3 r' \\ &= 2\Delta f_0 \cdot (f_{0,R} - \rho_m V_R + f'_R(E)) \cdot \text{Re}(A_0(q)A_R(q)) \\ S_R(q, E) &= |\Delta f_R(E)|^2 \iint_{V_p} v(\vec{r})v(\vec{r}') \frac{\sin(q|\vec{r} - \vec{r}'|)}{q|\vec{r} - \vec{r}'|} d^3 r d^3 r' = |\Delta f_R(E)|^2 |A_R(q)|^2 \\ &= ((f_{0,R} - \rho_m V_R + f'_R(E))^2 + f''_R{}^2(E)) \iint_{V_p} v(\vec{r})v(\vec{r}') \frac{\sin(q|\vec{r} - \vec{r}'|)}{q|\vec{r} - \vec{r}'|} d^3 r d^3 r'\end{aligned}\quad (4)$$

Eq.4 gives the non-resonant scattering, $S_0(q)$, the cross-term or mixed-resonant scattering, $S_{0R}(q, E)$, originating from the superposition of the scattering amplitudes of the non-resonant and the resonant scattering atoms and finally, $S_R(q, E)$, which contains only the scattering

contributions of the resonant scattering atom species. As can be identified in the last line of Eq.4 the so-called pure-resonant scattering contribution, $(f'^2(E) + f''^2(E))|A_R(q)|^2$, appears, which is the form factor of the spatial distribution of the resonant scattering atomic species multiplied with the square of the anomalous dispersion corrections. Additionally there are further (mixed resonant and non-resonant) scattering contributions. In what is to follow, it will be shown, that the form factor $|A_R(q)|^2$ is a measurand gained from the measurement of three energy-dependent scattering curves, which carries the complete structural and quantitative information about the resonant scattering atomic species. Thus the other contributions can be ignored in the analysis and only the pure-resonant scattering contribution, more precisely the form factor of it, $|A_R(q)|^2$, will be considered.

The measurement of scattering curves at three energies in the vicinity of the absorption edge of the atoms with atomic number Z constitutes the following vector equation:

$$M_{ij}(E_i) \otimes A_j(q) = I_i(q, E_i) \quad (5)$$

$$\begin{pmatrix} \Delta f_0^2 & 2\Delta f_0 [\Delta f_{0,Z} + f'_Z(E_1)] & [(\Delta f_{0,Z} + f'_Z(E_1))^2 + f''_Z(E_1)^2] \\ \Delta f_0^2 & 2\Delta f_0 [\Delta f_{0,Z} + f'_Z(E_2)] & [(\Delta f_{0,Z} + f'_Z(E_2))^2 + f''_Z(E_2)^2] \\ \Delta f_0^2 & 2\Delta f_0 [\Delta f_{0,Z} + f'_Z(E_3)] & [(\Delta f_{0,Z} + f'_Z(E_3))^2 + f''_Z(E_3)^2] \end{pmatrix} \begin{pmatrix} |A_0(q)|^2 \\ \text{Re}(A_0(q)A_R(q)) \\ |A_R(q)|^2 \end{pmatrix} = \begin{pmatrix} I(q, E_1) \\ I(q, E_2) \\ I(q, E_3) \end{pmatrix}$$

where $\Delta f_{0,Z} = f_{0,R} - \rho_m V_0$. When solving the vector equation by the Gaussian algorithm (elimination procedure) the three basic scattering functions can be determined by the subsequent vector equation:

$$\begin{pmatrix} a_{11} & a_{12} & a_{13} \\ 0 & a_{22} & a_{23} \\ 0 & 0 & a_{33} \end{pmatrix} \begin{pmatrix} |A_0(q)|^2 \\ \text{Re}(A_0(q)A_R(q)) \\ |A_R(q)|^2 \end{pmatrix} = \begin{pmatrix} b_1 \\ b_2 \\ b_3 \end{pmatrix} \quad (6)$$

where the meaning of $a_{i,j}, b_j$ is published in more detail in [S1], or in analytical form:

$$|A_R(q)|^2 = \left[\frac{I(q, E_1) - I(q, E_2)}{f'_Z(E_1) - f'_Z(E_2)} - \frac{I(q, E_1) - I(q, E_3)}{f'_Z(E_1) - f'_Z(E_3)} \right] \cdot \frac{1}{F(E_1, E_2, E_3)}, \quad (7)$$

where $F(E_1, E_2, E_3)$ represents a normalization factor composed of the anomalous dispersion corrections at the related three energies E_1, E_2, E_3 [S9]. $|A_R(q)|^2$ is the pair correlation function of the resonant scattering atoms and thus represents the spatial distribution of the resonant scattering atoms. Due to Eq.7 ASAXS provides a technique to access directly the small-angle scattering and by this the related structural information of the distribution of the Z-atoms. More generally spoken, Eq.7 provides a method, which gives access to the pure-resonant scattering contribution of the selected constituent of a multi-component system by measuring the small-angle scattering at only three suitable energies [S4,S6].

A system of linear equations is termed ‘well conditioned’ when small errors in the coefficients M_{ij} , or in the right hand side vector in Eq.5 have little effect on the solution. If the solution is very sensitive to the values of the coefficients, the problem is ‘ill conditioned’. The reason for ill conditioning of a system of linear equations is, when the matrix is nearly singular or some of the matrix rows are almost linear dependent. From mathematics it is known, that all methods of solving an ill-conditioned system of linear equations are generally bad [10]. Thus it is necessary to specify a quantitative measure, which gives a realistic estimation of how reliable the solutions of a system of linear equations are if obtained by the matrix inversion. The latter should be directly related to errors, which occur during the measurement process i.e. the error bars of the scattering curves gained from the ASAXS measurements. The so-called Turing number of Eq.8 defines such a measure of condition as will be shown later.

$$T(M') = \frac{1}{3} \cdot \|M\| \cdot \|M'^{-1}\|$$

$$\|M\| = \sqrt{\sum_{i,j=1}^3 a_{ij}^2} \quad \|M'^{-1}\| = \sqrt{\sum_{i,j=1}^3 b_{ij}^2} \quad (8)$$

From the matrix (elements) M_{ij} or M'_{ij} respectively of Eqs.5-6 the Turing numbers [10,11] of the three different systems (NaPA-solution with Sr^{2+} counter ions, hydrogenated Si-Ge-alloys and metallic glasses of $\text{Ni}_{68}\text{Nb}_{16}\text{Y}_{16}$) have been calculated giving a measure of confidence. This will be outlined in more detail in the discussion.

From $|A_R(q)|^2$ and Eq.6 the three basic scattering functions of Eq.4 can be calculated analytically as is shown for the energies E_1 and E_2 as follows [S6]:

$$\begin{aligned}
S_R(q, E_1) &= |\Delta f_R(E_1)|^2 \cdot |A_R(q)|^2 \\
S_{0R}(q, E_1) &= (\Delta I(q, E_1, E_2) - S_R(q, E_1) + S_R(q, E_2)) \frac{(f_{0,R} - \rho_m V_R) + f'_R(E_1)}{f'_R(E_1) - f'_R(E_2)} \\
S_0(q) &= I(q, E_1) - S_{0R}(q, E_1) - S_R(q, E_1)
\end{aligned} \tag{9}$$

The basic scattering functions, $S_{0R}(q, E)$, $S_0(q)$, carry important structural and quantitative information for instance the sign of the contrast between the nano-phases and the structural information of the non-resonant scattering component (see example amorphous Si-Ge).

With the definition of S_{0R} in Eq.4 the three basic scattering functions fulfill the Cauchy-Schwarz inequality because the integrals in S_0 and S_R of Eq.10 define a positive definite metric in the vector space of functions [S6]:

$$S_{0R}(q, E)^2 \leq 4 \cdot S_0(q) \cdot S_R(q, E) \tag{10}$$

This criterion is essential but not sufficient for the reliability of the basic scattering functions obtained from the matrix inversion. If it is not fulfilled, the basic scattering functions are meaningless.

3. Experimental

ASAXS needs a SAXS camera together with synchrotron radiation. In the last three decades several ASAXS beam lines have been established with special optics, having easily tuneable monochromatic photon energy without degrading the beam alignment or in other words to measure the small-angle scattering routinely and avoiding re-alignment of the beam line setup. In this respect, it is far easier to align optics with fixed exit double monochromators (D22 at former LURE [12] or former JUSIFA at HASYLAB/DESY [13,14]) than optics with vertical & horizontal focusing (D2AM at ESRF [15,16], 7T-MPW-SAXS at BESSY II [17]). For a more instrumental based survey see also [18].

Most monochromators are made of Si-111 or Si-311 (the numbers give the Miller indices of the diffracting planes, which are parallel to the surface of the silicon crystals) in order to remove the second order harmonic. The Si-311 with an energy resolution of $\Delta E/E < 5 \cdot 10^{-5}$ constitutes a narrow bandgap, thus providing an excellent energy resolution for ASAXS measurements in the near edge range of the X-ray absorption edges. Special attention has to be devoted to the detector concept. Nowadays, all ASAXS beam lines use two-dimensional position sensitive detectors, but quantitative measurements clearly benefit from single photon counters due to the absence of electronic noise. Because the anomalous variations represent a very small fraction of the overall scattered intensity, high stability and linearity are required for all experimental components. The most important are: (1) the beam stability of the storage ring (beam stabilities better 5 microns are required for high precision measurements see below), (2) a high energy resolution, $\Delta E/E < 5 \cdot 10^{-5}$, for instance achieved by the Si-311 JUSIFA monochromator, (3) the counting assembly (flux monitors, detector, transmission measurements), (4) the precise calibration of the scattering curves into scattering cross sections for instance in (macroscopic) units of cross section per unit volume [$\text{cm}^2/\text{cm}^3 = \text{cm}^{-1}$], the latter being mandatory for quantitative ASAXS measurements. Special attention must be paid to precise transmission measurements (see below).

Precise quantitative ASAXS measurements in the resolution regime $10^{-3} < \Delta I/I < 10^{-2}$ (separated scattering with respect to the overall scattering) have been performed in the last decade [S1-S4,S6]. Here the term quantitative means the separation of the pure-resonant scattering contribution with a subsequent analysis of the invariant, the so-called Resonant-Invariant (RI-analysis). These measurements required very precise corrections for background, sensitivity, transmission, normalization, dead time correction, subtraction of solvent scattering etc. i.e. the corrections should be better by one order of magnitude compared to $\Delta I/I$ (the expected relative variation of the small-angle scattering signal due to anomalous scattering). In order to meet these accuracies the measurements followed the JUSIFA standard procedures as following. The detector sensitivity of the 2-dimensional gasdetector (MWPC: Multi-Wire Proportional Counter) [19] in the different energy ranges was obtained by measurement of the fluorescence of suitable foils (i.e Cu-, Se-, Zr- and Mo-foils with K- α lines at 8, 11.2, 15.8 and 17.5 keV). The error of these sensitivity measurements due to the counting statistics was better 0.5% for each detector pixel. Due to the integration of the scattering curves the propagating error is smaller by one to two orders of magnitude. Within an energy range of 2 keV the sensitivity of the MWPC-detector does not change significantly and thus can be used

for corrections within an ASAXS sequence in the related energy ranges of up to 1000 eV. Transmission measurements were performed with a precision of 10^{-4} using a special (windowless) photodiode (Hamamatsu S2387-1010N) [S2,S4,S6]. Corrections of the sensitivity of the diode are not necessary because it cancels out in the transmission measurement. The dead-time correction of the MWPC-detector was measured for each exposure (scattering pattern) and corrected for in the data reduction [14]. The normalization of the scattering pattern was performed by measurements of the primary photon flux with a Sodium-Iodine scintillation counter with an accuracy of better than 10^{-4} . The background scattering and scattering from the solvent (respective substrate) was measured with the same exposure times like the samples and subtracted from the sample scattering. The scattering curves of all sample measurements (including the solvent and substrate measurements) have been calibrated into macroscopic scattering cross section in units of cross-section per unit volume [$\text{cm}^2 / \text{cm}^3$]= $[\text{cm}^{-1}]$ by repeating the calibration measurements (with the JUSIFA glassy carbon standards) up to 20 times and averaging over these measurements. The errors have been calculated via error propagation law of the statistical errors of the photon counts of all contributing measurements (i.e. measurements of sample and solvent or substrate scattering, sensitivity, background...).

From the pure-resonant scattering contribution and the subsequent analysis of the Resonant Invariant (RI) the chemical concentrations in the related nano-phases were deduced. Additionally from the separated pure-resonant scattering the contributions of the other chemical components entering the so-called mixed-resonant and non-resonant scattering can be reconstructed. All measurements were carried out at the JUSIFA beam line at HASYLAB, DESY Hamburg [13,14].

4. ASAXS measurements on the distribution of Sr^{2+} counter ions around polyacrylate chains in highly diluted aqueous solution

4.1. Sample preparation and ASAXS measurements

The example focuses on the change in size and shape of sodium polyacrylate (NaPA) in aqueous solution, followed by the addition of alkaline earth cations. Alkaline earth cations are known to specifically interact with the anionic carboxylate residues, located on every other carbon atom of the polymer backbone. Formation of complex bonds between the anionic

groups and alkaline earth cations neutralizes electric charges and thereby changes the nature of the respective chain segments. As a consequence, solubility of the polyelectrolyte is lowered which leads to a significant coil shrinking and eventually causes a precipitation of the respective alkaline earth salt [20,21]. A first (non-quantitative) ASAXS study on such diluted solutions which the above mentioned formalism has been developed for, have been performed in 2004 [S9] supplemented by a study combining ASAXS with light scattering [S7]. In the next step the formalism was extended to the quantitative aspects of this method, i.e. the analysis of the Resonant Invariant (RI-analysis). On four Sr^{2+} containing solutions of [NaPA] with the concentration between $[\text{NaPA}] = 3.232$ and 3.326 mM with ratios between $[\text{Sr}^{2+}]/[\text{NaPA}] = 0.451$ and 0.464 have been analyzed by ASAXS. The detailed description of the sample preparation (4 mm capillaries) and the ASAXS experiment is given in [S4]. Here we focus on the separation of the form factor of the spatial distribution of the Sr^{2+} counter ions obtained from Eqs.1-7 and the subsequent RI-analysis of Eqs.11-12.

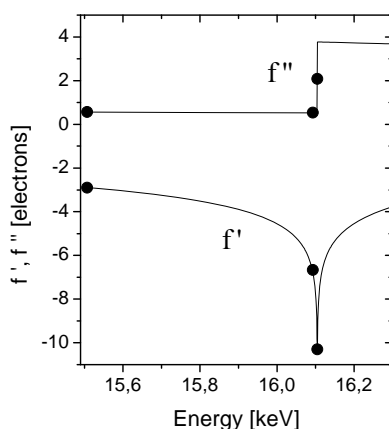


Figure 1: Anomalous dispersion corrections of Sr [22,23].

The ASAXS measurements were carried out at the JUSIFA beam line at HASYLAB, DESY Hamburg [13,14] covering a q -range between 0.075 and 2.5 nm^{-1} at three energies in the vicinity of the K-absorption edge of Sr at 16105 eV . The Sr-K-edge was measured from the solutions. From the change of the absorption coefficient the Sr-concentration of the solutions was confirmed. Figure 1 provides the anomalous dispersion corrections for Sr at the three energies used here based on the calculations of Cromer and Liberman [22,23].

4.2. Quantitative results from ASAXS measurements on diluted polyelectrolyte solutions

Figure 2 shows the total (black squares) and the difference (calculated from 2 energies, blue triangles) scattering curves and the form factor (red circles) of the Sr-counter ion distribution. The shape of the total scattering curve is compatible with the form factor of spherical objects, which is modulated by inter-spherical scattering contributions. The latter was already suggested by former SANS measurements [24]. This interpretation is strongly confirmed by

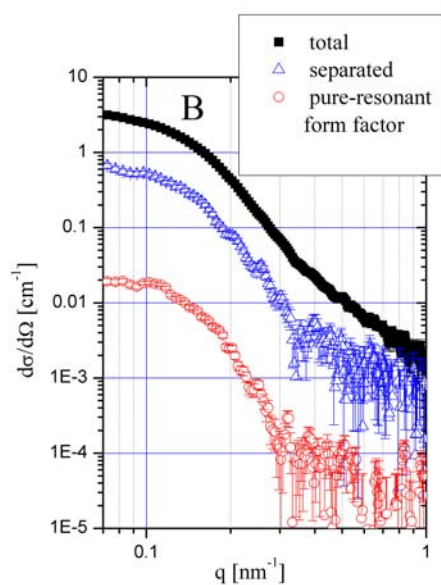


Figure 2: Total scattering, difference (separated) scattering and the form factor of the pure-resonant scattering contribution of an aqueous polyacrylate solution with Sr^{2+} -counter ions. The error bars have been calculated by error propagation of the statistical errors of the measured scattering curves.

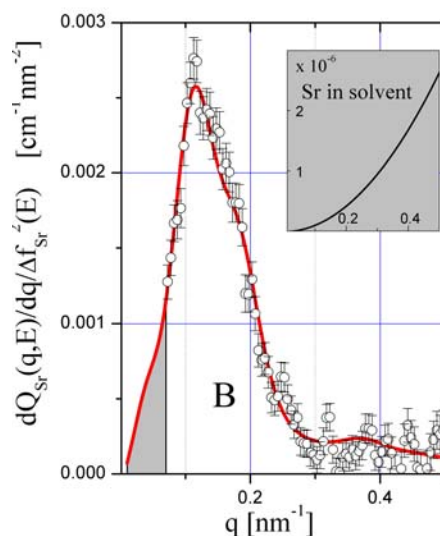


Figure 3: The first derivative of the Resonant Invariant with upper integration limit q (Eq.11) of sample B. The model function was calculated in order to estimate the contribution of the missing scattering to the Resonant Invariant beyond the resolution of the ASAXS experiment (grey area on the left). The error bars have been calculated by error propagation.

the difference scattering curve (triangles) and the separated form factor (circles) of the Sr-ion distribution. Both curves exhibit a number of characteristic structures for $q > 0.1 \text{ nm}^{-1}$ with pronounced maxima, minima and shoulders revealing a scattering function, which is strongly influenced by correlation effects between rather mono-disperse sub-domains within the collapsing chains. Especially the form factor of the spatial distribution of the Sr-counter ions reveals a correlation maximum at 0.1 nm^{-1} . For a counter ion condensation-induced shrinking process such a model was first suggested by Rubinstein et al. [25] and was confirmed later by computer simulations [26-28]. The model, denoted as pearl-necklace, gives the scattering function of N spheres with radius R and with a distance d between the spheres.

In addition to the structural information, which can be obtained from $|A_R(q)|^2$ [S9], important quantitative information related to the amount of inhomogeneously distributed Sr-ions can be deduced from the integral Q_Z :

$$Q_Z(E) = |\Delta f_Z(E)|^2 \int_Q |A_R(q)|^2 d^3q \quad (11)$$

In analogy to the so-called invariant [1,2], we will call $Q_Z(E)$ the Resonant Invariant (RI) of the inhomogeneously distributed resonant scattering Sr-ions. The Resonant Invariant, $Q_Z(E)$, as defined in Eq.11, is related to the number density of inhomogeneously distributed (i.e. condensed) Sr-ions, \bar{v}_Z , as was outlined in detail in [S2,S4,S6]:

$$\bar{v}_Z = \frac{1}{2V_Z} \pm \sqrt{\frac{1}{4V_Z^2} - \frac{1}{(2\pi)^3 r_0^2} \int_Q |A_R(q)|^2 d^3q} \quad (12)$$

where $V_Z = 4\pi/3R_Z^3$ is the volume of the Z-atoms (here Sr^{2+} -ions) with ion radius R_Z and r_0 is the classical electron radius. In this presentation only one of the two solutions is significant i.e. the negative sign. Due to the integral Eq.12 provides the quantitative analysis of chemical fluctuations independent of their structural distribution i.e. either in a two phase system or in short range order. It should be mentioned that the number density calculated from Eq.12 includes the Z-atoms, which are homogeneously distributed in the solvent. These Sr-ions provide an isotropic scattering contribution at small q-values. As will be shown in more detail below, the amount of the isotropic scattering contribution originating from these remaining Sr-ions in the solvent can be neglected.

From the RI-analysis performed on SAXS measurements of four samples with different ratios $[\text{Sr}^{2+}]/[\text{NaPA}]$ the concentrations of specifically interacting Sr^{2+} -ions were obtained (Table 1 and Figure 3). Because the concentration of Sr-ions known from the compositions of the as-prepared solutions (and absorption measurements) amounts to $9 \cdot 10^{17} \text{ cm}^{-3}$ only between 8.9 and 22.3% of the Sr-ions condensate on the polymer chains corresponding to values between $0.041 < r < 0.102$ of Sr-ions, which condensate per carboxylate residue on the polymer backbone for the ratios $0.451 < [\text{Sr}^{2+}]/[\text{NaPA}] < 0.464$. As can be seen from the inset in Figure 3, the Sr-ions, which remain in the solvent, do not contribute significantly to the invariant in the q-regime under consideration and thus can be neglected.

Table 1: Structural and quantitative parameters of the four diluted NaPA samples with different concentration ratios $[\text{Sr}^{2+}]/[\text{NaPA}]$ obtained from the ASAXS analysis. \bar{v} represents the concentration of Sr-atoms in the condensed phase deduced from the experimentally accessible section of the Resonant Invariant. Values of \bar{v}^u represent the upper limits of these concentrations calculated with a theoretical model function of the dumb bell for details see [S4]. c is the relative amount of Sr-atoms in the condensed phase with respect to the total concentration of Sr-ions in the entire solution and r represents the ratio of Sr-cations to carboxylate side groups. Sample A represents an outlier possibly due to degradation of the sample. The latter was evidenced by LS-experiments showing strong differences of the radius of gyration taken before and after the ASAXS-measurements.

Sample	$[\text{Sr}^{2+}]/[\text{NaPA}]$	\bar{v}	\bar{v}^u	$c^{1)}$	r
		$10^{17}[\text{cm}^{-3}]$	$10^{17}[\text{cm}^{-3}]$	[%]	
A	0.464	0.77(14)	0.94	10.5	0.049
B	0.458	1.50(8)	1.92	21.4	0.097
C	0.4575	1.73(21)	2.01	22.3	0.102
D	0.451	0.73(12)	0.80	8.9	0.041

¹⁾The values refers to $9.0 \cdot 10^{17} \text{ Sr}^{2+}$ cations per cm^3 which correspond to 1.5 mM

This result can be compared to a value of $r=0.25$ extracted from the phase diagram established by light scattering in [S7]. The value of $r=0.25$ indicates the amount which is needed to cross the phase border along the collapsed state. For a quantitative discussion of the r values in Table I, sample A has to be considered with great care because light scattering of the samples performed prior to and after the ASAXS experiments indicated a slight instability [S7]. Except for this sample A, the values of r follow our expectations. Samples B and C are close together and sample D shows a smaller degree of Sr^{2+} binding in line with a drop of $[\text{Sr}^{2+}] / [\text{NaPA}]$ from B/C to D. The drastic effect confirms that small changes in $[\text{Sr}^{2+}] / [\text{NaPA}]$ cause strong changes in the conformation and hence in r once we get close to the phase boundary, as has been already observed in our preceding experiment [S9]. The closer the sample gets to the phase boundary, the higher the degree of Sr^{2+} binding becomes.

The discrepancy between the value obtained from the phase diagram and the values deduced from the Resonant Invariant can be explained as follows: [i] There is an error of the slope in the phase diagram established by light scattering experiments due to the scattering of the points, which is fairly large. [ii] At the phase border, an upper limit of Sr^{2+} ions is considered to be captured by the PA coils, while the Sr^{2+} condensation is a process gradually starting before the phase border is reached. Under the assumption that we have not yet reached the phase border with our samples B–D, the actual degree of Sr binding may still be considerably lower than the characteristic value at the phase boundary. Thus, the discrepancy between

$r=0.11$ and $r=0.25$ corresponding to the phase boundary implies another steep increase of the bound Sr^{2+} , in agreement with the drastic changes observed at the precipitation edge. The latter explanation demonstrates that precise quantitative ASAXS measurements employing the above mentioned algorithm with the goal to obtain the Resonant Invariant can serve as a suitable tool for detailed quantitative analysis of those phase diagrams.

5. Temperature induced differences in the nanostructure of hot-wire deposited silicon-germanium alloys analyzed by Anomalous Small-Angle X-ray Scattering

5.1. Sample preparation and ASAXS measurements

Hydrogenated amorphous silicon-germanium alloys are used in solar cell technology, where the germanium is added to produce lower band gap material to absorb the longer wavelength photons of the solar spectrum and to achieve higher efficiencies in converting solar light into electrical energy. Previous small-angle X-ray scattering (SAXS) and anomalous small-angle X-ray scattering (ASAXS) studies revealed that, in addition to voids, non-uniformly distributed Ge contributes to the material inhomogeneities [29-32], which are strongly related to the degradation of the opto-electronic properties. In recent years there has been a growing interest especially in the hot-wire chemical-vapour deposition (HWCVD) technique [33] due to evidence of improved stability and improved opto-electronic properties of the material, as well as the potentially beneficial manufacturing feature of higher deposition rates than the current industrial technique of plasma-enhanced chemical vapor deposition (PECVD) [34,35].

A group at NREL (National Renewable Energy Laboratory, U.S.A.) found evidence of improved photo response from HWCVD a-Si-Ge:H alloys with narrow band gaps deposited at different filament temperatures, filament diameters, and optimized substrate temperatures [36,37]. In what is to follow results from a series of six alloys of a-Si_xGe_x:H ($x=0.6-0.69$) deposited at different substrate temperatures between 130 and 360 °C are presented. The experiment demonstrates the determination of the amount of Ge located in mass fractals of 40 nm size employing the Resonant Invariant (RI) obtained from ASAXS measurements at the K-absorption edge of germanium at 11.103 keV over an energy range of more than 1 keV. Moreover from the Non-resonant Invariant (NI) the amount of voids was estimated depending on the substrate (deposition) temperatures. The correlation between the reduction of

(hydrogen containing) voids and enhanced formation of (Ge containing) mass fractals explains the improvement of the photo conductivity of the materials at medium deposition temperatures by more than half an order of magnitude [S6].

5.2. Quantitative results from ASAXS measurements on hot-wire deposited silicon-germanium alloys – A combined invariant analysis

Because the properties of the electronic contrast between the analyzed nano-phases were not clear (high in case of two phases of Si and Ge, low in case of slight concentration variations) the ASAXS measurements were extended over an energy range larger than 1 keV in order to reduce the Turing number as far as possible. Figure 4 shows the scattering curves of an alloy deposited at a substrate temperature of 305°C. The blue triangles represent the pure-resonant scattering of the Ge-containing structures. The solid line passing through the blue symbols represent a fractal model function due to the Unified Exponential/Power Law Approach of Beaucage [38] giving evidence of Ge-containing mass fractals with a size of about 40 nm. Here the term mass fractal means, that the mass of the structure scales with R^D where D is the fractal dimension with $1 < D < 3$. Figure 5 summarizes the results obtained from the analysis of the Resonant-Invariant and the Non-resonant-Invariant (NI) at six different substrate temperatures. Figure 5a summarizes the results of the integrated pure-resonant scattering of the Ge component normalized to the total (known) amount of Ge i.e. $\overline{v_{Ge}}/n_{Ge}$. At lower temperatures (below 250°C) only between 20 and 40% of the Ge-atoms are located in the mass fractals, while a dramatic change takes place at temperatures beyond, where more than 60% of the Ge-atoms are located in fractals. We shall now perform an analysis of the Non-resonant Invariant. According to Eq.4 the non-resonant term only includes contributions from hydrogen. Thus the Non-resonant Invariant addresses the chemical concentration of the hydrogen in the ternary alloy. As a result Figure 5b shows the reduction of hydrogen containing voids, when the substrate temperature is decreased. The blue triangles represent $\overline{v_H}/n_H$, which is the hydrogen quantity calculated from the Non-resonant scattering of Eq.13 normalized to the known hydrogen content of the alloys n_H .

$$\overline{v_H} = \frac{1}{2V_H} - \sqrt{\frac{1}{4V_H^2} - \frac{1}{(2\pi)^3 r_0^2} \int_Q |A_0(q)|^2 d^3q} \quad (13)$$

Especially for the temperatures beyond 250 °C the ratio shows values which are far too high, i.e. 20, 40 and 60 times higher than expected from the hydrogen concentration. From this the conclusion can be drawn that the non-resonant scattering represents not only the scattering of hydrogen-filled inhomogeneities but also gives evidence for the existence of voids, which dominate the non-resonant scattering contribution.

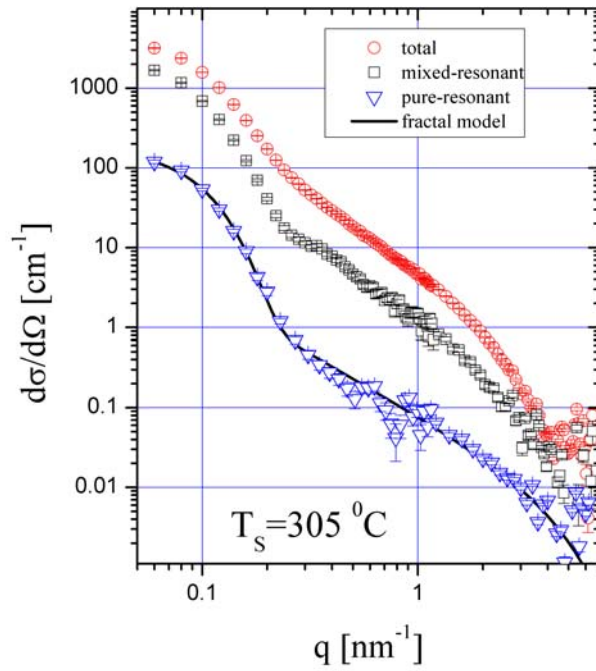


Figure 4: Total scattering, difference (separated) scattering and the pure-resonant scattering contribution of Ge-containing inhomogeneities of a hot-wire deposited hydrogenated Si-Ge-alloy (blue triangles). The solid line passing the blue triangles represents a mass fractal model function taken from [38].

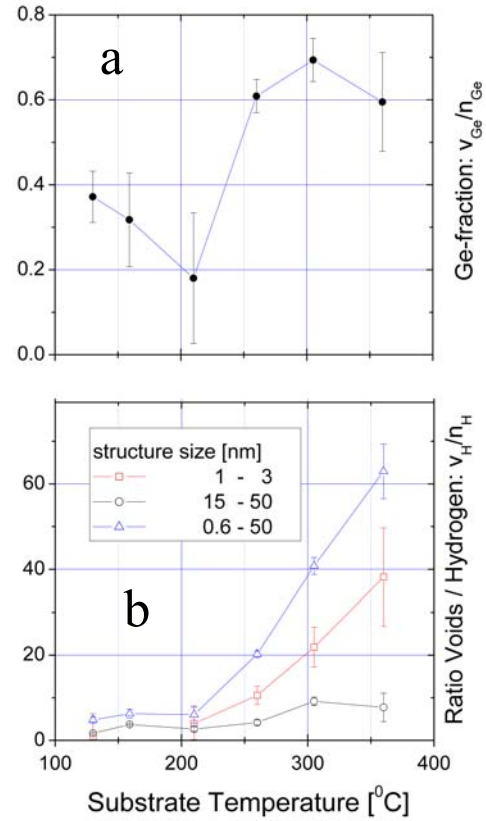


Figure 5: The fraction of Ge-atoms implemented in the suggested fractal structure (a). The ratio of void scattering relative to the scattering expected from the hydrogen implemented in the amorphous matrix (b).

When the integral intensity of the non-resonant contribution is calculated in the q -range between 1 and 3 nm^{-1} (corresponding to structure sizes between 3 and 1 nm) the integral value reaches more than 50% of the value obtained from the overall integration (red symbols), while the integration in the q -range between 0.06 and 0.2 (corresponding to structure sizes between 50 and 15 nm) shows only a weak dependence on the temperature with clearly lower values of $\overline{v_H}/n_H$ (black symbols). So one can conclude that the ratio $\overline{v_H}/n_H$ represents the

ratio of voids to hydrogen atoms (i.e the volume fractions) and that the non-resonant scattering contribution is clearly dominated by the scattering of voids with sizes of about several nm at higher substrate temperatures. These voids are strongly reduced when the substrate temperature is lowered and the optimum is reached, when the formation of the Ge mass fractals reaches a relative maximum in coincidence with a strongly reduced void fraction. The two processes cause the structural re-organization of Hydrogen from voids into Ge-fractals with enhanced Ge-H bonding, thereby improving the material photoconductivity. The latter was confirmed by IR-measurements indicating enhanced GeH bonding for these temperatures [36,37].

6. Spinodal decomposition of Ni-Nb-Y metallic glasses probed by quantitative Anomalous Small-Angle X-ray Scattering

6.1. Sample preparation and ASAXS measurements

The ternary Ni-Nb-Y system exhibits an extended miscibility gap in the liquid [39]. By means of rapid quenching technique the decomposed melt can be frozen into a phase separated metallic glass [40]. The critical temperature of liquid-liquid decomposition depends on the composition. For Ni-content < 60 at% a hierarchical heterogeneous microstructure is obtained with size distribution from 10 nm up to 500 nm which can be analyzed by transmission electron microscopy (TEM). Such microstructures represent a coarsened state of spinodal decomposition, growth of the melts, and secondary decomposition within the liquids. For such phase separated Ni-Nb-Y glasses SAXS curves with fractal q-dependence have been observed [41]. For alloys with Ni-contents > 60 at% early stages of phase separation can be obtained due to reduced critical temperature having fluctuations in nm dimensions with almost no contrast in TEM images [42]. By means of ASAXS quantitative parameters of the fluctuation can be determined.

In the following results from a sample with the composition $\text{Ni}_{68}\text{Nb}_{16}\text{Y}_{16}$ are presented. The sample was prepared by single-roller melt spinning under argon atmosphere. The casting temperature was 1923 K. Details of sample preparation are published in [39]. Additionally, a partly crystallized sample, $c\text{-Ni}_{68}\text{Nb}_{16}\text{Y}_{16}$, was produced by heating part of the ribbons in a

differential scanning calorimeter (DSC 7, Perkin Elmer) just above the temperature of the first exothermic crystallization event at 773 K over 30 min.

ASAXS sequences were performed for both samples with four X-ray energies in the vicinity of the K-absorption edges of nickel at 8333 eV, yttrium at 17038.4 eV and niobium at 18985.6 eV [S2]. For the three very different energy ranges nearly the same q-range was covered.

6.2. The determination of chemical concentrations located in the thermal fluctuations caused by spinodal decomposition in ternary Ni-Nb-Y metallic glasses

The influence of partial crystallization on the SAXS curves is shown in Figure 6 by the comparison of the scattering curves of the two alloys. Both samples show a correlation maximum corresponding to a correlation length of 12.2 nm, which represents the spatial extension (wavelength) of the concentration fluctuations or the distance between the crystallized domains in case of the partially crystallized sample. The heat treated sample consists of a nanocrystalline Ni_2Y phase and a remaining amorphous Ni-Nb phase. In the SAXS curves a dramatic change takes place for the sample, which was heat treated beyond the 1st crystallization temperature. Though the correlation maximum remains unchanged on the q-axis, it is shifted on the y-axis by nearly an order of magnitude probably due to a higher electron density contrast caused by a larger concentration gradient. Additionally the asymptotic behaviour changes from q^{-2} to q^{-4} indicating the formation of small crystallites with smooth interfaces to the surrounding phase. Obviously the fluctuation length of the as-

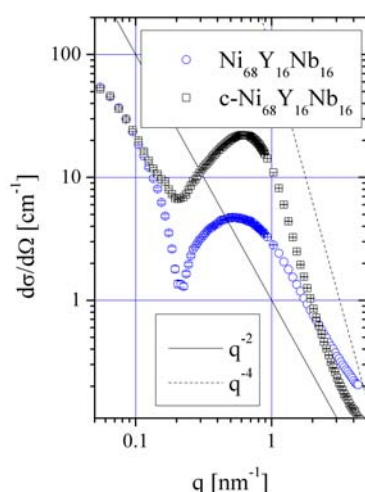


Figure 6. Total scattering curves of the alloy $\text{Ni}_{68}\text{Nb}_{16}\text{Y}_{16}$ with different heat treatments: as-quenched (blue circles) and heat-treated above the first crystallization point at 773 K but below the second crystallization point (black squares). Above the first crystallization point the asymptotic behavior of the scattering curves changes from q^{-2} to q^{-4} , indicating smooth interfaces probably between the small crystallites and the surrounding amorphous phase.

quenched state determines the size of the nanocrystals. Because the nickel component serves as the matrix, the important quantitative parameters of decomposition are related to the concentration fluctuations of yttrium and niobium and thus have been obtained from quantitative ASAXS measurements at the K-absorption edges of yttrium and niobium.

Figure 7 shows the first derivative of the Resonant Invariant for yttrium of the as-quenched sample (a) and the crystallized sample (b). The grey areas represent the integrals, deduced from Q_Z (i.e. the Resonant Invariant), which are inserted into Eq.12 for the calculation of the amount of yttrium atoms, \bar{v}_Y , which enter the concentration fluctuations of the as-quenched sample and the crystallites of the heat-treated sample respectively.

From Eq.12 an amount of $2.13(28) \cdot 10^{21} \text{ cm}^{-3}$ yttrium (excess) atoms, which enter the crystallites, was calculated corresponding to about 19% of the Y-atoms in the alloy. A completely different result was obtained from the analysis of the Resonant Invariant of the as-quenched sample. As can be seen already from a simple comparison of the integrals of both samples in Figure 7, the amount of yttrium atoms, which enter the concentration fluctuations must be smaller. From Eq.12 a concentration of $0.39(20) \cdot 10^{21} \text{ cm}^{-3}$ yttrium atoms was deduced, which corresponds to an amount of only 4% yttrium atoms.

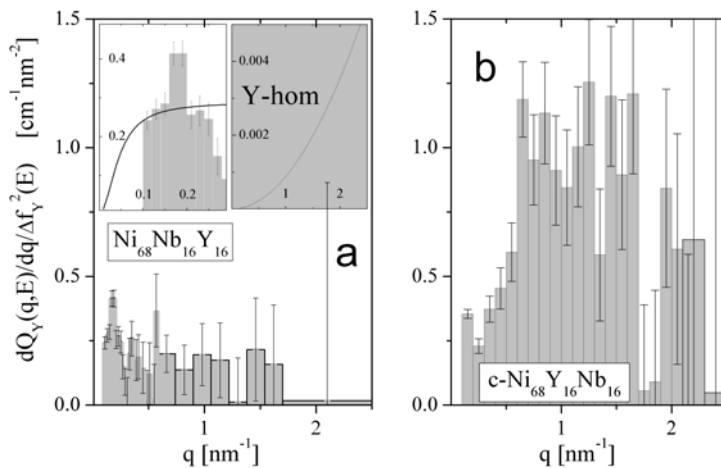


Figure 7. The first derivative of the Resonant Invariant (Eq.11) of (a) as-quenched and (b) partially crystallized $\text{Ni}_{68}\text{Nb}_{16}\text{Y}_{16}$ obtained from ASAXS sequences at the Y K-edge (17038 eV). The integrals (grey area) represent the Resonant Invariant from which the Y concentrations can be calculated. The right inset represents the upper limit of 16 at.% homogeneously distributed Y, contributing to the Resonant Invariant. The left inset explains the contribution that is missing due to the q-resolution.

Though this result is significant, it is near the resolution limits of the experiment as can be seen from the error bars in Figure 7a. For a more quantitative discussion of the result, the limited integration area has to be extended onto the whole regime $0 \leq q < \infty$. Because no comprehensive description of the scattering curves of a ternary alloy undergoing spinodal decomposition is at hand, a model function with a q^{-2} -behaviour (Ornstein-Zernike originally for binary systems) was employed. The model function serves only as a guide for the eye with the aim to estimate the amount of the ‘missing’ scattering contributions at higher and lower q -values i.e. beyond the resolution of the experiment (left inset in Figure 7a).

At $q=0$ the model function reaches a finite value defined by thermodynamic parameters of the alloy and the first derivative of the Resonant Invariant approaches 0 with $q \rightarrow 0$. The amount of the missing contribution to the Resonant Invariant can be neglected as can be seen from the left inset in Figure 7a, which shows a magnified part of the Resonant Invariant in the low q -range. The missing part below the resolution at q -values smaller q_{\min} is the area between the grey histogram and the solid line of the model function.

The right inset in Figure 7a represents the contribution of homogeneously distributed Y-atoms with a concentration of 16 at% to the Resonant Invariant. Although this corresponds to the maximum possible amount – a considerable portion of the Y-atoms are localized in the fluctuations – the contribution is many orders of magnitude smaller than the contribution detected from the Y-atoms in the concentration fluctuations and thus can be also neglected.

Considering the scattering contributions beyond the q -resolution at higher q -values the result must be interpreted as a lower limit as is demonstrated by the model function (Figure 7a). At higher q -values a cut-off of the scattering function is expected, because otherwise the integral of Eq.11 would become infinite and no characteristic would ascertainable anymore. As can be seen from Figure 7a the cut-off of the pure-resonant contribution cannot be resolved due to the large error bars (at 2 nm^{-1} the error bar is more than an order of magnitude larger compared to the value) and if the cut-off is located at q -values beyond 2 nm^{-1} , the concentration of yttrium atoms must be higher. An extension of the upper integration limit to $q_{\max}=15\text{nm}^{-1}$, which roughly corresponds to the nearest neighbor atomic distance cannot provide additional significant contributions. On the other hand recent atom probe measurements on similar alloys $\text{Ni}_{66}\text{Nb}_{17}\text{Y}_{17}$ [43] have confirmed the quantitative results of

the RI-analysis outlined in this paper. In the case of the crystallized sample the scattering curve at larger q -values extends deeply into the Porod regime and no significant contribution can appear in the integral at higher q -values. Similar results were deduced for niobium from RI-analysis at the K-absorption edge of niobium [S2].

7. Discussion

The central issue solved by this habilitation thesis was the achievement of accuracies of ASAXS measurements which enables the separation of the pure-resonant scattering contribution of different chemical species in multi-component systems followed by a quantitative analysis of the Resonant-Invariant. This was documented by the concentration analysis of the Sr-counter ion condensation on polyanions, the analysis of the Ge-content in mass fractals of Si-Ge-alloys and finally the determination of the chemical concentrations of yttrium respectively niobium atoms in the concentration fluctuations of spinodal decomposed metallic glasses of Ni-Nb-Y. The comparison of the three examples shows, that the method of quantitative Anomalous Small-Angle X-ray Scattering has been successfully applied to very different systems from chemistry and solid state physics. Additionally these selected examples were supplemented by ASAXS studies performed on further (again very different) systems like highly porous structures with metal components, which serve as catalysts [S3] or bio-membranes used for the synthesis of semiconductor colloids [S5]. Another study analyzed the localisation of dibromophenol in a multilamellar vesicle system constituted from DPPC and water [S8]. The studies [S1-S9] have been the first, making use of the above-mentioned Gaussian elimination procedure for separating the pure-resonant scattering, followed by subsequent quantitative analysis of the Resonant Invariant (RI-analysis) [S1-S4,S6]. Though these systems are physically and chemically very diverse (solid and fluid aggregate states) and belong to very different structure classes (sphere-like colloids, spinodal concentration fluctuations, mass fractals, metal components on highly porous substrate structures, multilamellar vesicles), precise ASAXS measurements in combination with the Gauss algorithm of data analysis turned out to be a very efficient experimental technique, for the combined structural and quantitative analysis of the related chemical nano-phases and their correlation with the related phase diagrams (i.e. chemical concentrations) or the macroscopic properties of the materials. It is worth to shed some light on the mathematics, which give information

about the conditioning of the vector equation allowing the matrix to be safely inverted and thus rendering the mentioned information.

Of course the Gauss algorithm minimizes the errors when inverting Eq.5, but other methods do the same and a more general concept is needed with the aim, to quantify the required accuracies in the experiment, which are necessary to successfully separate the pure-resonant scattering contribution from measured scattering curves with a relative error of $\Delta I/I$. In other words, it is important to analyze whether the matrix is well conditioned (i.e. it can be safely inverted), which can be done by the determination of the so-called Turing number, $T(M)$, associated with this matrix (Eq.8), where $T(M) = 1/3 \cdot \|M\| \cdot \|M^{-1}\|$ with $\|M\|$ the square root of the sum on i and j of M_{ij}^2 and $\|M^{-1}\|$ the same for the inverse matrix of Eq.5 or $\|M'\|$, $\|M'^{-1}\|$ in case of Eq.6 respectively. A pioneering theoretical analysis of the mathematical problem related to ASAXS measurements has been done in an early study in 1985 [11] with the conclusion that ASAXS with the accuracy of the synchrotron radiation based experiments in those days could not cope with the better (concerning the mathematical conditioning) neutron experiments. Within the last decade results of synchrotron based ASAXS-experiments (see above) became available, which can be directly compared to the theoretical predictions in [11] with the following result: Due to the strongly improved accuracy of synchrotron radiation experiments mentioned in chapter 3 in combination with a suitable algorithm (Gauss) safe matrix inversions have been achieved giving direct access to the basic scattering functions especially to the pure-resonant scattering thereby offering a subsequent quantitative analysis. The Turing number quantifies the amount of error propagation due to Eq.14 [10]:

$$\frac{\|\Delta A\|}{\|A\|} \leq 3 \cdot T(M) \cdot \frac{\|\Delta I\|}{\|I\|}, \quad (14)$$

where

$$\|\Delta I\| = \sqrt{\sum_{i=1}^3 \Delta I_i^2}, \quad \|I\| = \sqrt{\sum_{i=1}^3 I_i^2}$$

and

$$\|\Delta A\| = \sqrt{\sum_{i=1}^3 \Delta A_i^2}, \quad \|A\| = \sqrt{\sum_{i=1}^3 A_i^2} \quad (15)$$

mean the norm of the vectors (respectively of the related error vectors) in the Eqs.5-6:

$$I = \begin{pmatrix} I(E_1) \\ I(E_2) \\ I(E_3) \end{pmatrix}, \quad A = \begin{pmatrix} |A_0(q)|^2 \\ \text{Re}(A_0(q)A_R(q)) \\ |A_R(q)|^2 \end{pmatrix} \quad (16)$$

$\|\Delta I\|/\|I\|$ and $\|\Delta b\|/\|b\|$ are the relative errors of the vectors on the right hand (Eq.5) and left hand side of Eq.6 respectively, where the vector components b_i represent composites of the vector components I_i . Thus the right hand side of Eq.14 gives the maximum error of $\|\Delta A\|/\|A\|$, which can occur due to error propagation, when inverting Eq.5 or Eq.6 [10,11]. To calculate a simple example let us assume an accuracy of the basic scattering functions of $\|\Delta A\|/\|A\| < 0.1$ is desired. If a Turing number of the system of linear equations amounts 33.3, then an accuracy of $\|\Delta I\|/\|I\| = 10^{-3}$ is required for the scattering curves measured at the three different energies in order to achieve the desired accuracy of 10% for the basic scattering functions when inverting the matrix. The identity matrix will give the lowest possible Turing number equal to 1 (i.e. lowest amplification of the errors). The relative errors on the components A_j , when inverting Eq.5, are indeed related to this number. The higher it is the higher the amplification of the errors will be.

For demonstration the Turing numbers of the three outlined scientific examples are summarized in Table 2. It is interesting to compare the Turing numbers of the different matrix inversion procedures due to Eq.5 and Eq.6 respectively. As can be seen from the 3rd column in Table 2 the Turing numbers $T(M')$ are much smaller, when the Gauss algorithm is applied. Taking example 3 (the Ni-Nb-Y alloy) the Turing number $T(M)$ of the matrix inversion of Eq.5 is 7 seven times larger compared to the Turing number $T(M')$ of the elimination procedure represented by the matrix in Eq.6. This suggests that better results can be obtained by employing the Gauss algorithm but as can be seen from Eq.14 the Turing condition depends not only on the Turing number $T(M)$ but also on the relative error $\|\Delta I\|/\|I\|$ of the vector on the right hand side. When changing from $T(M)$ to $T(M')$ in Eq.14 the relative error of the right side vector changes via error propagation to:

$$\|\Delta b\|/\|b\| = k \cdot \|\Delta I\|/\|I\|; \quad k \approx \sqrt{5 + 2 \cdot \left(\frac{f'(E_3) - f'(E_1)}{f'(E_2) - f'(E_1)} \right)^2} \quad (17)$$

provided that the scattering curves I_i have nearly the same magnitude and thus nearly the same error ΔI_i . For details see Eq.7 in [S1]. The factor k is listed in the 5th column of Table 2. Now we imagine as a gedankenexperiment two independent measurements of scattering curves I_i and J_i . For the 1st set of scattering curves, I_i , we perform the inversion of Eq.5 with the Turing number $T(M)$ and for the 2nd set, J_i , we use the inversion due to Eq.6 with Turing number $T(M')$. The relative errors of the basic functions write:

$$\begin{aligned} \frac{\|\Delta A\|}{\|A\|} &\leq 3 \cdot T(M) \cdot \frac{\|\Delta I\|}{\|I\|} \\ \frac{\|\Delta A'\|}{\|A'\|} &\leq 3 \cdot T(M') \cdot \frac{\|\Delta b\|}{\|b\|} = 3 \cdot T(M') \cdot k \cdot \frac{\|\Delta J\|}{\|J\|} \end{aligned} \quad (18)$$

In the next step we demand, that the errors of the basic scattering functions calculated from both measurements are the same: $\|\Delta A\|/\|A\| = \|\Delta A'\|/\|A'\|$. From the latter we obtain:

$$3 \cdot T(M) \cdot \frac{\|\Delta I\|}{\|I\|} = 3 \cdot T(M') \cdot k \cdot \frac{\|\Delta J\|}{\|J\|} \quad \text{or} \quad \frac{\|\Delta J\|/\|J\|}{\|\Delta I\|/\|I\|} = \frac{T(M)}{T(M') \cdot k} = \varepsilon \quad (19)$$

In other words the relative accuracy of the two independent measurements, which lead to the same accuracy for the calculated basic scattering functions scale with the ratio $\varepsilon = T(M)/T(M')/k$. in the 6th column of Table 2. The number ε gives a measure of error propagation due to the employed inversion. Eq.19 tells that the same accuracy in the basic scattering functions is obtained with less accuracy in the measured scattering curves, when the Gauss algorithm is employed. To explain in more detail we take the most striking example in Table 2 i.e. the Ni-Nb-Y-alloy with $\varepsilon = 2.4$. When using the Gauss algorithm the relative accuracy of the measured scattering curves can be 2.4 times smaller, thereby the exposure time can be 5.3 (!) times shorter, because the error predominantly is caused by the statistics of the count rates i.e. the error reduces with the square root of the measurement time.

When introducing the typical relative error of the scattering curves obtained from the ASAXS measurements of chapters 4,5,6, which amounts $\Delta I/I = 10^{-3}$, the maximum error of the basic

scattering function is estimated to be about 35% ($\|\Delta A\|/\|A\|_{0.001}$ in the 7th column of Table2). These numbers represent upper limits due to the inequality of the Turing condition i.e. the real errors are smaller.

The examples demonstrate the decisive relevance of the precise measurement of all related experimental parameters entering the ASAXS sequence (see chapter 3) in context with a suitable mathematical algorithm, when dealing with the quantitative analysis of the pure-resonant scattering contribution by analysis of the Resonant-Invariant (*q*-ASAXS). Concerning the mathematical algorithm it is necessary to employ reliable confidence tests in order to provide the degree of error propagation introduced by the conducted matrix inversion. The Turing number represents in this sense a powerful tool for the ASAXS technique not only for the estimation of the error, which must be expected for a given ASAXS sequence, but also for planning a complete ASAXS beam time. The required statistical accuracies, which have to be achieved for the scattering curves defines important parameters of the whole ASAXS sequence like measurement time, the energies to be chosen, accuracies of flux and transmission measurements, calibration accuracy etc. Moreover a straight forward error calculation, which starts with the (statistical) errors of the measurements and calculates the error propagation through the Eqs.6-7 is required. The error bars of Fig.2-7 are the result of such straight forward calculations of the error propagation.

Table 2: Comparison of the Turing numbers calculated for the ASAXS sequences of (a) Sr²⁺ counter ion distributions around polyacrylates, (b) amorphous hydrogenated silicon germanium alloys, and (c) metallic glasses Ni-Nb-Y. The different Turing numbers T(M) and T(M') refer to the different matrix inversions due to Eq.5 and Eq.6 respectively. T(M') is the Turing number of the Gauss elimination procedure. In the case of Sr-PAA two values are possible because the scattering data are compatible with a positive respectively negative contrast Δf_0 . The negative contrast is confirmed by the negative sign of the Mixed-Resonant scattering term S_{0R} . In the 7th columns the worst error $\|\Delta A\|/\|A\|$ for the basic scattering functions after Gauss inversion is listed assuming a relative error of 10^{-3} in the scattering curves. These numbers represent upper limits due to the inequality of the Turing condition i.e. the real errors are smaller.

System	T(M)	T(M')	T(M)/T(M')	k	ϵ	$\ \Delta A\ /\ A\ _{0.001}$
SrPAA +/-	158/184	54/52	2.9/3.5	2.6	1.1/1.3	0.42/0.41
Si-Ge	176	39	4.5	3.0	1.5	0.35
Ni-Nb-Y	283	38	7.4	3.1	2.4	0.35

8. Summary and future perspectives

In the last decade Anomalous Small-Angle X-ray Scattering became a precise quantitative method for element specific structural analysis on the mesoscopic length scale. Due to the precision of the techniques small-angle scattering contributions in the resolution regime $10^{-3} < \Delta I/I < 10^{-2}$ can be reliably separated and the pure-resonant scattering of numerous multi-component systems becomes accessible for quantitative analysis.

The pure-resonant scattering contributions (1) of a diluted chemical solution of negatively charged polyacrylates surrounded by divalent Sr-counter ions, (2) of hydrogenated semiconductor (silicon-germanium) alloys and (3) of metallic glasses (Ni-Nb-Y) one of them in the state of spinodal decomposition have been analyzed quantitatively. From the calculation of the Resonant Invariant (RI) the amount of Sr-ions localized in the partially collapsed sub-domains of polyacrylate colloids was deduced. From the RI-analysis of hotwire deposited hydrogenated silicon-germanium alloys the amount of germanium atoms located in 40 nm sized mass fractals was determined. Moreover from the analysis of the Non-resonant Invariant (NI-analysis) the structural reorganization of hydrogen from voids into mass fractals was deduced. The latter could be correlated to enhanced photo conductivity of the semiconductor alloy. In a 3rd example the amount of Y-atoms (respectively Nb-atoms) located in concentration fluctuations with a correlation length of 15 nm was determined by RI-analysis and compared to an alloy of the same composition, after heat treatment causing partially re-crystallization.

For the separation of the basic scattering functions the Gauss algorithm was employed. The error propagation of the measurement errors through the vector equation stated by the ASAXS measurements of the three different systems was estimated by calculation of the Turing number. The estimated errors have been confirmed by subsequent straight forward calculations of the error propagation.

All examples underline that 3rd generation sources with superior beam stabilities and photon flux properties are needed to improve the experimental accuracy of ASAXS measurements towards $\Delta I/I=10^{-4}$ or even below this value. Moreover the 3rd generation machines with sufficient machine energies (> 3 GeV) and an emittance of about 1 nmrad will offer extraordinary possibilities for ASAXS for instance (1) access to the K-absorption edges of the heavier elements enabling the construction of spatially extended in-situ cell structures for fuel cell or catalysis research [44]. (2) In combination with the high photon flux of such machines

quantitative time-resolved ASAXS studies below the millisecond regime will become possible. (3) The vanishing beam divergence (at high β) gives access to q -values down to 10^{-3} nm^{-1} , which correspond to the length scale of large scale structures in the micrometer range. This size scale is up to now routinely accessible only for neutron experiments i.e. Very Small-Angle Neutron Scattering with limited neutron flux (V-SANS) [45].

9. References

9.1. Contributions by the author establishing the habilitation

[S1] G. Goerigk, and N. Mattern,
Spinodal Decomposition in Ni-Nb-Y Metallic Glasses Analyzed by Quantitative Anomalous
Small-Angle X-ray Scattering,
Journal of Physics: Conference Series 247, 012022 (2010)

[S2] G. Goerigk, and N. Mattern,
Critical Scattering of Ni-Nb-Y Metallic Glasses Probed by Quantitative Anomalous Small-
Angle X-ray Scattering
Acta Materialia, 57, 3652-3661 (2009)

[S3] A. Bota, Z. Varga, and G. Goerigk,
Structural Description of the Nickel Part of a Raney-Type Catalyst by Using Anomalous
Small-Angle X-ray Scattering
Journal of Physical Chemistry C, 112(12), 4427 (2008)

[S4] G. Goerigk, K. Huber, and R. Schweins,
Probing the Extent of the Sr^{2+} - Ion Condensation to Anionic Polyacrylate Coils: A
Quantitative Anomalous Small-Angle X-ray Scattering Study
J. Chem. Phys., 127, 154908-1 (2007)

[S5] A. Bota, Z. Varga, and G. Goerigk,
Biological Systems as Nanoreactors: Anomalous Small-Angle Scattering Study of the CdS
Nanoparticle Formation in Multilamellar Vesicles
J. Phys. Chem. B, 111(8), 1911 (2007)

[S6] G. Goerigk, and D.L. Williamson,
Temperature Induced Differences in the Nanostructure of Hot-wire Deposited Silicon-
Germanium Alloys Analyzed by Anomalous Small-Angle X-ray Scattering
J. Appl. Phys. 99, 084309 (2006)

[S7] R. Schweins, G. Goerigk, and K. Huber,
Shrinking of Anionic Polyacrylate Coils Induced by Ca^{2+} , Sr^{2+} and Ba^{2+} : A Combined Light
Scattering and ASAXS Study
Eur. Phys. J. E 21, 99-110 (2006)

[S8] Z.Varga, A. Bota, and G. Goerigk,
Localization of Dibromophenol in DPPC/Water Liposomes Studied by Anomalous Small-
Angle X-ray Scattering
J. Phys. Chem. B, Vol. 110, No. 23, 11029- 11032 (2006)

[S9] G. Goerigk, R. Schweins, K. Huber, and M. Ballauff,
The Distribution of Sr^{2+} Counterions around Polyacrylate Chains Analyzed by Anomalous
Small-Angle X-ray Scattering
Europhys. Lett. 66 (3), pp. 331-337 (2004)

9.2. Other References

- [1] A. Guinier, and G. Fournet: Small-Angle Scattering of X-rays. New York: Wiley (1955)
- [2] O. Glatter, and O. Kratky: Small-Angle X-ray Scattering. London: Academic Press (1982)
- [3] O. Kratky, Die Welt der vernachlässigten Dimensionen und die Kleinwinkelstreuung von Röntgenstrahlen und Neutronen an biologischen Makromolekülen. Nova Acta Leopoldina 55 (256) 72 (1983)
- [4] J. P. Simon, J. Appl. Cryst. (2007). 40, 1–9
- [5] F.B. Rasmussen, A.M. Molenbrock, B.S. Clausen & Feidenhans'l R., J. Catalysis, 190, 205-208 (2000)
- [6] G. Zehl, G. Schmidhals, A. Hoell, S. Haas, C. Hartnig, I. Dorbrandt, P. Bogdanoff, and S. Fiechter, Angew. Chem. Int. Ed., 46, 7311 – 7314 (2007)
- [7] D. Tatchev, A. Hoell, M. Eichelbaum, and K. Rademann, Phys. Rev. Lett., 106,085702-1 – 0857702-4 (2011)
- [8] M. Patel, S. Rosenfeldt, M. Ballauff, N. Dingenouts, D. Pontoni, and T. Narayanan, Phys. Chem. Chem. Phys., 6, 2962-2967 (2004)
- [9] H.B. Stuhmann, Advances in Polymer Science, 67, 123-163 (1985)
- [10] J. Westlake, A Handbook of Numerical Matrix Inversion and Solution of Linear Equations. New York: J. Wiley and Sons (1968)

- [11] J.P. Simon, O. Lyon, D. de Fontaine, *J. Appl. Cryst.* 18, 230-236 (1985)
- [12] J.M. Dubuisson, J.M. Dauvergne, C. Depautex, P. Vachette, C.E. Williams, *Nuclear Instruments and Methods*, 246, 1-3, 636-640 (1986)
- [13] H.-G. Haubold, K. Gruenhagen, M. Wagener, H. Jungbluth, H. Heer, A. Pfeil, H. Rongen, G. Brandenburg, R. Moeller, J. Matzerath, P. Hiller & H. Halling, *Rev.Sci.Instrum.* 60, 1943 (1989)
- [14] G. Goerigk 'Electronic and Computer Upgrade at ASAXS Beamline JUSIFA', *HASYLAB Annual Report*; p. 77 (2006)
- [15] J.L. Ferrer, J.-P. Simon, J.-F. Bézar, B. Caillot, E. Fanchon, O. Kaikati, S. Arnaud, M. Guidotti, M. Pirocchi, and M. Roth, *J. Synchr. Rad.* 5, 1346-1356. (1998)
- [16] J.-P. Simon, S. Arnaud, F. Bley, J.F. Bézar, B. Caillot, V. Comparat, E. Geissler, A. de Geyer, P. Jeantet, F. Livet, and H. Okuda, *J. Appl. Cryst.* 30, 900-904 (1997)
- [17] A. Hoell, I. Zizak, H. Bieder, L. Mokrani, Patent DE 10 2006 029 449
- [18] G. Goerigk, H-G. Haubold, O. Lyon, and J.-P. Simon, *J. Appl. Cryst.* 36, 425-429 (2003)
- [19] A. Gabriel, *Rev. Sci. Instrum.* 48, 1303-1305 (1977)
- [20] I.J. Michaeli, *Polym. Sci.*, 48, 291 (1960)
- [21] K. Huber, *J. Phys. Chem.*, 97, 9825 (1993)
- [22] D.T. Cromer, & D. Liberman, *J.Chem.Phys.* 53, 1891 (1970)
- [23] D.T. Cromer, & D. Liberman, *Acta Cryst.* A37, 267 (1981)
- [24] R. Schweins, P. Lindner, & K. Huber, *Macromolecules*, 36, 9564 (2003)
- [25] A.V. Dobrynin, M. Rubinstein, & S.P. Obukhov, *Macromolecules* 29 2974 (1991)
- [26] U. Micka, Ch. Holm, & K. Kremer, *Langmuir*, 15, 4033 (1999)
- [27] P. Chodanowski, & S. Stoll, *J. Chem. Phys.* 111, 6069 (1999)
- [28] H.J. Limbach, & Ch. Holm, *J. Phys. Chem. B*, 107, 8041 (2003)
- [29] D.L. Williamson, *Mater. Res. Soc. Symp. Proc.* 377, 251 (1995)
- [30] G. Goerigk, and D.L. Williamson, *Solid State Commun.* 108, 419 (1998)
- [31] G. Goerigk, and D.L. Williamson, *J. Non-Cryst. Solids* 281, 181 (2001)
- [32] G. Goerigk, and D.L. Williamson, *J. Appl. Phys.* 90, 5808 (2001)
- [33] E.C. Molenbroek, A.H. Mahan, and A. Gallagher, *J. Appl. Phys.* 82, 1909 (1997)

- [34] B.P. Nelson, Y. Xu, D.L. Williamson, B. von Roedern, A. Mason, S. Heck, A.H. Mahan, S.E. Schmitt, A.C. Gallagher, J. Webb, and R. Reedy, *Mat. Res. Soc. Symp. Proc.* 507, 447 (1998)
- [35] B.P. Nelson, Y. Xu, D.L. Williamson, D. Han, R. Braunstein, M. Boshta, and B. Alavi, *Thin Solid films* 430, 104 (2003)
- [36] Y. Xu, B.P. Nelson, D.L. Williamson, L.M. Gedvilas, and R.C. Reedy, *Mat. Res. Soc. Symp. Proc.* 762, A 10.2 (2003)
- [37] Y. Xu, B.P. Nelson, L.M. Gedvilas, and R.C. Reedy, *Thin Solid Films* 430, 197 (2003)
- [38] G. Beaucage, *J. Appl. Cryst.* 28, 717-728 (1995)
- [39] N. Mattern, M. Zinkevich, W. Löser, G. Behr, J.J. Acker, *Phase Equil. Diff.*; 29: 141 (2008)
- [40] N. Mattern, U. Kühn, A. Gebert, T. Gemming, M. Zinkevich, H. Wendrock, L. Schultz, *Scripta Materialia*; 53: 271 (2005)
- [41] N. Mattern, T. Gemming, G. Goerigk, J. Eckert, *Scripta Mater.*; 57: 29 (2007)
- [42] N. Mattern, G. Goerigk, U. Vainio, M.K. Miller, T. Gemming, and J. Eckert, *Acta Mater.*; 57: 903 (2009)
- [43] A. Shariq, N. Mattern, *Ultramicroscopy*; 111: 1370 (2011)
- [44] G. Goerigk, in *PETRA-III Technical Design Report* Editors: K. Balewski, W. Brefeld, W. Decking, H. Franz, R. Röhlberger, E. Weckert, DESY, Hamburg, Germany, 316 (2003)
- [45] G. Goerigk, and Z. Varga, *J. Appl. Cryst.*, 44, 337-342 (2011)

[S1]

G. Goerigk, and N. Mattern,

Spinodal Decomposition in Ni-Nb-Y Metallic Glasses Analyzed by

Quantitative Anomalous Small-Angle X-ray Scattering,

Journal of Physics: Conference Series 247, 012022 (2010)

Spinodal Decomposition in Ni-Nb-Y Metallic Glasses Analyzed by Quantitative Anomalous Small-Angle X-ray Scattering

G.Goerigk¹ and N.Mattern²

¹Institut für Festkörperforschung, Forschungszentrum Jülich, Postfach 1913, D-52425 Jülich, Federal Republic of Germany, ²Leibniz-Institute IFW Dresden, Institute for Complex Materials, P.O. Box 270116, D-01171 Dresden, Federal Republic of Germany

G.Goerigk@fz-juelich.de

Abstract. Phase separated Ni-Nb-Y metallic glasses were prepared by means of rapid quenching from the melt. Quantitative Anomalous Small-Angle X-ray Scattering experiments were performed at the K-absorption edges of Nickel, Niobium and Yttrium. The paper outlines, that the separation of the pure-resonant scattering contribution is obtained by employing the Gaussian algorithm on a vector equation. Moreover the quantitative analysis of the Resonant Invariant at the K-absorption edges of Niobium and Yttrium provided the chemical concentrations of Yttrium and Niobium in the random density fluctuations, which are attributed to spinodal decomposition. The results are compared to a partially crystallized sample annealed at 773 K over 30 minutes.

1. Introduction

In the last 3 decades the Synchrotron Radiation (SR) provided the small-angle X-ray scattering technique with major improvements. Among other improvements SR provides a photon flux, which is many orders higher compared to classical X-ray sources giving access to systems with only weak SAXS contributions like highly diluted chemical solutions or solid state systems like glasses or amorphous alloys, which are to a high degree homogeneous. Additionally the continuous energy spectrum of SR allows energy tunability in the vicinity of the K- and L_{III}-absorption edges of most of the elements. This technique - known as Anomalous Small-Angle X-ray Scattering (*ASAXS*) – is based on the anomalous variations of the atomic scattering factors near the absorption edges and allows the element-specific structural and quantitative characterization of the sample under investigation. After the exploratory studies of the 1980s [1-3] *ASAXS* became in the last decade a precise quantitative technique (*q-ASAXS*), which combines the structural analysis with the quantitative analysis of chemical concentrations (i.e. fluctuations) of the different atomic species of a multi-component system by addressing the elements via the X-ray absorption edges [4-10].

The ternary Ni-Nb-Y system exhibits an extended miscibility gap in the liquid [11]. By means of rapid quenching technique the decomposed melt can be frozen in to a phase separated metallic glasses [12]. The critical temperature of liquid-liquid decomposition depends on the composition. For Ni content < 60 at% a hierarchical heterogeneous microstructure is obtained with size distribution from

10 nm up to 500 nm which can be analyzed by transmission electron microscopy (TEM). Such microstructures represent a coarsened state of spinodal decomposition, growth of the melts, and secondary decomposition within the liquids. For such phase separated Ni-Nb-Y glasses SAXS curves with fractal q-dependence have been observed [13]. For alloys with Ni > 60 at% early stages of phase separation can be obtained due to reduced critical temperature having fluctuation in nm dimensions with almost no contrast in TEM images. By means of *ASAXS* quantitative parameters of the fluctuation can be determined.

In this presentation, the application of the Gauss algorithm to the vector equation established by *ASAXS* measurements at three X-ray energies is demonstrated with the aim to separate the pure-resonant scattering contribution. Moreover the question shall be addressed, how to determine the amount of Yttrium respective Niobium atoms localized in the periodic fluctuations of Ni-Nb-Y metallic glasses undergoing spinodal decomposition with respect to the total amount of Y- respective Nb-atoms in the alloy, by quantitative analysis of what was introduced as the Resonant Invariant in a former publication [7].

2. ASAXS measurements

The remarkable possibilities of the *ASAXS* technique are based on the energy dependence of the atomic scattering factors giving selective access to the specific SAXS contributions of nanophases, which are built up by different chemical constituents in composites like for instance metallic glasses. In general the atomic scattering factors are complex quantities and energy dependent:

$$f_Z(E) = f_{0,Z} + f'_Z(E) + if''_Z(E) \quad (1)$$

where Z represents the atomic number. In this presentation we will deal with the atomic scattering factors of Ni, Y and Nb: $f_Z =: f_{Ni}(E), f_Y(E), f_{Nb}(E)$. When performing a SAXS experiment at energies in the vicinity of the absorption edge of one of the elements, three different scattering contributions can be distinguished as a consequence of Eq.(1)[1]:

$$I(q, E) = \Delta f_A^2 |A(q)|^2 + 2\Delta f_A \operatorname{Re} A(q) [\Delta f_{0,Z} + f'_Z(E)] \operatorname{Re} B(q) + [(\Delta f_{0,Z} + f'_Z(E))^2 + f''_Z(E)^2] |B(q)|^2 \quad (2)$$

$A(q)$ represents the scattering amplitude of the non-resonant scattering atoms and $B(q)$ represents the scattering amplitude of the resonant scattering atoms in the energy range of the absorption edge. The quantity $\Delta f_{0,Z} = f_{0,Z} - \rho_m V_Z$ is the electron density difference between the atom with the volume V_Z and the surrounding matrix of the alloy with the electron density ρ_m . q is the magnitude of the scattering vector $[= (4\pi/\lambda) \sin \Theta]$, where 2Θ is the scattering angle and λ the X-ray wavelength. For instance in the case of the Ni-Nb-Y alloys $[\Delta f_{0,Y} + f'_Y(E)] \operatorname{Re} B(q)$ represents the scattering amplitude (real part) of the inhomogeneously distributed Y-atoms in the alloy, when performing SAXS measurements in the energy range of the K-absorption edge of Yttrium, while $\Delta f_A \operatorname{Re} A(q)$ represents the scattering amplitude (real part) of the non-resonant scattering atoms i.e. Ni and Nb, with the contrast, Δf_A , of the non-resonant scattering atoms with respect to the entire matrix.

When measuring the scattering curves at three energies in the vicinity of the absorption edge of the atoms with atomic number Z the following vector equation can be established:

$$M_{ij}(E_i) \otimes A_j(q) = I_i(q, E_i) \quad (3a)$$

$$\begin{pmatrix} \Delta f_A^2 & 2\Delta f_A[\Delta f_{0,Z} + f'_Z(E_1)] & [(\Delta f_{0,Z} + f'_Z(E_1))^2 + f''_Z(E_1)^2] \\ \Delta f_A^2 & 2\Delta f_A[\Delta f_{0,Z} + f'_Z(E_2)] & [(\Delta f_{0,Z} + f'_Z(E_2))^2 + f''_Z(E_2)^2] \\ \Delta f_A^2 & 2\Delta f_A[\Delta f_{0,Z} + f'_Z(E_3)] & [(\Delta f_{0,Z} + f'_Z(E_3))^2 + f''_Z(E_3)^2] \end{pmatrix} \begin{pmatrix} |A(q)|^2 \\ \text{Re}(A(q)B(q)) \\ |B(q)|^2 \end{pmatrix} = \begin{pmatrix} I(q, E_1) \\ I(q, E_2) \\ I(q, E_3) \end{pmatrix} \quad (3b)$$

The vector on the right side represents the scattering curves measured at the three different energies E_1, E_2, E_3 while the vector on the left side represents the squared, respectively multiplied, scattering amplitudes. The matrix, $M_{ij}(E_i)$, contains the atomic scattering factors, which are energy dependent in case of the resonant scattering atoms. Combining the matrix with the vector on the right side of the equal sign yields the so-called extended matrix:

$$\begin{array}{ccc|c} \Delta f_A^2 & 2\Delta f_A[\Delta f_{0,Z} + f'_Z(E_1)] & [(\Delta f_{0,Z} + f'_Z(E_1))^2 + f''_Z(E_1)^2] & I(q, E_1) \\ \Delta f_A^2 & 2\Delta f_A[\Delta f_{0,Z} + f'_Z(E_2)] & [(\Delta f_{0,Z} + f'_Z(E_2))^2 + f''_Z(E_2)^2] & I(q, E_2) \\ \Delta f_A^2 & 2\Delta f_A[\Delta f_{0,Z} + f'_Z(E_3)] & [(\Delta f_{0,Z} + f'_Z(E_3))^2 + f''_Z(E_3)^2] & I(q, E_3) \end{array} \quad (4)$$

When applying the Gaussian algorithm (elimination procedure) to the extended matrix the so-called triangle matrix is obtained,

$$\begin{array}{ccc|c} a_{11} & a_{12} & a_{13} & b_1 \\ 0 & a_{22} & a_{23} & b_2 \\ 0 & 0 & a_{33} & b_3 \end{array} \quad (5)$$

where the $a_{i,j}, b_j$ are written in the matrix of Eq.(6):

$$\begin{array}{ccc|c} G & F(E_1) & H(E_1) & I(q, E_1) \\ 0 & F(E_2) - F(E_1) & H(E_2) - H(E_1) & I(q, E_2) - I(q, E_1) \\ 0 & 0 & H(E_3) - H(E_1) - \frac{F(E_3) - F(E_1)}{F(E_2) - F(E_1)}(H(E_2) - H(E_1)) & I(q, E_3) - I(q, E_1) - \frac{F(E_3) - F(E_1)}{F(E_2) - F(E_1)}(I(q, E_2) - I(q, E_1)) \end{array} \quad (6)$$

with

$$\begin{aligned} G &= \Delta f_A^2 \\ F(E_i) &= 2\Delta f_A(\Delta f_{0,Z} + f'_Z(E_i)) \\ H(E_i) &= (\Delta f_{0,Z} + f'_Z(E_i))^2 + f''_Z(E_i)^2 \end{aligned} \quad (7)$$

When introducing the formula of Eq.(7) into the matrix of Eqs.(5-6) the squared Fourier transform (FT) of the form factor, $|B(q)|^2$, of the spatial distribution of the atoms with atomic number Z can be calculated:

$$\begin{aligned} |B(q)|^2 &= \left[\frac{I(q, E_1) - I(q, E_2)}{f'_Z(E_1) - f'_Z(E_2)} - \frac{I(q, E_1) - I(q, E_3)}{f'_Z(E_1) - f'_Z(E_3)} \right] \cdot \frac{1}{F(E_1, E_2, E_3)} \\ F(E_1, E_2, E_3) &= f'_Z(E_2) - f'_Z(E_3) + \frac{f''_Z(E_1) - f''_Z(E_2)}{f'_Z(E_1) - f'_Z(E_2)} - \frac{f''_Z(E_1) - f''_Z(E_3)}{f'_Z(E_1) - f'_Z(E_3)} \end{aligned} \quad (8)$$

For this elimination procedure the matrix element M_{11} of the starting matrix - the so-called Pivotelement - must not be zero. After the first step the new 2x2 submatrix, $M'_{i,j}$ with the new Pivotelement $M'_{22} = F(E_2) - F(E_1)$ is obtained. Again the new Pivotelement must be not zero or in

other words the difference $M'_{22} = f'(E_2) - f'(E_1)$ obtained from Eq.(7) must be large enough to gain significant accuracy from the employed algorithm.

Due to Eq. (8) *ASAXS* provides a technique to access directly the scattering of the Z-atoms i.e. Ni or Y or Nb depending at which X-ray absorption edge the *ASAXS* measurements are performed. The structural information of the distribution of the Z-atoms (Ni or Y or Nb) in the alloy can be obtained from the analysis of $|B(q)|^2$, which we will call form factor for reason of convenience. More generally spoken, Eq. (8) provides a method, which gives access to the pure-resonant scattering contribution of the selected constituent of an alloy by measuring the small-angle scattering at only three suitable energies [5-10].

In addition to the structural information, which can be obtained from $|B(q)|^2$, important quantitative information related to the amount of inhomogeneously distributed Z-atoms can be deduced from the integral Q_Z :

$$Q_Z(E) = |\Delta f_Z(E)|^2 \int_Q |B(q)|^2 d^3q \quad (9)$$

In analogy to the so-called invariant [14], we will call $Q_Z(E)$ the Resonant Invariant of the inhomogeneously distributed resonant scattering Z-atoms. The invariant, $Q_Z(E)$, as defined in Eq. (9), is related to the number density of inhomogeneously distributed Z-atoms, \bar{v}_Z , as was outlined in detail in a previous publication [7,10]:

$$Q_Z(E) = |\Delta f_Z(E)|^2 \int_Q |B(q)|^2 d^3q = (2\pi)^3 r_0^2 |\Delta f_Z(E)|^2 \bar{v}_Z \left(\frac{1}{V_Z} - \bar{v}_Z \right) \quad (10a)$$

$$\frac{dQ_Z(E)}{dq} = |\Delta f_Z(E)|^2 4\pi |B(q)|^2 q^2 \quad (10b)$$

where $V_Z = 4\pi/3R_Z^3$ is the volume of the Z-atoms with atom radius R_Z and r_0 is the classical electron radius. Eq. (10b) represents the first derivative of the resonant invariant with respect to q . Finally from the quadratic Eq. (10a) two values for the number density of the Z-atoms can be calculated:

$$\frac{1}{\bar{v}_Z} - \bar{v}_Z = \frac{V_Z \cdot Q_Z(E)}{(2\pi)^3 \cdot r_0^2 |\Delta f_Z(E)|^2} = \frac{V_Z}{(2\pi)^3 \cdot r_0^2} \int_Q |B(q)|^2 d^3q \quad (11a)$$

$$\bar{v}_Z = \frac{1}{2V_Z} \pm \sqrt{\frac{1}{4V_Z^2} - \frac{1}{(2\pi)^3 r_0^2} \int_Q |B(q)|^2 d^3q} \quad (11b)$$

In this presentation only one of the two solutions is significant i.e. the negative sign. It should be mentioned that the number density calculated from Eq.(11b) includes the Z-atoms, which are homogeneously distributed in the alloy. These Z-atoms provide an isotropic scattering contribution at small q -values similar to the isotropic scattering of the alloys matrix atoms but with a different amount. As will be discussed in more detail below, the amount of the isotropic scattering contribution originating from these remaining Z-atoms in the matrix can be neglected.

3. Experimental

Pre-alloyed ingots were prepared by arc-melting elemental Ni, Nb and Y with purities of 99.9% or higher in a Ti-gettered argon atmosphere. To ensure homogeneity, the samples were remelted several

times. From these pre-alloys, thin ribbons (3 mm in width and 30 μm in thickness) with nominal compositions $\text{Ni}_{68}\text{Nb}_{16}\text{Y}_{16}$ were prepared by single-roller melt spinning under argon atmosphere. The casting temperature was 1923 K. The chemical compositions were determined by the titration technique. The resulting values were $\text{Ni}_{67.9}\text{Nb}_{17.3}\text{Y}_{14.8}$ for the as-prepared ribbons. These composition exhibit only slight deviations from the nominal value of up to ~ 1 at.%. For convenience, the nominal compositions are used in the following sections. Additionally, a partly crystallized sample, c- $\text{Ni}_{68}\text{Nb}_{16}\text{Y}_{16}$, was produced by heating part of the ribbons in a differential scanning calorimeter (DSC 7, Perkin Elmer) just above the temperature of the first exothermic crystallization event at 773 K over 30 min.

Anomalous small angle X-ray scattering (*ASAXS*) was measured with the JUSIFA beam line [15,16] at the DORIS storage ring at HASYLAB/DESY Hamburg. *ASAXS* sequences were performed for both samples $\text{Ni}_{68}\text{Nb}_{16}\text{Y}_{16}$ and c- $\text{Ni}_{68}\text{Nb}_{16}\text{Y}_{16}$ with three X-ray energies in the vicinity of the K-absorption edges of Nickel at 8333 eV and with four X-ray energies at the K-absorption edges of Yttrium at 17038.4 eV and Niobium at 18985.6 eV. The tables in Fig.1a-c provide the related anomalous dispersion corrections of Nickel, Yttrium and Niobium at the energies used in the experiment based on the calculations of Cromer and Liberman [17,18]. These were used to permit the separation of the Ni-, Y- and Nb-related pure-resonant scattering described in detail by Eqs. (1)-(8). The scattering intensity is calibrated into macroscopic scattering cross sections in units of cross section per unit volume [cm^2/cm^3]= $[\text{cm}^{-1}]$. Transmission measurements were performed with a precision of better 10^{-3} ($\Delta t/t=2.8 \times 10^{-4}$) using a special (windowless) photodiode (Hamamatsu S2387-1010N).

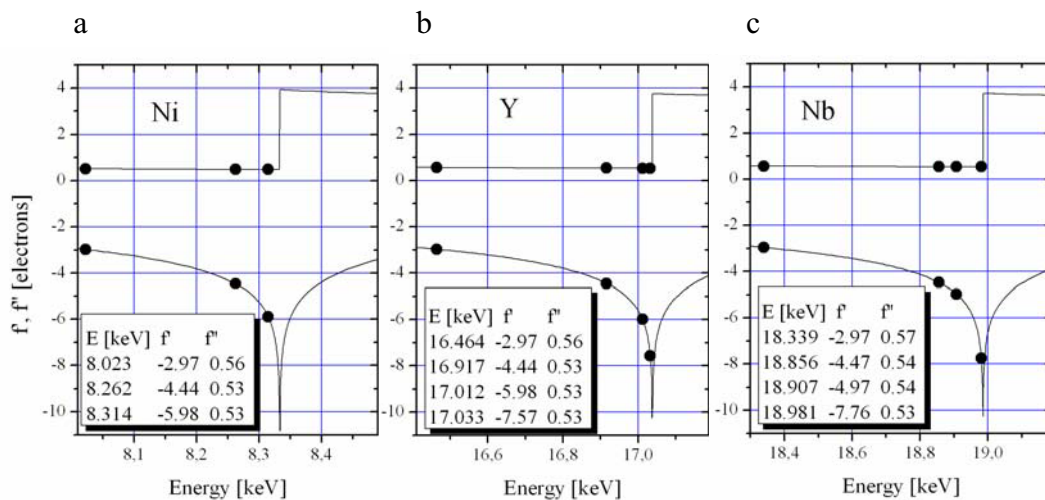


Figure 1: Anomalous dispersion corrections of Nickel, Niobium and Yttrium obtained by Cromer-Liberman calculations [17,18]. The dots represent the X-ray energies, where the *ASAXS* measurements were performed. The minimum distance of 5 eV to the K-absorption edges was kept, to omit as far as possible the Resonant Raman Scattering, which is for all components of the alloys significant, due to the high chemical concentrations.

Background measurements took 15 min followed by measurements of a calibration standard (glassy carbon, 5 min) and subsequent measurements of the sample frames (15 min). This measurement cycle was repeated for the four different energies. The measurements were performed at two sample-detector distances (935 and 3635 mm) covering a q -range between 0.005 and 0.6 \AA^{-1} . After the completion of the *ASAXS* measurements at four energies, the complete cycle of four energies was repeated four times for accumulation of intensity. In total for the samples and the background

measurements a beam time of 1h and for the related reference measurements a beam time of 20 min was accumulated at each energy and distance. This strategy was used in numerous publications emerging from the JUSIFA beam line in the last decade (see examples [5-8]) and compromises between the goal of accumulating sufficient scattering intensity (reducing the statistical error bars of the scattering curves) and reducing the influence of the significant beam instabilities of DORIS (2nd generation) as much as possible.

4. Results and Discussion

The SAXS curves, $d\sigma/d\Omega(q)$, of the two samples - $\text{Ni}_{68}\text{Nb}_{16}\text{Y}_{16}$, and $\text{c-Ni}_{68}\text{Nb}_{16}\text{Y}_{16}$ - measured at the energy $E=8029$ eV, 304 eV below the Ni-K edge are shown in Figure 2. The increasing intensity below $q < 0.2 \text{ nm}^{-1}$ probably originates from surface scattering also present in the Ni-Nb-Y data. Additionally, the presence of a maximum in the curves gives clear evidence for the existence of correlated fluctuations in electron density for the Ni-Nb-Y alloys. Variation of the energy at the Y- and Nb- K-edges changes the cross section of the SAXS curves in opposite directions indicating that the inhomogeneities are related to clusters enriched in Y or in Nb in agreement with atom probe tomography results [19]. The occurrence of the maximum in the SAXS curves is due to the high density of electron density fluctuations with a dominant correlation length. Using the relationship correlation length ζ and peak maximum in reciprocal distances $\zeta = 2\pi/q_{\text{max}}$ one obtains $\zeta=12.2 \text{ nm}$.

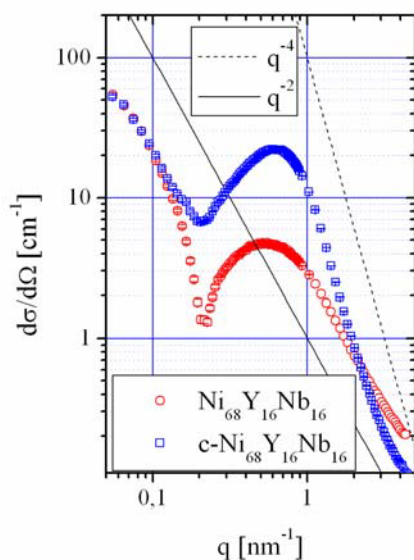


Figure 2: Total scattering curves of the alloy $\text{Ni}_{68}\text{Nb}_{16}\text{Y}_{16}$ with different heat-treatment: as-quenched (red circles) and heat-treated above the first crystallization point at 773 K but below the second crystallization point (blue squares). Above the first crystallization point the asymptotic behaviour of the scattering curves changes from q^{-2} to q^{-4} indicating smooth interfaces probably between the small crystallites and a surrounding amorphous phase.

The influence of partial crystallization on the SAXS curves is shown by the comparison of the scattering curves of the alloy $\text{Ni}_{68}\text{Nb}_{16}\text{Y}_{16}$ far below the K-absorption edge at about 8 keV. ($\text{Ni}_{68}\text{Nb}_{16}\text{Y}_{16}$ as quenched, $\text{c-Ni}_{68}\text{Nb}_{16}\text{Y}_{16}$: heat treated at 773 K i.e. beyond the 1st crystallization event). The heat treated sample consists of a nanocrystalline Ni_2Y phase and a remaining amorphous Ni-Nb phase. The mean crystallite size is about 5 nm as can be seen from the TEM image in Figure 3b. The lattice parameter of the Ni_2Y phase indicates that to some extent Nb is still solved. No inhomogeneous structures could be resolved from the TEM image of the as-cast sample (Figure 3a). In the SAXS curves a dramatic change takes place for the sample, which was heat treated beyond the 1st crystallization temperature. Though the correlation maximum remains unchanged on the q-axis, it is shifted on the y-axis by nearly an order of magnitude probably due to a higher electron density contrast caused by a larger concentration gradient. Additionally the asymptotic behaviour changes from q^{-2} to q^{-4} indicating the formation of small crystallites with smooth interfaces to the surrounding

phase. Obviously the fluctuation length of the as-quenched state determines the size of the nanocrystals. The phase separation of the glass is also the reason for different crystallization steps of the two phases (the amorphous Ni-Nb phase crystallizes into NbNi_3 at higher a temperature of about 900K). The *ASAXS* sequences of the alloys at three selected X-ray energies in the vicinity of the K-absorption edge of Ni show systematic but very small declination of the cross section in the range between 0.2 and 2 nm^{-1} indicating small differences of Ni-amount in the concentration fluctuations, which constitute the correlation maxima of the alloy. A closer analysis of the resonant invariant obtained from the *ASAXS* sequences near the Ni-K-edge could not provide reliable numbers for a Ni-gradient (concentration), indicating that the difference of the Ni-concentration in the fluctuations is too small i.e. below the resolution of this experiment. Anyway, because the Nickel component serves as the matrix, the important quantitative parameters of decomposition are related to the concentration fluctuations of Yttrium and Niobium and thus can be only obtained from quantitative *ASAXS* (*q-ASAXS*) measurements at the K-absorption edges of Yttrium and Niobium.

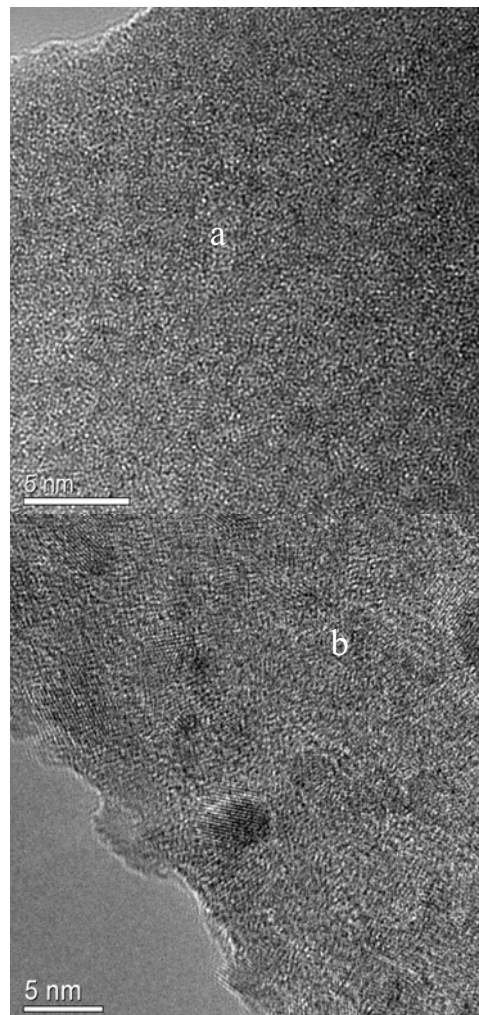


Figure 3: TEM pictures of the alloy $\text{Ni}_{68}\text{Nb}_{16}\text{Y}_{16}$ as-quenched (a) and partially crystallized (b).

Detailed quantitative information was obtained from the measurements at the K-absorption edges of Yttrium and Niobium. Figure 4a-b summarizes the results obtained from the Yttrium K-edge (17038 eV) for the two samples $\text{Ni}_{68}\text{Nb}_{16}\text{Y}_{16}$ and $\text{c-Ni}_{68}\text{Nb}_{16}\text{Y}_{16}$. The black squares in Figure 4

represent the total scattering of the as-quenched sample (a) and the heat-treated sample (b). The correlation maximum appears for both samples at about 0.6 nm^{-1} as known already from the *ASAXS* measurements at the Ni-K-edge. The total scattering curves are superimposed by a strong isotropic scattering contribution, which originates mainly from the fluorescence of the Ni-component (68at%). By calculating the separated scattering curves, $I(q, E_1) - I(q, E_3)$, this isotropic fluorescence contribution is removed revealing a q^{-4} behaviour in the asymptotic part of the separated scattering curve (blue triangles) of the heat-treated (crystallized) sample, which is already known from the measurements at the Ni-K-edge. As can be seen from the error bars of the separated scattering curve of the as-quenched sample (blue triangles) the asymptotic behaviour above 1 nm^{-1} is not clear i.e. beyond the resolution and needs a closer consideration by analyzing the pure-resonant scattering contribution with larger q -bins (see below). The solid lines in Figure 4a and 4b represent the q^{-2} and q^{-4} behaviour respectively.

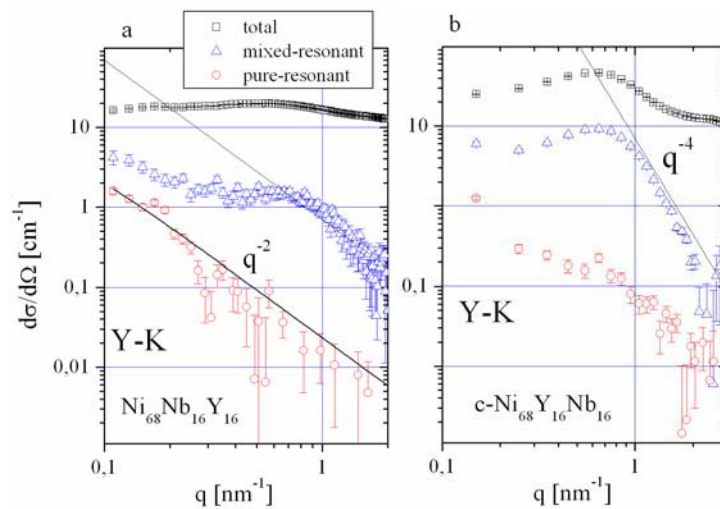


Figure 4: Total scattering curves (squares), separated scattering curves (triangles) and the form factors of the pure-resonant scattering contribution (circles) of the Y-related concentration fluctuations. Figures 6a-b represent the different heat-treatment: as-quenched (a) and partially crystallized (b). Above the first crystallization point the asymptotic behaviour of the scattering curves changes from q^{-2} to q^{-4} indicating smooth interfaces probably between the small crystallites and a surrounding amorphous phase. The solid line passing through the red circles of the pure-resonant scattering in Figure 6a represents a model function (see text).

From Eq. 8, the pure-resonant scattering (or more precisely the form factor of the pure-resonant scattering) was calculated for both samples. Because the error bars of the pure-resonant scattering become rather large at higher q -values, especially for the as-quenched sample, the number of q -bins was reduced in comparison to the mixed-resonant and the total scattering curves, with the aim to obtain smaller error bars at q -values larger 0.5 nm^{-1} . The procedure was as follows: the cross-section of the pure-resonant form factor was averaged over neighbouring q -bins. The result gives the cross-section at the centre of the averaged q -interval. The error of the averaged cross-section is the averaged squared error calculated from the errors of the single q -bins. Though the error bars are still large at higher q -values, the pure-resonant scattering for both samples was clearly resolved. Especially at

higher q -values of about 1 nm^{-1} the pure-resonant scattering contribution of the crystallized sample is nearly an order of magnitude higher compared to the as-quenched sample, indicating a larger amount of Yttrium atoms localized in the crystalline phase. Ni_2Y has more Y than the average alloy, even when some Nb is solved

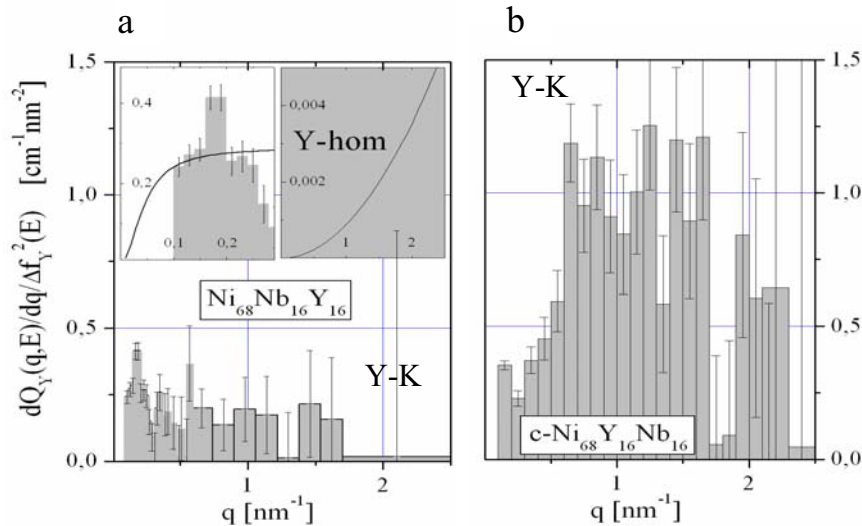


Figure 5: The first derivative of the Resonant Invariant (Eq.10b) of $\text{Ni}_{68}\text{Nb}_{16}\text{Y}_{16}$ as-quenched (a) and partially crystallized (b) obtained from *ASAXS* sequences at the Y-K-edge (17038 eV). The integrals (grey area) represent the Resonant Invariant (Eq.10a) from which the Y-concentrations can be calculated. The right inset represents the upper limit of 16at% homogeneously distributed Y, contributing to the Resonant Invariant. The left inset explains the contribution, which is missing due to the q -resolution. For reason of convenience the division by 4π is not written at the vertical axis.

The latter was analyzed more precisely by employing the Resonant Invariant of Eq. 10. Figure 5 shows the first derivative of the Resonant Invariant (Eq. 10b) of the as-quenched sample (a) and the crystallized sample (b). The grey areas represent the integrals, Q_Z (i.e. the Resonant Invariant), which are introduced into Eq. 11 for the calculation of the amount of Yttrium atoms, \bar{v}_Y , which enter the concentration fluctuations of the as-quenched sample and the crystallites of the heat-treated sample respectively. From Eq. 11 an amount of $2.13(28) \cdot 10^{21} \text{ cm}^{-3}$ Yttrium (excess) atoms, which enter the crystallites, was calculated corresponding to about 19% of the Y-atoms in the alloy.

A completely different result was obtained from the analysis of the Resonant Invariant of the as-quenched sample. As can be seen already from a simple comparison of the integrals of both samples in Figure 5, the amount of Yttrium atoms, which enter the concentration fluctuations must be much more smaller. From Eq. 11 a concentration of $0.39(20) \cdot 10^{21} \text{ cm}^{-3}$ Yttrium atoms was deduced, which corresponds to an amount of only 4% Yttrium atoms.

Though this result is significant, it is near the resolution limits of the experiment as can be seen from the error bars in Figure 5a. For a more quantitative discussion of the result, the limited integration area has to be extended onto the whole regime $0 \leq q < \infty$. Because no comprehensive description of the scattering curves of a ternary alloy undergoing spinodal decomposition is at hand, a model function with a q^{-2} -behaviour (Ornstein-Zernike originally for binary systems, Eq. 12) was

employed. The model function serves only as a guide for the eye with the aim to estimate the amount of the ‘missing’ scattering contributions at higher and lower q -values i.e. beyond the resolution of the experiment.

$$i(q) = \frac{const}{c + q^2} \quad (12)$$

At $q=0$ the model function reaches a finite value defined by thermodynamic parameters of the alloy (Eq.12) and the first derivative of the Resonant Invariant approaches 0 with $q \rightarrow 0$. The amount of missing contribution to the Resonant Invariant can be neglected as can be seen from the left inset in Figure 5a, which shows a magnified part of the Resonant Invariant in the low q -range. The missing part below the resolution at q -values smaller q_{min} is the area between the grey histogram and the solid line of the model function.

The right inset in Figure 5a represents the contribution of homogeneously distributed Y-atoms with a concentration of 16at% to the Resonant Invariant. Although this corresponds to the maximum possible amount – a considerable portion of the Y-atoms are localized in the fluctuations – the contribution is many orders of magnitude smaller than the contribution detected from the Y-atoms in the concentration fluctuations and thus can be also neglected.

Considering the scattering contributions beyond the q -resolution at higher q -values the result must be interpreted as a lower limit as is demonstrated by of the model function (Figure 5a). At higher q -values a cut-off of the scattering function is expected, because otherwise the integral of Eq. 11 would become infinite and the invariant would not exist. As can be seen from Figure 5a the cut-off of the pure-resonant form factor cannot be resolved due to the large error bars and if the cut-off is located at q -values beyond 2 nm^{-1} , the concentration of Yttrium atoms must be higher. In the case of the crystallized sample the scattering curve at larger q -values is deep in the Porod regime and no significant contribution can appear in the integral at higher q -values.

Table I: Structural and quantitative parameters of the two alloys (one of them with different heat-treatment). Column ζ is the correlation length. $\bar{v}(Y)$, $\bar{v}(Nb)$ give the amount of Yttrium respective Niobium atoms localized in the concentration fluctuations calculated from the Resonant Invariant at the related K-absorption edges. The two columns c_Y and c_{Nb} contain the amount in percent of the complete amount of Yttrium or Niobium atoms respectively. The latter concentrations were obtained from the averaged atomic volume, which was calculated from the average atomic weight (68.999 g/mol) and the average density (8.147 g/cm^3) of the alloy. Additionally the corresponding volume fractions, Φ_Y and Φ_{Nb} , have been calculated (see text).

Sample	ζ	$\bar{v}(Y)$	c_Y	Φ_Y	$\bar{v}(Nb)$	c_{Nb}	Φ_{Nb}
	[nm]	$10^{21}[\text{cm}^{-3}]$	[%]	[%]	$10^{21}[\text{cm}^{-3}]$	[%]	[%]
$\text{Ni}_{68}\text{Nb}_{16}\text{Y}_{16}$	12.2	0.39(2)	4	0.6	1.3(3)	12	1.9
c- $\text{Ni}_{68}\text{Nb}_{16}\text{Y}_{16}$	12.2	2.1(3)	19	3.0	1.8(3)	16	2.5

The same arguments hold for the interpretation of the results obtained from the *ASAXS* measurements at the Nb-K-edge. Again the asymptotic behaviour of the pure-resonant scattering turns from q^{-2} to q^{-4} , when applying a heat-treatment beyond the 1st crystallization temperature. The amount of Niobium atoms in the fluctuations of the as-quenched sample calculated from the Resonant Invariant turns out to be higher (with respect to Yttrium) corresponding to about 12% of the complete

Niobium amount in the alloy (Table 1). Surprisingly the amount of Niobium atoms is only slightly higher for the partially crystallized sample i.e. 16% of the complete Nb-amount, indicating that the spatial distribution of Niobium in the alloy does not change much, when the partial crystallization (Ni_2Y -phase) takes place. This may be attributed to the fact, that the Niobium component crystallizes beyond the 2nd crystallization temperature (beyond 900 K), which we have not yet reached.

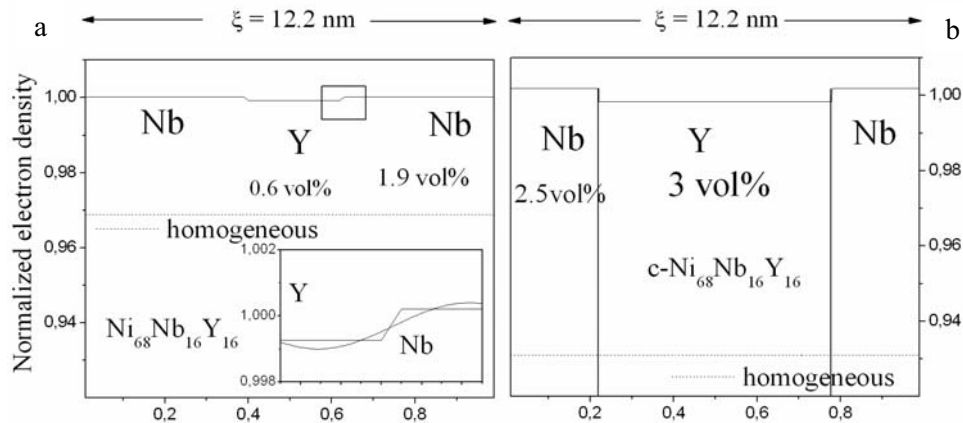


Figure 6: Normalized electron density of the as-quenched sample (a) and the partially crystallized alloy (b). The step functions represent the volume fractions of the two phases, Y-rich and Nb-rich respectively. The dashed lines show the normalized electron density of homogeneously distributed atoms in the two alloys.

From the concentrations of Y and Nb deduced from the Resonant Invariant in the as-quenched and the partially crystallized state respectively the related volume fractions, Φ_Y and Φ_{Nb} , can be estimated using the averaged atom volumes of the alloy for V_Y and V_{Nb} . In a further step the normalized electron densities have been calculated. The results are summarized in Figure 6. In Figure 6a the normalized electron density of the as-quenched sample is depicted within one correlation period. The dashed line represents the average electron density resulting from homogeneously distributed atoms in the alloy, which cover nearly 97% of the entire volume. The step function shows the different volume fractions of inhomogeneously distributed Yttrium, 0.6%, and Niobium, 1.9%, respectively. The integral of the step function over one correlation period amounts to 1. The inset shows a magnification of the step function with the oscillating function giving a more realistic sketch of a continuously changing concentration over the correlation length.

Again the dashed line in Figure 6b represents the average electron density resulting from homogeneously distributed atoms in the partially crystallized alloy. Because the amount of inhomogeneously distributed Y and Nb increased to 3% and 2.5% respectively (black step function) the value of the volume fraction covered by homogeneously distributed material is reduced to about 93%. The area between the two vertical lines, the step function and the dashed line depicts the volume fraction of the additional amount of Yttrium (excess) atoms in the crystallized phase with respect to the surrounding matrix, while the intersection of the vertical lines with the x-axis represent the volume fraction of the spatial extension of the crystallites, i.e. 55%.

In both Figures the contrast between the Y-rich and the Nb-rich phases is negative explaining the decline of the scattering cross section, when approaching the K-absorption edge of Niobium, while the scattering cross section becomes larger, when approaching the K-absorption edge of Yttrium.

5. Conclusions

In the last years Anomalous Small-Angle X-ray Scattering became a precise quantitative method (*q*-ASAXS) for element specific structural analysis on the mesoscopic length scale. Due to the precision of the techniques small-angle scattering contributions of Ni₆₈Nb₁₆Y₁₆ alloys in the resolution regime $10^{-3} < \Delta I/I < 10^{-2}$ were reliably separated from a superimposed, orders of magnitude larger inelastic background caused by fluorescence and Resonant Raman Scattering. The separated pure-resonant scattering contributions were obtained by employing the Gauss algorithm to a vector equation, which represents the ASAXS measurements at different X-ray energies.

The pure-resonant scattering contributions of inhomogeneously distributed Nickel, Niobium and Yttrium atoms in Ni₆₈Nb₁₆Y₁₆ alloys with different heat-treatment have been separated from the total scattering SAXS curves. The separated scattering curves obtained from the as-quenched sample, show the typical behaviour of concentration fluctuations (Ornstein-Zernike) with a correlation maximum corresponding to a correlation length of 12.2 nm. From the Resonant Invariant an amount of 4% and 12% of the Yttrium atoms and Niobium atoms respectively was found to be localized in the fluctuations corresponding to volume fractions of 0.6 and 1.9% respectively. This compares to about 19% (3% volume fraction) of enriched Yttrium atoms localized in the crystalline phase of the sample, which was heat-treated beyond the 1st crystallization temperature. Surprisingly the amount of enriched Niobium atoms does not change much due to the latter heat-treatment (from 12% to 16%) indicating that the crystallization temperature for the Niobium phases is not yet reached. A model calculation suggests a large volume fraction of 55% covered by small crystallites beyond the 1st crystallization temperature surrounded by an amorphous shell enriched with Nb with a volume fraction of 45%.

The example demonstrates the capability to determine quantitatively the extent of spinodal decomposition in metallic glasses by Anomalous Small-Angle X-ray Scattering.

References

- [1] Stuhrmann H B 1985 *Adv. Polym. Sci.* **67**, 123
- [2] Simon J P, Lyon O and de Fontaine D J 1985 *Appl. Cryst.* **18**, 230
- [3] Stuhrmann H B, Goerigk G and Munk B 1991 In: Ebashi S, Koch M, Rubenstein E, editors. *Handbook on Synchrotron Radiation Vol. 4*. Amsterdam: Elsevier; 555.
- [4] Goerigk G and Williamson D L 2001 *J. Non-Cryst. Solids* **281**, 181
- [5] Goerigk G, Schweins R, Huber K and Ballauff M 2004 *Europhys. Lett.* **66(3)**, 331
- [6] Goerigk G and Williamson D L 2006 *J. Appl. Phys.* **99**, 084309
- [7] Goerigk G, Huber K and Schweins R 2007 *J. Chem. Phys.* **127**, 154908
- [8] Bota A, Varga Z and Goerigk G 2007 *J. Phys. Chem. B* **111**, 1911
- [9] Bota A, Varga Z and Goerigk G 2008 *J. Phys. Chem. C* **112**, 4427
- [10] Goerigk G and Mattern N 2009 *Acta Mater.* **57**, 3652
- [11] Mattern N, Zinkevich M, Löser W, Behr G and Acker J 2008 *J. Phase Equil. Diff.* **29**, 141
- [12] Mattern N, Kühn U, Gebert A, Gemming T, Zinkevich M, Wendrock H and Schultz L 2005 *Scripta Materialia* **53**, 271
- [13] Mattern N, Gemming T, Goerigk G and Eckert J 2007 *Scripta Mater.* **57**, 29
- [14] Glatter O and Kratky O. 1982 *Small-Angle X-ray Scattering*, Academic Press, London
- [15] Haubold H G, Gruenhagen K, Wagener M, Jungbluth H, Heer H, Pfeil A, Rongen H, Brandenburg G, Moeller R, Matzerath J, Hiller P and Halling H 1989 *Rev. Sci. Instrum.* **60**, 1943
- [16] Goerigk G 2006 'Electronic and Computer Upgrade at ASAXS Beamline JUSIFA', HASYLAB Annual Report p. 77
- [17] Cromer D T and Liberman D 1970 *J. Chem. Phys.* **53**, 1891
- [18] Cromer D T and Liberman D 1981 *Acta Cryst.* **A37**, 267
- [19] Mattern N, Goerigk G, Vainio U, Miller M K, Gemming T and Eckert J 2009 *Acta Mat.* **57(3)**, 903

[S2]

G. Goerigk, and N. Mattern,

*Critical Scattering of Ni–Nb–Y Metallic Glasses Probed by Quantitative
Anomalous Small-Angle X-ray Scattering*

Acta Materialia, 57, 3652-3661 (2009)

Critical scattering of Ni–Nb–Y metallic glasses probed by quantitative anomalous small-angle X-ray scattering

G. Goerigk^{a,*}, N. Mattern^b

^a *Institut für Festkörperforschung, Forschungszentrum Jülich, Postfach 1913, D-52425 Jülich, Germany*

^b *Leibniz-Institute IFW Dresden, Institute for Complex Materials, P.O. Box 270116, D-01171 Dresden, Germany*

Received 12 February 2009; received in revised form 6 April 2009; accepted 16 April 2009

Available online 18 May 2009

Abstract

Phase-separated Ni–Nb–Y metallic glasses were prepared by means of rapid quenching from the melt. Different stages of spinodal decomposition were obtained for Ni-contents between 66 and 71 at.%. From anomalous small-angle X-ray scattering experiments performed at the K-absorption edges of nickel, yttrium and niobium different correlation lengths, of between 15 and 5.5 nm, were found for the different concentrations. Moreover, from the quantitative analysis of the resonant invariant the chemical concentrations of yttrium and niobium in the random density fluctuations were deduced. The results are compared to a partially crystallized sample annealed at 773 K over 30 min.

© 2009 Acta Materialia Inc. Published by Elsevier Ltd. All rights reserved.

Keywords: Quantitative ASAXS; Spinodal decomposition; Metallic glasses; Synchrotron radiation; Melt spinning

1. Introduction

The investigation of critical phenomena by scattering methods – formerly named critical scattering – has a long tradition. In the nineteenth century, after the discovery of the critical point (1869), Avenarius [1] found a strong increase in light scattering (LS), especially in the forward direction, in condensing gas just above the critical point. The same effect was observed later in binary liquid mixtures by several authors [2,3]. The phenomenon – named critical opalescence – is related to the thermodynamic state variables as outlined by Travers and Usher [4], and attracted the interest of numerous theoretical researchers [5], the most prominent being Einstein [6]. However, these theoretical papers could not explain the angular dependence of the critical opalescence. Ornstein and Zernike [7]

tried to explain the angular dependence using the concept of extended correlation lengths.

Until the 1950s the study of critical opalescence was restricted to fluids and gases, and nothing was known about analogous phenomena in solids. Theoretical investigations of the diffuse scattering of X-rays from binary alloys led Krivoglaz [8] and, independently, Münster and Sagel [9] to conclude that in the neighborhood of the critical point of decomposition the intensity of small-angle X-ray scattering (SAXS) should increase. These predictions were confirmed by SAXS experiments on aluminum–zinc alloys [10,11]. In a later combined experimental and theoretical study by Acuna and Craievich [12] a quasi-binary glass system was analyzed by numerical integration of the Cahn–Hilliard–Cook differential equation for SAXS curves, which includes the contribution of random density fluctuations. Meanwhile numerous studies on spinodal decomposition in alloys and polymer blends have been performed, a review of which can be found in Ref. [13]. Though, since Ornstein and Zernike, there is strong support from theory and experiments for an asymptotic q^{-2} -dependence of the scattering curves (from LS and SAXS)

* Corresponding author. Present address: JCNS-FRMII, c/o Technische Universität München, Lichtenbergstr. 1, D-85747 Garching, Germany. Tel.: +49 89 28910746; fax: +49 89 28910799.

E-mail address: G.Goerigk@fz-juelich.de (G. Goerigk).

related to the suspected concentration fluctuations occurring in spinodal decomposition, there is still no comprehensive description of the spinodal nanostructure in metallic alloys, and especially of the related quantitative parameters like the chemical concentrations amplitudes.

In the last three decades synchrotron radiation (SR) has provided major improvements to the small-angle X-ray scattering technique. Among other improvements, SR provides a photon flux that is many orders higher than classical X-ray sources, allowing access to systems with only weak SAXS contributions, like highly diluted chemical solutions, or solid state systems such as glasses or amorphous alloys, which to a large degree are homogeneous. Additionally the continuous energy spectrum of SR allows energy tunability in the vicinity of the K- and L_{III}-absorption edges of most of the elements. This technique, known as anomalous small-angle X-ray scattering (ASAXS), is based on the anomalous variations in the atomic scattering factors near the absorption edges and allows the element-specific structural and quantitative characterization of the sample under investigation. After the exploratory studies of the 1980s [14–16], ASAXS has become in the last decade a precise quantitative technique (*q*-ASAXS), which combines the structural analysis with the quantitative analysis of chemical concentrations (i.e. fluctuations) of the different atomic species of a multi-component system by addressing the elements via the X-ray absorption edges [17–22].

The ternary Ni–Nb–Y system exhibits an extended miscibility gap in the liquid [23]. By means of a rapid quenching technique the decomposed melt can be frozen into a phase-separated metallic glasses [24]. The critical temperature of liquid–liquid decomposition depends on the composition. For a Ni content <60 at.%, a hierarchical heterogeneous microstructure is obtained with a size distribution ranging from 10 to 500 nm that can be analyzed by transmission electron microscopy (TEM). Such microstructures represent a coarsened state of spinodal decomposition, the growth of melts and secondary decomposition within the liquids. For such phase-separated Ni–Nb–Y glasses SAXS curves with fractal *q*-dependence have been observed [25]. For alloys with Ni > 60 at.% early stages of phase separation can be obtained, due to reduced critical temperature, that have fluctuations in nanometer dimensions with almost no contrast in TEM images. By means of ASAXS, quantitative parameters of the fluctuation can be determined.

In this presentation, we address the question of how to determine the amount of yttrium (respectively niobium) atoms localized in periodic fluctuations of Ni–Nb–Y metallic glasses undergoing spinodal decomposition with respect to the total amount of Y (respectively, Nb) atoms in the alloy by quantitative analysis of what was introduced as the resonant invariant in a former publication [20].

2. ASAXS measurements

The exceptional possibilities of the ASAXS technique are based on the energy dependence of the atomic scatter-

ing factors giving selective access to the specific SAXS contributions of nanophases, which are built up by different chemical constituents in composites such as metallic glasses. In general, the atomic scattering factors are complex quantities and energy dependent:

$$f_Z(E) = f_{0,Z} + f'_Z(E) + if''_Z(E) \quad (1)$$

where *Z* represents the atomic number. In this presentation we will deal with the atomic scattering factors of Ni, Y and Nb: $f_Z(E) =: f_{\text{Ni}}(E), f_{\text{Y}}(E), f_{\text{Nb}}(E)$. When performing a SAXS experiment at energies in the vicinity of the absorption edge of one of the elements, three different scattering contributions can be distinguished as a consequence of Eq. (1) [14]:

$$I(q, E) = |A(q)|^2 + 2\text{Re}A(q)[\Delta f_{0,Z} + f'_Z(E)]\text{Re}B(q) + [(\Delta f_{0,Z} + f'_Z(E))^2 + f''_Z(E)^2]|B(q)|^2 \quad (2)$$

$A(q)$ represents the scattering amplitude of the non-resonant scattering atoms and $[\Delta f_{0,Z} + f'_Z(E)]\text{Re}B(q)$ represents the scattering amplitude (real part) of the resonant scattering atoms in the energy range of the absorption edge. The quantity $\Delta f_{0,Z} = f_{0,Z} - \rho_m V_Z$ is the electron density difference between the atom with volume V_Z and the surrounding matrix of the alloy with electron density ρ_m . q is the magnitude of the scattering vector $[= (4\pi/\lambda) \sin \Theta]$, where 2Θ is the scattering angle and λ is the X-ray wavelength. For instance, in the case of Ni–Nb–Y alloys $[\Delta f_{0,Y} + f'_Y(E)]\text{Re}B(q)$ represents the scattering amplitude (real part) of the inhomogeneously distributed Y atoms in the alloy, when performing SAXS measurements in the energy range of the K-absorption edge of yttrium, while $\text{Re}A(q)$ represents the scattering amplitude (real part) of the non-resonant scattering atoms, i.e. Ni and Nb.

By measuring the scattering curves at two energies in the vicinity of the absorption edge of the atom with atomic number *Z* and subtracting the two scattering curves $\Delta I(q, E_1, E_2) = I(q, E_1) - I(q, E_2)$, the non-resonant scattering contribution is vanishing:

$$\Delta I(q, E_1, E_2) = 2\text{Re}A(q)(f'_Z(E_1) - f'_Z(E_2))\text{Re}B(q) + [(f'_Z(E_1))^2 - f'_Z(E_2))^2 + f''_Z(E_1)^2 - f''_Z(E_2)^2]|B(q)|^2 \quad (3)$$

Now the scattering function is reduced to the resonant contributions – the so-called separated scattering – but the scattering of the non-resonant scattering atoms is still present in the cross-term. To overcome this problem, measurement at a third energy is performed. When subtracting the separated scattering curves obtained at the two energies E_1, E_3 from the separated scattering obtained from the two energies E_1, E_2 the cross-term is vanishing and the squared Fourier transform of the form factor, $B(q)$, of the spatial distribution of the atoms with atomic number *Z* remains after normalizing to the energy-dependent anomalous dispersion corrections of the related atomic scattering factor at the three energies:

$$|B(q)|^2 = \frac{\left[\frac{\Delta I_0(q, E_1, E_2)}{f'_Z(E_1) - f'_Z(E_2)} - \frac{\Delta I_0(q, E_1, E_3)}{f'_Z(E_1) - f'_Z(E_3)} \right]}{1} \cdot \frac{1}{F(E_1, E_2, E_3)}$$

$$F(E_1, E_2, E_3) = f'_Z(E_2) - f'_Z(E_3) + \frac{f''_Z(E_1) - f''_Z(E_2)}{f'_Z(E_1) - f'_Z(E_2)} - \frac{f''_Z(E_1) - f''_Z(E_3)}{f'_Z(E_1) - f'_Z(E_3)} \quad (4)$$

Due to Eq. (4), ASAXS provides a technique to access directly the scattering of the Z atoms, i.e. Ni, Y or Nb, depending at which X-ray absorption edge the ASAXS measurements are performed. The structural information of the distribution of the Z atoms in the alloy can be obtained from the analysis of the $|B(q)|^2$, which we will call the “form factor” for convenience. Generally speaking, Eq. (4) provides a method that gives access to the pure-resonant scattering contribution of the selected constituent of an alloy by measuring the small-angle scattering at only three suitable energies [18–22].

In addition to the structural information, which can be obtained from $|B(q)|^2$, important quantitative information relating to the amount of inhomogeneously distributed Z atoms can be deduced from the integral Q_Z :

$$Q_Z(E) = |\Delta f_Z(E)|^2 \int_Q |B(q)|^2 d^3q \quad (5)$$

In analogy to the so-called invariant [26], we will call $Q_Z(E)$ the resonant invariant of the inhomogeneously distributed resonant scattering Z atoms. The invariant, $Q_Z(E)$, as defined in Eq. (5), is related to the number density of inhomogeneously distributed Z atoms, \bar{v}_Z , as outlined in detail in a previous publication [20]:

$$Q_Z(E) = |\Delta f_Z(E)|^2 \int_Q |B(q)|^2 d^3q$$

$$= (2\pi)^3 r_0^2 |\Delta f_Z(E)|^2 \bar{v}_Z \left(\frac{1}{V_Z} - \bar{v}_Z \right) \quad (6a)$$

$$\frac{dQ_Z(E)}{dq} = |\Delta f_Z(E)|^2 4\pi |B(q)|^2 q^2 \quad (6b)$$

where $V_Z = 4\pi/3R_Z^3$ is the volume of the Z atoms with atom radius R_Z and r_0 is the classical electron radius. Eq. (6b) represents the first derivative of the resonant invariant with respect to q . Finally, from the quadratic Eq. (6a), two values for the number density of the Z atoms can be calculated:

$$\bar{v}_Z - \bar{v}_Z^2 V_Z = \frac{V_Z \cdot Q_Z(E)}{(2\pi)^3 \cdot r_0^2 |\Delta f_Z(E)|^2} = \frac{V_Z}{(2\pi)^3 \cdot r_0^2} \int_Q |B(q)|^2 d^3q \quad (7a)$$

$$\bar{v}_Z = \frac{1}{2V_Z} \pm \sqrt{\frac{1}{4V_Z^2} - \frac{1}{(2\pi)^3 r_0^2} \int_Q |B(q)|^2 d^3q} \quad (7b)$$

In this presentation only one of the two solutions is significant, i.e. the negative sign. It should be mentioned that the number density calculated from Eq. (7b) includes the Z

atoms, which are homogeneously distributed in the alloy. These Z atoms provide an isotropic scattering contribution at small q -values similar to the isotropic scattering of the alloys matrix atoms but of a different amount. As will be discussed in more detail below, the amount of the isotropic scattering contribution originating from these remaining Z atoms in the matrix can be ignored.

3. Experimental

Pre-alloyed ingots were prepared by arc-melting elemental Ni, Nb and Y with purities of 99.9% or higher in a Ti-gettered argon atmosphere. To ensure homogeneity, the samples were remelted several times. From these pre-alloys, thin ribbons (3 mm in width and 30 μm in thickness) with nominal compositions $\text{Ni}_{66}\text{Nb}_{17}\text{Y}_{17}$, $\text{Ni}_{68}\text{Nb}_{16}\text{Y}_{16}$ and $\text{Ni}_{70}\text{Nb}_{15}\text{Y}_{15}$ were prepared by single-roller melt spinning under an argon atmosphere. The casting temperature was 1923 K. The chemical compositions were determined by the titration technique. The resulting values were $\text{Ni}_{66.1}\text{Nb}_{17.6}\text{Y}_{16.3}$, $\text{Ni}_{67.9}\text{Nb}_{17.3}\text{Y}_{14.8}$ and $\text{Ni}_{71.3}\text{Nb}_{13.7}\text{Y}_{15.0}$, respectively, for the as-prepared ribbons. These compositions exhibit only slight deviations from the nominal value of up to ~ 1 at.%. For convenience, the nominal compositions are used in the following sections. Additionally, a partly crystallized sample, $\text{c-Ni}_{68}\text{Nb}_{16}\text{Y}_{16}$, was produced by heating part of the ribbons in a differential scanning calorimeter (DSC 7, Perkin Elmer) just above the temperature of the first exothermic crystallization event at 773 K over 30 min.

ASAXS was measured with the JUSIFA beam line [27,28] at the DORIS storage ring at HASYLAB/DESY Hamburg. ASAXS sequences were performed for all samples $\text{Ni}_{66}\text{Nb}_{17}\text{Y}_{17}$, $\text{Ni}_{68}\text{Nb}_{16}\text{Y}_{16}$, $\text{c-Ni}_{68}\text{Nb}_{16}\text{Y}_{16}$ and $\text{Ni}_{70}\text{Nb}_{15}\text{Y}_{15}$ with four (respectively, three) X-ray energies in the vicinity of the K-absorption edges of nickel at 8333 eV. For the samples $\text{Ni}_{68}\text{Nb}_{16}\text{Y}_{16}$ and $\text{c-Ni}_{68}\text{Nb}_{16}\text{Y}_{16}$ additional ASAXS measurements with four X-ray energies were performed at the K-absorption edges of yttrium at 17038.4 eV and niobium at 18985.6 eV. The tables in Fig. 1a–c provide the related anomalous dispersion corrections of nickel, yttrium and niobium at the energies used in the experiment based on the calculations of Cromer and Liberman [29,30]. These were used to permit the separation of the Ni-, Y- and Nb-related pure-resonant scattering described in detail by Eqs. (1)–(4). The scattering intensity is calibrated into macroscopic scattering cross-sections in units of cross-section per unit volume [cm^2/cm^3] = [cm^{-1}]. Transmission measurements were performed with a precision of better than 0.001 using a special (windowless) photodiode (Hamamatsu S2387-1010N).

Background measurements took 30 min followed by measurements of a calibration standard (glassy carbon, 15 min) and subsequent measurements of the sample frames (30 min). This measurement cycle was repeated for the four different energies. The measurements were performed at two sample–detector distances (935 and

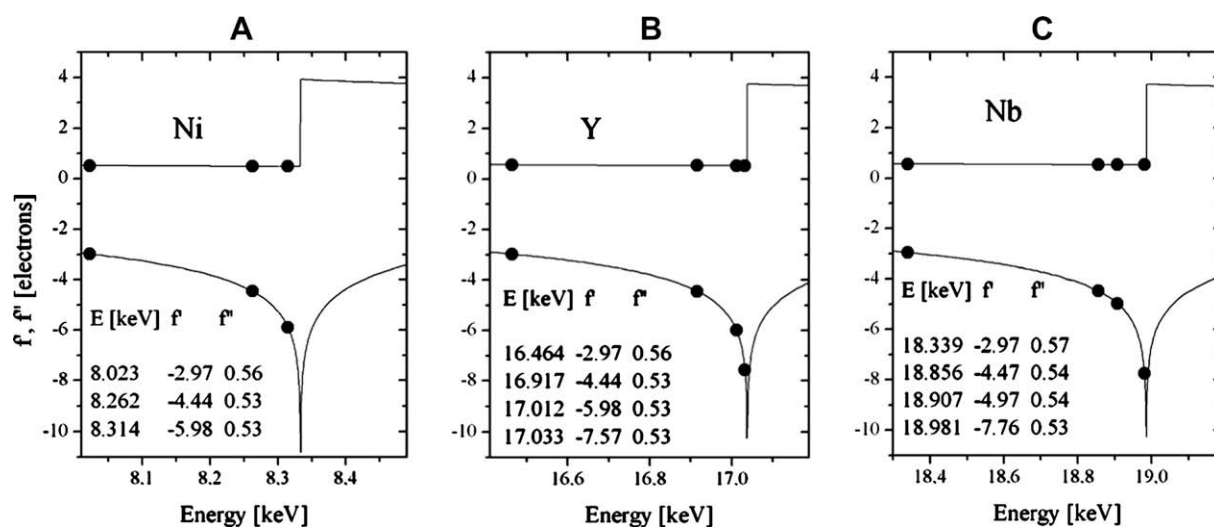


Fig. 1. Anomalous dispersion corrections of nickel, niobium and yttrium obtained by Cromer–Liberman calculations [29,30]. The dots represent the X-ray energies at which the ASAXS measurements were performed. The minimum distance of 5 eV to the K-absorption edges was kept to omit as far as possible the resonant Raman scattering, which is significant for all components of the alloys, due to the high chemical concentrations.

3635 mm) covering a q -range between 0.005 and 0.6 \AA^{-1} . After the completion of the ASAXS measurements at four energies, the complete cycle of four energies was repeated seven times for the accumulation of intensity. In total, for the samples and the background measurements a beam time of 3.5 h and for the related reference measurements a beam time of 105 min was accumulated at each energy and distance. This strategy has been used in numerous publications emerging from the JUSIFA beam line in the last decade [18–21], and provides the best compromise between the goals of accumulating sufficient scattering intensity (reducing the statistical error bars of the scattering curves) and reducing the influence of the significant beam instabilities of DORIS (second generation).

4. Results and discussion

We first discuss the influence of alloy composition on the microstructure. The SAXS curves, $d\sigma/d\Omega(q)$, of the three samples – $\text{Ni}_{66}\text{Nb}_{17}\text{Y}_{17}$, $\text{Ni}_{68}\text{Nb}_{16}\text{Y}_{16}$ and $\text{Ni}_{70}\text{Nb}_{15}\text{Y}_{15}$ – measured at the energy $E = 8029 \text{ eV}$, 304 eV below the Ni K-edge, are shown in Fig. 2. The increasing intensity below $q < 0.2 \text{ nm}^{-1}$ probably originates from surface scattering, which is also present in the Ni–Nb–Y data. Additionally, the presence of a maximum in the curves gives clear evidence for the existence of correlated fluctuations in electron density for the Ni–Nb–Y alloys. Variation of the energy at the Y and Nb K-edges changes the cross-section of the SAXS curves in opposite directions, indicating that the inhomogeneities are related to clusters enriched in Y or Nb, in agreement with atom probe tomography results [31]. The occurrence of the maximum in the SAXS curves is due to the high density of electron density fluctuations with a dominant correlation length. The correlation length ζ clearly varies with the Ni content. The shift in the position of the maximum with composition from

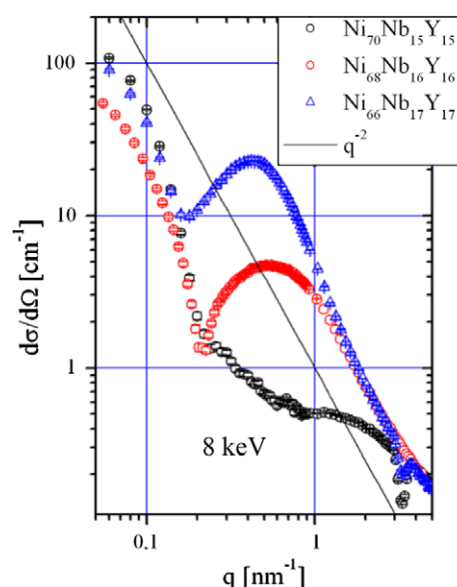


Fig. 2. Total scattering curves of the three alloys $\text{Ni}_{66}\text{Nb}_{17}\text{Y}_{17}$, $\text{Ni}_{68}\text{Nb}_{16}\text{Y}_{16}$ and $\text{Ni}_{70}\text{Nb}_{15}\text{Y}_{15}$. The correlation peak of the concentration fluctuations starts to appear at 70 at.% Ni concentration and is fully developed at 68 at.% while shifting to smaller q -values, i.e. larger correlation lengths. At 66 at.% (blue triangles) the asymptotic behavior of the scattering curve already shows slight deviations from q^{-2} . (For interpretation of the references to colour in this figure legend, the reader is referred to the web version of this article.)

$q_{\text{max}} = 0.42$ to 1.14 nm^{-1} indicates a reduction in ζ with increasing Ni content. Using the relationship correlation length ζ and peak maximum in reciprocal distances $\zeta = 2\pi/q_{\text{max}}$, one obtains $\zeta = 15 \text{ nm}$ for $\text{Ni}_{66}\text{Nb}_{17}\text{Y}_{17}$, $\zeta = 12.2 \text{ nm}$ for $\text{Ni}_{68}\text{Nb}_{16}\text{Y}_{16}$ and $\zeta = 5.5 \text{ nm}$ for $\text{Ni}_{70}\text{Nb}_{15}\text{Y}_{15}$.

The influence of partial crystallization on the SAXS curves is shown in Fig. 3 by the comparison of the scattering curves of the alloy $\text{Ni}_{68}\text{Nb}_{16}\text{Y}_{16}$ far below the K-absorption edge at about 8 keV. ($\text{Ni}_{68}\text{Nb}_{16}\text{Y}_{16}$ as

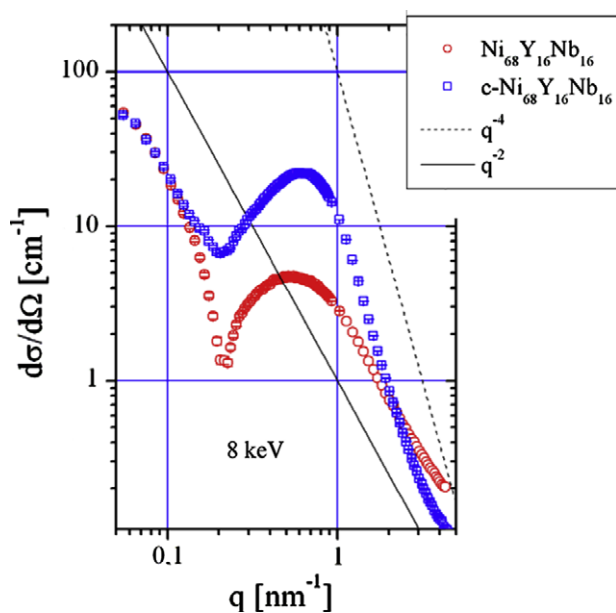


Fig. 3. Total scattering curves of the alloy $\text{Ni}_{68}\text{Nb}_{16}\text{Y}_{16}$ with different heat treatments: as-quenched (red circles) and heat-treated above the first crystallization point at 773 K but below the second crystallization point (blue squares). Above the first crystallization point the asymptotic behavior of the scattering curves changes from q^{-2} to q^{-4} , indicating smooth interfaces probably between the small crystallites and the surrounding amorphous phase. (For interpretation of the references to colour in this figure legend, the reader is referred to the web version of this article.)

quenched, $c\text{-Ni}_{68}\text{Nb}_{16}\text{Y}_{16}$ heat-treated at 773 K, i.e. beyond the first crystallization event). The heat-treated sample consists of a nanocrystalline Ni_2Y phase and a remaining amorphous Ni-Nb phase. The mean crystallite size is about 5 nm, as can be seen from the TEM image in Fig. 4b. The lattice parameter of the Ni_2Y phase indicates that to some extent Nb is still dissolved. No inhomogeneous structures could be resolved from the TEM image of the as-cast sample (Fig. 4a). In the SAXS curves a dramatic change takes place for the sample that was heat-treated beyond the first crystallization temperature. Though

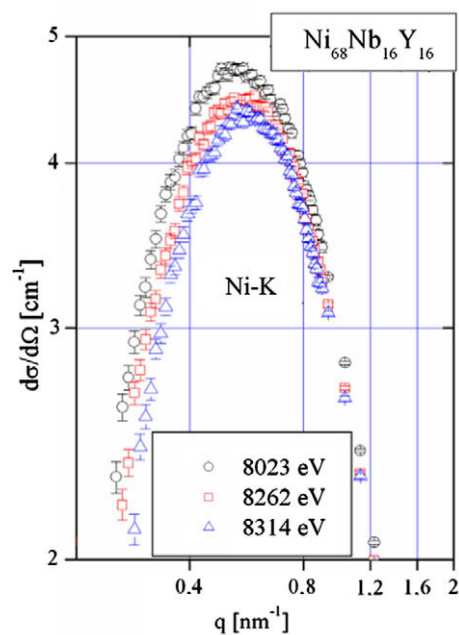


Fig. 5. ASAXS sequence obtained from as-quenched $\text{Ni}_{68}\text{Nb}_{16}\text{Y}_{16}$. The correlation peak at 0.52 nm^{-1} shows systematic energy dependence. When approaching the K-absorption edge of nickel the cross-section declines, indicating slight differences in Ni concentration in the fluctuations.

the correlation maximum remains unchanged on the q -axis, it is shifted on the y -axis by nearly an order of magnitude, probably due to a higher electron density contrast caused by a larger concentration gradient. Additionally, the asymptotic behavior changes from q^{-2} to q^{-4} , indicating the formation of small crystallites with smooth interfaces to the surrounding phase. Clearly the fluctuation length of the as-quenched state determines the size of the nanocrystals. The phase separation of the glass is also the reason for the different crystallization steps of the two phases (the amorphous Ni-Nb phase crystallizes into NbNi_3 at the higher temperature of about 900 K). The ASAXS sequences of the three alloys at three selected X-ray ener-

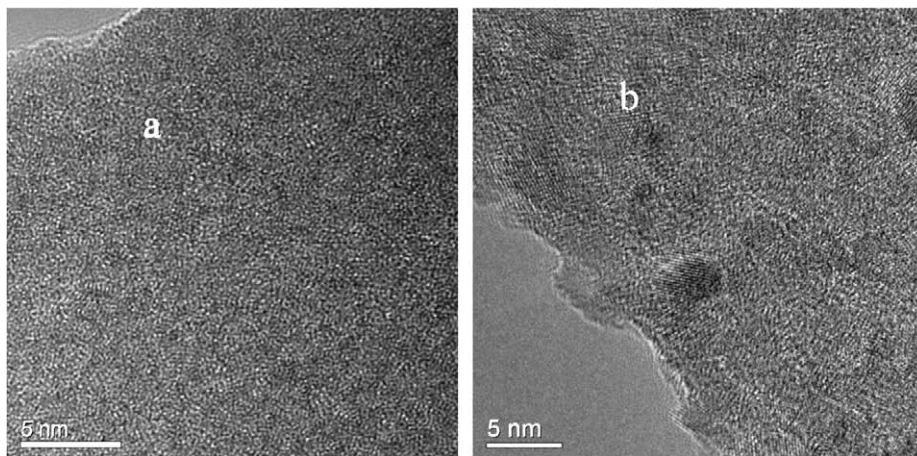


Fig. 4. TEM pictures of the alloy $\text{Ni}_{68}\text{Nb}_{16}\text{Y}_{16}$ as quenched (a) and partially crystallized (b).

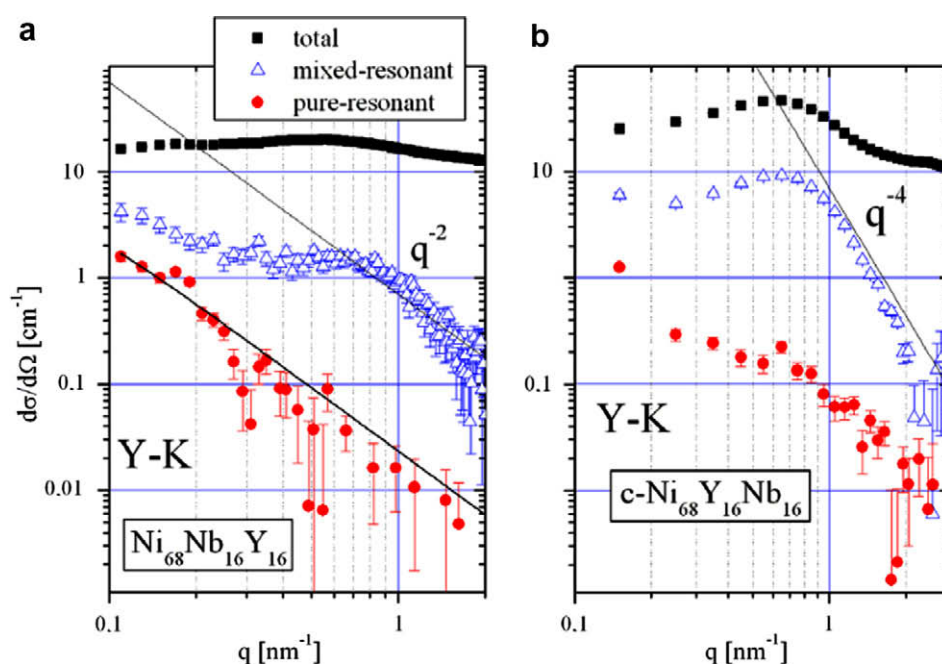


Fig. 6. Total scattering curves (squares), separated scattering curves (triangles) and the form factors of the pure-resonant scattering contribution (circles) of the Y-related concentration fluctuations. (a and b) The different heat treatments: (a) as-quenched and (b) partially crystallized. Above the first crystallization point the asymptotic behavior of the scattering curves changes from q^{-2} to q^{-4} , indicating that smooth interfaces probably exist between the small crystallites and the surrounding amorphous phase. The solid line passing through the red circles of the pure-resonant scattering in (a) represents a model function (see text). (For interpretation of the references to colour in this figure legend, the reader is referred to the web version of this article.)

gies in the vicinity of the K-absorption edge of Ni show systematic but very small declination of the cross-section in the range between 0.2 and 2 nm^{-1} (Fig. 5), indicating small differences in the amount of Ni in the concentration fluctuations, which constitute the correlation maxima of the three alloys. A closer analysis of the resonant invariant obtained from the ASAXS sequences near the Ni K-edge could not provide reliable numbers for a Ni gradient (concentration), indicating that the difference in the Ni concentration in the fluctuations is too small, i.e. below the resolution of this experiment. Anyway, because the nickel component serves as the matrix, the important quantitative parameters of decomposition are related to the concentration fluctuations of yttrium and niobium, and thus can be only obtained from q -ASAXS measurements at the K-absorption edges of yttrium and niobium.

Detailed quantitative information was obtained from the measurements at the K-absorption edges of yttrium and niobium. Fig. 6a and b summarizes the results obtained from the yttrium K-edge (17038 eV) for the two samples $\text{Ni}_{68}\text{Nb}_{16}\text{Y}_{16}$ and $\text{c-Ni}_{68}\text{Nb}_{16}\text{Y}_{16}$. The black squares in Fig. 6 represent the total scattering of the as-quenched sample (a) and the heat-treated sample (b). The correlation maximum appears for both samples at about 0.6 nm^{-1} , as known already from the ASAXS measurements at the Ni K-edge. The total scattering curves are superimposed by a strong isotropic scattering contribution, which originates mainly from the fluorescence of the Ni component (68 at.%). By calculating the separated scattering curves (Eq. (3)) this isotropic fluorescence contribution

is removed, revealing a q^{-4} behavior in the asymptotic part of the separated scattering curve (blue triangles) of the heat-treated (crystallized) sample, which is already known from the measurements at the Ni K-edge. As can be seen from the error bars of the separated scattering curve of the as-quenched sample (blue triangles), the asymptotic behavior above 1 nm^{-1} is not clear, i.e. it is beyond the resolution, and needs closer consideration by analyzing the pure-resonant scattering contribution with larger q -bins (see below). The solid lines in Fig. 6a and b represent the q^{-2} and q^{-4} behavior respectively.

From Eq. (4), the pure-resonant scattering (or, more precisely, the form factor of the pure-resonant scattering) was calculated for both samples. Because the error bars of the pure-resonant scattering become rather large at higher q -values, especially for the as-quenched sample, the number of q -bins was reduced in comparison to the mixed-resonant and total scattering curves, with the aim of obtaining smaller error bars at q -values larger than 0.5 nm^{-1} . The procedure was as follows: the cross-section of the pure-resonant form factor was averaged over neighboring q -bins. The result gives the cross-section at the center of the averaged q -interval. The error of the averaged cross-section is the averaged squared error calculated from the errors of the single q -bins. Though the error bars are still large at higher q -values, the pure-resonant scattering for both samples was clearly resolved. In particular, at higher q -values of about 1 nm^{-1} the pure-resonant scattering contribution of the crystallized sample is nearly an order of magnitude higher compared to the as-quenched

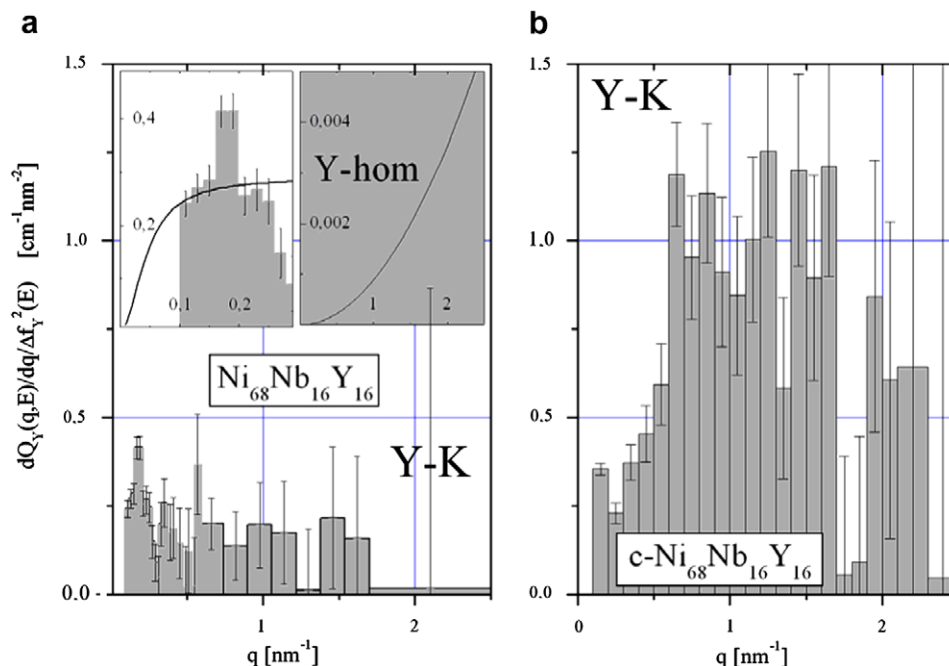


Fig. 7. The first derivative of the resonant invariant (Eq. (6b)) of (a) as-quenched and (b) partially crystallized $\text{Ni}_{68}\text{Nb}_{16}\text{Y}_{16}$ obtained from ASAXS sequences at the Y K-edge (17038 eV). The integrals (grey area) represent the resonant invariant (Eq. (6a)) from which the Y concentrations can be calculated. The right inset represents the upper limit of 16 at.% homogeneously distributed Y, contributing to the resonant invariant. The left inset explains the contribution that is missing due to the q -resolution. For convenience, the division by 4π is not written on the vertical axis.

sample, indicating a larger amount of yttrium atoms localized in the crystalline phase. Ni_2Y has more Y than the average alloy, even when some Nb is dissolved.

The latter was analyzed more precisely by employing the resonant invariant of Eq. (6a) and (6b). Fig. 7 shows the first derivative of the resonant invariant (Eq. (6b)) of the as-quenched sample (a) and the crystallized sample (b). The grey areas represent the integrals, Q_Z (i.e. the resonant invariant), which are introduced into Eq. (7a) and (7b) for the calculation of the amount of yttrium atoms, \bar{v}_Y , which enter the concentration fluctuations of the as-quenched sample and the crystallites of the heat-treated sample respectively. From Eq. (7a) and (7b), the number of (excess) yttrium atoms that enter the crystallites was calculated to be $2.13(28) \times 10^{21} \text{ cm}^{-3}$, corresponding to about 19% of the Y atoms in the alloy.

A completely different result was obtained from the analysis of the resonant invariant of the as-quenched sample. As can be seen already from a simple comparison of the integrals of both samples in Fig. 7, the number of yttrium atoms that enter the concentration fluctuations must be much more smaller. From Eq. (7a) and (7b), a concentration of $0.39(20) \times 10^{21} \text{ cm}^{-3}$ yttrium atoms was deduced, which corresponds to only 4% of the yttrium atoms.

Though this result is significant, it is near the resolution limits of the experiment, as can be seen from the error bars in Fig. 7a. For a more quantitative discussion of the result, the limited integration area has to be extended over the whole regime $0 \leq q < \infty$. Because no comprehensive description of the scattering curves of a ternary alloy

undergoing spinodal decomposition is to hand, a model function with a q^{-2} -behavior (Ornstein–Zernike originally for binary systems, Eq. (8)) was employed. The model function serves only as a guide for the eye with the aim of estimating the amount of the “missing” scattering contributions at higher and lower q -values, i.e. beyond the resolution of the experiment:

$$i(q) = \frac{\text{const}}{c + q^2} \quad (8)$$

At $q = 0$ the model function reaches a finite value defined by thermodynamic parameters of the alloy (Eq. (8)) and the first derivative of the resonant invariant approaches 0 with $q \rightarrow 0$. The amount of missing contribution to the resonant invariant can be ignored, as can be seen from the left inset in Fig. 7a, which shows a magnified part of the resonant invariant in the low q -range. The missing part below the resolution at q -values smaller than q_{min} is the area between the grey histogram and the solid line of the model function.

The right inset in Fig. 7a represents the contribution of homogeneously distributed Y atoms with a concentration of 16 at.% of the resonant invariant. Although this corresponds to the maximum possible amount – a considerable portion of the Y atoms are localized in the fluctuations – the contribution is many orders of magnitude smaller than the contribution detected from the Y atoms in the concentration fluctuations and can thus be also ignored.

Considering the scattering contributions beyond the q -resolution at higher q -values, the result must be interpreted as a lower limit, as is demonstrated by the model function

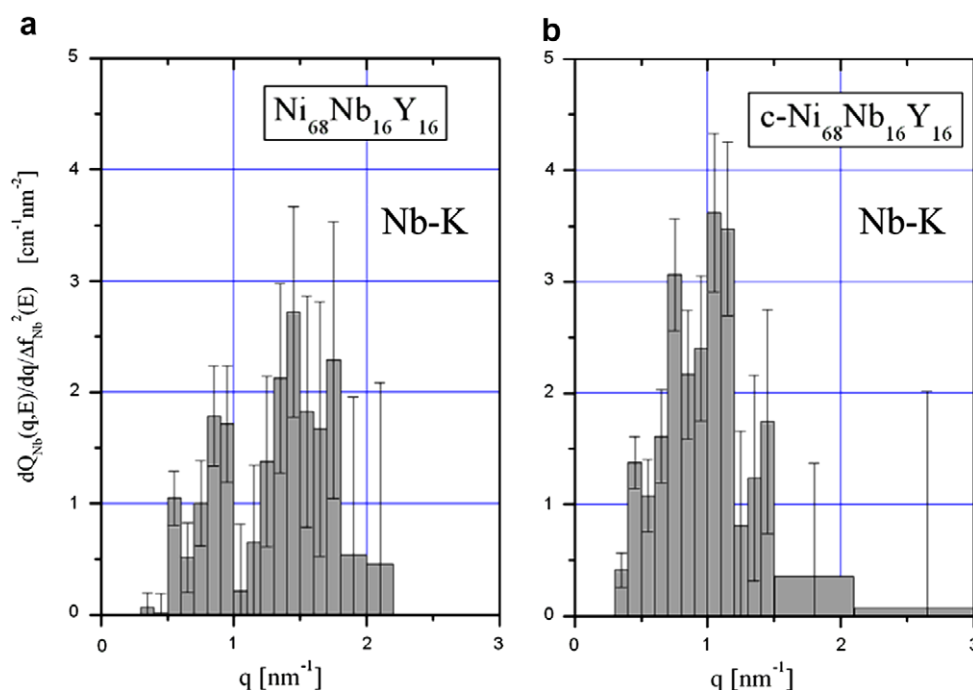


Fig. 8. The first derivative of the resonant invariant (Eq. (6b)) of (a) as-quenched and (b) partially crystallized $\text{Ni}_{68}\text{Nb}_{16}\text{Y}_{16}$ obtained from ASAXS sequences at the Nb K-edge (18986 eV). The integrals (grey area) represent the resonant invariant (Eq. (6a)) from which the Nb concentrations are calculated. For convenience, the division by 4π is not written on the vertical axis.

(Fig. 6a). At higher q -values a cut-off of the scattering function is expected, because otherwise the integral of Eq. (7a) and (7b) would become infinite and the invariant would not exist. As can be seen from Fig. 6a, the cut-off of the pure-resonant form factor cannot be resolved due to the large error bars, and if the cut-off is located at q -values beyond 2 nm^{-1} the concentration of yttrium atoms must be higher. In the case of the crystallized sample, the scattering curve at larger q -values is deep in the Porod regime and no significant contribution can appear in the integral at higher q -values.

The same arguments hold for the interpretation of the results obtained from the ASAXS measurements at the Nb K-edge. Again, the asymptotic behavior of the pure-resonant scattering turns from q^{-2} to q^{-4} when a heat treatment beyond the first crystallization temperature is applied. The amount of niobium atoms in the fluctuations of the as-quenched sample calculated from the resonant invariant (Fig. 8a) turns out to be higher than that of yttrium, corresponding to about 12% of the complete ni-

bium amount in the alloy (Table 1). Surprisingly, the amount of niobium atoms is only slightly higher for the partially crystallized sample (Fig. 8b), i.e. 16% of the complete Nb amount, indicating that the spatial distribution of niobium in the alloy does not change much when partial crystallization (Ni_2Y phase) takes place. This may be attributed to the fact that the niobium component crystallizes above the second crystallization temperature (above 900 K), which we have not yet reached.

From the concentrations of Y and Nb deduced from the resonant invariant in the as-quenched and partially crystallized states, the related volume fractions, Φ_Y and Φ_{Nb} , respectively, can be estimated using the averaged atom volumes of the alloy for V_Y and V_{Nb} . In a further step, the normalized electron densities have been calculated. The results are summarized in Fig. 9. In Fig. 9a the normalized electron density of the as-quenched sample is depicted within one correlation period. The dashed line represents the average electron density resulting from homogeneously distributed atoms in the alloy, which cover nearly 97% of

Table 1

Structural and quantitative parameters of the four samples (three alloys, one with two different heat treatments).

Sample	ζ [nm]	$\bar{v}(Y) 10^{21} [\text{cm}^{-3}]$	c_Y [%]	Φ_Y [%]	$\bar{v}(\text{Nb}) 10^{21} [\text{cm}^{-3}]$	c_{Nb} [%]	Φ_{Nb} [%]
$\text{Ni}_{66}\text{Nb}_{17}\text{Y}_{17}$	15	–	–	–	–	–	–
$\text{Ni}_{68}\text{Nb}_{16}\text{Y}_{16}$	12.2	0.39(2)	4	0.6	1.3(3)	12	1.9
$\text{Ni}_{70}\text{Nb}_{15}\text{Y}_{15}$	5.5	–	–	–	–	–	–
c- $\text{Ni}_{68}\text{Nb}_{16}\text{Y}_{16}$	12.2	2.1(3)	19	3.0	1.8(3)	16	2.5

Column ζ summarizes the increasing correlation length with decreasing Ni concentration. $\bar{v}(Y)$ and $\bar{v}(\text{Nb})$ give the amount of yttrium atoms and niobium atoms localized in the concentration fluctuations calculated from the resonant invariant at the related K-absorption edges. The columns c_Y and c_{Nb} contain the amount in percent of the complete amount of yttrium or niobium atoms, respectively. The latter concentrations were obtained from the averaged atomic volume, which was calculated from the average atomic weight ($68.999 \text{ g mol}^{-1}$) and the average density (8.147 g cm^{-3}) of the alloy. Additionally, the corresponding volume fractions, Φ_Y and Φ_{Nb} , have been calculated (see text).

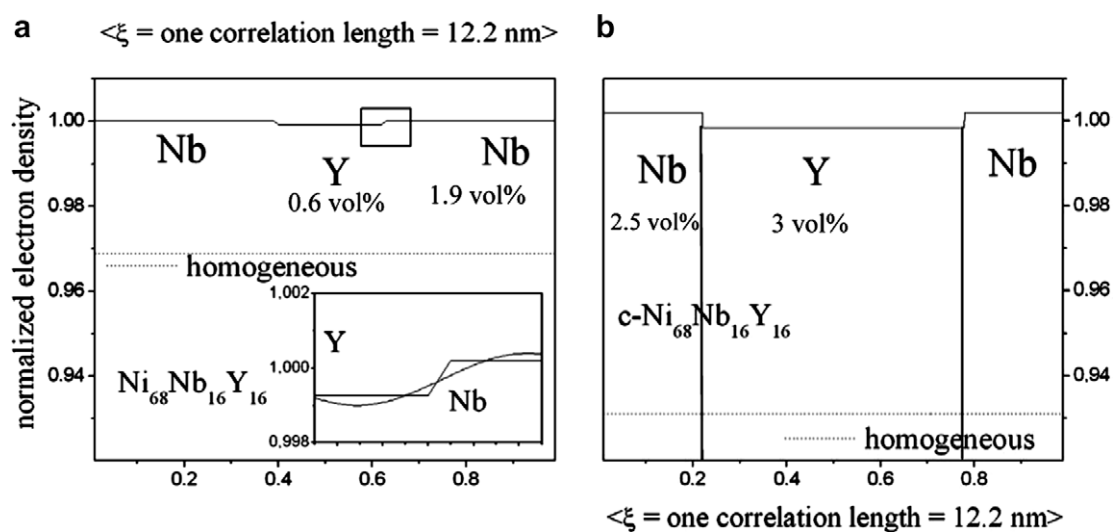


Fig. 9. Normalized electron density of (a) the as-quenched sample and (b) the partially crystallized alloy. The step functions represent the volume fractions of the two phases, Y-rich and Nb-rich, respectively. The dashed lines show the normalized electron density of homogeneously distributed atoms in the two alloys.

the entire volume. The step function shows different volume fractions of inhomogeneously distributed yttrium and niobium, of 0.6% and 1.9%, respectively. The integral of the step function over one correlation period amounts to one. The inset shows a magnification of the step function with the oscillating function, giving a more realistic sketch of a continuously changing concentration over the correlation length.

Again, the dashed line in Fig. 9b represents the average electron density resulting from homogeneously distributed atoms in the partially crystallized alloy. Because the amount of inhomogeneously distributed Y and Nb increased to 3% and 2.5%, respectively (black step function), the value of the volume fraction covered by homogeneously distributed material is reduced to about 93%. The area between the two vertical lines, the step function and the dashed line, depicts the volume fraction of the additional amount of yttrium (excess) atoms in the crystallized phase with respect to the surrounding matrix, while the intersection of the vertical lines with the x -axis represent the volume fraction of the spatial extension of the crystallites, i.e. 55%.

In both Fig. 9a and b the contrast between the Y-rich and Nb-rich phases is negative, explaining the declination of the scattering cross-section when approaching the K-absorption edge of niobium, while the scattering cross-section becomes larger when approaching the K-absorption edge of yttrium.

5. Conclusions

Recently, anomalous small-angle X-ray scattering has become a precise quantitative method (q-ASAXS) for element-specific structural analysis on the mesoscopic length scale. Due to the precision of the techniques, small-angle scattering contributions of $\text{Ni}_{68}\text{Nb}_{16}\text{Y}_{16}$ alloys in the reso-

lution regime $10^{-3} < \Delta I/I < 10^{-2}$ can be reliably separated from a superimposed, orders of magnitude larger inelastic background caused by fluorescence and resonant Raman scattering.

The pure-resonant scattering contributions of inhomogeneously distributed nickel, niobium and yttrium atoms in $\text{Ni}_{68}\text{Nb}_{16}\text{Y}_{16}$ alloys undergoing different heat treatments have been separated from the total scattering SAXS curves. The separated scattering curves obtained from the as-quenched sample show the typical behavior of concentration fluctuations (Ornstein–Zernike) with a correlation maximum corresponding to a correlation length of 12.2 nm. From the resonant invariant, 4% of the yttrium atoms and 12% of the niobium atoms were found to be localized in the fluctuations, corresponding to volume fractions of 0.6% and 1.9%, respectively. This compares to about 19% (3% volume fraction) of enriched yttrium atoms localized in the crystalline phase of the sample, which was heat-treated beyond the first crystallization temperature. Surprisingly, the amount of enriched niobium atoms does not change much due to the latter heat treatment (from 12% to 16%), indicating that the crystallization temperature for the niobium phases is not reached. A model calculation suggests a large volume fraction of 55% covered by small crystallites beyond the first crystallization temperature surrounded by an amorphous shell enriched with Nb with a volume fraction of 45%.

The example demonstrates the capability of quantitatively determining the extent of spinodal decomposition by anomalous small-angle X-ray scattering. Especially with third-generation synchrotron radiation sources, it will be a challenging task to perform time-resolved q -ASAXS measurements with the aim of contributing to a comprehensive theory of spinodal decomposition, e.g. the validation of the Cahn–Hilliard–Cook equation or extension towards a non-linear theory of spinodal decomposition in solids.

References

- [1] Avenarius M. *Ann Physik* 1874;151:303.
- [2] Guthrie F. *Phil Mag* 1884;18(30):497.
- [3] Friedländer J. *Z physik Chemie* 1901;38:385.
- [4] Travers MW, Usher FL. *Proc Roy Soc, A* 1906;78:247.
- [5] Smoluchowski M. *v Ann Physik* 1908;25:205.
- [6] Einstein A. *Ann Physik* 1910;33:1275.
- [7] Ornstein LS, Zernike F. *Proc Acad Sci Amsterdam* 1914;17:793.
- [8] Krivoglaz MA. *Zh Eksperim i Teor Fiz* 1956;31:625.
- [9] Münster A, Sagel K. *Z physik Chem Frankfurt* 1957;12:145.
- [10] Münster A, Sagel K. *Naturwiss* 1957;44:535.
- [11] Münster A, Sagel K. *Mol Phys* 1958;1:23.
- [12] Acuna RJ, Craievich AF. *J Non-Cryst Solids* 1979;34:13.
- [13] Binder K, Fratzl P. In: Kostorz G, editor. *Phase transformations in materials*. Weinheim: Wiley-VHC; 2001. p. 409–80.
- [14] Stuhmann HB. *Adv Polym Sci* 1985;67:123.
- [15] Simon JP, Lyon O, de Fontaine D. *J Appl Cryst* 1985;18:230.
- [16] Stuhmann HB, Goerigk G, Munk B. In: Ebashi S, Koch M, Rubenstein E, editors. *Handbook on synchrotron radiation*, vol. 4. Amsterdam: Elsevier; 1991. p. 555.
- [17] Goerigk G, Williamson DL. *J Non-Cryst Solids* 2001;281:181.
- [18] Goerigk G, Schweins R, Huber K, Ballauff M. *Europhys Lett* 2004;66(3):331.
- [19] Goerigk G, Williamson DL. *J Appl Phys* 2006;99:084309.
- [20] Goerigk G, Huber K, Schweins R. *J Chem Phys* 2007;127:154908.
- [21] Bota A, Varga Z, Goerigk G. *J Phys Chem B* 2007;111:1911.
- [22] Bota A, Varga Z, Goerigk G. *J Phys Chem C* 2008;112:4427.
- [23] Mattern N, Zinkevich M, Löser W, Behr G, Acker J. *J Phase Equil Diff* 2008;29:141.
- [24] Mattern N, Kühn U, Gebert A, Gemming T, Zinkevich M, Wendrock H, et al. *Scripta Materialia* 2005;53:271.
- [25] Mattern N, Gemming T, Goerigk G, Eckert J. *Scripta Mater* 2007;57:29.
- [26] Glatter O, Kratky O. *Small-angle X-ray scattering*. London: Academic Press; 1982.
- [27] Haubold HG, Gruenhagen K, Wagener M, Jungbluth H, Heer H, Pfeil A, et al. *Rev Sci Instrum* 1989;60:1943.
- [28] Goerigk G. *HASYLAB annual report*; 2006. p. 77.
- [29] Cromer DT, Liberman D. *J Chem Phys* 1970;53:1891.
- [30] Cromer DT, Liberman D. *Acta Cryst* 1981;A37:267.
- [31] Mattern N, Goerigk G, Vainio U, Miller MK, Gemming T, Eckert J. *Acta Mat* 2009;57(3):903.

[S3]

A. Bota, Z. Varga, and G. Goerigk,

*Structural Description of the Nickel Part of a Raney-Type Catalyst by
Using Anomalous Small-Angle X-ray Scattering*

Journal of Physical Chemistry C, 112(12), 4427 (2008)

Structural Description of the Nickel Part of a Raney-Type Catalyst by Using Anomalous Small-Angle X-ray Scattering

Attila Bóta,^{*,†} Zoltán Varga,[†] and Günter Goerigk[‡]

Chemical Research Center, Hungarian Academy of Sciences, Institute of Surface Chemistry and Catalysis, HU-1025 Budapest, Pusztaszeri út 59-67. Hungary, and Institute of Solid State Physics, Research Centre Jülich, D-52425 Jülich, Germany

Received: January 10, 2008; In Final Form: February 21, 2008

The evaluation of the “pure resonant term” of the anomalous small-angle X-ray scattering (ASAXS) and the exclusive characterization of the spatial distribution of the Ni particles in a Raney-type catalyst are presented. The ASAXS method not only gives a qualitative characterization of catalytic nanoparticles without any separation technique but it also provides a quantitative determination of these active particles. By using the experimentally determined pure resonant term and the linear X-ray absorption of the sample, we got 38.5 ± 0.5 mol % nanostructured form of nickel and 40.3 mol % total nickel content, demonstrating a unique further advantage of ASAXS method.

Introduction

The detailed characterization of catalysts requires applications of different methods. Among them, the SAXS is an excellent tool because the description of the solid matrix and the pores is possible in a very large size range, extending from nanometers to several hundred nanometers.¹ Moreover, the anomalous small-angle X-ray scattering (ASAXS) gives further advantages providing selective information about the different parts of the catalyst.^{2,3} For example, by choosing a characteristic element of the catalyst particles or of the support, separate structural descriptions related to these parts are possible. The theory of ASAXS is based on the energy dependence of the scattering factor of atoms. Consequently, this method can only be executed at synchrotron stations, where the application of the tunable X-ray radiation is insured. Now, we present the applicability of the ASAXS technique in the case of a nonpyrophoric nickel catalyst. This catalyst was thoroughly characterized by different methods, such as adsorption (nitrogen), X-ray powder diffraction, small-angle X-ray scattering, transmission electron microscopy, and scanning electron microscopy.^{4,5} It consists of at least four parts: finely dispersed nickel particles and gibbsite and bayerite as support and pores. The mean crystallite size of the nickel particles deduced from its (111) wide-angle diffraction profile is 54 Å, while the anomalous small-angle X-ray scattering (ASAXS) has provided further information about their shape, which is cylindrical (17.7 Å radius and 56 Å height), in good agreement with the transmission electron microscopy study that also showed stocky shaped particles. In previous studies, however, a strict condition has been supposed, namely that the separated ASAXS curves carry the entire structural information

about the catalyst particles and the cross term in the scattering intensity; the product of the intensity of the considered element of the catalyst and the intensity of the surrounding matrix can be neglected. In this work, we present the evaluation of the “pure resonant term” of the ASAXS whereby the exclusive characterization of the spatial distribution of the Ni particles is given.

Experimental Section

The new, nonpyrophoric Raney-type catalyst was prepared from Ni–Al alloy powder (for details of preparation see ref 4). The dried powder sample was placed in a sandwich sample holder covered with thin foil.

The anomalous small-angle X-ray scattering (ASAXS) measurements were performed at the JUSIFA small-angle scattering apparatus of the DORIS synchrotron radiation source in DESY (Hamburg).⁶ This beamline is designed especially for anomalous scattering studies and enables XANES and ASAXS studies near the X-ray absorption edge in a relatively wide energy range from 4.5 to 35 keV with an energy resolution $\Delta E/E < 2 \times 10^{-4}$.⁶ For the contrast variation, the SAXS curves were detected at 8037, 8323, 8332 eV near the nickel X-ray absorption edge (at 8333 eV). The energy calibration of the beamline was executed by the measurement of the absorption edge of metal Ni. The net scattering data collected at different energies were computed to the same abscissa and were normalized for the primary beam intensity and corrected for absorption. Finally, the scattering curves were calibrated to absolute units of macroscopic cross sections ($\text{cm}^2/\text{cm}^3 = \text{cm}^{-1}$). The scattering variable, q , is defined as $q = (4\pi/\lambda)\sin \Theta$, where λ is the wavelength of the beam, and Θ is the half value of the scattering angle. For data evaluation, the anomalous dispersion corrections of Ni were calculated according to the method described by Cromer and Liberman.⁷ The calculated values of f' and f'' are also shown in Figure 1. The fluorescence and the resonant Rahman scattering were considered as a constant background terms and were subtracted. The values of f' and f'' at 8332 eV, the nearest

* To whom correspondence may be addressed. Tel: +36 1 463 2473. Fax: +36 1 463 3767. E-mail: abota@mail.bme.hu. On leave from Budapest University of Technology and Economics, Dep. of Phys. Chem. and Mat. Sci.

[†] Hungarian Academy of Sciences.

[‡] Research Centre Jülich.

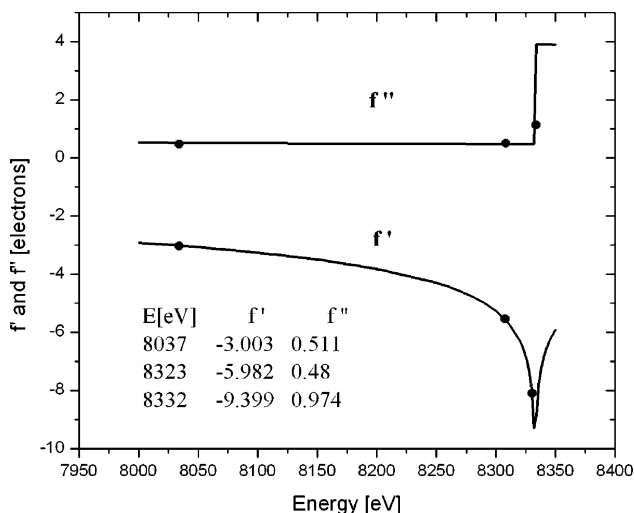


Figure 1. Energy dependence of the anomalous dispersion corrections (f' and f'') for nickel.

energy to the Ni absorption edge, were smeared by the profile of the energy distribution of the incident beam, which was approximated by a Gaussian function ($\sigma = 1$ eV).⁸

Results and Discussion

The unique applicability of the ASAXS method is based on the energy dependence of the scattering factor of nickel, which is a complex quantity:⁹

$$f_{\text{Ni}}(E) = f_{0,\text{Ni}} + f'_{\text{Ni}}(E) + if''_{\text{Ni}}(E) \quad (1)$$

Consequently, the scattering amplitude of the whole catalyst can be described as the sum of the terms corresponding to the energy independent (A) and to the dependent ($(f' + if'')B$) ones.⁹ It is worth mentioning, that the “A” term is the scattering amplitude of all parts (Ni, matrix, pores) while “ $(f' + if'')B$ ” is only that of Ni. In this case the energy dependent intensity (ASAXS curve) contains three terms as follows:¹⁰

$$I(q, E) = [A(q)^2 + 2f'(E)A(q)B(q) + (f'^2(E) + f''^2(E))B(q)^2] \quad (2)$$

The scattering curve of the nickel catalyst measured at 8037 eV is intense and extends in a wide regime of the scattering variable (q), from 2×10^{-2} to 0.3 $1/\text{\AA}$ as is shown in the upper curve in Figure 2.

Changing the energy of the incident beam near the absorption edge (from 8037 eV close to 8333 eV) causes a slight difference in the measured scattering curves that can be characterized by their difference, known as separated ASAXS curves, shown in the middle curve of the Figure 2. About 10% effect appears in the separated curves due to the energy-dependence scattering factor of Ni. The separated ASAXS curve, however, contains two terms, the “cross” and the “pure” resonant” ones as is described by the next equation:

$$\Delta I(q, E_1, E_2) = I(q, E_1) - I(q, E_2) = [2(f'(E_1) - f'(E_2))A(q)B(q) + (f'^2(E_1) - f'^2(E_2) + f''^2(E_1) - f''^2(E_2))B^2(q)] \quad (3)$$

The shapes of the ASAXS (upper in Figure 2) and the separated (middle in Figure 2) curves, are different indicating

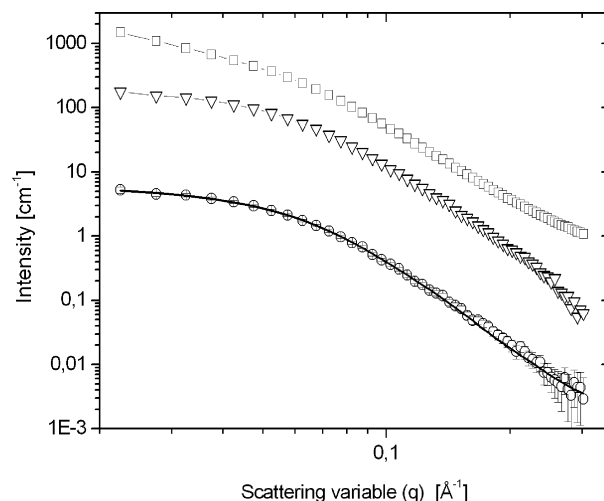


Figure 2. ASAXS (squares), separated ASAXS (triangles), and the pure resonant scattering curve (circles) of Raney-type nickel catalyst. The pure resonant curve is fitted by the “pearl necklace” model (solid line).

the significant contribution of the scattering of the other components beside the nickel particles (such as support, pores) corresponding to the different terms of eqs 2 and 3.

To eliminate the contribution of scattering of the matrix entirely, the measurements were performed at three different energies (at 8037, 8323, 8332 eV); thus, we can obtain the $B^2(q)$ “pure resonant” term as is described by the next (eq 4) equation:

$$B_{\text{Ni}}^2(q) = \frac{1}{C(E_1, E_2, E_3)} \left[\frac{\Delta I(q, E_1, E_2)}{f'(E_1) - f'(E_2)} - \frac{\Delta I(q, E_1, E_3)}{f'(E_1) - f'(E_3)} \right] \quad (4)$$

$$C(E_1, E_2, E_3) = f'(E_2) - f'(E_3) + \frac{f''^2(E_1) - f''^2(E_2)}{f'(E_1) - f'(E_2)} - \frac{f''^2(E_1) - f''^2(E_3)}{f'(E_1) - f'(E_3)}$$

The $B^2(q)$ “pure resonant” term is also plotted in the bottom of Figure 2. The intensity of this curve is extremely reduced underlining the importance of the measurement with low error range. The separated and the pure resonant curves exhibit high similarity supporting our previous assumption that the cross term can be neglected in a first approximation. However, under a closer inspection, we can reveal some differences between the shapes of the separated and the pure resonant curves, which is also visible in a logarithmic plot. The resonant term has no straight line section in the regime of the small scattering variable; its declination is more expressed than that of the separated one, indicating some differences in the shape of the nickel particles deduced from the pure resonant term and the separated curve. This curve was described by the “pearl necklace” model as meant by Rubinstein et al.¹¹

$$B_{\text{Ni}}(q) = \text{const} \int_0^\infty P(R) \cdot \left(\frac{\sin(qR) - qR \cos(qR)}{q^3} \right)^2 \cdot \left(N + 2 \sum_{n=1}^{N-1} (N-n) \frac{\sin(nqd)}{nqd} \right) dR \quad (5/a)$$

$$P(R) = \frac{1}{\sqrt{2\pi}} \frac{1}{\sigma R} \exp\left(-\frac{\ln^2 \frac{R}{R_0}}{2\sigma^2}\right) \quad (5/b)$$

This model involves the correlation of the neighboring spherical compact units (with radius R) that are displaced nearly in a linear form. The distance between the connecting spheres (with number of N) is d . The scattering of the spheres and the correlation are expressed by the second and third terms in eq 5/a, respectively. The size distribution of the spheres is described by a log-normal function, as is shown in eq 5/b. The best fit results in a size distribution with a characteristic radius of 20.8 ($\sigma = 0.24$) Å, shown in Figure 3. This characteristic value is smaller than that determined on the separated ASAXS curves by the method of Shull and Roess.⁵ Moreover, the size distribution derived from the pure resonant curve does not indicate particles smaller than those with a radius of 10 Å. The number of the connected spheres is 2, and their distance is 41.6 Å, which is approximately double the value of the characteristic radius. Therefore, we can suppose that the nickel is present in the form of particle pairs in the catalyst. It must be mentioned that Toth et al. have also obtained 2 neighboring spheres by using a reverse Monte Carlo-type computer simulation of the SAXS data of this catalyst.¹²

The anomalous small-angle scattering not only gives a qualitative characterization of catalytic nanoparticles without any separation technique but it also provides a quantitative determination of these active particles. This information about the Ni content of the catalyst can be deduced from the experimentally accessible part of the pure resonant term by calculating the so-called resonant invariant¹³

$$Q_{\text{Ni}}(E) = \frac{1}{4\pi} |\Delta f_{\text{Ni}}(E)|^2 \int_Q B_{\text{Ni}}(q) q^3 q \quad (6)$$

where $\Delta f_{\text{Ni}}(E)$ is the contrast of the scattering factor for the Ni atoms. From the invariant, the nickel content of the sample can be determined because it is connected to the excess electron density of the resonant atoms. The number density of the nickel atoms is as follows

$$c[1/\text{cm}^3] = \frac{V_{\text{Ni}} Q_{\text{Ni}}}{(2\pi)^3 r_0^2 |\Delta f_{\text{Ni}}(E)|^2} \quad (7)$$

where V_{Ni} is the volume of a nickel atom and r_0 is the classical electron radius. For the calculation of these quantities, the

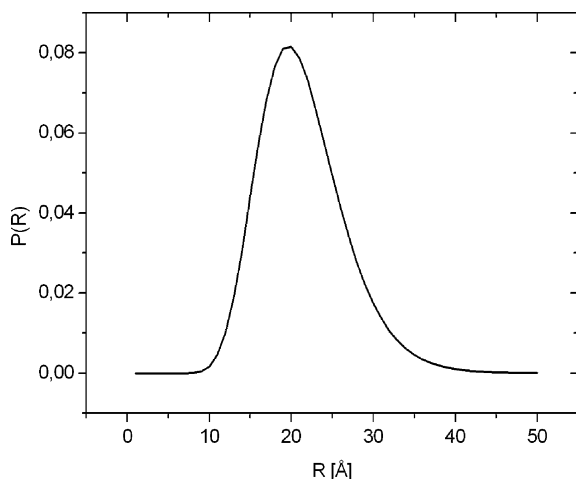


Figure 3. Log-normal particle size-distribution of the nickel catalyst nanoparticles.

calibration to absolute units of macroscopic cross section and the small error in the measured intensity is mandatory.

In the present case, by using the experimentally determined pure resonant term and an approximated specific weight of the sample of $\rho_{\text{catalyst}} = 1.08 \text{ g/cm}^3$, we got $38.5 \pm 0.5 \text{ mol } \%$ for the nickel content in the active, nanostructured form of the catalyst examined above.

For the determination of the full Ni content, we measured the linear X-ray absorption of the sample before and after the nickel edge. By assuming that the atomic absorption cross section of the matrix does not change significantly on this energy range ($\Delta\sigma^a(\text{matrix}) \approx 0$), the jump in the measured linear absorption coefficient can be related to the nickel content as follows:

$$\Delta\mu D = \frac{N_A}{MW} (x_{\text{Ni}} \Delta\sigma_{\text{Ni}}^a) \rho D \quad (8)$$

where N_A is the Avogadro number, MW and ρ are the molar weight and the specific weight of the catalyst, respectively, x_{Ni} is the molar ratio of nickel in the system, D is the thickness of the sample, and $\Delta\sigma_{\text{Ni}}^a$ is the change in the atomic cross section of nickel. Using the tabulated values for the latter¹⁴ and the approximated specific weight described above, we got 40.3 mol % for the total nickel content. This value, however, is smaller than that (50%) that was used in the beginning of the preparation procedure, indicating loss of nickel during the synthesis.⁴

With the methods described above, one can determine the ratio of the effectively utilized and the total amount of the active component of the catalyst, demonstrating a further advantage of the ASAXS method.

The possibility of a qualitative description and at the same time a quantitative determination of the catalyst particles by the ASAXS method can give new perspectives of the tunable synchrotron radiation in the catalyst research and the scientific facilities can be utilized more effectively in industrial fields.

Acknowledgment. This work was supported by the Contract RII3-CT-2004-506008 of the European Community at DESY/HASYLAB (Hamburg, Germany) and by the Hungarian Scientific Funds OTKA (Bóta, T 43055). We thank Professor J. Petro for the offered sample.

References and Notes

- (1) Lemaitre, J. L.; Menon, P. G.; Delannay, F. In *Characterization of Heterogeneous Catalysts*; Delannay, F., Ed.; Dekker: New York, 1984; pp 299–365.
- (2) Rasmussen, F. B.; Molenbroek, A. M.; Clausen, B. S.; Feidenhans, R. *J. Catal.* **2000**, *190*, 205.
- (3) Goerigk, G.; Haubold, H.-G.; Schilling, W. *J. Appl. Crystallogr.* **1997**, *30*, 1041.
- (4) Petró, J.; Bóta, A.; László, K.; Beyer, H.; Kálmán, E.; Dódon, I. *Appl. Catal., A* **2000**, *190*, 73.
- (5) Bóta, A.; Goerigk, G.; Drucker, T.; Haubold, H. G.; Petró, J. *J. Catal.* **2002**, *205*, 354.
- (6) Haubold, H.-G.; Gruenhagen, K.; Wagener, M.; Jungbluth, H.; Heer, H.; Pfeil, A.; Rongen, H.; Brandenburg, G.; Moeller, R.; Matzerath, J.; Hiller, P.; Halling, H. *Rev. Sci. Instrum.* **1989**, *60*, 1943.
- (7) Cromer, D. T.; Liberman, D. *J. Chem. Phys.* **1970**, *53*, 1891.
- (8) Ballauff, M.; Jusufi, A. *Colloid Polym. Sci.* **2006**, *284*, 1303.
- (9) Materlik, G.; Sparks, C. J.; Fischer, K., Eds. In *Resonant Anomalous Scattering, Theory and Applications*; Elsevier Sci.: Amsterdam, 1994.
- (10) Goerigk, G.; Williamson, D. L. *J. Appl. Phys.* **2006**, *99*, 84309.
- (11) Dobrynin, A. V.; Rubinstein, M.; Obukhov, S. P. *Macromolecules* **1996**, *32*, 3264.
- (12) Tóth, G.; Körmendi, K.; Vrabcz, A.; Bóta, A. *J. Chem. Phys.* **2004**, *121* (21), 10634.
- (13) Goerigk, G.; Huber, K.; Schweins, R. *J. Chem. Phys.* **2007**, *127*, 154908.
- (14) Henke, B. L.; Gullikson, E. M.; Davis, J. C. *Data Nucl. Data Tables* **1993**, *54*, 181; for updated values, see http://www.wcxro.lbl.gov/optical_constants/.

[S4]

G. Goerigk, K. Huber, and R. Schweins,

*Probing the Extent of the Sr²⁺ - Ion Condensation to Anionic Polyacrylate
Coils: A Quantitative Anomalous Small-Angle X-ray Scattering Study*

J. Chem. Phys., 127, 154908-1 (2007)

Probing the extent of the Sr^{2+} ion condensation to anionic polyacrylate coils: A quantitative anomalous small-angle x-ray scattering study

G. Goerigk^{a)}

*Institut für Festkörperforschung, Forschungszentrum Jülich, Postfach 1913,
D-52425 Jülich, Federal Republic of Germany*

K. Huber

*Department Chemie, Fakultät für Naturwissenschaften, Universität Paderborn, Warburgerstr. 100,
D-33098 Paderborn, Federal Republic of Germany*

R. Schweins

*Large Scale Structures Group, Institut Laue-Langevin, 6 rue Jules Horowitz, B.P. 156, F-38042 Grenoble
CEDEX 9 France*

(Received 29 June 2007; accepted 28 August 2007; published online 18 October 2007)

The shrinking process of anionic sodium polyacrylate (NaPA) chains in aqueous solution induced by Sr^{2+} counterions was analyzed by anomalous small-angle x-ray scattering. Scattering experiments were performed close to the precipitation threshold of strontium polyacrylate. The pure-resonant scattering contribution, which is related to the structural distribution of the Sr^{2+} counterions, was used to analyze the extent of Sr^{2+} condensation onto the polyacrylate coils. A series of four samples with different ratios $[\text{Sr}^{2+}]/[\text{NaPA}]$ (between 0.451 and 0.464) has been investigated. From the quantitative analysis of the resonant invariant, the amount of Sr cations localized in the collapsed phase was calculated with concentrations \bar{v} between 0.94×10^{17} and $2.01 \times 10^{17} \text{ cm}^{-3}$ corresponding to an amount of Sr cations in the collapsed phase between 9% and 23% of the total Sr^{2+} cations in solution. If compared to the concentration of polyacrylate expressed in moles of monomers $[\text{NaPA}]$, a degree of site binding of $r = [\text{Sr}^{2+}]/[\text{NaPA}]$ between 0.05 and 0.11 was estimated. These values clearly differ from $r = 0.25$, which was established from former light scattering experiments, indicating that the counterion condensation starts before the phase border is reached and increases rather sharply at the border. © 2007 American Institute of Physics.

[DOI: 10.1063/1.2787008]

I. INTRODUCTION

The density of charges along a polyelectrolyte chain makes the chain conformation sensitive to electric charges. The two most efficient techniques to control changes in polyelectrolyte conformation are (i) the screening of electrostatic interactions among charged polymer segments by adding an inert salt¹ and (ii) the extinction of charges on the polyelectrolyte chain by adding specifically interacting counterions.^{2,3} Synthetic polyelectrolytes may therefore be used as simple models for biopolymers, where the role of electric charges is essential for the proper functioning of nucleic acids, numerous enzymes, and proteins.

Theoretical understanding of the mechanism underlying the first technique has made significant progress. With increasing electrostatic screening, the shape of the polyelectrolyte gradually changes from a coil to a compact sphere, passing a cascade of transition states. For these transition states, cigarlike or pearl necklace structures are discussed. The latter were predicted in analogy to the Rayleigh instability of oil droplets while being electrically charged.^{4,5} Beyond all

doubt, the actual shape depends in a subtle way on the counterion concentration and interactions between solvent and chain backbone.⁴⁻¹⁰ Although, the pearl necklace model has attracted much attention,¹¹⁻¹⁵ a quantitative analysis of the condensed phase is still lacking.

The present investigation focuses on the behavior of sodium polyacrylate (NaPA) chains, subjected to the addition of alkaline earth cations as an example for technique (ii). Alkaline earth cations are known to specifically interact with the anionic carboxylate residues, located on every other carbon atom of the polymer backbone. Formation of complex bonds between the anionic groups and alkaline earth cations neutralizes electric charges and thereby changes the nature of the respective chain segments. As a consequence, solubility of the polyelectrolyte is lowered, which leads to a significant coil shrinking and eventually causes a precipitation of the respective alkaline earth salt.^{2,3,14,15}

The precipitation depends on the concentration of NaPA and of the alkaline earth cations, denoted as M^{2+} . Beyond a threshold concentration $[\text{M}^{2+}]_0$, an additional stoichiometric amount of M^{2+} per NaPA function is required to precipitate the polycarboxylate chains. This correlation can be represented in a phase diagram by means of a linear relation of the form $[\text{M}^{2+}]_c = [\text{M}^{2+}]_0 + r_0[\text{NaPA}]_c$ which separates the one phase regime of a dilute solution from the precipitate, thus

^{a)} Author to whom correspondence should be addressed. Also at JCNS-FRMII, c/o Technische Universität München, Lichtenbergstr. 1, D-85747 Garching, Federal Republic of Germany. Tel: +49-89-28910746. Fax: +49-89-28910798. Electronic mail: g.goerigk@fz-juelich.de.

acting as a phase boundary.^{3,14} Based on light scattering measurements, changes in coil shape and size are expected to be more pronounced the closer one gets to this phase boundary. Although the coils adopt a spherelike shape prior to precipitation,¹⁴ the shape of intermediates along the coil-to-sphere transition and especially the extent of M^{2+} condensation close to the phase border is still an unsettled question.

In this presentation, the question of how to determine the amount of Sr cations localized in the collapsed phase with respect to the total amount of Sr cations in the solvent, by precise analysis of what will be introduced below as the resonant invariant, while approaching the phase boundary of strontium polyacrylate (i.e., $M^{2+} = Sr^{2+}$) shall be addressed.

Anomalous small-angle x-ray scattering enables the quantitative and structural characterization of the counterion distribution around the macroions by tuning the energy in the vicinity of the absorption edge of the counterion (i.e., Sr^{2+}) in question. The distribution of the counterions is not accessible by conventional small-angle x-ray scattering measurements because the scattering contributions of the counterions and the macroions superimpose and cannot be distinguished. The first anomalous small-angle x-ray scattering (ASAXS) experiment on counterion distributions was reported by Stuhmann.¹⁶ Interest in the application of this promising method to macromolecules only revived at the turn of the century, propelled by the synthesis of new model polyelectrolytes.^{17–21}

II. ASAXS MEASUREMENTS

In the case of a dilute solution of negatively charged polymers, which are surrounded by positively charged Sr counterions, the scattering amplitude writes

$$A(\mathbf{q}) = \int_V \Delta\rho_{\text{poly}}(\mathbf{r}) \cdot \exp(-i\mathbf{q}\mathbf{r})d^3r + \int_V \Delta\rho_{\text{Sr}}(\mathbf{r}) \cdot \exp(-i\mathbf{q}\mathbf{r})d^3r. \quad (1)$$

q is the magnitude of the scattering vector $[=(4\pi/\lambda)\sin\Theta]$, where 2Θ is the scattering angle and λ the x-ray wavelength. $\Delta\rho_{\text{poly}}$ and $\Delta\rho_{\text{Sr}}$ are the excess electron densities of the polyelectrolyte chains and the counterions,

$$\begin{aligned} \Delta\rho_{\text{poly}}(\mathbf{r}) &= \Delta f_{\text{poly}} \cdot u(\mathbf{r}) = (f_{\text{poly}} - \rho_m V_{\text{poly}}) \cdot u(\mathbf{r}), \\ \Delta\rho_{\text{Sr}}(\mathbf{r}, E) &= \Delta f_{\text{Sr}}(E) \cdot v(\mathbf{r}) = ((f_{0,\text{Sr}} - \rho_m V_{\text{Sr}}) + f'_{\text{Sr}}(E) \\ &\quad + if''_{\text{Sr}}(E)) \cdot v(\mathbf{r}), \end{aligned} \quad (2)$$

calculated from the electron density ρ_m of the solvent and the volume of the chain V_{poly} and the Sr^{2+} ion V_{Sr} , respectively, while $u(\mathbf{r})$ and $v(\mathbf{r})$ are the particle densities of the polymer chains and the Sr^{2+} ions, respectively. The molecular scattering factor (number of electrons) of the chain $f_{\text{poly}}(E) \approx \text{const}$ is nearly energy independent, while the atomic scattering factor of the counterions $f_{\text{Sr}}(E) = f_{0,\text{Sr}} + f'_{\text{Sr}}(E) + if''_{\text{Sr}}(E)$ shows strong energy dependent variation in the vicinity of the absorption edge of the Sr^{2+} ion due to the so-called anomalous dispersion corrections, $f'_{\text{Sr}}(E)$ and $f''_{\text{Sr}}(E)$. Calculating the scattering intensity $I(\mathbf{q}) = |A(\mathbf{q})|^2 = A(\mathbf{q}) \cdot A^*(\mathbf{q})$ by means of Eqs. (1) and (2) and averaging over all orientations

of the polymer yields a sum of three contributions $I(q, E) = |A_{\text{poly}}(q)|^2 + 2 \text{Re} A_{\text{poly}}(q) \text{Re} A_{\text{Sr}}(q, E) + |A_{\text{Sr}}(q, E)|^2$, with the integrals¹⁶

$$\begin{aligned} |A_{\text{poly}}(q)|^2 &= 4\pi\Delta f_{\text{poly}}^2 \int_V \int_V u(\mathbf{r})u(\mathbf{r}') \frac{\sin(q|\mathbf{r}-\mathbf{r}'|)}{q|\mathbf{r}-\mathbf{r}'|} d^3r d^3r', \\ 2 \text{Re} A_{\text{poly}}(q) \text{Re} A_{\text{Sr}}(q, E) &= 4\pi 2\Delta f_{\text{poly}}(f_{0,\text{Sr}} - \rho_m V_{\text{Sr}} \\ &\quad + f'_{\text{Sr}}(E)) \int_V \int_V u(\mathbf{r})v(\mathbf{r}') \frac{\sin(q|\mathbf{r}-\mathbf{r}'|)}{q|\mathbf{r}-\mathbf{r}'|} d^3r d^3r', \\ |A_{\text{Sr}}(q, E)|^2 &= 4\pi |\Delta f_{\text{Sr}}(E)|^2 \int_V \int_V v(\mathbf{r})v(\mathbf{r}') \frac{\sin(q|\mathbf{r}-\mathbf{r}'|)}{q|\mathbf{r}-\mathbf{r}'|} d^3r d^3r'. \end{aligned} \quad (3)$$

Equation (3) gives the nonresonant scattering of the polymer chains $|A_{\text{poly}}(q)|^2$, the cross-term or mixed-resonant scattering $2 \text{Re} A_{\text{poly}}(q) \text{Re} A_{\text{Sr}}(q, E)$ originating from the superposition of the scattering amplitudes of the polymer and the Sr^{2+} ions, and the scattering of the counterions $|A_{\text{Sr}}(q, E)|^2$, which contains the so-called pure-resonant scattering. By measuring the scattering curves at two energies in the vicinity of the absorption edge of the Sr^{2+} ions and subtracting the two scattering curves $\Delta I(q, E_1, E_2) = I(q, E_1) - I(q, E_2)$, the nonresonant scattering contribution of the polymer is vanishing:

$$\begin{aligned} \Delta I(q, E_1, E_2) &= 4\pi 2\Delta f_{\text{poly}}(f'_{\text{Sr}}(E_1) \\ &\quad - f'_{\text{Sr}}(E_2)) \int_V \int_V u(\mathbf{r})v(\mathbf{r}') \\ &\quad \times \frac{\sin(q|\mathbf{r}-\mathbf{r}'|)}{q|\mathbf{r}-\mathbf{r}'|} d^3r d^3r' + 4\pi (|\Delta f_{\text{Sr}}(E_1)|^2 \\ &\quad - |\Delta f_{\text{Sr}}(E_2)|^2) \int_V \int_V v(\mathbf{r})v(\mathbf{r}') \\ &\quad \times \frac{\sin(q|\mathbf{r}-\mathbf{r}'|)}{q|\mathbf{r}-\mathbf{r}'|} d^3r d^3r'. \end{aligned} \quad (4)$$

Now the scattering function is reduced to the resonant contributions—the so-called separated scattering—but the scattering of the polymer is still present in the cross-term. The significance of this term was outlined by Jusufi and Ballauff, who were able to demonstrate that it may lead directly to the Fourier transform of the density distribution of the polyelectrolyte component if the polyelectrolyte component is a rigid colloid.^{22,23} However, additional knowledge of the third integral in Eq. (3) is required. One route to determine the third integral is to perform measurement at a third energy. When subtracting the separated scattering curves obtained at the two energies E_1 and E_3 from the separated scattering obtained from the two energies E_1 and E_2 , the cross-term is vanishing and the form factor $S_{\text{Sr}}^{\text{form}}(q)$ of the spatial

distribution of the Sr^{2+} ions remains after normalizing to the energy dependent anomalous dispersion corrections of the atomic scattering factor of the Sr^{2+} ions at the related energies:

$$S_{\text{Sr}}^{\text{form}}(q) = 4\pi \int_V \int_V v(\mathbf{r})v(\mathbf{r}') \frac{\sin(q|\mathbf{r}-\mathbf{r}'|)}{q|\mathbf{r}-\mathbf{r}'|} d^3r d^3r'$$

$$= \left[\frac{\Delta I_0(q, E_1, E_2)}{f'_{\text{Sr}}(E_1) - f'_{\text{Sr}}(E_2)} - \frac{\Delta I_0(q, E_1, E_3)}{f'_{\text{Sr}}(E_1) - f'_{\text{Sr}}(E_3)} \right] \frac{1}{F(E_1, E_2, E_3)},$$

$$F(E_1, E_2, E_3) = f'_{\text{Sr}}(E_2) - f'_{\text{Sr}}(E_3) + \frac{f''_{\text{Sr}}(E_1) - f''_{\text{Sr}}(E_2)}{f'_{\text{Sr}}(E_1) - f'_{\text{Sr}}(E_2)} - \frac{f''_{\text{Sr}}(E_1) - f''_{\text{Sr}}(E_3)}{f'_{\text{Sr}}(E_1) - f'_{\text{Sr}}(E_3)}. \quad (5)$$

Due to Eq. (5), ASAXS provides a technique to access directly the scattering of the Sr^{2+} ions. The structural information of the Sr^{2+} ion distribution surrounding the macroions can be obtained from the analysis of the form factor $S_{\text{Sr}}^{\text{form}}(q)$. Generally speaking, Eq. (5) provides a method which gives access to the pure-resonant scattering contribution by measuring the small-angle scattering at only three suitable energies.^{15,24,25} An alternative route to separate all three integrals was achieved by Ballauff and co-workers,^{26,27} which could afford to record scattering curves at 4 (Ref. 26) and 13 (Ref. 27) different energies below the absorption edge of the fluctuating counterions. This enabled them to determine the three scattering contributions (nonresonant, mixed-resonant, and resonant terms) by means of a plot of $I(q, E)$ vs f_{eff}' and a fit with a sum of the integrals of Eq. (3) at variable q .

In addition to the structural information, which can be obtained from $S_{\text{Sr}}^{\text{form}}(q)$, important quantitative information related to the amount of Sr atoms localized in the collapsed phase can be deduced from the integral Q_{Sr} :

$$Q_{\text{Sr}}(E) = \frac{1}{4\pi} \int_Q |A_{\text{Sr}}(q, E)|^2 d^3q$$

$$= \frac{1}{4\pi} |\Delta f_{\text{Sr}}(E)|^2 \int_Q S_{\text{Sr}}^{\text{form}}(q) d^3q. \quad (6)$$

In analogy to the so-called invariant,²⁸ we will call Q_{Sr} the resonant invariant of the inhomogeneously distributed resonant scattering Sr ions. The invariant Q_{Sr} , as defined in Eq. (6), is related to the averaged squared excess electron density of the resonant scattering atoms,²⁸ $\overline{\eta_{\text{Sr}}^2}$:

$$Q_{\text{Sr}}(E) = (2\pi)^3 V \overline{\eta_{\text{Sr}}^2(E)}. \quad (7)$$

where V is the sample volume. With the averaged squared excess electron density of the Sr ions, $\overline{\eta_{\text{Sr}}^2(E)} = (\rho_{\text{Sr}}(E) - \overline{\rho_{\text{Sr}}(E)})^2 = \rho_{\text{Sr}}^2(E) - \rho_{\text{Sr}}(E)^2$, Eq. (7) writes

$$Q_{\text{Sr}}(E) = (2\pi)^3 V (\overline{\rho_{\text{Sr}}^2(E)} - \overline{\rho_{\text{Sr}}(E)}^2). \quad (8)$$

Introducing $\rho_{\text{Sr}}(\mathbf{r}, E) = f_{\text{Sr}}(E)v(\mathbf{r})$, which represents the electron density distribution of the Sr ions in the solution [Eq. (2)], into Eq. (8) yields

$$Q_{\text{Sr}}(E) = (2\pi)^3 V |f_{\text{Sr}}(E)|^2 (\overline{v^2} - \overline{v}^2). \quad (9)$$

For the subsequent calculations, the calibration of the scattering curves into macroscopic scattering cross sections in units of cross section per unit volume (cm^{-1}) is mandatory. To obtain the calibration, Eq. (9) must be multiplied with r_0^2/V , where r_0 is the classical electron radius:

$$Q_{\text{Sr}}(E) = (2\pi)^3 r_0^2 |f_{\text{Sr}}(E)|^2 (\overline{v^2} - \overline{v}^2). \quad (10)$$

Because only the excess electron density of the Sr ions with respect to the solvent contributes to the scattering, $f_{\text{Sr}}(E)$ can be replaced by $\Delta f_{\text{Sr}}(E)$ from Eq. (2):

$$Q_{\text{Sr}}(E) = (2\pi)^3 r_0^2 |\Delta f_{\text{Sr}}(E)|^2 (\overline{v^2} - \overline{v}^2). \quad (11)$$

The averaged squared number density of Sr ions can be written as

$$\overline{v^2} = \frac{N_{\text{Sr}} V_{\text{Sr}}}{V} \frac{1}{V_{\text{Sr}}} = \frac{\overline{v}}{V_{\text{Sr}}}, \quad (12)$$

where $V_{\text{Sr}} = 4\pi/3 R_{\text{Sr}}^3$ is the volume of a single Sr ion with the radius $R_{\text{Sr}} = 0.126$ nm. N_{Sr} represents the total number of Sr ions in the solvent. Inserting Eq. (12) into Eq. (11) yields

$$Q_{\text{Sr}}(E) = (2\pi)^3 r_0^2 |\Delta f_{\text{Sr}}(E)|^2 \overline{v} \left(\frac{1}{V_{\text{Sr}}} - \overline{v} \right)$$

$$\approx (2\pi)^3 r_0^2 |\Delta f_{\text{Sr}}(E)|^2 \frac{\overline{v}}{V_{\text{Sr}}}. \quad (13)$$

Combining Eqs. (6) and (13) yields

$$Q_{\text{Sr}}(E) = \frac{|\Delta f_{\text{Sr}}(E)|^2}{4\pi} \int_Q S_{\text{Sr}}^{\text{form}}(q) d^3q$$

$$\approx (2\pi)^3 r_0^2 |\Delta f_{\text{Sr}}(E)|^2 \frac{\overline{v}}{V_{\text{Sr}}}, \quad (14a)$$

$$\frac{dQ_{\text{Sr}}(E)}{dq} = |\Delta f_{\text{Sr}}(E)|^2 S_{\text{Sr}}^{\text{form}}(q) q^2. \quad (14b)$$

Equation (14b) represents the first derivative of the resonant invariant with respect to q and will be used in Fig. 3. Finally, from Eq. (14a) the number density of the Sr ions can be calculated:

$$\overline{v} = \frac{V_{\text{Sr}} Q_{\text{Sr}}}{(2\pi)^3 r_0^2 |\Delta f_{\text{Sr}}(E)|^2}. \quad (15)$$

It should be mentioned that the number density calculated from Eq. (15) includes the Sr ions, which are homogeneously distributed in the solvent. These Sr ions provide an isotropic scattering contribution at small q values similar to the isotropic scattering of the solvent but with a different amount. As will be discussed in more detail below, the amount of the isotropic scattering contribution originating from these remaining Sr ions in the solvent can be neglected.

III. EXPERIMENTAL

Preparation of NaPA solutions with Sr^{2+} in aqueous NaCl was performed in two steps. In the first step, a solution of NaPA in bidistilled water with 0.01M NaCl at pH 9 (solution I) was prepared together with another solution of 3 mM SrCl_2 and 4 mM NaCl in bidistilled water at pH 9 (solution II). The pH was set with 0.01M NaOH. It is noteworthy to mention that both solutions had the same number of cationic charges, which was $2[\text{Sr}^{2+}] + [\text{Na}^+] = 0.01\text{M}$. After 3 days of storage, equal volumes of both solutions were combined. Thus, a stock solution of NaPA in distilled water with 1.5 mM SrCl_2 and 7 mM NaCl with a pH of 9 was obtained (solution III). In an analogous way, an amount of solution II was combined with an equal amount of bidistilled water with 0.01M NaCl, resulting in a NaPA-free solution of 1.5 mM SrCl_2 and 7 mM NaCl at a pH of 9 (solution IV). Solution IV is denoted as solvent and served as the solvent background for all scattering experiments. The phase boundary for Sr^{2+} -PA precipitation was approached by diluting the stock solution (III) with the solvent (IV). By means of this procedure,²⁵ four different ratios of $[\text{Sr}^{2+}]/[\text{NaPA}]$ were obtained at constant concentrations of $[\text{Sr}^{2+}]$ and $[\text{Na}^+]$ ($[\text{Sr}^{2+}]/[\text{NaPA}] = 0.451, 0.4575, 0.458, \text{ and } 0.464$), denoted as samples D, C, B, and A, respectively. As the shape of the polymer chains in solution depends on the extent of complexation, different ratios correspond to different intermediates, bordering the precipitation threshold of SrPA.

Combined static and dynamic light scattering measurements (ALV 5000E CGS) allowed us to locate the precipitation threshold and to characterize the global dimensions of the polymer chains in dependence on the ratio of $[\text{Sr}^{2+}]/[\text{NaPA}]$.²⁵

The four samples selected for ASAXS as well as the solvent were filled into capillaries from Hilgenberg GmbH, Malsfeld, Germany. The capillaries are made of borosilicate glass with an inner diameter of 4 mm and a wall thickness of 0.05 mm. The inner diameter of 4 mm is nearly the optimal size for the energy range of the Sr *K* edge at 16.105 keV. The capillaries were closed with a pipette plug fixed by two component quick setting adhesive.

ASAXS measurements were performed at the JUSIFA beamline²⁹ at HASYLAB, DESY Hamburg at three different

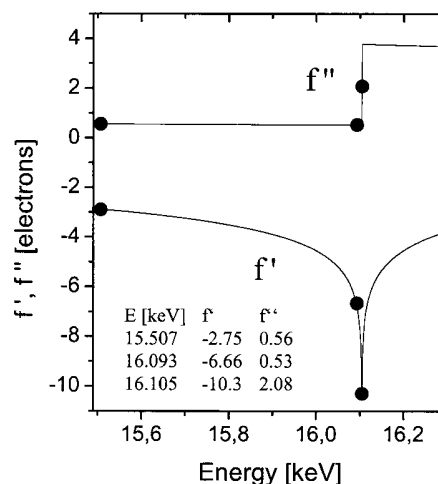


FIG. 1. Anomalous dispersion corrections obtained by Cromer-Lieberman calculations (Refs. 30 and 31). The values at 16.105 keV result from the convolution with the energy resolution of the JUSIFA beamline.

energies in the energy range of the *K* absorption edge of strontium at 16.105 keV. Measurements were made with a two-dimensional detector at three energies. A *q* range from about 0.07 to 2.7 nm^{-1} was covered. A detailed description of the experiments can be found in Ref. 25.

The table in Fig. 1 provides the anomalous dispersion corrections for Sr at the three energies used here based on the calculations of Cromer and Liberman.^{30,31} These were used to permit the separation of the Sr-related pure-resonant scattering described in detail by Eqs. (1)–(5). Constant background effects due to resonant raman scattering and fluorescence occurring near the *K* absorption edge at 16.105 keV have been subtracted from the measured intensities. The scattering intensity is calibrated into macroscopic scattering cross sections in units of cross section per unit volume ($\text{cm}^2/\text{cm}^3 = \text{cm}^{-1}$). Transmission measurements were performed with a precision of 0.001 using a special (windowless) photodiode (Hamamatsu S2387-1010N). The amount of the integrated form factors [Eq. (5)] with respect to the integrated total scattering, i.e., $\varepsilon = \int S_{\text{Sr}}^{\text{form}}(q) d^3q / \int I(q, E) d^3q$, of the four samples was between 0.25% and 0.60% (last column in Table I).

TABLE I. Structural and quantitative parameters of the four diluted NaPA samples with different concentration ratios $[\text{Sr}^{2+}]/[\text{NaPA}]$ obtained from the ASAXS analysis. \bar{v} represents the concentration of Sr atoms in the condensed phase deduced from the experimentally accessible section of resonant invariant. Values of \bar{v}^u represent the upper limits of these concentrations calculated with the different theoretical model functions of the dumbbell (PD and PS+D). *c* is the relative amount of Sr atoms in the condensed phase with respect to the total concentration of Sr ions in the entire solution and *r* represents the ratio of Sr cations to carboxylate side groups in the collapsed phase. Sample A represents an outlier possibly due to degradation of the sample. The latter was evidenced by LS experiments showing strong differences of the radius of gyration taken before and after the ASAXS measurements (Ref. 25).

Sample	$[\text{Sr}^{2+}]/[\text{NaPA}]$	\bar{v} (10^{17} cm^{-3})	\bar{v}^u (PD) (10^{17} cm^{-3})	\bar{v}^u (PS+D) (10^{17} cm^{-3})	<i>c</i> ^a (%)	<i>r</i>	ε (%)
A	0.464	0.77(14)	0.94	1.17	10.5–13.1	0.049–0.061	0.30
B	0.458	1.50(8)	1.92	2.09	21.4–23.3	0.097–0.106	0.50
C	0.4575	1.73(21)	2.01	2.09	22.3–23.2	0.102–0.106	0.60
D	0.451	0.73(12)	0.80	...	8.9	0.041	0.25

^aThe values refers to $9.0 \times 10^{17} \text{ Sr}^{2+}$ cations per cm^3 which correspond to 1.5 mM.

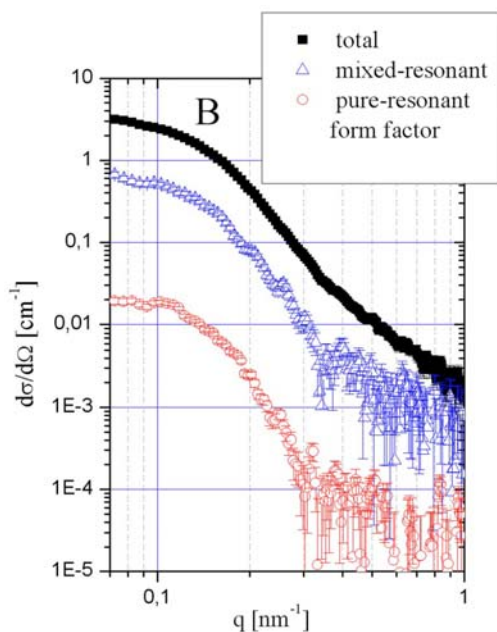


FIG. 2. (Color online) Total scattering (squares), separated scattering (triangles), and the form factor of the pure-resonant scattering contribution (circles) of the aqueous polyacrylate solution with Sr ions from sample B with a concentration ratio $[\text{Sr}^{2+}]/[\text{NaPA}]=0.458$.

IV. RESULTS AND DISCUSSION

The focus of the present work is the development of the resonant invariant of the Sr^{2+} ions. A detailed description of the scattering pattern is given only for sample B with $[\text{Sr}^{2+}]/[\text{NaPA}]=0.458$ in Fig. 2. The shape of the total scattering curve (black squares) is compatible with the form factor of spherical objects. The latter was already suggested by former small-angle neutron scattering measurements.³² This interpretation is strongly confirmed by the separated scattering curve (blue triangles) and the separated form factor (red circles) of the Sr ion distribution. The error bars of the separated form factor were calculated from the error bars of the total scattering curves measured at the three energies considering the error propagation through Eq. (5). In the q range between 0.07 and 0.3 nm^{-1} , relative errors between 10% and 40% have been obtained. Both curves exhibit a number of characteristic structures for $q > 0.1 \text{ nm}^{-1}$ with pronounced maxima, minima, and shoulders revealing a scattering function, which is strongly influenced by correlation effects between rather monodisperse subdomains within the collapsing chains. Especially, the form factors of the spatial distribution of the Sr counterions reveal a correlation maximum at 0.1 nm^{-1} . For a counterion condensation-induced shrinking process, an appropriate model was first suggested by Dobrynin *et al.*⁵ which was confirmed later by computer simulations.^{7,8,10} The model, denoted as pearl necklace, gives the scattering function of N spheres with radius R and with a distance d between the spheres.

Scattering data corresponding to the resonant scattering curves can also be represented by means of Eq. (14b). This representation is shown in Fig. 3 for all four samples. The area corresponding to these data represents the experimentally accessible portion of the invariant, denoted as $Q_{\text{Sr}}(\text{exp})$.

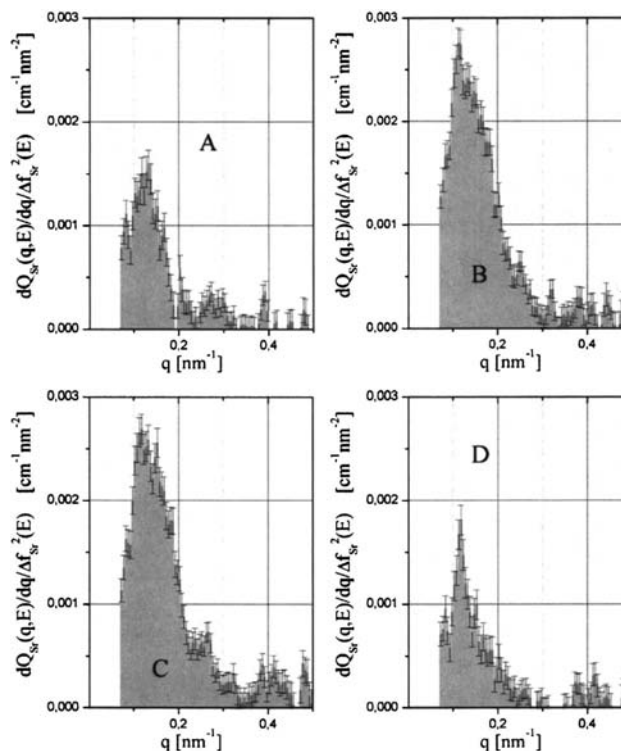


FIG. 3. The first derivative of the resonant invariant [Eq. (14b)] of the four samples $[[\text{Sr}^{2+}]/[\text{NaPA}]=0.451$ (D), 0.4575 (C), 0.458 (B), and 0.464 (A).

Table I summarizes the concentrations \bar{v} of Sr ions in the condensed phase obtained from this resonant invariant depicted with Eqs. (14b) and (15).

For a more quantitative discussion of the data, this limited area has to be extended onto the whole regime of $0 \leq q < \infty$. Estimation of the extensions (especially to very small q values, $q < 0.075 \text{ nm}^{-1}$) will be carried out by three sphere-based models being capable of reproducing the scattering data under consideration. It has to be emphasized that the major purpose of these model applications in the present case is to estimate the contribution of the low and high q regimes of the $S_{\text{Sr}}^{\text{form}}(q)$ to the resonant invariant of Eq. (15), determined experimentally.

Two models have already been applied to the same data in a preceding work.²⁵ The model consisting of a polydisperse sphere, denoted as the PS model, is the simplest model. It provided already a good representation of the data.²⁵ The PS model is based on a Schulz-Flory type of distribution $P(M)$ of the polymer mass M ,^{25,33}

$$P(M) = \left(\frac{z+1}{M_w} \right)^{z+1} \frac{M^z}{\Gamma(z+1)} \exp\left(-\frac{(z+1)M}{M_w} \right). \quad (16)$$

In Eq. (16), the polydispersity is fixed by $z=1/(M_w/M_n - 1)$, with M_w and M_n the weight averaged and the number averaged mass of the spheres. However, the averaged particle size of this model was considerably smaller than the respective value established independently by light scattering. Hence, we added an appropriate portion of monodisperse dumbbells, which increased the average size of the model without significantly affecting the scattering curves at $q > 0.1 \text{ nm}^{-1}$. This second model is denoted as the PS+D

TABLE II. Model representations have been applied to the scattering curves obtained from ASAXS experiments in order to estimate the extension of these scattering curves beyond the limits accessible to the experiment. Representation with the PS model and the PS+D model was inferred from Ref. 25. Representation of the data with the PD model was performed by means of a least squares fit making use of Eq. (17). The symbols have the following meaning: The values for R_g in column 3 represent values for the radii of gyration of the polymer particles determined experimentally by light scattering. (Ref. 25). The PS model is a polydisperse sphere model where R_z denotes the z -averaged outer sphere radius. In the PS+D model, R_z , d , and R_D denote the z -averaged radius of the outer sphere radius of the sphere component, the distance between two spheres in the dumbbell component, and the outer sphere radius of the monodisperse spheres in the dumbbell component, respectively. In the PD model, R_z , d , and z denote the z -averaged radius of the outer sphere radius of the spheres in the dumbbells, the distance between two spheres in the dumbbell component, and the polydispersity parameter $z=1/(M_w/M_n-1)$ of the spheres of the dumbbell component, respectively. Model parameters of the models are applied to reproduce the resonant invariants in Fig. 3.

Sample	$[\text{Sr}^{2+}]/[\text{NaPA}]$	R_g^a (nm)	PS model R_z (nm)	PS+D model			PD model		
				R_z^a	d	R_D	R_z	d	z
A	0.464	17.3	16	16	55	16	15	55	1.30
B	0.458	23.2	15	16	55	16	13	71	1.31
C	0.4575	21.3	15	16	55	16	13	56	1.42
D	0.451	30.7	15	16	55	16	14	67	1.13

^aThe sphere fraction is characterized by a polydispersity parameter of $z=5$.

model in what follows. In order to provide one more curve, which is easily accessible from a least squares fit to data, a third model will be introduced here. This model represents a pearl necklace with N identical spheres and a distribution of the sphere size according to the Schulz-Flory type of distribution. The sphere size is R and the distance between two neighboring spheres on a dumbbell is d .

In Eq. (17), the form factor of a sphere is multiplied with the correlations (first bracket) introduced by the interference of the scattering from the two spheres. Polydispersity of the pearls is considered by means of a Schulz-Flory type of distribution $P(M)$, again following Eq. (16).^{25,33} The particle mass M in Eq. (17) is proportional to $2R^3$ and the polydispersity is fixed by $z=1/(M_w/M_n-1)$, with M_w and M_n the weight averaged and the number averaged mass of the dumbbells.

$$S_{\text{Sr}}^{\text{form}}(q) = \text{const} \int_0^\infty P(M(R)) \left(2 + 2 \frac{\sin(qd)}{qd} \right) \times \left(\frac{4\pi R^3}{3} \frac{3(\sin(qR) - qR \cos(qR))}{(qR)^3} \right)^2 dR. \quad (17)$$

This PD model has to provide only an alternative estimation of the portion of the invariant not accessible to the ASAXS experiment. No further development of a structural concept of the collapsing PA coils which goes beyond the interpretation given in Ref. 25 is intended in the present work. Model parameters for all three models which succeeded to reproduce the experimentally determined resonant scattering curves are summarized in Table II.

From the resonant invariant in Figs. 3(a)–3(d), an amount between $0.73 \times 10^{17} < \bar{v} < 1.73 \times 10^{17}$ Sr atoms per cm^3 was calculated to be in the condensed phase for the four samples (column 3 in Table I). An estimation of the amount of scattering contributions, which could not be detected due to the limited q resolution of the experiment, is outlined in Fig. 4 for sample B. The gray area represents this contribution of the anomalous small-angle x-ray scattering from the q range below the resolution of the experiment. It has been extrapolated from the different model functions as mentioned above. Above the resolution, we integrated up to q

$= 10 \text{ nm}^{-1}$ obtaining additional contributions, which can be neglected with respect to the contributions of the gray area. Addition of the values from the gray area to the respective \bar{v} values of column 3 derived from $Q_{\text{Sr}}(\text{exp})$ via Eq. (15) results in estimations of the Sr^{2+} concentrations shown in columns 4 and 5 of Table I. The numbers in columns 4 and 5 are considered to be upper limits for the Sr concentration in the collapsed phase suggested from the different models and are denoted \bar{v}^u . In addition, the inset of Fig. 4 represents the contribution of homogeneously distributed Sr ions with a concentration of 1.5 mM to the resonant invariant. Although this corresponds to the maximum possible amount—a considerable portion of the Sr^{2+} ions are condensed on the NaPA chains—the contribution is many orders of magnitude

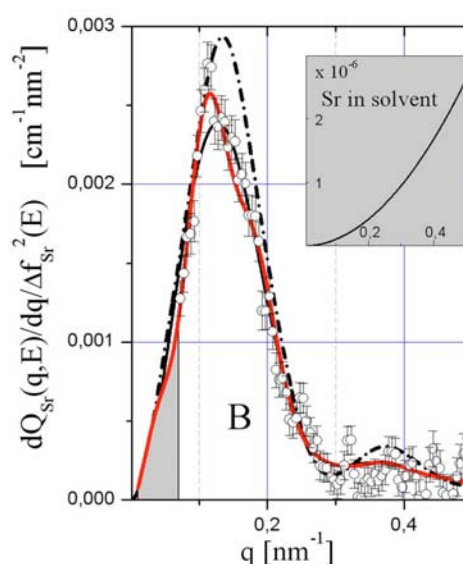


FIG. 4. (Color online) The first derivative of the resonant invariant [Eq. (14b)] of sample B compared to three different model functions, PD (solid red line), PS+D (black dashed line), and PS (black solid line). The different model functions were calculated in order to estimate the contribution of the missing scattering to the resonant invariant beyond the resolution of the ASAXS experiment (gray area on the left). The inset 4 represents the upper limit of the scattering from 1.5 mM of homogeneously distributed Sr ions in the solution, contributing to the resonant invariant.

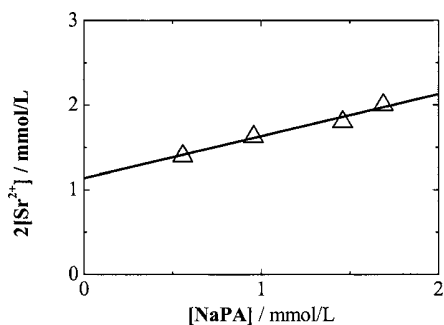


FIG. 5. Phase diagram established for SrPA precipitation in 0.01M NaCl (Ref. 25). The Sr^{2+} -counterion concentration is plotted vs the macroion (polyacrylate) concentration. The triangles correspond to results obtained from light scattering. The solid line represents the phase border between the collapsed and the noncollapsed polymer chains with a slope of $r=0.25$.

smaller than the contribution detected from the Sr ions in the collapsed phase and thus can be neglected. Hence, the resonant invariant estimated here can be attributed unambiguously to the condensed Sr^{2+} ions.

As inferred from the preparation, the concentration of Sr ions of 1.5 mM corresponds to $9 \times 10^{17} \text{Sr}^{2+}$ ions per cm^{-3} . Together with the concentration values \bar{v}^u deduced from the resonant invariant, this led to a fraction of condensed Sr ions lying between 9% and 23% of the total Sr ions in the entire solution. From the concentrations of condensed Sr^{2+} ions, \bar{v}^u , the corresponding ratios, $r = [\text{Sr}^{2+}]/[\text{NaPA}]$, were calculated by taking into account the q regimes beyond the experimental cutoff. The values depend on the ratio of the component concentrations expressed as $[\text{Sr}^{2+}]/[\text{NaPA}]$ and fall in a regime of $0.05 < 0.11$ Sr ions, which are bound per carboxylate residue on the polymer backbone. This result can be compared to a value of $r=0.25$ extracted from the phase diagram in Fig. 5 established by Schweins *et al.*²⁵ The straight line in Fig. 5 represents the phase border between Sr-polyacrylate precipitates and the collapsed polymer or partially collapsed macroions in solution. The value of $r=0.25$ indicates the amount which is needed to cross the phase border along the collapsed state. For a quantitative discussion of the r values in Table I, sample A has to be considered with great care because light scattering of the samples performed prior to and after the ASAXS experiments indicated a slight instability.²⁵ Except for this sample A, the values of r follow our expectations. Samples B and C are close together and sample D shows a smaller degree of Sr^{2+} binding in line with a drop of $[\text{Sr}^{2+}]/[\text{NaPA}]$ from B/C to D. The drastic effect confirms that small changes in $[\text{Sr}^{2+}]/[\text{NaPA}]$ cause strong changes in the conformation and hence in r once we get close to the phase boundary, as has been already observed in our preceding experiment.¹⁵ The closer the sample gets to the phase boundary, the higher the degree of Sr^{2+} binding becomes.

Noteworthy, Molnar and Rieger³⁴ published a molecular dynamics simulation¹³ of the interaction of NaPA oligomers with Ca^{2+} cations. They found an abrupt increase of free Na^+ ions if more than three Ca^{2+} cations have been added to the “simulated cubic solution box.” This supports the feature of a rather abrupt increase of the decoration of the PA coils with Sr^{2+} if the system gets close to the phase boundary.

The discrepancy between the value obtained from the phase diagram and the values deduced from the resonant invariant can be explained as follows: (i) There is an error of the slope due to the scattering of the points, which is fairly large. Beyond this, the exact location of the phase boundary may depend on the molar mass of the polyacrylate sample actually used.^{2,14} (ii) At the phase border, an upper limit of Sr^{2+} ions is considered to be captured by the PA coils, while the Sr^{2+} condensation is a process gradually starting before the phase border is reached. Under the assumption that we have not yet reached the phase border with our samples B–D, the actual degree of Sr binding may still be considerably lower than the characteristic value at the phase boundary. Thus, the discrepancy between $r=0.11$ and $r=0.25$ corresponding to the phase boundary implies another steep increase of the bound Sr^{2+} , in agreement with the drastic changes observed at the precipitation edge.

The latter explanation demonstrates that precise quantitative ASAXS measurements employing the algorithm in Sec. II. with the goal to obtain the resonant invariant could serve as a suitable tool for detailed quantitative analysis of those phase diagrams in the future.

V. CONCLUSIONS

In the last years, anomalous small-angle x-ray scattering became a precise quantitative method for element specific structural analysis on the mesoscopic length scale. Due to the precision of the techniques, small-angle scattering contributions in the resolution regime $10^{-3} < \Delta I/I < 10^{-2}$ can be reliably separated and the form factor of the pure-resonant scattering of counterion distributions around macroions becomes accessible, as was demonstrated for Sr-counterion-induced shrinking of polyacrylates.

The form factor of inhomogeneously distributed Sr counterions was separated with an amount between 0.3% and 0.6% with respect to the total scattering. The form factor is attributed to a collapsed phase in a diluted aqueous polyacrylate solution with the Sr counterions condensing in the collapsed phase. From the integral of the separated form factor (resonant invariant), different amounts between 9% and 23% of the Sr counterions were deduced as being captured in the collapsed phase. The numbers also indicate a sharp increase of Sr^{2+} binding close to the phase border established from light scattering (LS) measurements. The example demonstrates the capability to determine quantitatively the extent of ion binding to polyelectrolytes which condense to or interact specifically with the polyelectrolyte.

¹M. Nagasawa, *Studies in Polymer Science* (Elsevier Science, Amsterdam, 1988), Vol. 2, p. 49.

²K. Huber, *J. Phys. Chem.* **97**, 9825 (1993).

³I. Michaeli, *J. Polym. Sci.* **48**, 291 (1960).

⁴Y. Kantor and M. Kardar, *Europhys. Lett.* **27**, 643 (1994).

⁵A. V. Dobrynin, M. Rubinstein, and S. P. Obukhov, *Macromolecules* **29**, 2974 (1996).

⁶F. J. Solis and M. Olvera de la Cruz, *Macromolecules* **31**, 5502 (1998).

⁷U. Micka, Ch. Holm, and K. Kremer, *Langmuir* **15**, 4033 (1999).

⁸P. Chodanowski and S. Stoll, *J. Chem. Phys.* **111**, 6069 (1999).

⁹A. V. Lyulin, B. Dünweg, O. V. Borisov, and A. A. Darinskii, *Macromolecules* **32**, 3264 (1999).

¹⁰H. J. Limbach and Ch. Holm, *J. Phys. Chem. B* **107**, 8041 (2003).

- ¹¹V. O. Aseyev, S. I. Klenin, H. Tenhu, I. Grillo, and E. Geissler, *Macromolecules* **34**, 3706 (2001).
- ¹²M.-J. Li, M. M. Green, and H. Morawetz, *Macromolecules* **35**, 4216 (2002).
- ¹³S. Minko, A. Kiriy, G. Gorodyska, and M. Stamm, *J. Am. Chem. Soc.* **124**, 10192 (2002).
- ¹⁴R. Schweins and K. Huber, *Eur. Phys. J. E* **5**, 117 (2001).
- ¹⁵G. Goerigk, R. Schweins, K. Huber, and M. Ballauff, *Europhys. Lett.* **66**(3), 331 (2004).
- ¹⁶H. B. Stuhmann, *Adv. Polym. Sci.* **67**, 123 (1985).
- ¹⁷Q. de Robilliard, X. Guo, N. Dingenouts, M. Ballauff, and G. Goerigk, *Macromol. Symp.* **164**, 81 (2001).
- ¹⁸B. Guillaume, M. Ballauff, G. Goerigk, M. Wittemann, and M. Rehahn, *Colloid Polym. Sci.* **279**, 829 (2001).
- ¹⁹B. Guillaume, J. Blaul, M. Ballauff, M. Wittemann, M. Rehahn, and G. Goerigk, *Eur. Phys. J. E* **8**, 299 (2002).
- ²⁰I. Sabbagh, M. Delsanti, and P. Lesieur, *Eur. Phys. J. B* **12**, 253 (1999).
- ²¹R. Das, T. T. Mills, L. W. Kwok, G. S. Maskel, L. S. Millet, S. Doniach, K. D. Finkelstein, D. Herschlag, and L. Pollack, *Phys. Rev. Lett.* **90**, 188103 (2003).
- ²²M. Ballauff and A. Jusufi, *Colloid Polym. Sci.* **284**, 1303 (2006).
- ²³A. Jusufi and M. Ballauff, *Macromol. Theory Simul.* **15**, 193 (2006).
- ²⁴G. Goerigk and D. L. Williamson, *J. Appl. Phys.* **99**, 084309 (2006).
- ²⁵R. Schweins, G. Goerigk, and K. Huber, *Eur. Phys. J. E* **21**, 99 (2006).
- ²⁶M. Patel, S. Rosenfeldt, N. Dingenouts, D. Pontoni, T. Narayanan, and M. Ballauff, *Phys. Chem. Chem. Phys.* **6**, 2962 (2004).
- ²⁷N. Dingenouts, M. Patel, S. Rosenfeldt, D. Pontoni, T. Narayanan, and M. Ballauff, *Macromolecules* **37**, 8152 (2004).
- ²⁸O. Glatter and O. Kratky, *Small-Angle X-ray Scattering* (Academic, London, 1982).
- ²⁹H.-G. Haubold, K. Gruenhagen, M. Wagener, H. Jungbluth, H. Heer, A. Pfeil, H. Rongen, G. Brandenburg, R. Moeller, J. Matzerath, P. Hiller, and H. Halling, *Rev. Sci. Instrum.* **60**, 1943(1989).
- ³⁰D. T. Cromer and D. Liberman, *J. Chem. Phys.* **53**, 1891 (1970).
- ³¹D. T. Cromer and D. Liberman, *Acta Crystallogr., Sect. A: Cryst. Phys., Diffraction, Theor. Gen. Crystallogr.* **A37**, 267 (1981).
- ³²R. Schweins, P. Lindner, and K. Huber, *Macromolecules* **36**, 9564 (2003).
- ³³B. Zimm, *J. Chem. Phys.* **16**, 1099 (1978).
- ³⁴F. Molnar and J. Rieger, *Langmuir* **21**, 786 (2005).

[S5]

A. Bota, Z..Varga, and G. Goerigk,

*Biological Systems as Nanoreactors: Anomalous Small-Angle Scattering
Study of the CdS Nanoparticle Formation in Multilamellar Vesicles*

J. Phys. Chem. B, 111(8), 1911 (2007)

Biological Systems as Nanoreactors: Anomalous Small-Angle Scattering Study of the CdS Nanoparticle Formation in Multilamellar Vesicles

Attila Bóta,^{*,†} Zoltán Varga,[†] and Günter Goerigk[‡]

Institute of Physical Chemistry, Budapest University of Technology and Economics, Műgyetem rkp 3, H-1521 Budapest, Hungary, and Institute of Solid State Physics, Research Centre Jülich, D-52425 Jülich, Germany

Received: November 22, 2006; In Final Form: January 15, 2007

The formation of cadmium sulfide (CdS) particles in the gaps between the layers of the multilamellar vesicles is described, introducing a new pathway in the preparation of nanometer-scale particles. The in situ structural characterization of both the CdS particles and the vesicles as a reaction medium was performed in the early and final states of the process by using anomalous small-angle X-ray scattering (ASAXS) and freeze-fracture methods. The ASAXS method provides the separation of the scattering of nanoparticles present in a small amount, whereby the monitoring of their formation and growth in the whole time range of manufacturing has become possible.

Introduction

In the last decades, significant research interest has turned to nanoparticles due to their unusual properties that can be employed in a great number of applications.^{1–3} Among the different nanometer-scale particles, the preparation and the characterization of the semiconductor particles represent an important field as a consequence of their potential utilization in nonlinear optics, photocatalysis, and photodegradation.^{4–6} Several methods provide the in situ synthesis of these particles using reverse micelles, Langmuir–Blodgett films, clay minerals, microemulsions, polyelectrolyte/surfactant complexes, ordered polypeptide or other organic matrixes, hydrated derivatives of polysaccharide prepared from bacteria, vesicles, and very recently multiwalled carbon nanotubes as reaction mediums.^{7–16} Due to its optimum characteristics among many semiconductor nanoparticles, cadmium sulfide (CdS) is the most often studied and described. Unilamellar vesicles (or in an other word, liposomes) consisting of natural or artificial amphiphilics are ideal systems for the synthesis of CdS nanoparticles.^{17,18} The unilamellar vesicle preparation, however, requires high-purity chemicals and very precise processes to ensure the quality of nanoproductions.

Here, we show that the water shells of multilamellar vesicles may prove to be adequate reaction compartments instead of the aqueous core of the unilamellar vesicle. The multilamellar vesicles are generally used as model systems of biological cell membranes because of their similarities.^{19,20} They form spontaneously, and they are thermodynamically stable, while the unilamellar ones are rather metastable. Consequently, the application of the multilamellar vesicles as nanoreactors insures more extended versatility for both the particle size modification and shape modification than that of their unilamellar form.

Especially, the anomalous small-angle X-ray scattering (ASAXS) can provide information about the matrix and at the same time about the formation of the nanoparticles. This method gives the description of local structures induced by different elements, for example, Cd ions.^{21,22} The theory of this method is based on the energy dependence of the scattering factors (f_{Cd}) of the type of the resonant atoms:

$$f_{\text{Cd}}(E) = f_{0,\text{Cd}} + f'_{\text{Cd}}(E) + if''_{\text{Cd}}(E) \quad (1)$$

Thus, the scattering amplitude of the system can be divided into an energy-independent term (A) and an energy-dependent ($(f' + if'')V$) term. In this case, the total intensity contains three terms as follows:^{23,24}

$$I(q, E) = A(q)^2 + 2f'(E) A(q) V(q) + (f'^2(E) + f''^2(E)) V(q)^2 \quad (2)$$

The ASAXS study requires measurements at two different energies at least, at an energy close to the absorption edge of cadmium and at another one far away from it. The difference of two ASAXS curves measured at two different energies (known as separated ASAXS curves) is characteristic of the structure of the domains having Cd ions. This separated ASAXS curve, however, contains two terms, the cross-term and the “pure resonant” term, as is described by the next equation:^{24,25}

$$\begin{aligned} \Delta I(q, E_1, E_2) &= I(q, E_1) - I(q, E_2) = \\ &= 2(f'(E_1) - f'(E_2)) A(q) V(q) \\ &+ (f'^2(E_1) - f'^2(E_2) + f''^2(E_1) - f''^2(E_2)) V^2(q) \quad (3) \end{aligned}$$

Executing the ASAXS measurements at three different energies, the determination of the pure resonant term (the

* To whom correspondence should be addressed. Phone: +36 1 463 2473. Fax: +36 1 463 3767. E-mail: abota@mail.bme.hu.

[†] Budapest University of Technology and Economics.

[‡] Research Centre Jülich.

scattering of the CdS nanoparticles) is possible by using the next expressions:

$$V_{\text{Cd}}^2(q) = \frac{1}{C(E_1, E_2, E_3)} \left[\frac{\Delta I(q, E_1, E_2)}{f'(E_1) - f'(E_2)} - \frac{\Delta I(q, E_1, E_3)}{f'(E_3) - f'(E_2)} \right]$$

$$C(E_1, E_2, E_3) = f'(E_2) - f'(E_3) + \frac{f''^2(E_1) - f''^2(E_2)}{f'(E_1) - f'(E_2)} - \frac{f''^2(E_1) - f''^2(E_3)}{f'(E_1) - f'(E_3)} \quad (4)$$

The anomalous method not only gives a qualitative description about the system without any separation technique, but it also provides a quantitative determination of the nanoparticles present in very low concentration with a high statistical significance, providing a precise tool in quantitative chemistry.

Materials and Methods

The fully hydrated DPPC/water vesicles (20 w/w %) containing Cd²⁺ ions were prepared from synthetic high-purity 1,2-dipalmitoyl-*sn*-glycero-3-phosphatidylcholine (DPPC, obtained from Avanti Lipids, AL) and from aqueous Cd(NO₃)₂ neutral buffer solution (17 mmol/dm³, insures a 0.05 Cd²⁺/lipid molar ratio) by simple mixing and by vortex homogenization. Aqueous (NH₄)₂S (20 w/w %) was added to the vesicle system (in a 1.2 (NH₄)₂S/Cd²⁺ molar ratio) then mixed by vortex intensively.

The small-angle X-ray scattering (SAXS) and the anomalous small-angle X-ray scattering (ASAXS) measurements were carried at the JUSIFA facility (Jülich's user-dedicated small-angle scattering facility) at the DORIS synchrotron radiation source in DESY (German Electron Synchrotron, Hamburg).²⁶ The studies of the vesicles covered a range in real-space resolution on the length scale from 1 up to 50 nm, corresponding to a scattering interval of the scattering variable (q) (defined as $(4\pi/\lambda) \sin \Theta$, where $\lambda = 0.464 \text{ \AA}$ is the wavelength of the selected X-ray beam and 2Θ is the scattering angle) from 0.013 to 0.6 1/Å. The ASAXS curves were detected at 26 711, 26 653, and 26 120 eV in the vicinity of the Cd–K absorption edge (26 711 eV). The intensity is given in absolute units of macroscopic cross section (cm⁻¹). The anisotropic scattering patterns were monitored with a two-dimensional position sensitive detector, a multiwire proportional counter (MWPC) with 256 × 256 resolution pixels on a 180 × 180 mm² active area.

The freeze-fracture electron microscopy was used for the direct visualization of local structures of vesicles with CdS nanoparticles.²⁷ The gold sample holders used in freeze fracture were preincubated at 24 °C at the same temperatures as the samples. Droplets of about 1 μL from the samples were pipetted onto the gold holders which were then immediately plunged into liquid-nitrogen-cooled partially solidified Freon for freezing. The fracturing was carried out at -110 °C in a Balzers freeze-fracture device (Balzers AG, Vaduz, Liechtenstein). The freeze-fractured faces were etched for 30 s at -100 °C followed by unidirectional platinum/carbon coating at an angle of 45°. Replicas of the samples were removed by submersion into distilled water and subsequently cleaned with a detergent solution; they were then examined using a JEOL JEM-100 CX II (Japan) electron microscope.

The separation of the CdS nanoparticles was executed after a gentle drying of the vesicle system, and then, it was kept under vacuum. The dry sample was dispersed in chloroform and

centrifuged. The CdS particles suspended in chloroform were placed onto amorphous graphite foil and investigated in a Philips CM20 (200 kV) (Holland) electron microscope.

Results and Discussion

The fully hydrated DPPC/water vesicles exhibit at least five Bragg rings in their two-dimensional small-angle X-ray scattering (SAXS) pattern corresponding to a well ordered multi-lamellar and macroscopically not oriented structure formed in the gel phase at 24 °C.^{28,29} The divalent metal ions cause significant destructions in the layer arrangement of the multi-lamellar vesicles indicated by their small-angle X-ray scattering, as the characteristic Bragg reflections of the scattering curve can only be detected in a reduced order number of diffraction.^{30–32} This phenomenon occurs if the liposomes contain Cd²⁺ ions. The two-dimensional SAXS pattern monitored on the system shows only one diffuse ring, as presented in Figure 1A. The ring extends from 0.06 up to 0.24 1/Å in the scattering variable scale, and it can be interpreted as a sum of the extremely broadened first and second orders of reflection. This character of the SAXS pattern indicates that the lamellarity, the correlation of the bilayers, and the bilayer structure itself are severely destroyed. More detailed information about the location of the Cd ions can only be obtained by means of anomalous scattering.

These ASAXS curves exhibit great similarity, but the closer inspection reveals that their shapes depend on the energy. The closer the X-ray energy is to the cadmium absorption edge, the smaller is the intensity. The difference in the ASAXS curves measured at the two different energies, shown in Figure 1A, is characteristic of the structure of the domains having the Cd ions under investigation. Exactly, this difference provides information about the displacement of the Cd ions. The separated curves are due to the contrast variation resulting from the change in energy, and the shape exhibits an inhomogeneous distribution of Cd ions. It extends up to 5% in the beginning part of the curve and vanishes at a scattering variable of about 0.05 1/Å, indicating the formation of domains rich in Cd ions with a characteristic size in the range of several hundred Å-s. Moreover, the appearance of the diffuse peak in the separated curves indicates that Cd ions are partly located in periodical shell forms corresponding to the diffuse layer arrangement of the destroyed liposomes.

An independent method, the freeze-fracture method, can reveal the defects of the centrosymmetrical lamellar arrangement of the vesicle. In Figure 1B, a vesicle completely broken through is shown and its cross section exhibits a significant irregularity between the lamellae. Some stacks of lamellae are crumpled and gaps are visible between them, which may terminate the long range periodicity, giving an explanation for the diffuse character of the scattering pattern of the system having Cd ions.

Adding (NH₄)₂S to the system, the two-dimensional SAXS pattern is drastically changed, as shown in Figure 2A. At least three rings of the Bragg reflections appeared, indicating a significant reconstruction of the ordered vesicle structure. Presumably, the collapse of gaps filled with Cd ions occurs during the formation of compact CdS particles. The position of the first reflection corresponds to a periodicity of 65.1 Å, which is slightly longer than that of the pure DPPC/water system (64.2 Å). The formation of the CdS particles with a cubic crystal structure was confirmed by using wide angle X-ray diffraction in agreement with the reported results.¹⁶ The electron micrograph of a characteristic vesicle is presented in Figure 2B in which we can observe the closely packed parallel layers in the outer leaflets. This is the sign of a rearrangement of a more regular

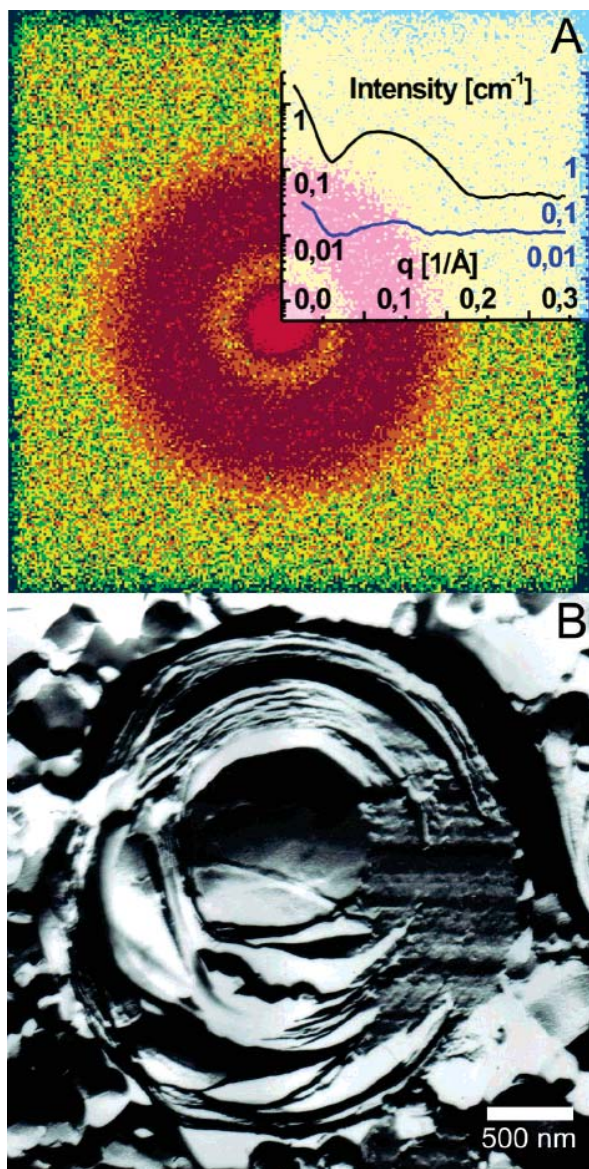


Figure 1. (A) Two-dimensional SAXS pattern of the multilamellar dipalmitoylphosphatidylcholine (DPPC)/water vesicles having $\text{Cd}(\text{NO}_3)_2$ (0.05 Cd^{2+} /lipid molar ratio, neutral buffer system, measured at 26 120 eV). The broadened single ring is the consequence of a weakly correlated lamellar arrangement. The inset plot shows the shape of this ring in the representation of the one-dimensional scattering intensity vs the scattering variable (q). Moreover, the difference of two anomalous small-angle X-ray scattering (ASAXS) curves measured at 26 120 and 26 711 eV is also plotted (blue line). The intense beginning part of this separated form indicates larger domains rich in Cd^{2+} ions, and its broadened peak with reduced intensity corresponds to the diffuse character of the layer arrangement of the vesicles. (B) Surface morphology of a giant vesicle broken through, completely. The regular, periodic arrangement of shells is damaged; gaps between the stacks of lamellae appear which are especially visible in the outer leaflets.

layer structure, giving an explanation for the increased number of the Bragg rings. What is even more interesting is that many small grains appear, concentrated locally, in certain layers between the stacks of lamellae. The characteristic size of these particles falls into the range of approximately 5–10 nm. Presumably, these grains are the agglomeration of the CdS nanoparticles. The anomalous scattering provides more structural information about these particles. The ASAXS curves measured at three different energies, plotted in Figure 3A, indicate a trend;

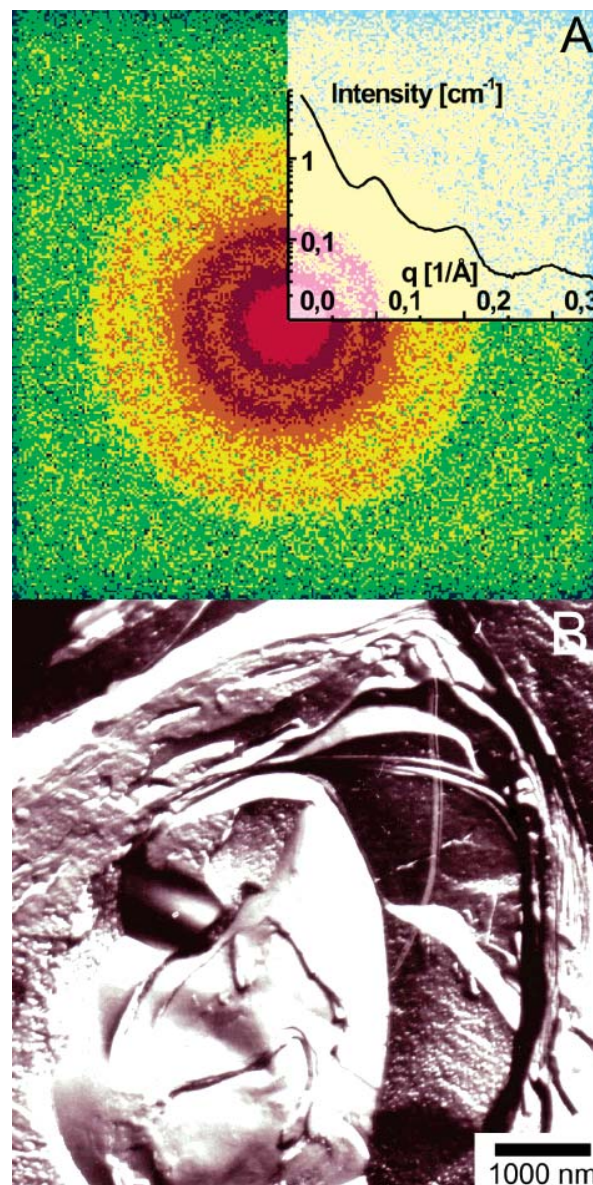


Figure 2. (A) Two-dimensional SAXS pattern of the multilamellar DPPC/water vesicles having CdS nanoparticles. The Bragg reflections appearing in three orders are unambiguous signs of the reconstructed multilamellar arrangement. The inset plot exhibits the corresponding one-dimensional scattering intensity vs the scattering variable (q). (B) Fractured surface of the inert part of a giant vesicle broken through, completely. Two types of the characteristic morphologies can be recognized; the regular, periodic multilamellar arrangement in the outer leaflets and the great number of CdS nanoparticles embedded between the stacks of lamellae.

the difference in the ASAXS curves diminishes with increasing energy in the first part of the scattering variable range and the differences between them vanish in the scattering variable range of the first Bragg reflection, indicating that the Cd ions are not located in a periodic arrangement of the multilayers. To eliminate the scattering contribution of the vesicles, the measurements were performed at three different energies; thus, we can obtain the pure resonant term, as is described in the Introduction.^{33,34} The separated and pure resonant curves exhibit different shapes; the latter diminishes in a narrower range of scattering variables than the former, as is shown in Figure 3B, representing the importance of the determination of the pure

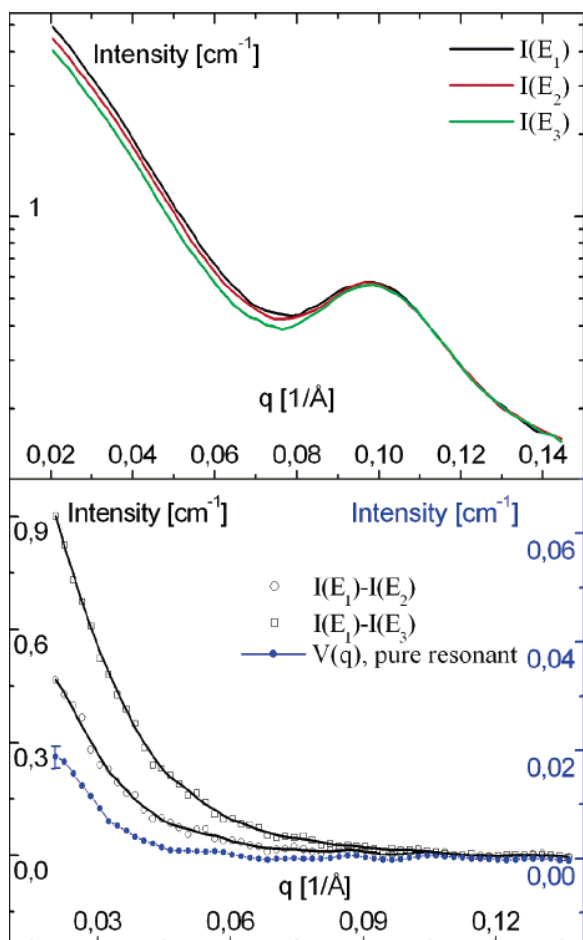


Figure 3. (A) ASAXS curves of the DPPC/water vesicles having CdS nanoparticles measured at three different energies ($E_1 = 26\,120$, $E_2 = 26\,653$, and $E_3 = 26\,711$ eV). The curves exhibit reduced intensity as the energy of the X-ray is shifted to the vicinity of the K absorption edge of cadmium. In the range of the first Bragg reflection, the vanished differences between the separated curves indicate the nonperiodic form of the location of the CdS nanoparticles. (B) Separated ASAXS curves measured at E_1 , E_2 and E_1 , E_3 , respectively (open circles), and the pure resonant term (filled circles) deduced from these separated forms. The latter curve is strictly characteristic only for the spatial distribution of the Cd^{2+} ions of the CdS particles.

resonant term. From this term, a characteristic average diameter of 6.9 nm was derived by assumption of a log-normal size distribution of a spherical form (Figure 4A) corresponding to the next expressions:²⁵

$$V_{\text{Cd}}^2(q) = \text{const} \int_0^\infty P(R) \left(\frac{4\pi R^3}{3} \frac{3(\sin(qR) - qR \cos(qR))}{(qR)^3} \right)^2 dR$$

$$P(R) = \frac{1}{\sqrt{2\pi}} \frac{1}{\sigma R} \exp \left[-\frac{\ln^2 R/R_0}{2\sigma^2} \right] \quad (5)$$

The characteristic size shows a very good agreement with the estimation of the freeze-fracture method. Finally, the CdS nanoparticles were separated from the vesicle system and their size analysis was carried out by using transmission electron microscopy (TEM) (Figure 4B). In the electron micrograph, less spherical but rather squared stocky shaped particles appear and their sizes (6–7 nm) fall exactly into the range of that deduced

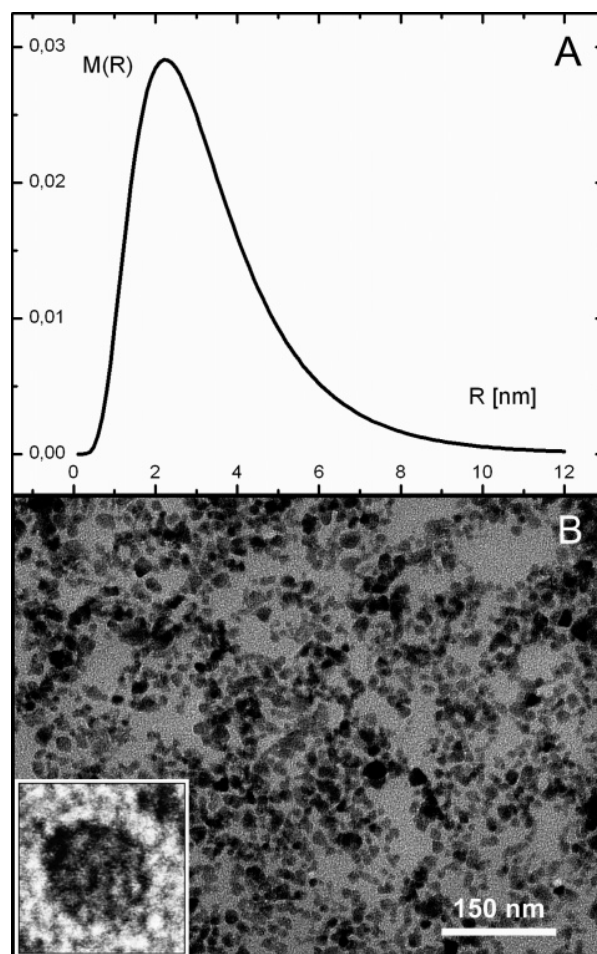


Figure 4. (A) Log-normal size distribution of the CdS nanoparticles calculated from the pure resonant term. (B) Typical TEM image of the CdS nanoparticles. The inset (represents a length scale of 10 nm) shows a single CdS nanoparticle.

by the freeze-fracture electron microscopy and more precisely by the ASAXS method.

The application of the ASAXS technique proved to be a useful tool not only to determine but also to follow the formation of nanoparticles during their synthesis. This advantage of the tunable synchrotron radiation may open further new perspectives in nanotechnology.³⁵ The simultaneous ASAXS studies of the reaction zones of nanoparticles provide an observation and regulation technique of the necessary engineering parameters of synthesis without any separation of the nanoparticles that are present in low concentration in the reaction medium.

Acknowledgment. We are grateful to T. Kiss and to Gy. Radnóczy (Research Institute for Technical Physics and Materials Science, Budapest, Hungary) for the electron microscopical investigation of CdS particles. This work was supported by the contract RI13-CT-2004-506008 of the European Community at DESY/HASYLAB (Hamburg, Germany) and by the Hungarian Scientific Funds OTKA (Bóta, T 43055).

References and Notes

- (1) Valden, M.; Lai, X.; Goodman, D. W. *Science* **1998**, *281*, 1647.
- (2) Huynh, W. U.; Dittmer, J. J.; Alivisatos, A. P. *Science* **2002**, *295*, 2425.
- (3) Bell, A. T. *Science* **2003**, *299*, 1688.

- (4) Colvin, V. L.; Schlamp, M. C.; Alivisatos, A. P. *Nature* **1994**, *370*, 354.
- (5) Ramsden, J.; Gratzel, M. J. *J. Chem. Soc., Faraday Trans. 1* **1984**, *80*, 919.
- (6) Mills, A.; Williams, G. J. *J. Chem. Soc., Faraday Trans. 1* **1989**, *85*, 503.
- (7) Fendler, J. H. *Chem. Rev.* **1987**, *87*, 877.
- (8) Pileni, M. P.; Motte, L.; Petit, C. *Chem. Mater.* **1992**, *4*, 338.
- (9) Zhu, R.; Min, G. W.; Wei, Y. J. *J. Phys. Chem.* **1992**, *96*, 8210.
- (10) Dékány, I.; Turi, L.; Tombácz, E.; Fendler, J. H. *Langmuir* **1995**, *11*, 2285.
- (11) Caponetti, E.; Pedone, L.; Martino, D. C.; Panto, V.; Liveri, V. T. *Mater. Sci. Eng., C* **2003**, *23*, 531.
- (12) Nelson, E. J.; Samulski, E. T. *Mater. Sci. Eng., C* **1995**, *2*, 133.
- (13) Pedone, L.; Caponetti, E.; Leone, M.; Militello, V.; Pantó, V.; Polizzi, S.; Saladino, M. L. *J. Colloid Interface Sci.* **2005**, *284*, 495.
- (14) Li, Z.; Du, Y. *Mater. Lett.* **2003**, *57*, 2480.
- (15) Mann, S.; Hannington, J. P.; Williams, R. J. P. *Nature* **1986**, *324*, 565.
- (16) Shi, J.; Quin, Y.; Wu, W.; Li, X.; Guo, Z.-X.; Zhu, D. *Carbon* **2004**, *42*, 423.
- (17) Tricot, Y.-M.; Fendler, J. H. *J. Phys. Chem.* **1986**, *90*, 3369.
- (18) Korgel, B. A.; Monbouquette, H. G. *Langmuir* **2000**, *16*, 3588.
- (19) Cevc, G.; Marsh, D. *Phospholipid Bilayers, Physical Principles and Models*; John Wiley & Sons: New York, 1987.
- (20) Epanand, R.M. *Current topics in Membranes: Lipid Polymorphism and Membrane Properties*; Academic Press: San Diego, CA, 1997.
- (21) Stuhrmann, H. B. *Adv. Polym. Sci.* **1985**, *67*, 123.
- (22) Guinier, A. *X-Ray Diffraction*; Freeman: San Francisco, CA, 1963.
- (23) de Robbilard, Q.; Guo, X.; Dingenouts, N.; Ballauff, M.; Goerigk, G. *Macromol. Symp.* **2001**, *164*, 81.
- (24) Goerigk, G.; Schweins, R.; Huber, K.; Ballauff, M. *Europhys. Lett.* **2004**, *66*, 331.
- (25) Varga, Z.; Bóta, A.; Goerigk, G. *J. Phys. Chem. B* **2006**, *110*, 11029.
- (26) Haubold, H.-G.; Gruenhagen, K.; Wagener, M.; Jungbluth, H.; Heer, H.; Pfeil, A.; Rongen, H.; Brandenburg, G.; Moeller, R.; Matzerath, R.; Hiller, P.; Halling, H. *Rev. Sci. Instrum.* **1989**, *60*, 1943.
- (27) Meyer, H. W.; Richter, W. *Micron* **2001**, *32*, 615.
- (28) Wiener, M. C.; Suter, R. M.; Nagle, J. F. *Biophys. J.* **1989**, *53*, 315.
- (29) Bóta, A.; Drucker, T.; Kriechbaum, M.; Réz, G.; Pálfi, Zs. *Langmuir* **1999**, *15*, 3101.
- (30) Iniko, Y. T.; Yamaguchi, T.; Furuya, K.; Mitsui, T. *Biochim. Biophys. Acta* **1975**, *413*, 24.
- (31) Graddick W. F.; Stamatoff, J. B.; Eisenberger, P.; Bereman D. W.; Spielberg, N.; *Biochem. Biophys. Res. Commun.* **1979**, 907.
- (32) Bóta, A.; Klumpp, E. *Colloids Surf., A* **2005**, *65*, 124.
- (33) Cromer, D. T.; Liberman, D. *J. Chem. Phys.* **1970**, *53*, 1891.
- (34) Cromer, D. T.; Liberman, D. *Acta Crystallogr.* **1981**, *A37*, 267.
- (35) Renaud, G.; Lazzari, R.; Revenant, C.; Barbier, A.; Noblet, M.; Ulrich, O.; Leroy, F.; Jupille, J.; Borensztein, Y.; Henry, C. R.; Deville, J.-P.; Scheurer, F.; Mane-Mane, J.; Fruchart, O. *Science* **2003**, *300*, 1416.

[S6]

G. Goerigk, and D.L. Williamson,

*Temperature Induced Differences in the Nanostructure of Hot-wire
Deposited Silicon-Germanium Alloys Analyzed by Anomalous Small-
Angle X-ray Scattering*

J. Appl. Phys. 99, 084309 (2006)

Temperature induced differences in the nanostructure of hot-wire deposited silicon-germanium alloys analyzed by anomalous small-angle x-ray scattering

G. Goerigk^{a)}

Institut für Festkörperforschung, Forschungszentrum Jülich, Postfach 1913, D-52425 Jülich, Federal Republic of Germany

D. L. Williamson

Department of Physics, Colorado School of Mines, Golden, Colorado 80401

(Received 15 September 2005; accepted 16 December 2005; published online 27 April 2006)

The nanostructure of hydrogenated amorphous silicon-germanium alloys, $a\text{-Si}_{1-x}\text{Ge}_x\text{:H}$ ($x=0.62\text{--}0.70$), prepared by the hot-wire deposition technique applying different substrate and filament temperatures was analyzed by anomalous small-angle x-ray scattering experiments. The pure-resonant scattering contribution, which is related to the structural distribution of the Ge component in the alloy, was separated from the total small-angle scattering for one sample series. For all alloys the Ge component was found to be inhomogeneously distributed. The shape of the pure-resonant and the mixed-resonant scattering curves reveal significant differences indicating the presence of a third phase, probably hydrogen clusters and/or voids. The thin films showed improved microstructure when lowering the filament temperature to 1800 °C. Additional improvement was achieved by optimizing the substrate temperature (between 260 and 305 °C) resulting in suggested mass fractal structures of Ge with the fractal dimension $p < 1.6$ and a size of about 40 nm. The nature of the microstructural changes induced by changes in filament temperature compared to those induced by the changes in substrate temperature were clearly different. The improved microstructure of the alloys could be correlated with improved optoelectronic properties of the material. © 2006 American Institute of Physics. [DOI: 10.1063/1.2187088]

I. INTRODUCTION

Hydrogenated amorphous silicon-germanium alloys are used in solar cell technology, where the germanium is added to produce a lower band gap material to absorb the longer wavelength photons of the solar spectrum and to achieve higher efficiencies. Previous small-angle x-ray scattering (SAXS) and anomalous small-angle x-ray scattering (ASAXS) studies revealed that, in addition to voids, nonuniformly distributed Ge contributes to the material inhomogeneities,^{1–4} which are strongly related to the degradation of the optoelectronic properties. In recent years there has been a growing interest especially in the hot-wire chemical-vapor deposition (HWCVD) technique⁵ due to the evidence of improved stability and improved optoelectronic properties of the material, as well as the potentially beneficial manufacturing feature of higher deposition rates than the current industrial technique of plasma-enhanced chemical-vapor deposition (PECVD).^{6,7} A group at National Renewable Energy Laboratory, U.S.A. (NREL) found evidence of improved photoresponse from HWCVD $a\text{-SiGe:H}$ alloys with narrow bandgaps deposited at different filament temperatures, filament diameters, and optimized substrate temperatures.^{8,9} Here we report on ASAXS results from a series of narrow band gap films [1.21 eV

$< E_{\text{Tauc}} < 1.32$ eV] made by HWCVD at different filament and substrate temperatures. ASAXS enables the structural characterization of inhomogeneously distributed Ge in the material. The distribution of Ge is not accessible by conventional SAXS measurements, because the scattering contributions of the Ge-related structures cannot be distinguished from those of other inhomogeneities caused by voids and/or hydrogen clusters.

II. ASAXS MEASUREMENTS

In the case of a ternary silicon-germanium-hydrogen alloy the scattering amplitude is

$$A(\mathbf{q}) = \int_{V_p} \Delta\rho_{\text{H}}(\mathbf{r}) \exp(-i\mathbf{q}\mathbf{r}) d^3r + \int_{V_p} \Delta\rho_{\text{Ge}}(\mathbf{r}) \times \exp(-i\mathbf{q}\mathbf{r}) d^3r, \quad (1)$$

where q is the magnitude of the scattering vector [$= (4\pi/\lambda)\sin\Theta$], 2Θ is the scattering angle, λ the x-ray wavelength, and V_p is the irradiated sample volume. $\Delta\rho_{\text{H}}$, $\Delta\rho_{\text{Ge}}$ are the difference electron densities of the hydrogen and the Ge atoms,

$$\Delta\rho_{\text{H}}(\mathbf{r}) = \Delta f_{\text{H}} \cdot u(\mathbf{r}) = (f_{\text{H}} - \rho_{\text{Si}} V_{\text{H}}) u(\mathbf{r}),$$

^{a)} Author to whom correspondence should be addressed; present address: c/o DESY-HASYLAB, Notkestrasse 85, D-22603 Hamburg, Federal Republic of Germany; FAX: +49-40-89984475; electronic mail: guenter.goerigk@desy.de

$$\begin{aligned}\Delta\rho_{\text{Ge}}(\mathbf{r}, E) &= \Delta f_{\text{Ge}}(E)v(\mathbf{r}) \\ &= [(f_{0,\text{Ge}} - \rho_{\text{Si}}V_{\text{Ge}}) + f'_{\text{Ge}}(E) + if''_{\text{Ge}}(E)]v(\mathbf{r}),\end{aligned}\quad (2)$$

calculated from the electron density, ρ_{Si} , of the silicon and the atomic volumes of the hydrogen, V_{H} , and the Ge atoms, V_{Ge} , respectively, while $u(\mathbf{r}), v(\mathbf{r})$ are the number densities of the H and Ge atoms, respectively. The atomic scattering factor of H (one electron), $f_{\text{H}}(E) \approx \text{const}$, is nearly energy independent, while the atomic scattering factor of the Ge atoms, $f_{\text{Ge}}(E) = f_{0,\text{Ge}} + f'_{\text{Ge}}(E) + if''_{\text{Ge}}(E)$, shows strong variation with the energy in the vicinity of the K-absorption edge of Ge due to the so-called anomalous dispersion corrections $f'_{\text{Ge}}(E), f''_{\text{Ge}}(E)$. Calculating the scattering intensity $I(\mathbf{q}) = |A(\mathbf{q})|^2 = A(\mathbf{q})A^*(\mathbf{q})$ by means of Eqs. (1) and (2) and averaging over all orientations yields a sum of three contributions $I(q, E) = |A_{\text{H}}(q)|^2 + |A_{\text{HGe}}(q, E)|^2 + |A_{\text{Ge}}(q, E)|^2$, with the integrals:¹⁰

$$\begin{aligned}S_{\text{H}}(q) &= |A_{\text{H}}(q)|^2 \\ &= 4\pi\Delta f_{\text{H}}^2 \int_{V_p} \int u(\mathbf{r})u(\mathbf{r}') \frac{\sin(q|\mathbf{r} - \mathbf{r}'|)}{q|\mathbf{r} - \mathbf{r}'|} d^3r d^3r', \\ S_{\text{HGe}}(q, E) &= |A_{\text{HGe}}(q, E)|^2 \\ &= 4\pi \cdot 2\Delta f_{\text{H}} [f_{0,\text{Ge}} - \rho_{\text{Si}}V_{\text{Ge}} \\ &\quad + f'_{\text{Ge}}(E)] \int_{V_p} \int u(\mathbf{r})v(\mathbf{r}') \\ &\quad \times \frac{\sin(q|\mathbf{r} - \mathbf{r}'|)}{q|\mathbf{r} - \mathbf{r}'|} d^3r d^3r', \\ S_{\text{Ge}}(q, E) &= |A_{\text{Ge}}(q, E)|^2 \\ &= 4\pi \cdot |\Delta f_{\text{Ge}}(E)|^2 \int_{V_p} \int v(\mathbf{r})v(\mathbf{r}') \\ &\quad \times \frac{\sin(q|\mathbf{r} - \mathbf{r}'|)}{q|\mathbf{r} - \mathbf{r}'|} d^3r d^3r'.\end{aligned}\quad (3)$$

Equations (3) give the nonresonant scattering of the H, $S_{\text{H}}(q)$, the cross-term or mixed-resonant scattering, $S_{\text{HGe}}(q, E)$, originating from the superposition of the scattering amplitudes of the H and Ge atoms and the scattering of the Ge, $S_{\text{Ge}}(q, E)$, which contains the so-called pure-resonant scattering. By measuring the scattering curves $I(q, E_1)$, $I(q, E_2)$, and $I(q, E_3)$ at three energies in the vicinity of the K-absorption edge of Ge the two separated scattering curves $\Delta I(q, E_1, E_2) = I(q, E_1) - I(q, E_2)$ and $\Delta I(q, E_1, E_3) = I(q, E_1) - I(q, E_3)$ are obtained and from these the form factor, $S_{\text{Ge}}^{\text{form}}(q)$, of the spatial distribution of the Ge component in the alloy can be calculated as described in more detail in¹¹

$$\begin{aligned}S_{\text{Ge}}^{\text{form}}(q) &= 4\pi \int_{V_p} \int v(\mathbf{r})v(\mathbf{r}') \frac{\sin(q|\mathbf{r} - \mathbf{r}'|)}{q|\mathbf{r} - \mathbf{r}'|} d^3r d^3r' \\ &= \left[\frac{\Delta I(q, E_1, E_2)}{f'_{\text{Ge}}(E_1) - f'_{\text{Ge}}(E_2)} - \frac{\Delta I(q, E_1, E_3)}{f'_{\text{Ge}}(E_1) - f'_{\text{Ge}}(E_3)} \right] \\ &\quad \cdot \frac{1}{F(E_1, E_2, E_3)}, \\ F(E_1, E_2, E_3) &= f'_{\text{Ge}}(E_2) - f'_{\text{Ge}}(E_3) + \frac{f''_{\text{Ge}}(E_1) - f''_{\text{Ge}}(E_2)}{f'_{\text{Ge}}(E_1) - f'_{\text{Ge}}(E_2)} \\ &\quad - \frac{f''_{\text{Ge}}(E_1) - f''_{\text{Ge}}(E_3)}{f'_{\text{Ge}}(E_1) - f'_{\text{Ge}}(E_3)}.\end{aligned}\quad (4)$$

With Eq. (4) ASAXS provides a technique to access directly the scattering of the Ge component and structural information on the Ge distribution in the alloy can be obtained from the analysis of the form factor $S_{\text{Ge}}^{\text{form}}(q)$. More generally, Eq. (4) provides a method to access directly, by analytical means, the pure-resonant scattering contribution by measuring the small-angle scattering at only three suitable energies. From $S_{\text{Ge}}^{\text{form}}(q)$ the three basic scattering functions of Eq. (3) can be calculated as is shown for the energies E_1 and E_2 as follows:

$$\begin{aligned}S_{\text{Ge}}(q, E_1) &= |\Delta f_{\text{Ge}}(E_1)|^2 \cdot S_{\text{Ge}}^{\text{form}}(q), \\ S_{\text{HGe}}(q, E_1) &= [\Delta I(q, E_1, E_2) - S_{\text{Ge}}(q, E_1) \\ &\quad + S_{\text{Ge}}(q, E_2)] \frac{(f_{0,\text{Ge}} - \rho_{\text{Si}}V_{\text{Ge}}) + f'_{\text{Ge}}(E_1)}{f'_{\text{Ge}}(E_1) - f'_{\text{Ge}}(E_2)}, \\ S_{\text{H}}(q) &= I(q, E_1) - S_{\text{HGe}}(q, E_1) - S_{\text{Ge}}(q, E_1).\end{aligned}\quad (5)$$

In addition to the structural information obtained from the three basic functions, important quantitative information related to the amount of H and Ge localized in different types of inhomogeneities can be deduced from the integrals of the basic scattering functions. The integral of the total scattering curve $I(q, E)$ (the so-called invariant¹²) can be correlated to the photoconductivity as shown later.

$$\begin{aligned}Q_{\text{tot}}(E) &= \frac{1}{4\pi} \int_Q I(q, E) d^3q, \\ Q_{\text{Ge}}(E) &= \frac{1}{4\pi} \int_Q S_{\text{Ge}}(q, E) d^3q, \\ Q_{\text{H}} &= \frac{1}{4\pi} \int_Q S_{\text{H}}(q) d^3q.\end{aligned}\quad (6)$$

III. EXPERIMENT

Two series of HWCVD films ($0.60 < x < 0.70$) were made at NREL applying different filament and substrate temperatures, T_f and T_s , respectively. The deposition conditions are described elsewhere along with some optoelectronic properties of the first series of such alloys made by the HWCVD method.⁶ For ASAXS, films were deposited on high purity, 10- μm -thick Al foils, which were then folded

TABLE I. Amorphous silicon-germanium alloys $a\text{-Si}_x\text{Ge}_{1-x}:\text{H}$ prepared by the HWCVD technique at different filament and substrate temperatures T_f and T_s . C_H is the hydrogen content and E_{Tauc} the materials band gap and d the thickness of the films. In the eighth column the calculated atomic number densities of Ge in the alloys are listed assuming a mass density of 96% that of $c\text{-Si}_{1-x}\text{Ge}_x$. The last two columns give the photoconductivities (PC) and the deposition rates (DR), respectively.

Sample series	T_f (°C)	T_s (°C)	x	C_H (at %)	E_{Tauc} (eV)	d (μm)	n_{Ge} 10^{22} (cm^{-3})	PC 10^{-6} ($\text{Ohm cm})^{-1}$	DR (nm/sec)
L990	2150	180	0.62	15.0	1.30	0.53	2.611	0.239	0.89
L991	2065	180	0.63	15.2	1.29	0.51	2.653	0.28	0.75
L992	1975	180	0.64	15.5	1.28	0.54	2.695	0.356	0.64
L993	1885	180	0.64	15.8	1.28	0.44	2.695	0.751	0.46
L994	1800	180	0.67	14.5	1.25	0.33	2.821	6.11	0.27
L995	1750	180	0.70	12.5	1.22	0.32	2.948	5.11	0.14
Series									
L998	1800	360	0.60	3.0	1.21	0.45	2.527	0.353	0.37
L999	1800	305	0.63	5.0	1.24	0.42	2.653	0.898	0.32
L1000	1800	260	0.64	9.5	1.27	0.48	2.695	1.95	0.33
L1001	1800	210	0.66	12.0	1.29	0.49	2.779	2.10	0.33
L1002	1800	159	0.68	19.0	1.31	0.49	2.864	0.825	0.33
L1003	1800	130	0.69	21.0	1.32	0.48	2.906	0.965	0.32

into four layers (one into eight layers) for the ASAXS measurements. Table I summarizes deposition parameters, film thickness, and optoelectronic parameters of the samples under investigation.

The ASAXS measurements were carried out at the JUSIFA beamline at HASYLAB, DESY Hamburg.¹³ Measurements were made for each sample with a two-dimensional detector at four energies. A q range from about $0.06\text{--}7\text{ nm}^{-1}$ (fix exponent—note) was covered. Table II provides the anomalous dispersion corrections for Si and Ge at the four energies used here based on the calculations of Cromer and Liberman.^{14,15} These were used to permit the separation of the Ge-related pure-resonant scattering described in detail by Eqs. (1)–(5). From the four energies different combinations, $E_1, E_2,$ and E_3 and $E_1, E_2,$ and E_4 , were used to calculate the form factor of the spatial Ge distribution in the alloy. Constant background effects due to diffuse scattering¹ and due to resonant Raman scattering occurring near the K-absorption edge at 11.103 keV have been subtracted from the measured intensities. The scattering intensity is calibrated into macroscopic scattering cross section in units of cross section per unit volume (cm^2/cm^3) ($=\text{cm}^{-1}$).

IV. RESULTS

Figures 1(a) and 1(b) show the total (a) and separated (b) scattering curves of the series 1 of HWCVD-alloys prepared

TABLE II. Anomalous dispersion corrections of Si and Ge (Refs. 14 and 15).

No.	E (keV)	f'_{Ge}	f''_{Ge}	f'_{Si}	f''_{Si}
1	10.053	-2.093	0.592	0.181	0.215
2	10.996	-4.005	0.504	0.158	0.180
3	11.083	-5.996	0.495	0.155	0.176
4	11.098	-7.458	0.493	0.155	0.176

at different T_f between 1750 and 2150 °C and a fixed T_s of 180 °C. The separated scattering curves were obtained by subtracting the total scattering curves measured at the energies 11 083 and 10 053 eV. The SAXS curves strongly depend on the filament temperature especially in the q range between 0.2 and 5 nm^{-1} . The integrated SAXS Q_{tot} [invariant—Eq. (6)] shows a monotonic increase with the filament temperature (Fig. 2 left ordinate) and is correlated with a strong decrease of the photoconductivity of the films (Fig. 2 right ordinate). No pure-resonant scattering contribution could be obtained from this series. When calculating the $S_{\text{Ge}}^{\text{form}}(q)$ of the pure-resonant scattering contribution [Eq. (4)] the data points scatter along the abscissa indicating little or no pure-resonant contribution (probably less than 0.001 of the total scattering).

The second series (variable T_s) shows a completely different behavior. Figures 3–5 show the scattering curves of three samples from the second series prepared at a fixed T_f and the three substrate temperatures, $T_s=360, 305,$ and 210 °C . The circles represent the total scattering curves measured at 10 053 eV, while the squares show the separated scattering curves (mixed resonant) obtained from SAXS measurements at the two energies 10 053 and 11 083 eV. When calculating the $S_{\text{Ge}}^{\text{form}}(q)$ of the spatial distribution of Ge [Eq. (4)] for all six samples, significant scattering cross sections were obtained (triangles). The integrated form factor amounts to between 0.4% and 5% of the integrated total scattering intensity (last column in Table III). From the different combinations of the energies $E_1, E_2,$ and E_3 and $E_1, E_2,$ and E_4 , form factors with the same shape within the error bars were obtained and for the further calculations the averaged form factor of the two calculations was employed. The triangles in Figs. 3–5 represent the form factors of three samples and the solid lines passing through the data points are fitted model functions according to the following q dependence:

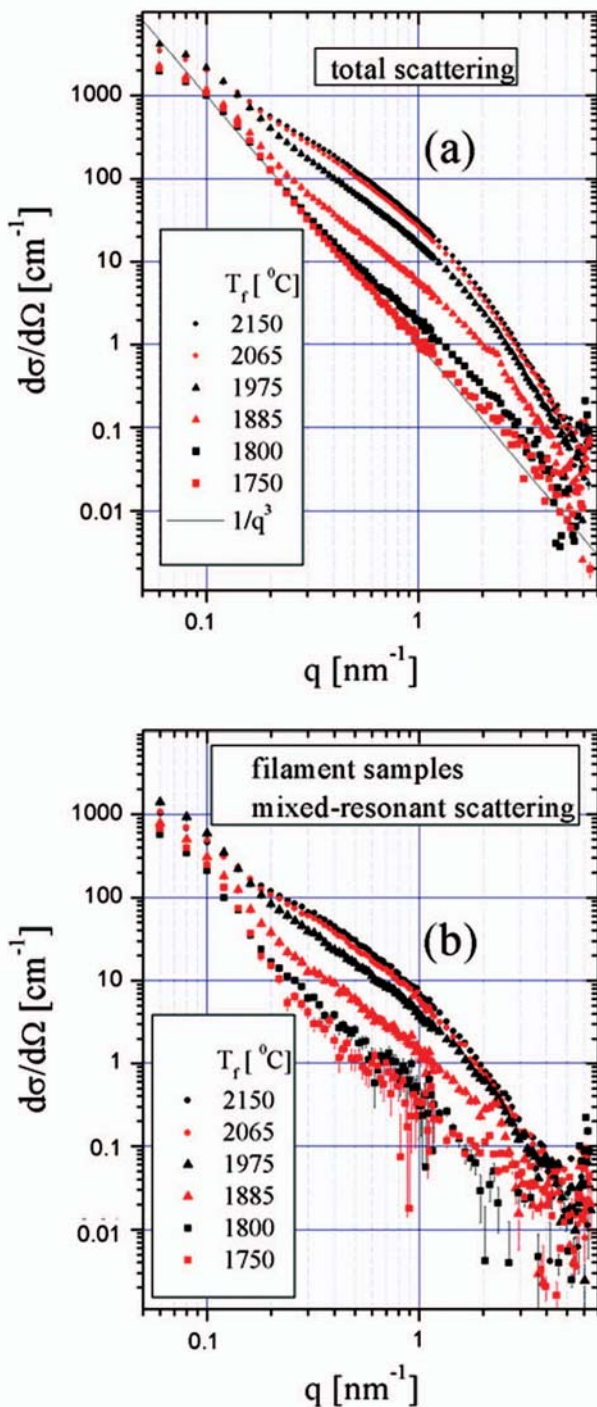


FIG. 1. (Color) SAXS curves obtained from hot-wire deposited $\text{Si}_{1-x}\text{Ge}_x$ alloys. The scattering curves of Fig. 1(a) show the total scattering measured at 10.053 keV from the samples of the first series, which was prepared at different filament temperatures. Figure 1(b) shows the separated scattering curves obtained from the total scattering of Figure 1 and a second SAXS measurement at 11.083 keV. The cross section of the total (a) and the separated (b) scattering curves is consequently reduced over the entire q range with each temperature step. The alternating color sequence (black, red, black, red, black, and red) in both fig. [(a) and (b)] from the top to the bottom curve follows the temperature sequence.

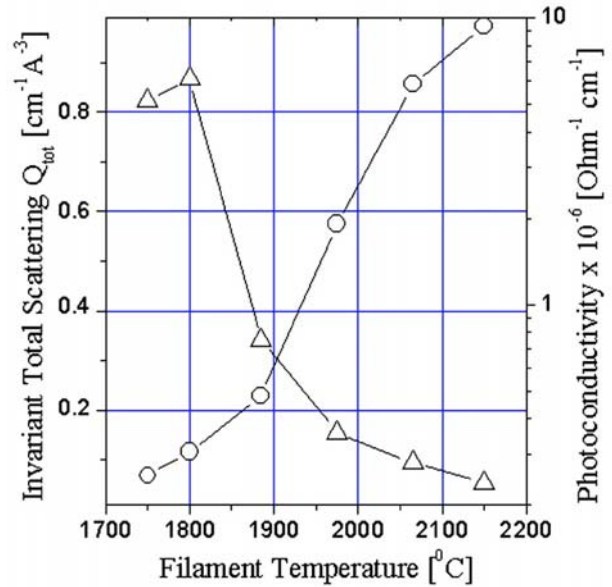


FIG. 2. Total integrated scattering and photoconductivities (right ordinate) of the filament samples plotted vs the filament temperature.

$$S_{\text{Ge}}^{\text{form}}(q) = A \exp\left(\frac{-q^2 R_g^2}{3}\right) + B \exp\left(\frac{-q^2 R_{\text{sub}}^2}{3}\right) \times \left\{ \frac{[\text{erf}(qR_g/\sqrt{6})]^3}{q} \right\}^p. \quad (7)$$

Equation (7) represents the Unified Exponential/Power-Law Approach of Beaucage¹⁶ and can be used for the analysis of small-angle scattering curves from complex systems that contain multiple levels of related structural features such as mass fractals, where two structural levels are the overall radius of gyration R_g and a substructural length R_{sub} . The fractal nature of the system can be deduced from the power-law exponent p . If $I(q)$ varies as q^{-p} in a q range with $qR_g \gg 1$, then $p < 3$ denotes a system that may be a mass fractal and $3 < p < 4$ corresponds to a surface fractal. As can be seen from Figs. 3 and 5, relatively large error bars and scattering of the data points occur for the curves representing the form factor of the Ge component. Due to this it was not possible to obtain a reliable value of R_{sub} for the sample prepared at the substrate temperature of 360 °C. Furthermore the Ge form factors of the three samples with the lower substrate temperatures (130, 159, and 210 °C) show a strong decrease with the result of statistically noisy data (Fig. 5). Especially at q values beyond 3 nm^{-1} the data points scatter around zero causing strong variations of the fitted power-law exponent. This is demonstrated in Fig. 5 by the two solid lines, which represent different fits of the model function, when the fitting procedure is restricted to different q intervals. From the form factors of these three samples no reliable structure information concerning the power-law exponent could be obtained. Table III summarizes the results for the samples of the second series obtained from the fitting procedure. Beaucage's model is used in the following course of the paper for a quantitative description of suggested fractal structures, because other models such as a bimodal size distribution of

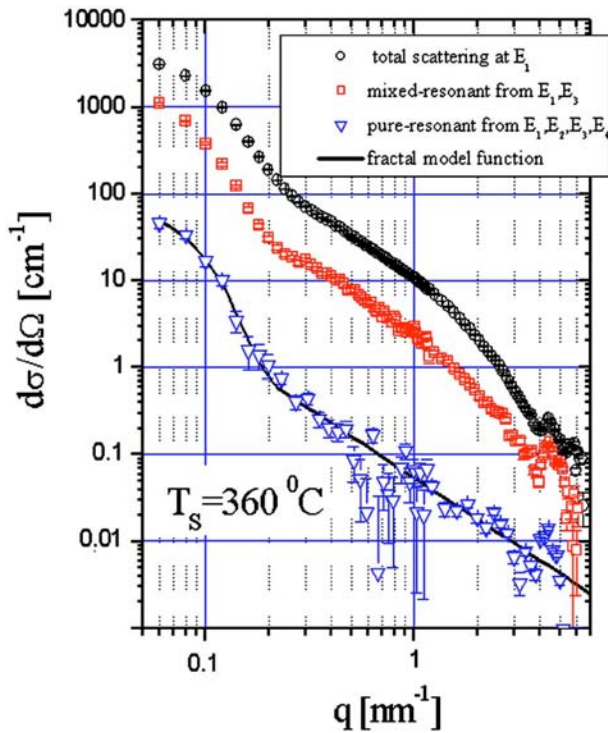


FIG. 3. Total scattering, separated scattering and the form factor of the pure-resonant scattering contribution of one sample from the second series prepared at the substrate temperature of 360 °C. The solid line represents the fractal model function. The origin of the peaklike structure at 4.5 nm⁻¹ in the total scattering curve is unknown.

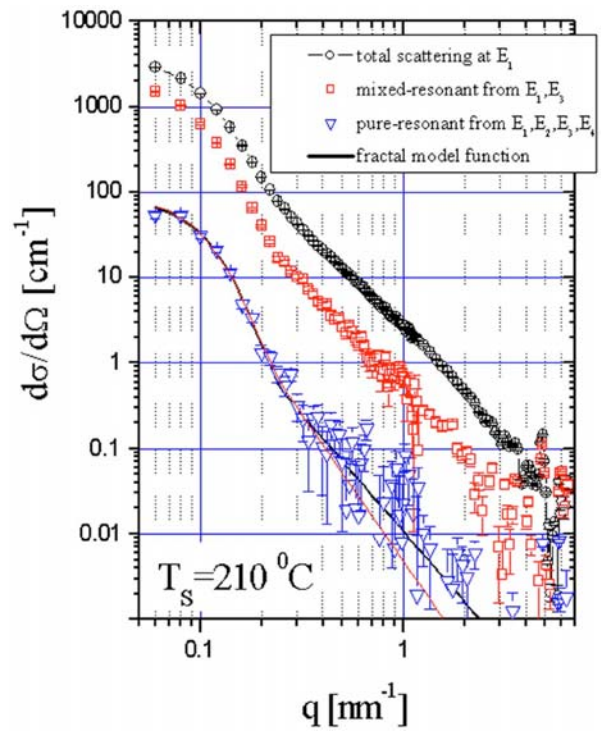


FIG. 5. Total scattering, separated scattering, and the form factor of the pure-resonant scattering contribution of one sample from the second series prepared at the substrate temperature of 210 °C. The solid line represents the fractal model function.

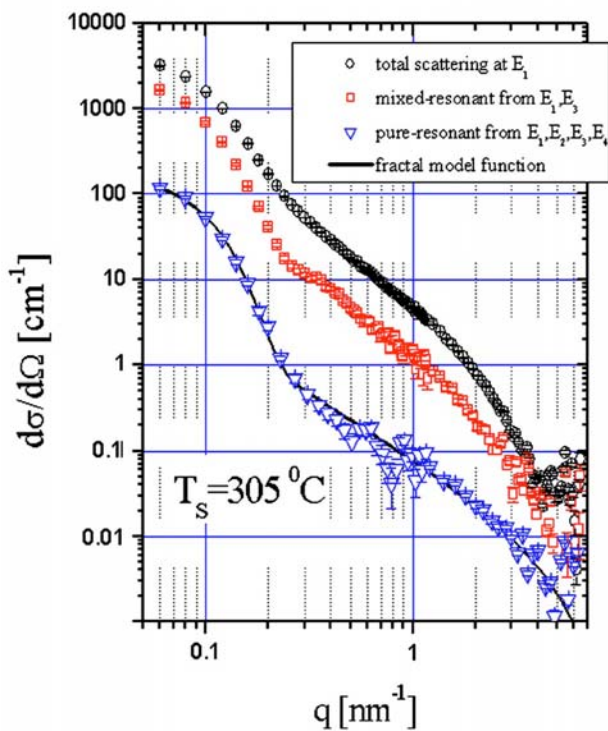


FIG. 4. Total scattering, separated scattering, and the form factor of the pure-resonant scattering contribution of one sample from the second series prepared at the substrate temperature of 305 °C. The solid line represents the fractal model function.

spherically shaped clusters or a size distribution of cylinders failed, when employed to fit the form factors of the Ge component. Definitive proof of fractal structures in these alloys will require further research.

V. DISCUSSION

As mentioned in the previous chapter the data points scatter around zero when calculating the form factor, $S_{Ge}^{form}(q)$, of the T_f series indicating that the variation of the scattering curves due to the pure-resonant scattering contribution is so small it cannot be resolved. On the other hand the separated scattering curves [Fig. 1(b)] from two energies show clearly that the Ge must be inhomogeneously distributed in the alloy. Additionally one can note that the separated

TABLE III. Fit results of the six substrate alloys based on Eq. (6). The fitted scattering curves of the alloys with $T_s=360, 305, 210$ °C are plotted in Figs. 3–5. The parameters with quotation mark indicate the fits to the form factors with poor or no statistical significance at the higher q values. The last column gives the amount of the integrated form factor to the integrated total scattering.

T_s (°C)	A (cm ⁻¹)	R_g (nm)	R_{sub} (nm)	$B \times 10^{-4}$ (cm ⁻¹)	p	Q_{Ge}^{form}/Q_{tot} (%)
360	88.3	22.3	...	14.26	1.58	1.07
305	185.9	19.3	0.4	21.91	1.56	3.92
260	177.6	18.9	0.3	20.03	1.37	4.87
210	106.0	19.2	...	0.02(?)	3.4 (?)	0.41
159	316.7	18.9	...	0.18(?)	2.8 (?)	0.68
130	119.5	21.0	...	1.08(?)	1.9 (?)	0.75

scattering curves have similar or identical shape compared to the related total scattering curves. The most probable explanation for this behavior is the presence of voids or a two-phase mixture in the alloys especially at the temperatures beyond $T_f=1800$ °C as discussed in an earlier paper.³ It is noteworthy that the asymptotic behavior of the scattering curves change from a q^{-4} behavior (smooth interfaces) to a different power law with an exponent smaller than 4 at the two lower filament temperatures, where the invariant is diminished by an order of magnitude. Due to the minimum of the integrated intensity at the lowest filament temperature the film reaches a minimum of inhomogeneity at 1750 °C.

The scattering curves of the second sample series show a significantly different behavior. Again the scattering curves strongly depend on the preparation parameters, here the variation of the substrate temperature. But in contrast to the T_f series the form factor, $S_{\text{Ge}}^{\text{form}}(q)$, can be extracted for all samples of the T_s series. The shape of the separated (mixed resonant) and the pure-resonant (Ge form factor) scattering curves reveal significant differences indicating the presence of a third phase probably voids or hydrogen clusters. From three phases—for example, a region in the alloy with Si containing only a small amount of Ge and H, a second region with a higher amount of Ge and additional H, and finally voids with only small amount of H—the two difference electron densities $\Delta\rho_{\text{H}}, \Delta\rho_{\text{Ge}}$ of Eq. (2) originate. Because the functions $u(\mathbf{r}), v(\mathbf{r})$, which describe the spatial distributions of H and Ge atoms, respectively, are different, the shape of the separated scattering curve changes with the energy, because it is composed of the two contributions, $S_{\text{HGe}}(q, E)$, $S_{\text{Ge}}(q, E)$, which contribute differently at different energies. Due to this the separated scattering curves and the form factors of Figs. 3–5 show different shape. In the case of a two-phase mixture (only one contrast) the functions, $u(\mathbf{r}), v(\mathbf{r})$, are linearly dependent and the basic functions of Eq. (3) simply scale.

Figure 6(a) shows on the left ordinate the integrated intensity (invariant) of the T_s series with a minimum at 260 °C. For comparison the integrated intensity of the pure-resonant scattering, which was calculated from the Ge form factor [Eqs. (5)], divided by the invariant $Q_{\text{Ge}}/Q_{\text{tot}}$ [Eqs. (6)] is plotted on the right ordinate. While the invariant reaches a minimum the ratio of integrated pure-resonant and total scattering reaches a maximum at the same $T_s=260$ °C. The mixed-resonant and the nonresonant scattering contributions were calculated from Eqs. (5). The integrals of Eqs. (3) define a symmetric, positive definite bilinear form in the space of functions. Due to this the Cauchy-Schwarz-Inequation must be valid $S_{\text{HGe}}^2 \leq 4 \cdot S_{\text{Ge}} \cdot S_{\text{H}}$. The basic functions calculated from Eqs. (5) fulfill this inequation within the error bars. From these scattering curves the integrated scattering $Q_{\text{HGe}}, Q_{\text{H}}$ and subsequently the ratios $Q_{\text{HGe}}/Q_{\text{tot}}$ and $Q_{\text{H}}/Q_{\text{tot}}$ were calculated. The results are shown in Fig. 6(b). The sign of the mixed-resonant scattering contribution [right ordinate of Fig. 6(b)] is negative due to the negative sign of the electron density difference caused by the hydrogen atoms in the amorphous Si matrix [Eqs. (3) and (5)]. The absolute units of the three scattering contributions can be obtained by multiplying the normalized values with the related values of the

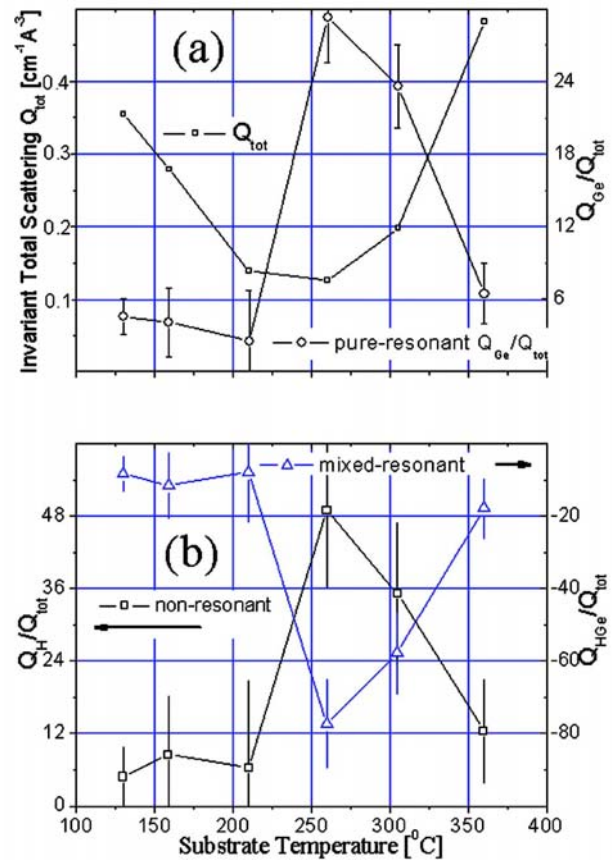


FIG. 6. The integrated intensities (invariant) of: (a) the total scattering Q_{tot} (left ordinate), (a) the normalized pure-resonant scattering $Q_{\text{Ge}}/Q_{\text{tot}}$ (right), (b) the normalized nonresonant scattering $Q_{\text{H}}/Q_{\text{tot}}$ (left) and (b) the normalized mixed-resonant scattering $Q_{\text{HGe}}/Q_{\text{tot}}$ (right). Note the negative sign of the mixed-resonant contribution. The absolute units of $Q_{\text{Ge}}, Q_{\text{HGe}},$ and Q_{H} can be obtained by multiplying with the related total scattering in Fig. 6(a).

invariant, which can be read on the left ordinate of Fig. 6(a). From Figs. 6(a) and 6(b) it is obvious that the total small-angle scattering reaches a minimum while the ratio of integrated pure-resonant and total scattering $Q_{\text{Ge}}/Q_{\text{tot}}$ reaches a maximum at 260 °C, i.e., the formation of Ge-related (fractal) structures reaches a relative maximum while the degree of total inhomogeneity in the film is declining as T_s approaches this intermediate substrate temperature.

This can be expressed more quantitatively. Because voids contribute to the scattering nearly in the same way as H (Ref. 17) the following argumentation will hold for hydrogen clusters and voids. The integrated intensities of Eqs. (6)¹² are

$$Q_{\text{Ge}}(E) = (2\pi)^3 r_0^2 \cdot \Delta f_{\text{Ge}}^2(E) \Delta n_{\text{Ge}}^2 \cdot \Phi_{\text{Ge}}(1 - \Phi_{\text{Ge}}),$$

$$Q_{\text{H}} = (2\pi)^3 r_0^2 \cdot \Delta f_{\text{H}}^2 \cdot \Delta n_{\text{H}}^2 \cdot \Phi_{\text{H}}(1 - \Phi_{\text{H}}), \quad (8)$$

where $\Delta n_{\text{Ge}}, \Delta n_{\text{H}}$ are the excess atomic number densities of Ge and hydrogen (and/or voids) with respect to the surrounding matrix and $\Phi_{\text{Ge}}, \Phi_{\text{H}}$ are the volume fractions of the inhomogeneities caused by Ge and hydrogen clusters (and/or voids), respectively. $r_0=2.82 \times 10^{-13}$ cm is the classical electron radius. From the integrated intensities $Q_{\text{Ge}}, Q_{\text{H}}$ the quantities $n_{\text{Ge}}^f, n_{\text{H}}^f$ can be calculated, where the index f indicates a

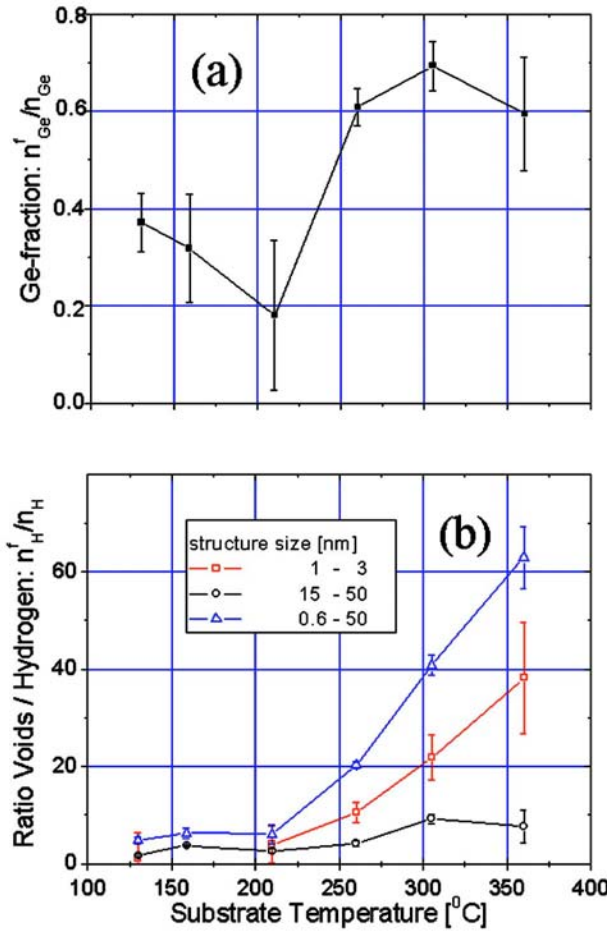


FIG. 7. The fraction of Ge atoms implemented in the suggested fractal structure (a). The ratio of void scattering relative to the scattering expected from the hydrogen implemented in the amorphous matrix (b).

fraction of Ge and H atoms (and/or voids), respectively

$$n_{\text{Ge}}^f = \Delta n_{\text{Ge}} \sqrt{\Phi_{\text{Ge}}(1 - \Phi_{\text{Ge}})} = \sqrt{\frac{Q_{\text{Ge}}(E)}{(2\pi)^3 r_0^2 \cdot \Delta f_{\text{Ge}}^2(E)}},$$

$$n_{\text{H}}^f = \Delta n_{\text{H}} \sqrt{\Phi_{\text{H}}(1 - \Phi_{\text{H}})} = \sqrt{\frac{Q_{\text{H}}}{(2\pi)^3 r_0^2 \cdot \Delta f_{\text{H}}^2}}. \quad (9)$$

The product between the equal signs is composed from the contrast between the atomic number densities in the inhomogeneities and the surrounding matrix and the volume fractions of inhomogeneities caused by Ge and H (and/or voids), respectively. For the determination of both—contrast and volume fraction—SAXS measurements at more than three or four energies are necessary as was outlined in a previous publication.³ This is beyond the scope of the present investigation but nevertheless the quantities n_{Ge}^f , n_{H}^f give the number densities of Ge and H atoms (and/or voids) in the sample, which contribute to the small-angle scattering, i.e., n_{Ge}^f , n_{H}^f give the numbers of Ge and H atoms (and/or voids) which are inhomogeneously distributed.

Figure 7(a) shows n_{Ge}^f normalized to the atomic number density of Ge atoms in the sample n_{Ge} (eighth column of Table I) plotted versus the substrate temperature. In this dia-

gram two groups of samples can be distinguished, which correspond to the sharp decrease in Fig. 7(a) at a substrate temperature below 260 °C. At $T_s=260$ °C and beyond, more than 60% of the Ge atoms are localized in the fractal structures, while at the lower T_s the amount of Ge atoms incorporated into the fractals is strongly reduced. This can be due to the reduction of the volume fraction (less fractals) or due to the reduction of the contrast between the fractals and the surrounding matrix by reducing the number of Ge atoms in the fractals, or due to both. As a consequence a larger amount of Ge atoms remains homogeneously distributed in the matrix for the lower substrate temperatures.

Finally, it should be possible to gain structural and quantitative information about the hydrogen clusters or voids from the analysis of the nonresonant scattering contribution and the quantity n_{H}^f . Again, it is not possible to distinguish between the contrast of the atomic number densities and the volume fraction filled by hydrogen or voids, but the normalization to the hydrogen concentration in the alloys can give interesting information as is shown in Fig. 7(b). The triangles in Fig. 7(b) represent $n_{\text{H}}^f/n_{\text{H}}$, which is the quantity n_{H}^f of Eq. (9) normalized to the hydrogen concentration n_{H} , which was calculated from the fifth column in Table I. Especially for the temperatures beyond 250 °C the ratio shows values which are far too high, i.e., 20, 40, and 60 times higher than expected from the hydrogen concentration. From this the conclusion can be drawn that the nonresonant scattering represents not only the scattering of hydrogen-filled inhomogeneities but also gives evidence for the existence of voids, which dominate the nonresonant scattering contribution. When the integral intensity of the nonresonant contribution is calculated in the q range between 1 and 3 nm^{-1} (corresponding to structure sizes between 3 and 1 nm) the integral value reaches more than 50% of the value obtained from the overall integration, while the integration in the q range between 0.06 and 0.2 nm^{-1} (corresponding to structure sizes between 50 and 15 nm) shows only weak dependence on the temperature with clearly lower values of $n_{\text{H}}^f/n_{\text{H}}$. So one can conclude that the ratio $n_{\text{H}}^f/n_{\text{H}}$ represents the ratio of voids to hydrogen atoms (i.e., the volume fractions) and that the nonresonant scattering contribution is clearly dominated by the scattering of voids with sizes of about several nanometers at higher substrate temperatures. These voids are strongly reduced when the substrate temperature is reduced and the optimum is reached, when the formation of the Ge mass fractals reaches a relative maximum in coincidence with a strongly reduced void fraction.

This can be demonstrated by the correlation of the integrated total scattering Q_{tot} with the measured values of the photoconductivity of the T_s series shown in Fig. 8. The photoconductivity reaches maximum values where the integrated total intensities Q_{tot} reaches minimum values at $T_s=210$ and 260 °C. The minimum value at 260 °C is produced by the high amount of the mixed-resonant contribution $S_{\text{HGc}}(q, E)$ at this temperature [Fig. 7(b) right ordinate] caused by a large value of the convolution integral in Eq. (3) with respect to the total scattering. Note that the negative sign is introduced by the negative sign of the contrast Δf_{H} . The large value of the convolution integral indicates a strong overlap in space

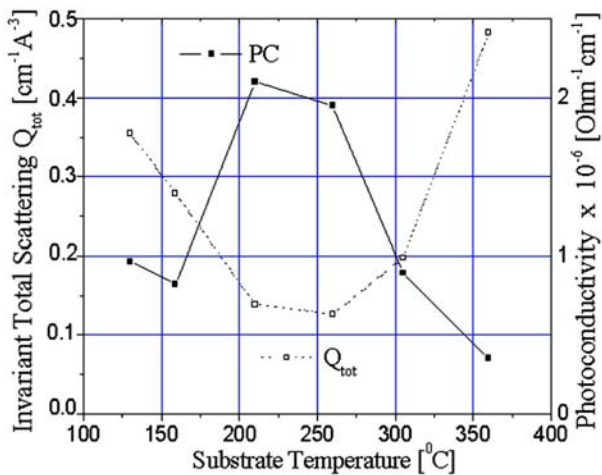


FIG. 8. Total integrated scattering and photoconductivities (right ordinate) of the substrate samples plotted vs the substrate temperature.

of the two number density functions $u(\mathbf{r}), v(\mathbf{r})$ of H and Ge atoms and from this it can be concluded that a larger amount of H atoms is probably bonded to Ge atoms. This is confirmed by IR results, which show a maximum of Ge–H bonding fraction at 260 °C.^{8,9} At 210 °C the photoconductivity is still high though the amount of the mixed-resonant contribution is strongly reduced. Here the competing influence of the voids comes into play. Because a strong reduction of the void fraction is still going on when T_s is reduced to 210 °C [Fig. 7(b)] the photoconductivity remains high though the fraction of Ge–H bonding starts to decline (known from IR measurements^{8,9}) due to the reduced number of Ge atoms incorporated in the fractals. For the two lowest values of T_s 159 and 130 °C no further reduction of voids takes place and the number of Ge atoms incorporated in the fractals remains on a low level with the result of low photoconductivities.

VI. CONCLUSIONS

ASAXS measurements obtained from hot wire deposited $a\text{-Si}_{1-x}\text{Ge}_x\text{:H}$ alloys with x between 0.6 and 0.7 reveal clear evidence of nonuniformly distributed Ge. Due to the preparation parameters strong differences of the material nanostructures were found. From the separation of the pure-resonant scattering contribution, the alloys Ge component is suggested to be mainly distributed in mass fractals with the fractal dimension between 1.3 and 1.6 and sizes of about 40 nm. More than 60% of the Ge atoms are incorporated in these structures at substrate temperatures beyond 250 °C.

This amount is drastically reduced when lowering the substrate temperature. From the nonresonant scattering, evidence for the existence of voids with a size of a few nanometers was found. The scattering of the voids exceeds the scattering expected from hydrogen clusters by more than one order of magnitude. Improved material properties are reached at a substrate temperature of 260 °C, where the formation of the suggested mass fractals caused by nonuniformly distributed Ge reaches a relative maximum in coincidence with a strongly reduced void fraction, and increased H–Ge bonding.

The effect of the T_f reduction at fixed T_s was to dramatically reduce the voids and Ge nonuniformity and thereby improve the photoconductivity by about a factor of 20. A further optimization by varying T_s at fixed T_f produced different changes in the Ge substructure indicative of enhanced Ge mass fractals, in addition to void reduction, that also improved the photoconductivity by about a factor of 5.

ACKNOWLEDGMENT

The work was supported in part by the United States National Renewable Energy Laboratory under Subcontract No. XAK-8-17619-31 to the Colorado School of Mines.

- ¹D. L. Williamson, *Mater. Res. Soc. Symp. Proc.* **377**, 251 (1995).
- ²G. Goerigk and D. L. Williamson, *Solid State Commun.* **108**, 419 (1998).
- ³G. Goerigk and D. L. Williamson, *J. Non-Cryst. Solids* **281**, 181 (2001).
- ⁴G. Goerigk and D. L. Williamson, *J. Appl. Phys.* **90**, 5808 (2001).
- ⁵E. C. Molenbroek, A. H. Mahan, and A. Gallagher, *J. Appl. Phys.* **82**, 1909 (1997).
- ⁶B. P. Nelson *et al.*, *Mater. Res. Soc. Symp. Proc.* **507**, 447 (1998).
- ⁷B. P. Nelson, Y. Xu, D. L. Williamson, D. Han, R. Braunstein, M. Boshta, and B. Alavi, *Thin Solid Films* **430**, 104 (2003).
- ⁸Y. Xu, B. P. Nelson, D. L. Williamson, L. M. Gedvilas, and R. C. Reedy, *Mater. Res. Soc. Symp. Proc.* **762**, A 10.2 (2003).
- ⁹Y. Xu, B. P. Nelson, L. M. Gedvilas, and R. C. Reedy, *Thin Solid Films* **430**, 197 (2003).
- ¹⁰H. B. Stuhmann, *Adv. Polym. Sci.* **67**, 123 (1985).
- ¹¹G. Goerigk, R. Schweins, K. Huber, and M. Ballauff, *Europhys. Lett.* **66**, 331 (2004).
- ¹²O. Glatter and O. Kratky, *Small-Angle X-ray Scattering* (Academic, London 1982).
- ¹³H.-G. Haubold *et al.*, *Rev. Sci. Instrum.* **60**, 1943 (1989).
- ¹⁴D. T. Cromer and D. Liberman, *J. Chem. Phys.* **53**, 1891 (1970).
- ¹⁵D. T. Cromer and D. Liberman, *Acta Crystallogr., Sect. A: Cryst. Phys., Diffraction, Theor. Gen. Crystallogr.* **37**, 267 (1981).
- ¹⁶G. Beaucage, *J. Appl. Crystallogr.* **28**, 717 (1995).
- ¹⁷In the case of voids the electron density contrast simply is the electron density of the surrounding material with negative sign, while in the case of a H cluster it is the difference between the atomic number density of H atoms minus the electron density of the surrounding material. Due to only one electron of H the values are nearly the same.

[S7]

R. Schweins, G. Goerigk, and K. Huber,

Shrinking of Anionic Polyacrylate Coils Induced by Ca^{2+} , Sr^{2+} and Ba^{2+} :

A Combined Light Scattering and ASAXS Study

Eur. Phys. J. E 21, 99-110 (2006)

Shrinking of anionic polyacrylate coils induced by Ca^{2+} , Sr^{2+} and Ba^{2+} : A combined light scattering and ASAXS study

R. Schweins¹, G. Goerigk², and K. Huber^{3,a}

¹ Institut Laue-Langevin, LSS Group, B.P. 156, 6 rue Jules Horowitz, F-38042 Grenoble cedex 9, France

² Institut für Festkörperforschung, Forschungszentrum Jülich, Postfach 1913, D-52425 Jülich, Germany

³ Universität Paderborn, Fakultät für Naturwissenschaften, Department Chemie, Warburger Str.100, D-33098 Paderborn, Germany

Received 2 May 2006 /

Published online: 6 December 2006 – © EDP Sciences / Società Italiana di Fisica / Springer-Verlag 2006

Abstract. Anionic polyacrylate chains (NaPA) form precipitates if alkaline earth cations are added in stoichiometric amounts. Accordingly, precipitation thresholds were established for three different alkaline earth cations Ca^{2+} , Sr^{2+} and Ba^{2+} . Close to the precipitation threshold, the NaPA chains significantly decrease in size. This shrinking process was followed by means of combined static and dynamic light scattering. Intermediates were generated by varying the ratio $[\text{MCl}_2]/[\text{NaPA}]$ with M denoting the respective alkaline earth cation. All experiments were performed at an inert salt level of 0.01 M NaCl. Similar coil-to-sphere transitions could be observed with all three alkaline earth cations Ca^{2+} , Sr^{2+} and Ba^{2+} . Based on these findings, supplementary conventional and anomalous small-angle X-ray scattering experiments using selected intermediates close to the precipitation threshold of SrPA were performed. The distribution of Sr counterions around the polyacrylate chains in aqueous solution provided the desired scattering contrast. Energy-dependent scattering experiments enabled successful separation of the pure-resonant terms, which solely stem from the counterions. The Sr^{2+} scattering roughly reflects the monomer distribution of the polyacrylate chains. Different ratios of the concentrations of $[\text{SrCl}_2]/[\text{NaPA}]$ revealed dramatic changes in the scattering curves. The scattering curve at the lowest ratio indicated an almost coil-like behaviour, while at the higher ratios the scattering curves supported the model of highly contracted polymer chains. Most of X-ray scattering experiments on intermediate states revealed compact structural elements which were significantly smaller than the respective overall size of the NaPA particles.

PACS. 61.10.Eq X-ray scattering (including small-angle scattering) – 82.35.Rs Polyelectrolytes – 78.35.+c Brillouin and Rayleigh scattering; other light scattering

1 Introduction

Polyelectrolytes are electrically charged, water soluble macromolecules. Due to intramolecular electrostatic interactions, the dissolved chains are highly extended. Addition of an inert salt screens these interactions and modifies the solubility and conformation of the polyelectrolyte chains. If the inert salt level is high enough, the chains can be described by the model of a random walk, also denoted as unperturbed or Θ -dimensions of the chain [1,2]. For sodium polyacrylate (NaPA) in water, this state is achieved by addition of roughly 1.5 moles of alkali halogenides per liter [3–5].

Contrary to this non-specific screening with inert salts, earth alkaline cations strongly interact with the carboxylate functions of the anionic PA-backbone. The largest

body of evidence, provided for such specific interactions, also denoted as complex bonding, deals with the interaction between Ca^{2+} and anionic acrylates. This specific bond formation is driven partly by the liberation of water molecules from the hydration shells around the ionic residuals [6,7]. Complex bonding of the Ca^{2+} also neutralizes the NaPA chains [8–12], increases the hydrophobic nature of the backbone and eventually leads to a chain collapse [11–13]. The chain collapse borders precipitation of the resulting CaPA [8–10]. Therefore, investigation of the collapse mechanism is most promising close to the precipitation threshold [11–13].

By means of combined light scattering and small-angle neutron scattering (SANS), it was possible to present first evidence for the existence of CaPA intermediates with pearl-necklace-like structures [14] in solution. Agreement between scattering experiments and model scattering curves was best under the assumption that intermediates

^a e-mail: klaus.huber@upb.de

comprise a mixture of single spheres and pearl necklace chains with a very low average number of pearls per polyelectrolyte chain [14–16]. The shrinking process ended with the approach of a compact sphere-like shape [13]. Further indication for highly dense domains within polyelectrolyte chains was provided by NMR experiments [17], by ellipsometry [18], by small-angle X-ray [19–22] and anomalous small-angle X-ray scattering [11, 23], by small-angle neutron scattering [24–26] and by AFM [20, 27]. Part of the results refers to single-chain behaviour under dilute-solution conditions [11, 17, 18, 21–24, 27]. Various SAXS and SANS experiments, however, predominantly deal with semi-dilute solutions of the polyelectrolyte [19, 20, 25, 26], which makes conclusions on single-chain behaviour in dilute solution difficult. In most cases, the impact of specifically interacting cations was investigated [11, 17, 22, 23, 25, 26]. In other cases, contraction of the polyelectrolyte was induced by chemical variation of the charge fraction on the polyelectrolyte chains [18–20], by lowering the *pH* [21], by addition of an organic solvent to aqueous solutions [24] or by addition of an inert salt [27]. Only some of those authors attempted to explicitly discriminate between compact spheres and pearl necklace chains [18, 23, 24, 27], or at least considered their results to be a consequence of pearl necklace chains [17, 20, 21]. Although, the AFM technique revealed the first direct evidence of pearl necklace chains [27], results measured with dried films cannot be unambiguously transferred to the original solution. The same principal reservation holds for the ellipsometric study [18]. Thus, the body of experimental evidence on pearl necklace chains and conditions under which pearl necklace chains may exist is still extremely poor.

Pearl necklace structures are introduced as intermediates of collapsing polyelectrolyte chains by theoretical calculations by Kantor and Kardar [28] and Rubinstein *et al.* [29]. The pearl necklace shape resulted from an analogy between the shrinking polyelectrolyte chain and the Rayleigh instability of charged oil droplets. The collapse could be induced by a subtle interplay of changes of the solvent quality, of the number of charges per chain and of the strength of electrostatic interactions. A crucial part of the process is the condensation of counterions. However, the range of parameters, where pearl-necklace-like shapes are likely to occur is fairly narrow [15, 30, 31]. A necessary prerequisite for the generation of pearl-necklace-like transition states is a hydrophobic backbone and a possibility to tune the charge of the chains [15, 30, 31], *e.g.* by addition of specifically interacting counterions.

If specific interactions between anionic polyacrylate in solution and alkaline earth cations or transition metal cations are to be investigated, small-angle X-ray scattering (SAXS) is a highly promising method. Complex bonding fixes the counterions at COO^- residuals and decorates the shrinking chain with a component of high electron density. Thus, the chains act as a template and may provide access to their shape. Above this, anomalous small-angle X-ray scattering (ASAXS) offers additional information if the wavelength of the scattered X-rays is varied [32–38]. This enabled Goerigk *et al.* [23] and Ballauff *et al.* [37, 38] for

the first time to isolate the scattering factor of the counterions condensing on polyelectrolytes. In the present case, variation of the wavelength changes the scattering contrast of divalent strontium cations at a roughly constant scattering contrast of the anionic chains, which host the cations. However, this requires the extension of preceding results [12–14] on heavier alkaline earth cations.

Thus, the phase behaviour and shrinking process established for the precipitation of NaPA with Ca^{2+} ions [12–14] shall be extended to Ba^{2+} and Sr^{2+} in the present investigation. Combined static and dynamic light scattering is applied to locate the phase boundary of the respective M^{2+} -PA precipitation and to characterize the global dimensions of the chains while approaching the phase boundary [13]. The use of three different alkaline earth cations allows for a comparison of cations within the homologous series of alkaline earth cations. At the same time the phase behaviour of the cations with the higher-order number allows to design SAXS and ASAXS experiments of the PA shrinking. Hence, sets of solutions with Sr^{2+} including two different NaPA samples were selected for further SAXS and ASAXS experiments. Results are expected to yield new insight into the shape of the PA chains collapsing near the phase boundary.

2 Experimental

2.1 Materials

The NaPA samples were purchased from Polysciences, Eppeleheim (Germany). Two NaPA samples with different molar mass were used. Light scattering revealed a weight averaged molar mass $M_w = 950$ kDa (PA1) and 3300 kDa (PA2). The polydispersity index is $M_w/M_n = 1.2$ for both samples, where M_n and M_w is the number averaged and weight averaged molar mass, respectively [5]. The inorganic salts, NaCl and CaCl_2 , SrCl_2 and BaCl_2 were purchased from Fluka, Buchs (Switzerland) with puriss. p. a. grade.

2.2 Preparation of solutions for light scattering

Preparation of the solutions for light scattering was performed according to two different procedures (*route 1* and *route 2*). The procedure was introduced elsewhere [13] and will be outlined by means of Sr^{2+} .

Route 1. Preparation of NaPA solutions with Sr^{2+} in aqueous NaCl was performed in two steps. In the first step, a solution of NaPA in bidistilled water with 0.01 M NaCl at *pH* 9 (solution I) was prepared together with another solution of 3 mM SrCl_2 and 4 mM NaCl in bidistilled water at *pH* 9 (solution II). The *pH* was set with 0.01 M NaOH. It is noteworthy to mention that both solutions had the same number of cationic charges, which was

$$2[\text{Sr}^{2+}] + [\text{Na}^+] = 0.01 \text{ M}. \quad (1)$$

After 3 days of storage, equal volumes of both solutions were combined. Thus, a stock solution of NaPA in distilled water with 1.5 mM SrCl_2 and 7 mM NaCl with a pH of 9 was obtained (solution III). In an analogous way, an amount of solution II was combined with an equal amount of bidistilled water with 0.01 M NaCl, resulting in an NaPA-free solution of 1.5 mM SrCl_2 and 7 mM NaCl at a pH of 9 (solution IV). Solution IV is denoted as solvent and served as the solvent background for all scattering experiments.

The phase boundary for Sr^{2+} -PA precipitation was approached by diluting the stock solution (III) with the solvent (IV). By means of this procedure [13], different ratios of $[\text{Sr}^{2+}]/[\text{NaPA}]$ were obtained at constant concentrations of $[\text{Sr}^{2+}]$ and $[\text{Na}^+]$. As the shape of the polymer chains in solution depends on the extent of complexation, different ratios correspond to different intermediates, bordering the precipitation threshold of SrPA.

Route 2. In the first step, three different solutions were generated. A NaPA solution was prepared with 0.01 M NaCl and a pH of 9 (solution I). A second solution with pure SrCl_2 at pH of 9 was set to $[\text{SrCl}_2] = 0.005$ mM, ready to provide the Sr^{2+} ions. A third solution at $\text{pH} = 9$ contained only NaCl at $[\text{NaCl}] = 0.01$ M (solution III). Finally 10 mL of solution I was combined with X ml of solution II in a 20 ml graduated flask. The flask was filled to the mark with $(10 - X)$ mL of solution III. The corresponding solvent background was generated in the same way with 10 mL of solution III instead of solution I. The phase boundary was approached by increasing X in the range of $0 \text{ mL} < X \text{ mL} < 10 \text{ mL}$.

2.3 Light scattering

An ALV 5000E Compact Goniometer System with a 100 mW Nd:YAG laser as a light source was used. The scattering intensity was recorded with a photomultiplier in an angular range of 30° to 150° in steps of 10° . Net scattering intensities of polymers were expressed in terms of the Rayleigh ratio ΔR_θ with ΔR_θ referring to the Rayleigh ratio of the standard toluene at 298.15 K, $R = 2.737 \cdot 10^{-5} \text{ cm}^{-1}$. Data from static light scattering (SLS) were extrapolated to zero scattering angle according to

$$\frac{K \cdot c}{\Delta R_\theta} = \frac{1}{M_w} + \frac{R_g^2}{3M_w} \cdot q^2 \quad (2)$$

with K being the contrast constant, c the polymer concentration in g/mL, M_w the apparent molecular weight, R_g^2 the z -averaged squared radius of gyration and q the momentum transfer

$$q = \frac{4\pi n}{\lambda_0} \sin\left(\frac{\theta}{2}\right). \quad (3)$$

In equation (3), n is the refractive index at 532 nm of 0.01 M NaCl being 1.336, λ_0 is the laser wavelength in vacuum being 532 nm and θ is the scattering angle.

Correlation functions from dynamic light scattering (DLS) were evaluated by application of the cumulant method [39] with linear and quadratic terms of the correlation time t . The resulting diffusion coefficients $D(q)$ were extrapolated to zero momentum transfer according to

$$D(q) = D_Z(1 + CR_g^2q^2). \quad (4)$$

Here, C denotes a dimensionless shape sensitive constant and D_Z is the extrapolated diffusion coefficient. The latter can be transformed into a hydrodynamically effective radius R_h by use of the Stokes-Einstein equation:

$$R_h = \frac{k_B \cdot T}{6\pi \cdot \eta} \cdot \frac{1}{D_Z} \quad (5)$$

with k_B being the Boltzmann constant, $\eta = 890.37 \mu\text{Pas}$ the solvent viscosity of 0.01 M NaCl and T the absolute temperature.

All samples were located close to the phase boundary where the intramolecular shrinking process may increasingly compete with the onset of precipitation. Thus, care had to be taken to identify and discard samples with aggregates. Identification of the onset of aggregation was achieved by using two criteria, evaluated with LS. The first criterion was a significant increase of the apparent molar mass detected by SLS. The second criterion was based on the CONTIN analysis of the correlation functions from DLS. The CONTIN method [40] allows for distinguishing different diffusive modes, therefore directly indicating aggregation if a mode in addition to the diffusion of the single chains became observable.

2.4 Preparation of solutions for SAXS and ASAXS experiments

SAXS and ASAXS experiments were performed with two NaPA samples, PA1 and PA2. A series denoted SAXS-2 with two different ratios $[\text{Sr}^{2+}]/[\text{NaPA}]$ was prepared for the higher molar mass sample PA2, at $[\text{Sr}^{2+}] = 1$ mM, according to *route 2*. Both solutions were fully characterised by LS prior to the SAXS experiment. The solutions were denoted SAXS-2A and SAXS-2B. Solution SAXS-2B was further apart from the phase boundary than SAXS-2A.

Two series with varying ratio $[\text{Sr}^{2+}]/[\text{NaPA}]$, denoted as SAXS-1 and ASAXS-1, were prepared with sample PA1. Both series were generated according to *route 1* at a level of alkaline earth cations of $[\text{Sr}^{2+}] = 1.5$ mM. Series SAXS-1 was originally investigated at three different energies to additionally account for anomalous scattering. Corresponding ASAXS results have already been published [23] and we only review the total SAXS curves of series SAXS-1. SAXS-1A thereof, was selected on the basis of detailed LS results. This solution was directly transferred from the light scattering cell into the capillary. A second NaPA solution (SAXS-1B) was investigated without being characterized by LS prior to X-ray scattering experiments. The ratio $[\text{Sr}^{2+}]/[\text{NaPA}]$ of SAXS-1B was smaller than the one of SAXS-1A. Therefore, SAXS-1B was further apart from the phase boundary

Table 1. Specifications of the NaPA solutions used for SAXS experiments. The molar mass of SAXS-1A and -1B is 950 kDa (PA1) and of SAXS-2A and -2B 3300 kDa (PA2), respectively.

Solution	R_g (nm)	R_h (nm)	q_{Min} (nm^{-1})	ρ	α_s	$\alpha^{(1)}$ (DLS)	[NaPA] (mM)	$[\text{Sr}^{2+}]/[\text{NaPA}]$
SAXS-1A	15.9	15.0	0.25	1.06	0.32	0.52	3.25	0.46
SAXS-1B	–	–	–	–	–	–	3.61	0.42
SAXS-2A	22.2	18.2	0.3	1.22	0.275	0.33	1.4997	0.667
SAXS-2B	31.2	21.1	0.3	1.48	0.387	0.38	1.5346	0.651

⁽¹⁾ Calculated with the corresponding hydrodynamic radii from DLS.

than SAXS-1A. The parameters of all solutions selected for SAXS experiments are summarized in Table 1.

A second series of the same sample PA1 included four different ratios $[\text{Sr}^{2+}]/[\text{NaPA}]$. Each solution was investigated at three different energies. It is this series by means of which we are able to present new ASAXS experiments on the system SrPA. The solutions are denoted ASAXS-1X with $X = \text{A, B, C}$ and D indicating increasing distances from the phase boundary. Each solution was carefully characterized by means of light scattering prior and after X-ray scattering. Characterisation before and after the ASAXS experiment allows us for the first time to demonstrate long-term stability of the four samples under investigation.

2.5 SAXS and ASAXS measurements

SAXS and ASAXS experiments were performed in capillaries from Hilgenberg GmbH, Malsfeld (Germany). NaPA solutions and solvent was measured in glass capillaries. The solvent was 0.01 M in Cl^- and contained the same amount of Sr^{2+} ions as the respective NaPA solutions. The capillaries were made of borosilicate glass with an inner diameter of 4 mm and a wall thickness of 0.05 mm, specially designed for ASAXS experiments in the energy range of the K -absorption edge of Sr at 16.105 keV. They were filled through the open end and sealed by fixing an appropriate piece of glass with glue on top of the open end. This glass cap was made from an adequately cut Pasteur pipette which was melted off at the conical end. The sealed capillaries were horizontally mounted onto a sample holder which was screwed into the sample area.

All experiments were performed at the JUSIFA beamline [41] at HASYLAB, DESY Hamburg. The energies used for all three series are summarized in Table 2. The lowest energy of each series was significantly below the K -absorption edge of strontium at 16.1046 keV and was considered to provide the respective conventional scattering curves (SAXS) referring to the total scattering of the SrPA complex. The columns $f'_{\text{eff}}(E)$ and $f''_{\text{eff}}(E)$ in Table 2 represent the effective anomalous dispersion corrections calculated from the convolution with the energy resolution of the slit system and the monochromator (Si-311) at the JUSIFA experiment. The values at the energy of the Sr- K -edge are significantly changed compared to the the-

Table 2. Energies and anomalous contributions to the scattering factor f_{Ion} for the three series of $[\text{Sr}^{2+}]/[\text{NaPA}]$ investigated by SAXS and ASAXS. The f'_{Ion} , f''_{Ion} are the theoretical values obtained from the Cromer-Lieberman calculations [42,43] without taking the limited energy resolution of the experiment into account. The f'_{eff} , f''_{eff} represent the effective anomalous dispersion corrections estimated from the convolution with the energy resolution of the slit system and the monochromator at the JUSIFA experiment [41].

Series	E (keV)	$\Delta E^{(1)}$ (eV)	f'_{Ion}	f'_{eff}	f''_{Ion}	f''_{eff}
SAXS-1	15.506	599	-2.75	-2.75	0.56	0.56
ASAXS-1	15.507	598	-2.75	-2.75	0.56	0.56
	16.093	12	-6.66	-6.66	0.53	0.53
	16.105	0	-11.66	-10.3	3.77	2.08
SAXS-2	15.512	593	-2.90	-2.90	0.56	0.56

⁽¹⁾ Difference of the energy of the incident beam and the absorption edge.

oretical values obtained from the Cromer-Lieberman calculations without taking the limited energy resolution of the experiment into account.

The focus of the present work lies on series ASAXS-1 with sample PA1. For ASAXS-1, the energy dependence of the small-angle X-ray scattering near the K -absorption edge of Sr was measured in order to isolate the scattering from the Sr ions. Measurements were made with a two-dimensional detector at three energies. A q -range from about 0.075 to 2.5 nm^{-1} was covered. Table 2 provides the anomalous dispersion corrections for Sr at the energies used here based on the calculations of Cromer and Lieberman [42,43]. These were used to permit the separation of the Sr-related pure-resonant scattering described in detail in [23,44]. Constant background effects due to diffuse scattering of the solvent and due to resonant Raman scattering occurring near the K -absorption edge at 16.105 keV have been subtracted from the measured intensities before separating the pure-resonant scattering.

The ASAXS data were processed with the software available at the beamline. The program was used to integrate, to correct for transmission and detector sensitivity, to subtract the background and the dark current. All scattering curves have been calibrated into absolute units

(i.e. macroscopic scattering cross-sections in units of cross-section per unit volume $\text{cm}^2/\text{cm}^3 = \text{cm}^{-1}$).

3 Evaluation of ASAXS measurements

In the case of a dilute solution of polymers the scattering curve of the polymer is given by [45]

$$I(\vec{q}) = \frac{N}{V} \cdot I_0(\vec{q}) \cdot \psi(\vec{q}), \quad (6)$$

where N/V is the number of dissolved polymers per volume. $\psi(\vec{q})$ is the structure factor, which describes the influence of interparticle correlation and will not be considered further here ($\psi = 1$) due to the dilute solution of the polymers. The second angular dependent term in equation (6)

$$I_0(\vec{q}) = |A(\vec{q})|^2 = A(\vec{q}) \cdot A^*(\vec{q}) \quad (7)$$

is the scattering function of a single particle. In equations (6) and (7) q is the absolute value of the momentum transfer \vec{q} (cf. Eq. (3) for light waves). $A(\vec{q})$ is the scattering amplitude of the particle. In the case of negatively charged polyelectrolytes surrounded by positively charged counterions in dilute solution, the scattering amplitude of a single polymer chain writes

$$A(\vec{q}) = \int \Delta\rho_{\text{Poly}}(\vec{r}) \cdot \exp(-i\vec{q}\vec{r}) d^3r + \int \Delta\rho_{\text{Ion}}(\vec{r}) \cdot \exp(-i\vec{q}\vec{r}) d^3r \quad (8)$$

with

$$\begin{aligned} \Delta\rho_{\text{Poly}}(\vec{r}) &= \Delta f_{\text{Poly}} \cdot u(\vec{r}) = (f_{\text{Poly}} - \rho_m V_{\text{Poly}}) \cdot u(\vec{r}), \\ \Delta\rho_{\text{Ion}}(\vec{r}, E) &= \Delta f_{\text{Ion}}(E) \cdot v(\vec{r}) = ((f_{0,\text{Ion}} - \rho_m V_{\text{Ion}}) \\ &\quad + f'_{\text{Ion}}(E) + i f''_{\text{Ion}}(E)) \cdot v(\vec{r}). \end{aligned} \quad (9)$$

$\Delta\rho_{\text{Poly}}$, $\Delta\rho_{\text{Ion}}$ are the excess electron densities of the polyelectrolyte chains and the counterions calculated from the electron density ρ_m of the solvent and the volumes V_{Poly} and V_{Ion} of the chains and the counterions, while $u(\vec{r})$, $v(\vec{r})$ are the particle densities of the polymer chains and the counterions, respectively. The molecular scattering factor (number of electrons) of the chain f_{Poly} is nearly energy independent, whereas the atomic scattering factor of the counterions shows strong variations with the energy in the vicinity of the absorption edge of the counterion which are taken into account by the so-called anomalous dispersion corrections $f'_{\text{Ion}}(E)$, $f''_{\text{Ion}}(E)$:

$$\begin{aligned} f_{\text{Poly}}(E) &\approx \text{const}, \\ f_{\text{Ion}}(E) &= f_{0,\text{Ion}} + f'_{\text{Ion}}(E) + i f''_{\text{Ion}}(E). \end{aligned} \quad (10)$$

Calculating the scattering intensity due to equations (7–9) and averaging over all orientations of the polymer yields

$$\begin{aligned} I_0(q, E) &= 4\pi \Delta f_{\text{Poly}}^2 \iint_{V_p} u(\vec{r}) u(\vec{r}') \frac{\sin(q|\vec{r} - \vec{r}'|)}{q|\vec{r} - \vec{r}'|} d^3r d^3r' \\ &\quad + 4\pi \cdot 2\Delta f_{\text{Poly}} (f_{0,\text{Ion}} - \rho_m V_{\text{Ion}} + f'_{\text{Ion}}(E)) \\ &\quad \times \iint_{V_p} u(\vec{r}) v(\vec{r}') \frac{\sin(q|\vec{r} - \vec{r}'|)}{q|\vec{r} - \vec{r}'|} d^3r d^3r' \\ &\quad + 4\pi \Delta f_{\text{Ion}}^*(E) \cdot \Delta f_{\text{Ion}}(E) \\ &\quad \times \iint_{V_p} v(\vec{r}) v(\vec{r}') \frac{\sin(q|\vec{r} - \vec{r}'|)}{q|\vec{r} - \vec{r}'|} d^3r d^3r'. \end{aligned} \quad (11)$$

Equation (11) is composed of three terms: i) the scattering of the polymer chains; ii) the cross-term originating from the superposition of the scattering amplitudes of the polymer and the counterions; iii) the scattering of the counterions, which contains the so-called pure-resonant scattering of the counterions. By measuring the scattering curves at two energies in the vicinity of the absorption edge of the counterions and subtracting the two scattering curves the non-resonant scattering contribution of the polymer is vanishing:

$$\begin{aligned} \Delta I_0(q, E_1, E_2) &= I_0(q, E_1) - I_0(q, E_2) = \\ &= 4\pi \cdot 2\Delta f_{\text{Poly}} (f'_{\text{Ion}}(E_1) - f'_{\text{Ion}}(E_2)) \\ &\quad \times \iint_{V_p} u(\vec{r}) v(\vec{r}') \frac{\sin(q|\vec{r} - \vec{r}'|)}{q|\vec{r} - \vec{r}'|} d^3r d^3r' \\ &\quad + 4\pi (\Delta f_{\text{Ion}}^*(E_1) \cdot \Delta f_{\text{Ion}}(E_1) - \Delta f_{\text{Ion}}^*(E_2) \cdot \Delta f_{\text{Ion}}(E_2)) \\ &\quad \times \iint_{V_p} v(\vec{r}) v(\vec{r}') \frac{\sin(q|\vec{r} - \vec{r}'|)}{q|\vec{r} - \vec{r}'|} d^3r d^3r'. \end{aligned} \quad (12)$$

Now the scattering function is reduced to the resonant contributions —the so-called *separated scattering*— but the scattering of the polymer is still present in the cross-term. To overcome this drawback, a measurement at a third energy can be performed and when subtracting the separated scattering obtained at the two energies E_1 , E_3 from the separated scattering obtained at the two energies E_1 , E_2 the cross-term is vanishing and only the pure-resonant scattering contribution of the counterions remains:

$$\begin{aligned} &\frac{\Delta I_0(q, E_1, E_2)}{f'_{\text{Ion}}(E_1) - f'_{\text{Ion}}(E_2)} - \frac{\Delta I_0(q, E_1, E_3)}{f'_{\text{Ion}}(E_1) - f'_{\text{Ion}}(E_3)} = \\ &= 4\pi \left[f'_{\text{Ion}}(E_2) - f'_{\text{Ion}}(E_3) + \frac{f''_{\text{Ion}}(E_1) - f''_{\text{Ion}}(E_2)}{f'_{\text{Ion}}(E_1) - f'_{\text{Ion}}(E_2)} \right. \\ &\quad \left. - \frac{f''_{\text{Ion}}(E_1) - f''_{\text{Ion}}(E_3)}{f'_{\text{Ion}}(E_1) - f'_{\text{Ion}}(E_3)} \right] \\ &\quad \times \iint_{V_p} v(\vec{r}) v(\vec{r}') \frac{\sin(q|\vec{r} - \vec{r}'|)}{q|\vec{r} - \vec{r}'|} d^3r d^3r'. \end{aligned} \quad (13)$$

Due to equation (13) ASAXS is a technique to access directly the scattering of the counterions. From equation (13) the structural information of the counterion distribution surrounding the macroions can be obtained.

4 Results and discussion

4.1 Location of the phase boundary by light scattering

Fully dissociated sodium salts of polycarboxylates can be precipitated by addition of low amounts of an alkaline earth cation. The amount of alkaline earth cations $[M^{2+}]_c$ required for precipitation follows a linear relationship [9,12] with the polymer concentration expressed in terms of the molar concentration of anionic charges COO^- expressed as $[\text{NaPA}]_c$,

$$[M^{2+}]_c = m + r_0[\text{NaPA}]_c. \quad (14)$$

The intersection m corresponds to a lowest critical concentration threshold $[M^{2+}]_c$ necessary to precipitate the polyelectrolyte at infinite dilution. Beyond the threshold m , a slope r_0 points to a stoichiometric amount of M^{2+} per COO^- function, necessary to precipitate polycarboxylate chains. Addition of an inert salt increases the intersection m and gradually decreases [9,13] the slope r_0 . The latter effect was compatible with the recent findings [10] that the precipitates included a fraction of monovalent cations in addition to M^{2+} . This fraction obviously increases with increasing $[\text{NaCl}]$.

In a first step, a concentration regime close to the precipitation line of M^{2+} -PA has to be identified at a given inert salt level. This concentration regime was expected to provide the most significant conformational changes of the M^{2+} -PA chains. Identification of the appropriate concentration regime was performed by means of combined SLS and DLS. SLS yielded z -averaged radii of gyration R_g characterizing the geometric size of the shrinking coils. Supplementary DLS data led to a distribution of hydrodynamically effective radii and a z -averaged value R_h thereof. With a set of samples at varying $[M^{2+}]/[\text{NaPA}]$, the point with the minimum value in R_g was located and interpreted as the precipitation threshold. The threshold coordinates ($[M^{2+}]_c$, $[\text{NaPA}]_c$) were confirmed by DLS. As soon as aggregation sets in, SLS exhibited an increase of the apparent molar mass and DLS revealed a second particle fraction with an R_h value much larger than the one of the single chains.

For the system under investigation, the inert salt level was set to $[\text{NaCl}] = 0.01$ M. In order to evaluate the impact of cation variation within a homologous series, a comparative investigation was performed with Ca^{2+} , Sr^{2+} and Ba^{2+} added to PA2. All data are established along *route 1*. Results are summarized in Figure 1 and Table 3. Clearly, the phase boundaries lie on top of each other. A closer look reveals a slight decrease of the slope r_0 of equation (1) according to $\text{Ca}^{2+} > \text{Sr}^{2+} > \text{Ba}^{2+}$, which indicates that the larger the divalent earth alkaline cation is, the smaller is the stoichiometric amount of M^{2+} necessary

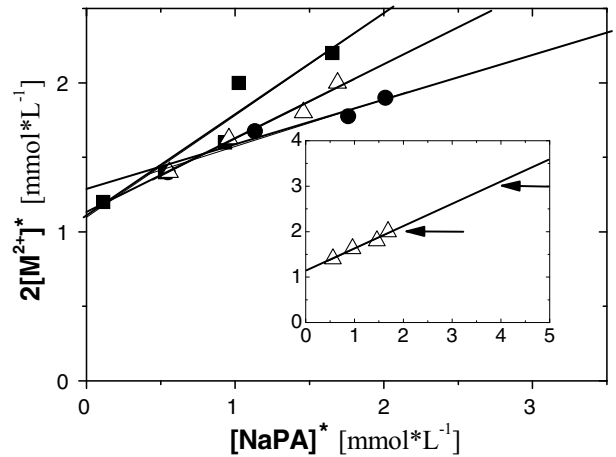


Fig. 1. Phase boundaries for three different earth alkaline cations in 0.01 M $[\text{NaCl}]$: Ca^{2+} (■); Sr^{2+} (△); Ba^{2+} (●). The polymer is PA2. For better clarity, the phase boundary of Sr^{2+} is shown by itself in the inset.

Table 3. Parameters of equation (1) for phase boundaries of the system PA2 with M^{2+} denoting earth alkaline cations at $T = 25^\circ\text{C}$.

$[\text{NaCl}]$ (M)	M^{2+}	m (mM)	r_0
0.01	Ca^{2+}	0.549	0.345
0.01	Sr^{2+}	0.563	0.249
0.01	Ba^{2+}	0.622	0.160

to precipitate NaPA. The trend is opposite to the observations of Pochard *et al.* [10] who found an increase of the amount of M^{2+} per COO^- groups required to precipitate NaPA if Ba^{2+} ions are used instead of Ca^{2+} .

Once the precipitation line with its adjoining one-phase regime was established, structural changes of dilute PA chains close to the precipitation threshold were characterized in a second step. Combined SLS and DLS, revealed a decrease of the radius of gyration R_g and the hydrodynamically effective radius R_h when the precipitation line is approached. From both radii, two dimensionless parameters can be calculated which are extremely valuable for the investigation of shape transformations along the shrinking process [13].

The first parameter α_s is the ratio of the radius of gyration R_g of any intermediate along the approach to the phase boundary and the radius of gyration $R_g(\Theta)$ under Θ -conditions. The value for $R_g(\Theta)$ was determined experimentally [5] in 1.5 M NaCl:

$$\alpha_s = R_g/R_g(\Theta). \quad (15)$$

This ratio quantifies the extent of expansion or shrinking of the intermediates in terms of the unperturbed chain. The second parameter ρ compares [46] the radius of gyration R_g of any intermediate along the approach to the phase boundary with the corresponding hydrodynamic radius R_h :

$$\rho = R_g/R_h. \quad (16)$$

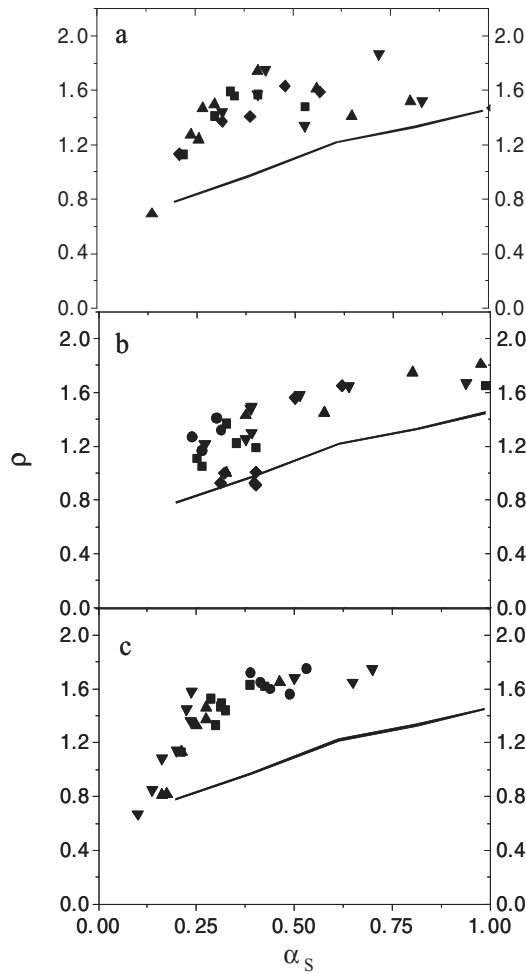


Fig. 2. ρ -ratios versus extent of shrinking α_s for three different earth alkaline cations: Ca^{2+} (a), Sr^{2+} (b) and Ba^{2+} (c). Different approaches to the phase boundary are denoted in panel a: $[\text{Ca}^{2+}] = 0.6 \text{ mmolL}^{-1}$ (\blacktriangle); $[\text{Ca}^{2+}] = 0.8 \text{ mmolL}^{-1}$ (\blacktriangledown); $[\text{Ca}^{2+}] = 1 \text{ mmolL}^{-1}$ (\blacklozenge); $[\text{Ca}^{2+}] = 0.7 \text{ mmolL}^{-1}$ (\blacktriangleleft); $[\text{NaPA}] = 0.803 \text{ mmolL}^{-1}$ (\bullet); panel b: $[\text{NaPA}] = 0.957 \text{ mmolL}^{-1}$ (\blacksquare); $[\text{NaPA}] = 0.559 \text{ mmolL}^{-1}$ (\bullet); $[\text{Sr}^{2+}] = 1.0 \text{ mmolL}^{-1}$ (\blacktriangledown); $[\text{NaPA}] = 0.9 \text{ mmolL}^{-1}$ (\blacktriangle); $[\text{NaPA}] = 1.5 \text{ mmolL}^{-1}$ of PA1 (\blacklozenge); panel c: $[\text{NaPA}] = 0.55 \text{ mmolL}^{-1}$ (\blacktriangle); $[\text{NaPA}] = 1.13 \text{ mmolL}^{-1}$ (\blacksquare); $[\text{NaPA}] = 1.76 \text{ mmolL}^{-1}$ (\bullet); $[\text{Ba}^{2+}] = 0.95 \text{ mmolL}^{-1}$ (\blacktriangledown). The curve represents the literature data for a coil-globule transition of neutral polymers below Θ -temperature [36]. Specification of $[\text{M}^{2+}]$ or $[\text{NaPA}]$ corresponds to *route 1* or to *route 2*, respectively [11]. Unless otherwise stated, PA2 was used as NaPA sample.

The ρ ratio is expected to be highly sensitive to the shape of the shrinking coil.

In a preceding paper [5], detailed molar-mass-dependent experiments with NaPA were performed at various inert salt levels. The resulting averages were $\rho = 1.84$ and $\rho = 1.53$ at $[\text{NaCl}] = 0.1 \text{ M}$ and $[\text{NaCl}] = 1.5 \text{ M}$, respectively. A similar drop in ρ was observed with neutral polymers when decreasing the solvent quality from good to Θ -conditions [47–49]. The small discrepancies in the absolute values may at least in part be due to the differ-

ent polydispersities. For the NaPA samples under present investigation, the ratio of the weight averaged and number averaged molar mass is $M_w/M_n = 1.2$ which is larger than the polydispersity of the investigated neutral polymers [47–49].

Specific interactions of M^{2+} ions with the carboxylate functions are expected to cause drastic changes in the conformation of NaPA chains, which have to be distinguished from the regular screening effects imposed by an inert salt [5]. Isolation of these specific interactions could be achieved by introducing the M^{2+} ions via replacing the corresponding amount of inert Na^+ ions at constant overall concentration of cationic charges. Thus, regular screening could be kept constant while inserting the specifically interacting M^{2+} ions.

As is outlined in Figure 2, results on the homologous series of M^{2+} in 0.01 M NaCl confirmed earlier findings [13] on Ca^{2+} . Constant ρ ratios were observed over a regime of shrinking of $1.0 > \alpha_s > 0.4$ for all three cations. Only when the shrinking ratios α_s dropped below 0.4 , the sphere limit of 0.77 was approached in a steep descent. In all three data sets of Figure 2 an additional curve is included. This curve corresponds to a plot derived from experimental data of poly-(N-isopropylacrylamide) (PNIPAM) in water [50]. At $T = 30.6 \text{ }^\circ\text{C}$, water is a Θ -solvent for PNIPAM and the resulting curve represents the collapse of a neutral-polymer chain if the Θ -point is crossed. The curve begins with $\rho = 1.5$ at $\alpha_s = 1$, gradually decreasing to a value of $\rho = 0.77$ at shrinking ratios close to $\alpha_s = 0.2$, which is compatible with a coil-to-sphere transition. PNIPAM thus provides an excellent reference system. This indicates a mechanism of NaPA coil shrinking in 0.01 M NaCl , which deviates from the mechanism for neutral PNIPAM in a Θ -solvent and which is independent of the type of alkaline earth cation in the first place. In principle, ρ values, which are independent of α_s over a large regime of shrinking down to $\alpha_s \sim 0.4$, are compatible with self-similar intermediates or increasingly anisotropic intermediates. In the latter case, the impact of shrinking on the value of ρ would be balanced by an increasing anisotropy. [51,52]

Unfortunately, data of the homologous series of M^{2+} under present investigation were of changeable quality. Data from Sr^{2+} ions scattered slightly more than those of Ca^{2+} (Figs. 2a and b). Barium as the largest cation in the row exhibited a trend (Fig. 2c) which was of even better quality than Ca^{2+} . Yet, SAXS experiments were only feasible at the K -edge of Sr^{2+} .

4.2 Total SAXS curves

In order to select appropriate solutions for SAXS experiments, three series of solutions of NaPA with Sr^{2+} were generated along approaches to the corresponding phase boundary. Approaches were performed with two different molecular weights (PA1 and PA2). Solutions where the collapse was not yet completed, *i.e.* where the limit of a spherical shape was not yet reached, were considered to be highly interesting shapes. Such shapes were signified

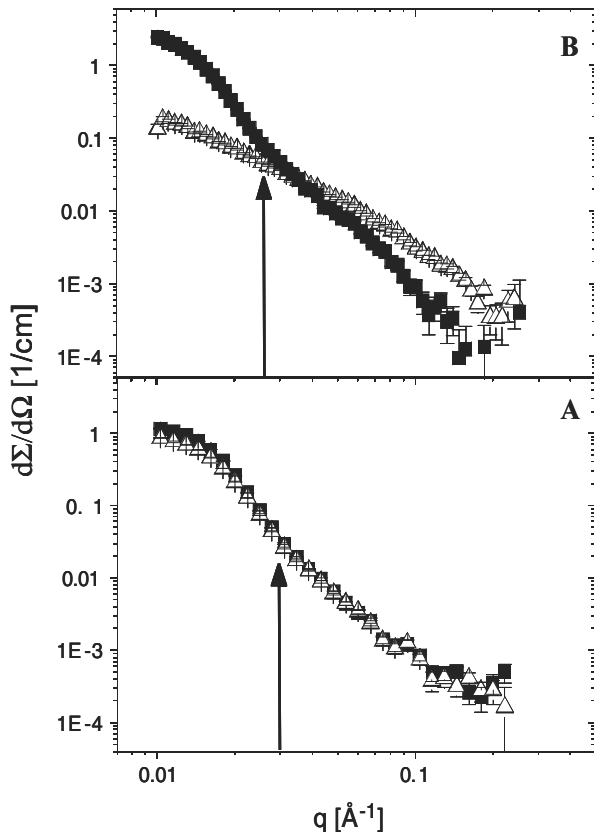


Fig. 3. Differential X-ray scattering cross-sections for series SAXS-2 (A) and SAXS-1 (B). All scattering curves stem from energies far apart from the absorption edge of Sr^{2+} corresponding to total scattering curves of the SrPA adducts. The symbols denote: SAXS-1A with $[\text{Sr}^{2+}]/[\text{NaPA}] = 0.46$ (■); SAXS-1B with $[\text{Sr}^{2+}]/[\text{NaPA}] = 0.42$ (△); SAXS-2A with $[\text{Sr}^{2+}]/[\text{NaPA}] = 0.667$ (■); SAXS-2B with $[\text{Sr}^{2+}]/[\text{NaPA}] = 0.651$ (△). Vertical arrows indicate estimates for q_{Min} used to calculate R according to equation (17).

by a large degree of shrinking, *i.e.* by values of α_s significantly smaller than 1.0 but with ρ values still larger than 1.0. In principle, both parameters were accessible by light scattering.

Figure 3A shows the SAXS curves of series SAXS-2 close to the phase boundary of PA2 with a molar mass of 3300 kDa. Both curves almost lie on top of each other. They exhibit a shoulder bordering a steep descent which can be well described by a power law according to Porod [53]. This is a characteristic feature of compact objects with smooth surfaces. Interpretation in terms of spherical particles is at hand. A shallow kink can be discerned at $q_{\text{Min}} = 0.3 \text{ nm}^{-1}$, which may correspond to the first minimum of the particle scattering factor of a sphere [16], blurred by polydispersity effects and irregularities in shape. Using the well-known relationship

$$R = 3\pi/2q_{\text{Min}}, \quad (17)$$

a sphere radius $R = 15.7 \text{ nm}$ can be estimated for both intermediates [16,54]. This value has to be compared with the radii of gyration $R_g = 22.2 \text{ nm}$ and 31.2 nm and

the hydrodynamically effective radii R_h of 18.2 nm and 21.1 nm, respectively, which characterize the overall size of the polymer chains. Noticeably, hydrodynamic radii as well as radii of gyration are larger than the estimated sphere radius thus indicating particles with larger overall dimensions than the spherical element revealed by the SAXS curves.

A further series of solutions was selected from sample PA1 with a molar mass of 950 kDa denoted SAXS-1. The series SAXS-1 includes the total SAXS curves of two concentrations. Sample properties from both selected concentrations are summarized in Table 1. Both SAXS curves were recorded [23] at the energy of 15.507 keV and are shown in Figure 3B. Unlike sample PA2, the comparison of the two curves of sample PA1 indicates striking differences between the corresponding shapes.

In the solution SAXS-1B, the scattering curve follows a power law close to $I_0(q, E_1) \sim q^{-2}$, typical for a structure with a Gaussian density profile. The latter profile has been well established for flexible polymer coils. The solution SAXS-1A shows a much steeper descent. As in the case of series SAXS-2 (sample PA2), a decay close to a q^{-4} power law suggests a structure with a sharp surface. A value of $q_{\text{Min}} = 0.25 \text{ nm}^{-1}$ for SAXS-1A (Fig. 3B) inserted in equation (17) yields a value of $R = 19.0 \text{ nm}$. The differences observed for the two solutions SAXS-1A and -1B are in line with the anticipated shrinking process. In SAXS-1B, the ratio $[\text{Sr}^{2+}]/[\text{NaPA}]$ is lower than in SAXS-1A which locates SAXS-1A closer to the phase boundary. As expected, the estimated size of 19 nm is in agreement with the pearl size extracted from the resonant part in a preceding work [23].

At this point, we have to stress two drawbacks of the preceding experiments [23]: i) radii of gyration measured by LS exhibit uncertainties which significantly exceed 10% once they approach values of 20 nm; ii) characterisation by LS was performed a few days before the ASAXS experiment and slight changes between LS and ASAXS experiments cannot be fully excluded.

In order to consider these drawbacks and to put the findings on a broader base, four additional intermediate states were generated with PA1 in series ASAXS-1 and investigated at three different energies. This time, the selected concentrations were characterised by means of LS prior to and after the SAXS and ASAXS experiments. Crude interpretation of the respective total scattering curves at $E = 15507 \text{ keV}$ with equation (17) and $q_{\text{Min}} \approx 0.3 \text{ nm}^{-1}$ in all four cases led to R close to 16 nm. As with series SAXS-2, the respective size is significantly smaller than the overall size of the polyelectrolyte chains estimated by light scattering (Table 4).

4.3 ASAXS at the phase boundary

In the case of series ASAXS-1, separation of the pure-resonant curves could be successfully carried out. The pure-resonant curves can unambiguously be attributed to the Sr^{2+} counterions. Figure 4 compares the total scattering curves with the corresponding mixed resonant or

Table 4. Size parameters of series ASAXS-1. Radii of gyration R_g and hydrodynamic radii stem from light scattering experiments prior to (1) and after (2) ASAXS experiments. The radius R_z corresponds to the averaged outer sphere radius extracted from curve fitting with equation (18). All radii are given in nm. All experiments were performed at $[\text{Sr}^{2+}] = 1.5 \text{ mM}$.

Solution	$[\text{Sr}^{2+}]/[\text{NaPA}]$	$R_g(1)$	$R_h(1)$	$R_g(2)$	$q_{\text{Min}} (\text{nm}^{-1})$	R_z
ASAXS-1A	0.464	17.3	19.3	24.4	0.38	16
ASAXS-1B	0.458	23.2	23.2	23.0	0.33	15
ASAXS-1C	0.4575	21.3	21	24.0	0.32	15
ASAXS-1D	0.451	30.7	25.2	30.7	0.33	15

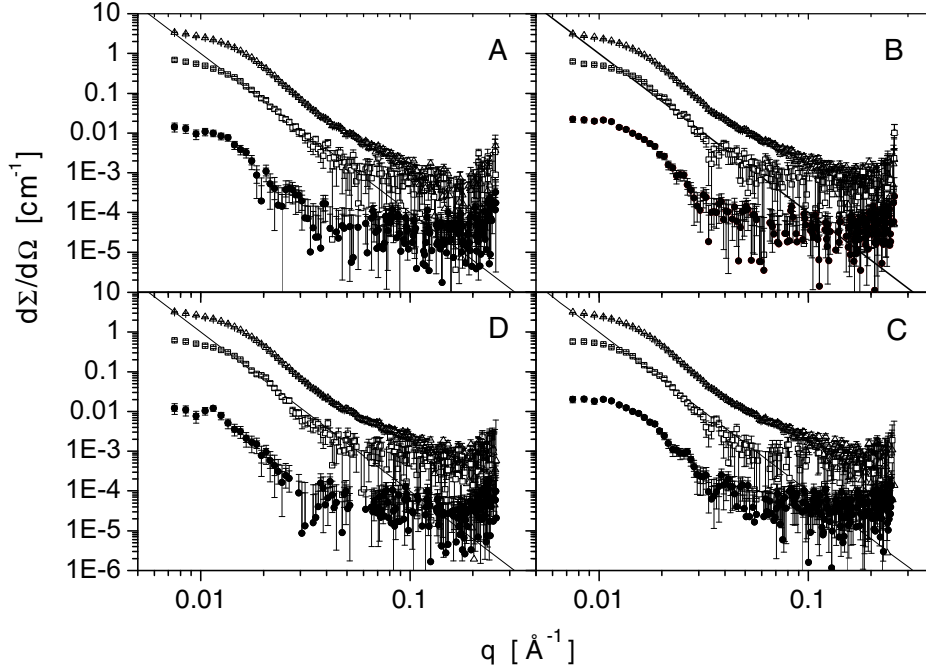


Fig. 4. SAXS and ASAXS measurements of the series ASAXS-1 on sample PA1 with $[\text{Sr}^{2+}] = 1.5 \text{ mM}$ at variable ratio $[\text{Sr}^{2+}]/[\text{NaPA}]$. (A) $[\text{Sr}^{2+}]/[\text{NaPA}] = 0.464$; (B) $[\text{Sr}^{2+}]/[\text{NaPA}] = 0.458$; (C) $[\text{Sr}^{2+}]/[\text{NaPA}] = 0.4575$; (D) $[\text{Sr}^{2+}]/[\text{NaPA}] = 0.451$. The symbols denote (□) total scattering from the polymer and the Sr^{2+} ions at $E = 15.507 \text{ keV}$; (△) mixed resonant curve according to equation (12); (●) form factor of the Sr^{2+} ions according to equation (13). The solid line indicates a q^{-4} power law typical for compact solid particles with smooth surfaces.

separated scattering curves (Eq. (12)) and the form factor of the pure-resonant curves (Eq. (13)). Qualitatively speaking, the trends of all three curves are similar confirming our expectation that the Sr counterions densely stick to the polyanionic chains thus reflecting essential features of the chain structure.

In order to interpret the pure-resonant curves, model fits were performed with theoretical curves for polydisperse spheres

$$S_{\text{Ion}}(q) = \text{const} \int_0^{\infty} P(M) \cdot \left(\frac{4\pi R^3}{3} \frac{3(\sin(qR) - qR \cos(qR))}{(qR)^3} \right)^2 \cdot dR. \quad (18)$$

The bracket in the integral contains the form factor of a single sphere of size R [54]. Polydispersity was considered

by means of a Schulz-Flory type of distribution $P(M)$ [55],

$$P(M) = \left(\frac{z+1}{M_w} \right)^{z+1} \frac{M^z}{\Gamma(z+1)} \exp\left(-\frac{(z+1)M}{M_w} \right). \quad (19)$$

The particle mass M in equations (18) and (19) is proportional to R^3 . Polydispersity is fixed by $z = 1/(M_w/M_n - 1)$ with M_w and M_n the weight averaged and number averaged particle mass and R_z is the mean radius of the spheres calculated from the z -averaged radius of gyration according to $R_z^2 = R_g^2/3$. As is demonstrated in Figure 5 for ASAXS-1B and ASAXS-1C, the resulting curves satisfactorily describe the experiments. Values for R_z are summarized in Table 4. All R_z values lie close to the results obtained with q_{Min} in equation (17) and are significantly smaller than the overall size of the collapsing chains. This clearly supports the fact that the objects indicated by the total scattering curves and by the pure-resonant curves

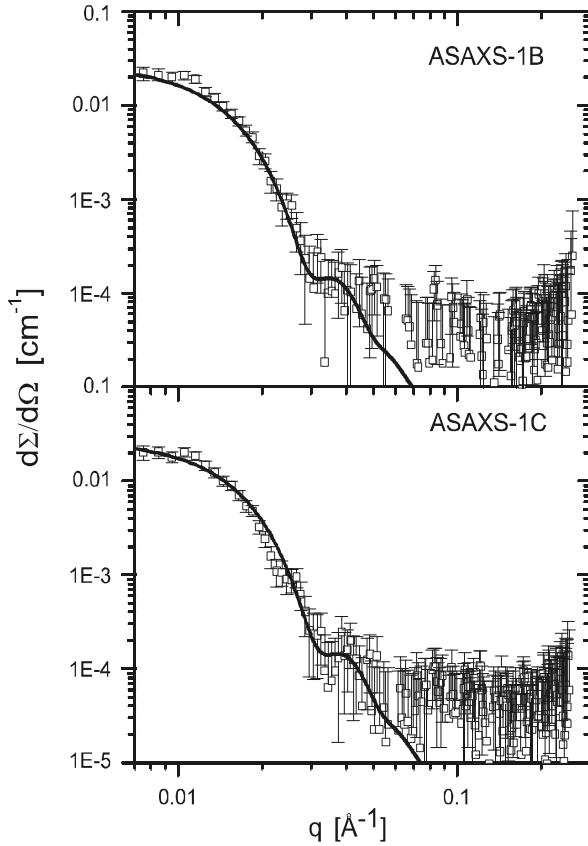


Fig. 5. Form factor of the Sr^{2+} ions according to equation (13) corresponding to the pure-resonant curve for samples ASAXS-1B (top) and ASAXS-1C (bottom). The theoretical curve is a model fit with a polydisperse sphere based on equations (18) and (19) with $z = 5$ and $R_z = 15$ nm.

correspond to spherical sub-particles formed within the larger PA chains.

In order to further support this statement, experimental scattering curves shall be described with particle scattering factors which are capable to reproduce the trend of scattering curves and at the same time are consistent with particle size values established by light scattering. The latter condition requires particle sizes which are significantly larger than the size from the fit with model spheres. To this end we used the model of a dumb-bell as the shortest representative for pearl necklace chains [16]. The same concept has already been applied to SANS data on the same system [14].

This goal was achieved by using 16 nm for the pearl size in the first place and by applying a distance $A = 40$ nm between two connected pearls which results in a radius of gyration identical to the one provided by light scattering. Although this procedure has been applied to all four solutions, we confined explicit representation to ASAXS-1B and ASAXS-1C because results are essentially the same in all four cases. As is clearly demonstrated by Figure 6, the theoretical curve of a monodisperse dumb-bell correctly reproduces the section between $0.07 \text{ nm}^{-1} < q < 0.2 \text{ nm}^{-1}$. At higher q the theoretical

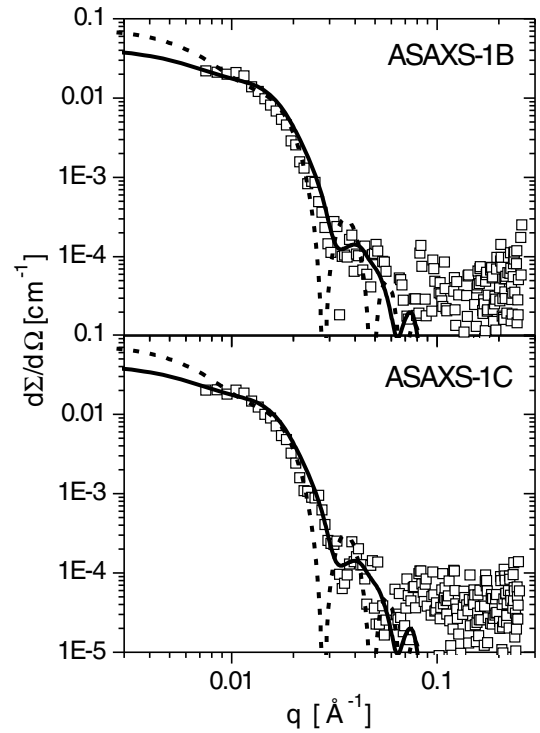


Fig. 6. Form factor of the Sr^{2+} ions according to equation (13) corresponding to the pure-resonant curve for samples ASAXS-1B (top) and ASAXS-1C (bottom). The two theoretical curves are model curves of a dumb-bell with pearl size $R = 16$ nm and a pearl-to-pearl distance $A = 40$ nm leading to an overall size of $R_g = 23.6$ nm (---) and of a mixture of monodisperse spheres (weighting factor 0.4) with monodisperse dumb-bells with a pearl size $R = 12.7$ nm and a pearl-to-pearl distance $A = 50$ nm leading to an overall size of $R_g = 22.1$ nm (—).

curve exhibits sharp minima caused by the regular spherical pearls, which are smeared in the real system due to shape irregularities and a polydispersity of the sphere size.

Significant improvement is achieved if the dumb-bell is mixed with spheres. In the examples of Figure 6, this is performed by mixing a monodisperse dumb-bell with a monodisperse sphere. The pearl size in the dumb-bell was set to $R = 12.7$ nm and its distance to the neighbouring pearl to $A = 50$ nm. The size of the sphere was chosen to be $R = 16$ nm resulting in the same volume as the dumb-bell. Weighting factors of the scattering curves of the dumb-bells and spheres were 0.6 and 0.4, respectively. This composition, together with the pearl distance A was selected to yield a radius of gyration in line with the light scattering results from the respective concentrations. Although the theoretical curves deviate slightly more in the intermediate regime of $q = 0.2 \text{ nm}^{-1}$ a qualitative description of the experiment is now extended to $q = 0.5 \text{ nm}^{-1}$, covering a regime of $0.07 \text{ nm}^{-1} < q < 0.5 \text{ nm}^{-1}$.

In a final attempt, monodisperse dumb-bells are mixed with a polydisperse spherical component. Similar mixtures were found already by Limbach and Holm with computer simulations [15]. The z -averaged radius of gyration of the

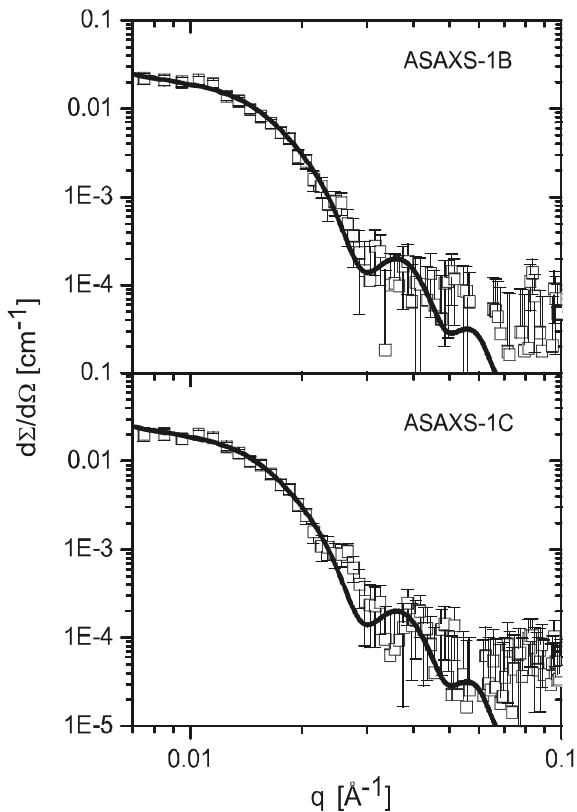


Fig. 7. Form factor of the Sr^{2+} ions according to equation (13) corresponding to the pure-resonant curve for samples ASAXS-1B (top) and ASAXS-1C (bottom). The theoretical curve is a model curve of a polydisperse sphere based on equations (18) and (19) with $z = 5$, $R_g = 12.4$ nm and $R_z = 16$ nm (weighting factor 0.5) mixed with a monodisperse dumb-bell (weighting factor 0.5) with a pearl size $R = 16$ nm and a pearl-to-pearl distance $A = 55$ nm leading to an averaged particle size of $R_g = 23$ nm.

spheres is $R_g = 12.4$ nm. This R_g value corresponds to an averaged value of the sphere radius $R_z = 16$ nm. The polydispersity is determined by $z = 5$. Pearl size R and pearl distance A in the dumb-bell are 16 nm and 55 nm, respectively. In calculating the total scattering curve, both component scattering curves are weighted with 0.5. Again weight factors and pearl distance A are selected to reproduce the correct overall size of the particles predetermined by light scattering. In comparison to the binary system with monodisperse components, the theoretical curves based on a polydisperse spherical component improve the description in the intermediate regime. Thus, a description of persisting quality is provided, now over the extended regime of $0.07 \text{ nm}^{-1} < q < 0.5 \text{ nm}^{-1}$ (Figure 7).

Real fits with model mixtures have been deliberately avoided in the above-described procedure for the following reasons: Aside from pearl size and pearl distance, additional parameters like the composition of multi-component structures, size polydispersity and shape irregularities have an influence on the system. The fact that experimental curves start at a q value

which is too high to include the essential aspects of the overall shape [16] renders such a fit almost useless. However, SAXS and ASAXS curves provide several interesting features of the collapsing polyacrylate chains: i) condensation leads to dense structures with spherical (sub-)particles; ii) SAXS and ASAXS provide an indirect indication of the existence of an elongated second component explaining the large overall particle size. Such a component may be a pearl necklace structure. Possibly the form factor of the pure-resonant scattering, indicates a higher correlated structure, which is suggested from a small correlation maximum at 0.01 \AA^{-1} and the shoulders in the q -range between 0.02 and 0.03 \AA^{-1} (Fig. 4).

5 Summary

The present work extends earlier findings [13] of the phase behaviour of NaPA chains in the presence of various amounts of Ca^{2+} cations and conformational changes of those chains in the proximity of the phase boundary. Extension considers Sr and Ba cations making accessible a comparison of precipitation thresholds in 0.01 M NaCl following equation (14). Although the phase boundaries lie on top of each other, the amount of M^{2+} required to precipitate the PA chains slightly decrease along $\text{Ca}^{2+} > \text{Sr}^{2+} > \text{Ba}^{2+}$. Light scattering at these phase boundaries lead to normalised plots of the dimensionless size parameters ρ versus α which exhibit the same trend for all three cations. This common trend suggests an anisotropic shape over a large regime of shrinking turning abruptly to a compact sphere at the respective phase boundary. At the same time light scattering enabled selection of intermediates for SAXS and ASAXS experiments.

We succeeded to separate the pure-resonant curves for a series of samples with varying ratio $[\text{Sr}^{2+}]/[\text{NaPA}]$ from energy-dependent scattering experiments. Results from this separation fully confirmed the expectation, that the specifically interacting Sr^{2+} counterions adopt a similar spatial distribution as the monomer segments. All but one of the SAXS curves reflecting total scattering exhibited a steep descent and a shallow kink, located at a momentum transfer denoted as q_{Min} . Under the assumption that this feature can be attributed to compact spherical structures with a finite polydispersity, the following feature appears for most of the solutions under investigation. Size parameters extracted from SAXS and ASAXS are smaller than the overall size of the corresponding polyacrylate chains. A simple explanation of this difference in size is that SAXS and ASAXS refer to substructures rather than the overall size. As anticipated in the theory [15], one way to realize substructures is the (partial) formation of pearl-necklace-like particles as possible intermediates in the vicinity of the precipitation threshold. These arguments are supported by a successful description of experimental scattering curves by means of model mixtures of spheres and dumb-bells. These mixtures reproduce the separated ASAXS curves as well as spheres do but at the same time they also result in the correct overall size values of the particles.

Finally, pure-resonant scattering ASAXS curves of Sr^{2+} ions could successfully be isolated, in line with an earlier attempt on the same system [23]. These curves indicate a high degree of condensation of the Sr^{2+} ions on length scales related to PA chains which are also present in the same solution. The curves clearly demonstrate that ASAXS can be used to reflect the essential features of a collapsing PA chain if decoration with Sr^{2+} ions can be achieved.

Financial support of the Deutsche Forschungsgemeinschaft, Schwerpunktprogramm "Polyelektrolyte mit definierter Molekülarchitektur" SPP 1009, is gratefully acknowledged.

References

- P.J. Flory, J.E. Osterheld, *J. Phys. Chem.* **58**, 653 (1954).
- P. Flory, *Principles of Polymer Chemistry* (Cornell University Press, Ithaca, 1953).
- A. Takahashi, S. Yamori, I. Kagawa, *Kogyo Kagaku Zasshi* **83**, 11 (1962).
- A. Takahashi, M. Nagasawa, *J. Am. Chem. Soc.* **86**, 543 (1964).
- R. Schweins, J. Hollmann, K. Huber, *Polymer* **44**, 7131 (2003).
- C.G. Sinn, R. Dimova, M. Antonietti, *Macromolecules* **37**, 3444 (2004).
- F. Molnar, J. Rieger, *Langmuir* **21**, 786 (2005).
- A. Ikegami, N. Imai, *J. Polym. Sci.* **56**, 133 (1962).
- I.J. Michaeli, *Polym. Sci.* **48**, 291 (1960).
- I. Pochard, A. Foissy, P. Couchot, *Colloid Polym. Sci.* **277**, 818 (1999).
- I. Sabbagh, M. Delsanti, P. Lesieur, *Eur. Phys. J. B* **12**, 253 (1999).
- K. Huber, *J. Phys. Chem.* **97**, 9825 (1993).
- R. Schweins, K. Huber, *Eur. Phys. J. E* **5**, 117 (2001).
- R. Schweins, P. Lindner, K. Huber, *Macromolecules* **36**, 9564 (2003).
- H.J. Limbach, Ch. Holm, *J. Phys. Chem. B* **107**, 8041 (2003).
- R. Schweins, K. Huber, *Macromol. Symp.* **211**, 25 (2004).
- M.-J. Lee, M.M. Green, F. Mikes, H. Morawetz, *Macromolecules* **35**, 4216 (2002).
- D. Baigl, M. Sferrazza, C.E. Williams, *Europhys. Lett.* **62**, 110 (2003).
- W. Essafi, F. Lafuma, C.E. Williams, *J. Phys. II* **5**, 1269 (1995).
- D. Baigl, D. Ober, A. Qu, A. Fery, C.E. Williams, *Europhys. Lett.* **62**, 588 (2003).
- C. Heitz, M. Rawiso, J. Francois, *Polymer* **40**, 1637 (1999).
- C. Heitz, J. Francois, *Polymer* **40**, 3331 (1999).
- G. Goerigk, R. Schweins, K. Huber, M. Ballauff, *Europhys. Lett.* **66**, 331 (2004).
- V.O. Aseyev, S.I. Klenin, H. Tenhu, I. Grillo, E. Geissler, *Macromolecules* **34**, 3706 (2001).
- E. Dubois, F. Boué, *Macromolecules* **34**, 3684 (2001).
- J. Combet, F. Isel, F. Rawiso, *Macromolecules* **38**, 7456 (2005).
- S. Minko, A. Kiriy, G. Gorodyska, M. Stamm, *J. Am. Chem. Soc.* **124**, 10192 (2002).
- Y. Kantor, M. Kardar, *Europhys. Lett.* **27**, 643 (1994).
- A.V. Dobrynin, M. Rubinstein, S.P. Obukhov, *Macromolecules* **29**, 2974 (1996).
- H. Schiessel, *Macromolecules* **32**, 5673 (1999).
- S. Uyaver, Ch. Seidel, *J. Phys. Chem. B* **198**, 18804 (2004).
- H.B. Stuhmann, *Adv. Polym. Sci.* **67**, 123 (1985).
- Q. de Robilliard, X. Guo, N. Dingenouts, M. Ballauff, G. Goerigk, *Macromol. Symp.* **164**, 81 (2001).
- B. Guillaume, M. Ballauff, G. Goerigk, M. Wittemann, M. Rehahn, *Colloid Polym. Sci.* **279**, 829 (2001).
- B. Guillaume, J. Blaul, M. Ballauff, M. Wittemann, M. Rehahn, G. Goerigk, *Eur. Phys. J. E* **8**, 299 (2002).
- M. Patel, S. Rosenfeldt, M. Ballauff, N. Dingenouts, D. Pontoni, T. Narayanan, *Phys. Chem. Chem. Phys.* **6**, 2962 (2004).
- N. Dingenouts, M. Patel, S. Rosenfeldt, D. Pontoni, M. Ballauff, T. Narayanan, *Macromolecules* **37**, 8152 (2004).
- J. Bolze, M. Ballauff, T. Rische, D. Rudhardt, J. Meixner, *Macromol. Chem. Phys.* **205**, 165 (2004).
- D.E. Koppel, *J. Phys. Chem.* **57**, 4814 (1972).
- S.W. Provencher, *Comput. Phys. Commun.* **27**, 213; 229 (1982).
- H.-G. Haubold, K. Gruenhagen, M. Wagener, H. Jungbluth, H. Heer, A. Pfeil, H. Rongen, G. Brandenburg, R. Moeller, J. Matzerath, P. Hiller, H. Halling, *Rev. Sci. Instrum.* **60**, 1943 (1989).
- D.T. Cromer, D. Liberman, *J. Chem. Phys.* **53**, 1891 (1970).
- D.T. Cromer, D. Liberman, *Acta Crystallogr. Sect. A* **37**, 267 (1981).
- G. Goerigk, D.L. Williamson, *J. Appl. Phys.* **99**, 084309 (2006).
- O. Glatter, O. Kratky (Editors), *Small Angle X-ray Scattering* (Academic Press, London, 1982).
- W. Burchard, *Adv. Polym. Sci.* **48**, 1 (1983).
- J.S. Vrentas, H.T. Liu, J.C. Duda, *J. Polym. Sci., Polym. Phys. Ed.* **18**, 633 (1980).
- M. Schmidt, W. Burchard, *Macromolecules* **14**, 210 (1981).
- K. Huber, W. Burchard, A.Z. Akcasu, *Macromolecules* **18**, 2743 (1985).
- C. Wu, S. Zhou, *Macromolecules* **28**, 5388; 8381 (1995).
- W. Burchard, M. Schmidt, W.H. Stockmayer, *Macromolecules* **13**, 580; 1265 (1980).
- W. Burchard, M. Frank, E. Michel, *Ber. Bunsenges. Phys. Chem.* **100**, 807 (1996).
- G. Porod, *Kolloid Z.* **124**, 83 (1951).
- Lord Rayleigh, *Proc. R. Soc. London, Ser. A* **90**, 219 (1914).
- B. Zimm, *J. Chem. Phys.* **16**, 1099 (1978).

[S8]

Z. Varga, A. Bota, and G. Goerigk,

*Localization of Dibromophenol in DPPC/Water Liposomes Studied by
Anomalous Small-Angle X-ray Scattering*

J. Phys. Chem. B, Vol. 110, No. 23, 11029- 11032 (2006)

Localization of Dibromophenol in DPPC/Water Liposomes Studied by Anomalous Small-Angle X-ray Scattering

Zoltán Varga,[†] Attila Bóta,^{*,†} and Günter Goerigk[‡]

Institute of Physical Chemistry, Budapest University of Technology and Economics, Műegyetem rkp 3, H-1521 Budapest, Hungary, and Institute of Solid State Physics, Research Centre Jülich, D-52425 Jülich, Germany

Received: March 21, 2006; In Final Form: April 27, 2006

The localization of 2,4-dibromophenol molecules along the bilayer normal was investigated by anomalous small-angle X-ray scattering (ASAXS) with synchrotron radiation. The ASAXS measurements, executed at three different energies, provide the separation of the scattering of the bromine atoms of dibromophenol molecules from that of the whole system. Using a full q -range model, the localization of the dibromophenol molecules was characterized at a lower (0.1) and a higher (1) dibromophenol/lipid molar ratio corresponding to the gel and to the interdigitated phases of the vesicle matrix, respectively.

Introduction

In recent years, the effect of brominated phenol compounds on living organisms has become a field of interest.^{1–7} It is known that bromophenols are present in a wide range of different kinds of environment. For example, these chemicals occur in sponges and algae and also in other marine organisms, and they can be found in the blood of fishes and mammals, too.

The ecological role of these molecules is still not clear, but it has been shown that they have hormone-like effects and disrupt the cellular Ca^{2+} homeostasis in endocrine cells.^{6,7} Recently, the importance of the elucidation of the brominated phenols' effect has been increased not only by their natural occurrence in the organisms but also by their industrial application as fungicides and flame retardants (e.g., 2,4,6-tribromophenol, tetrabromobisphenol A). These brominated contaminants act on basic cellular functions via complex interactions, which depend on many parameters; thus, it is worth examining the effect of bromophenols on separated components of the real cells. Consequently, vesicles (or liposomes) are frequently used as model membranes to study the effect of guest molecules on biological membranes.

In this paper, the localization of 2,4-dibromophenol in a multilamellar vesicle system constituted from 1,2-dipalmitoyl-*sn*-glycero-3-phosphatidylcholine (DPPC) and water is studied at 0.1 and 1 DBP/DPPC molar ratios. It was previously reported that the accumulation of lipophilic compounds like dichlorophenols causes lateral heterogeneity and cluster formation in the double lipid layers.^{8,9} Presumably, the localizations of the dichloro- and dibromophenol molecules in the vesicle system are the same because of their similar chemical behavior.¹⁰ We have studied the distribution of DBP molecules in vesicles with the anomalous small-angle X-ray scattering (ASAXS) method, which proved to be an excellent technique to determine the localization of atoms/molecules in a surrounding media. In other

words, by using ASAXS one can overcome the problem of separating the small-angle scattering of the guest molecules from that of the whole system. The basis of the method is the energy dependency of the scattering factors of the atoms, which are complex quantities and show a strong variation with the X-ray energy in the vicinity of the absorption edge of the atom under consideration, which is the bromine in our case.

Experimental Section

The method of anomalous small-angle X-ray scattering has been used in a great variety of fields, e.g., in the study of alloys,¹¹ examining thin films of electrocatalysts,¹² protein research,^{13,14} and describing the distribution of counterions around macroions and polyacrylate chains.^{15–17} In the latter paper, a method was introduced to separate the scattering of the guest atoms from that of the whole system. Hereinafter, this method will be reviewed with the specification for radially ordered systems.

From the small-angle X-ray scattering's point of view, a multilamellar vesicle can be considered as a stack of layers averaged over all orientations in the three-dimensional space; consequently, the scattered intensity can be expressed as

$$I(q) = S(q)|F(q)|^2/q^2 \quad (1)$$

where q denotes the magnitude of the scattering variable, $q = 4\pi \sin \theta/\lambda$; $F(q)$ is the bilayer form factor, and $S(q)$ is the structure factor of the layers.^{18,22,23} $S(q)$ represents the contribution of the layer structure, while $F(q)$ is the Fourier transform of the bilayer electron density (ED) profile.

Generally, the form factor of a bilayer with additive guest atoms can be written as $F(q) = F^{\text{vesicle}}(q) + F^{\text{guest}}(q)$ where

$$F^{\text{vesicle}}(q) = \int_{-d/2}^{d/2} \Delta\rho^{\text{vesicle}}(z) \cdot e^{-iqz} dz$$
$$F^{\text{guest}}(q) = \int_{-d/2}^{d/2} \Delta\rho^{\text{guest}}(z) \cdot e^{-iqz} dz \quad (2)$$

Here, d is the bilayer repeating unit, and $\Delta\rho^{\text{vesicle}}(z)$ and

* To whom correspondence may be addressed. Tel.: +36 1 463 2473. Fax: +36 1 463 3767. E-mail: abota@mail.bme.hu.

[†] Budapest University of Technology and Economics.

[‡] Research Centre Jülich.

$\Delta\rho^{\text{guest}}(z)$ are the average excess electron densities of the lipid layers and the guest molecules along the bilayer normal

$$\Delta\rho^{\text{vesicle}}(z) = (f_{\text{lipid}}' - \rho^{\text{water}}V^{\text{lipid}})u(z)$$

$$\Delta\rho^{\text{guest}}(z) = [(f_{0,\text{guest}}' - \rho^{\text{water}}V^{\text{guest}}) + if_{\text{guest}}''(E)]v(z) \quad (3)$$

Here, ρ^{water} is the electron density of the solvent; V^{lipid} and V^{guest} are the volumes of the lipid layers and the guest molecules, while $u(z)$ and $v(z)$ are the radial average of the particle densities of lipids and guest molecules. For the sake of simplicity in the following, we will denote f_{guest}' and f_{guest}'' with f' and f'' , respectively, since we only have to consider the anomalous dispersion corrections of the guest molecules, or more precisely of their resonant atoms. The molecular scattering factor of lipids, f_{lipid} , is nearly energy-independent, but that of the atoms of the guest molecules shows a strong variation with the energy in the vicinity of the absorption edge of the atom under consideration.

With the introduced quantities, one can rewrite the form factor of the system as a sum of a resonant, energy-dependent, and a nonresonant, energy-independent term: $F(q) = U(q) + (f'(E) + if''(E))V(q)$, where $V(q) = \int v(z) \exp(-iqz) dz$ is the geometrical part of the form factor of the bromine atoms of the bromophenol molecules. Then, the measured intensity can be calculated as follows:

$$I(q, E) = \{U^2(q) + 2f'(E)U(q)V(q) + [f'^2(E) + f''^2(E)]V^2(q)\} \frac{S(q)}{q^2} \quad (4)$$

From this, the difference of two scattering curves, measured at two different energies, will be the following:

$$\Delta I(q, E_1, E_2) = \{2[f'(E_1) - f'(E_2)]U(q)V(q) + [f'^2(E_1) - f'^2(E_2) + f''^2(E_1) - f''^2(E_2)]V^2(q)\} \frac{S(q)}{q^2} \quad (5)$$

To eliminate the mixed term, a measurement at a third different energy should be performed, and the separated scattering of bromine atoms can be expressed as follows:

$$V^2(q) \frac{S(q)}{q^2} = \frac{1}{C(E_1, E_2, E_3)} \left[\frac{\Delta I(q, E_1, E_2)}{f'(E_1) - f'(E_2)} - \frac{\Delta I(q, E_1, E_3)}{f'(E_3) - f'(E_2)} \right]$$

$$C(E_1, E_2, E_3) = f'(E_2) - f'(E_3) + \frac{f''^2(E_1) - f''^2(E_2)}{f'(E_1) - f'(E_2)} - \frac{f''^2(E_1) - f''^2(E_3)}{f'(E_1) - f'(E_3)} \quad (6)$$

According to eq 6, with ASAXS technique one can access the scattering of the guest atoms, so the distribution of these molecules in the vesicles can be directly observed.

Sample Preparation. Synthetic high-purity 1,2-dipalmitoyl-*sn*-glycero-3-phosphatidylcholine (DPPC) and 2,4-dibromophenol (DBP) were obtained from Avanti Polar Lipids (U.S.A.) and from Sigma (Germany), respectively. The pure DPPC without further purification was mixed with crystallized DBP in conformity with the different DBP/DPPC ratios, and then, deionized, triple quartz-distilled water was added to the system to gain a lipid concentration of 20 w/w %. The mixtures were

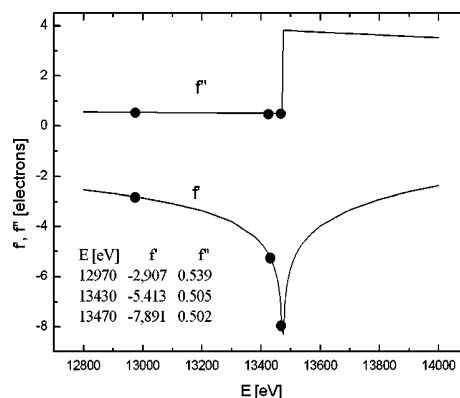


Figure 1. Anomalous dispersion corrections for bromine obtained by Cromer–Liberman calculations.^{20,21}

kept at 45 °C and vortexed intensively, then quenched to 4 °C. This process was repeated 40 times to get a homogeneous liposome system. The X-ray measurements were performed using Plexiglas-walled (without significant small-angle scattering) sample holders; for precise incubation, thin water flow in front of the walls was used.

ASAXS Experiments. Anomalous small-angle X-ray scattering (ASAXS) measurements were carried out at the Jusifa (B1) beamline¹⁹ at HASYLAB (DESY, Hamburg) in the scattering variable ($q = 4\pi \sin \theta/\lambda$) regime of 0.02–0.4 Å⁻¹. The measurements were made with a two-dimensional detector, at the energies 12 970, 13 434, and 13 470 eV, close to the absorption edge of bromine at 13 474 eV. These energies were chosen on the basis of an absorption measurement on DBP crystal. The net scattering data collected at different energies were computed to the same abscissa, normalized to the primary beam intensity, and corrected for transmission. Finally, the scattering curves have been calibrated to absolute units of macroscopic cross sections (e.u./nm³). For data evaluation, the anomalous dispersion corrections of Br were calculated according to Cromer and Liberman^{20,21} (Figure 1). The values of f' and f'' at the energies used are also shown in Figure 1.

Results and Discussion

By dispersing DPPC molecules in water, centrosymmetric multilamellar vesicles are formed spontaneously. According to the one-dimensional order (in radial direction), the scattering pattern of the system exhibits at least five Bragg peaks. In the case of the DPPC/water system doped with DBP molecules, depending on the concentration, the regular structure is damaged, but the periodicity is still present. As a result of the guest molecules, only two Bragg reflections can be observed on the scattering patterns. In Figure 2, scattering curves of the systems with 0.1 and 1 DBP/DPPC molar ratios are shown. All the measurements were carried out at $T = 20$ °C, which corresponds to the nonrippled gel phase (L_{β}') of the pure DPPC/water system. The squares denote the total scattering of the system measured at 12 970 eV, the farthest energy from the absorption edge of bromine (there is almost no anomalous effect from DBP molecules at this energy). Comparing the total scattering curves, one can identify drastic changes, which originate in the different phases of the systems induced by the different ratios of DBP molecules. At the lower concentration, DBP has a perturbation effect on the correlation of lamellae. The average periodicity (d) is 67.8 Å, which is larger than that of the regular nonrippled gel phase (64.2 Å). At higher concentration, the interdigitated form of the gel phase has appeared, as it can be recognized from the $d = 50.7$ Å repeating distance. In that phase, the

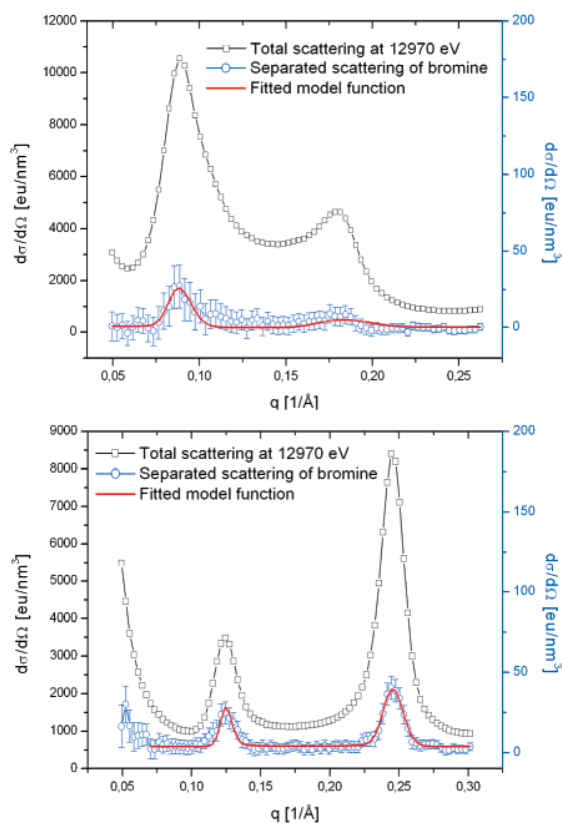


Figure 2. ASAXS measurements of DBP/DPPC systems at 0.1 (top) and 1 (bottom) molar ratios. Left ordinate belongs to the total scattering curves; right ordinate belongs to separated scattering curves from bromine atoms of DBP molecules.

hydrocarbon chains of the two lipid layers are fused, making it possible to form tighter packing. The ratios of the maximal intensities of the Bragg peaks are also different in the cases of the two DBP concentrations as a consequence of the changes in the radial electron densities of the bilayers (i.e., on one hand, the geometrical arrangement of the lipids and also the DBP molecules is changed, and on the other hand, drastic local enlargement in the electron density has been occurred by the DBP molecules).

The separated intensities of DBP molecules for the two DBP/DPPC ratios, derived from measured data by using the right-hand side of eq 6, are shown in Figure 2. Bragg reflections can be observed on these separated curves at the same position as on the total scattering curves, which provides clear evidence of the periodic displacement of DBP molecules corresponding to the periodicity of the vesicles.

To get more detailed information about the localization of DBP molecules in the bilayers, we performed a simple model fitting.^{22,23} For these calculations, the structure factor from paracrystalline theory was used, which takes the packing disorder into account

$$S_{PT}(q) = N + 2 \sum_{k=1}^{N-1} (N-k) \cos(kqd) \exp(-k^2 q^2 \Delta^2 / 2) \quad (7)$$

where N is the number of layers and Δ is the mean square fluctuation of the bilayers. The latter originates from the Debye–Waller temperature factor, but now, we consider it as the effect of the guest molecules.

The conventional way to determine the bilayer ED profile is to use Fourier synthesis on the Bragg intensities, which were previously corrected for $S(q)$ and the Lorentz factor q^2 according

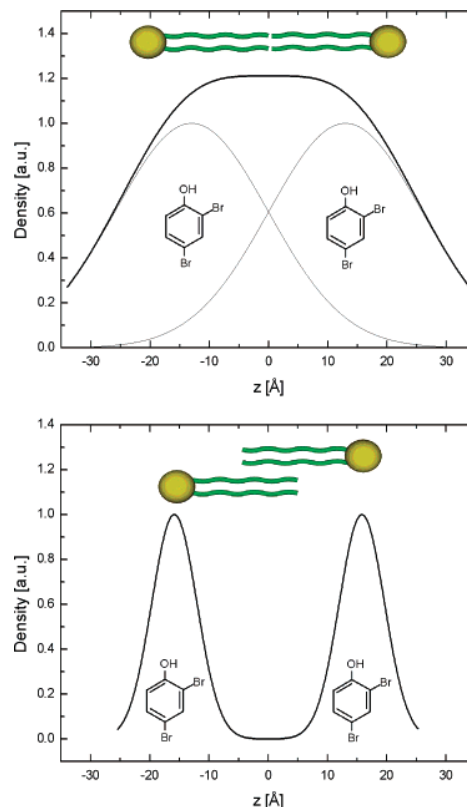


Figure 3. Particle densities along the bilayer normal at 0.1 (top) and 1 (bottom) DBP/DPPC molar ratio. The positions of the lipid molecules are also shown in the figure.

TABLE 1: Fitting Results: Number of Bilayers N , Repeating Unit d , Mean Square Fluctuation of the Bilayers Δ , Width and Position (from the bilayer Center) of the Gaussian Function σ and z_G , Respectively

DBP/DPPC	N	d	Δ	σ	z_G
0.1	25 ± 1	67.8 (87)	5.4 (33)	9.1 (59)	12.9 (74)
1	19 ± 1	50.7 (67)	1.4 (44)	2.6 (99)	15.8 (28)

to eq 1. This method, however, can be used only if the scattering pattern shows at least four diffraction orders. In our case, we have to consider a model ED profile because of the reduced number of Bragg peaks.

For modeling the ED profile along the bilayer normal, we have used a Gaussian model, which is based on describing the electron density as a sum of Gaussian functions. We have used only two Gaussian functions per bilayer located symmetrically to the center of the bilayer, because only the contribution of the guest molecules is present on the separated scattering curves. In the adumbrated case, the geometrical part of the form factor of the guest molecules will be the following:

$$V(q) = \sqrt{2\pi} [2\sigma \exp(-\sigma^2 q^2 / 2) \cos(qz_G)] \quad (8)$$

where σ and z_G are the width and the position from the bilayer center of the Gaussian function. The model fitting was performed using lsqcurvefit routine of MATLAB (The MathWorks, Inc.).

The fitted model functions agree convincingly with the measured data as can be seen in Figure 2 (The results of the fits are summarized in the Table 1). According to the form factor in eq 8, the distributions of the guest molecules along the bilayer normal are shown in Figure 3.

These results clearly show that the DBP molecules are embedded in the lipid layers. In the case of the lower DBP/

DPPC ratio, the localization of the guest molecules is less determined than in the case of the higher ratio, where their positions are more localized to the vicinity of the headgroups.

Conclusions

The location of 2,4-dibromophenol molecules in DPPC/water liposomes was studied by the ASAXS technique at 0.1 and 1 DBP/DPPC molar ratios. The ASAXS curves measured at three different energies provided the derivation of the scattering contribution of the guest molecules. On the basis of a Gaussian model, these separated curves were interpreted, giving the possibility to determine the distributions of the bromophenols along the bilayer normal. In the case of the higher DBP concentration, the displacement of the guest molecules is characterized by a sharp distribution function pointing out the essential role of these molecules in the formation of the interdigitated phase.

This study reveals the utility of the ASAXS method in examining the distribution of a third component in a lamellar system, in the concrete case, in DPPC/water liposomes. However, this method can be applied in a great variety of these kinds of systems, such as diblock copolymers, which have high interest in nanoindustry.

Acknowledgment. This work was supported by the Hungarian Scientific Funds OTKA (T 43055) and by the Contract RII3-CT-2004-506008 of the European Community at DESY/HASYLAB.

References and Notes

(1) Kotterman, M.; van der Veen, I.; van Hesselingen, J.; Leonards, P.; Osinga, R.; de Boer *J. Biomed. Eng.* **2003**, *20*, 425.

- (2) Lincoln, D. E.; Fielman, K. T.; Marinelli, R. L.; Woodin, S. A. *Biochem. Syst. Ecol.* **2005**, *33*, 559.
- (3) Ríos, J. C.; Repetto, G.; Jos, A.; del Peso, A.; Salguero, M.; Cameán A.; Repetto, M. *Toxicol. in Vitro* **2003**, *17*, 635.
- (4) Legler, J.; Brouwer, A. *Environ. Int.* **2003**, *29*, 879.
- (5) Wollenberger, L.; Dinan, L.; Breitholtz, M. *Environ. Toxicol. Chem.* **2005**, *24*, 400.
- (6) Hassenklöver, T.; Predehl, S.; Pilli, J.; Ledwolorz, J.; Assmann, M.; Bickmeyer, U. *Aquat. Toxicol.* **2006**, *76*, 37.
- (7) Olsen, C. M.; Meussen-Elholm, E. T. M.; Holme, J. A.; Hongso, J. K. *Toxicol. Lett.* **2002**, *129*, 55.
- (8) Sikkema, J.; de Bont, J. A.; Poolman, B. *Microbiol. Rev.* **1995**, *59*, 201.
- (9) Csiszár, Á.; Klumpp, E.; Bóta, A.; Szegedi, K. *Chem. Phys. Lipids* **2003**, *126*, 155.
- (10) Bóta, A.; Szegedi, K.; Goerigk, G.; Csiszár, Á.; Haubold, H.-G.; Subklew, G. *HASYLAB Annual Reports* **2002**.
- (11) Goerigk, G.; Williamson, D. L. *Solid State Commun.* **1998**, *108*, 419.
- (12) Vad, T.; Hajbolouri, F.; Haubold, H.-G.; Scherer, G. G.; Wokaun, A. *J. Phys. Chem. B* **2004**, *108*, 12442.
- (13) Phillips, J. C.; Wlodawer, A.; Goodfellow, J. M.; Watenpaugh, K. D.; Sieker, L. C.; Jensen, L. H.; Hodgson, K. O. *Acta Crystallogr.* **1977**, *A33*, 445.
- (14) Stührmann, H. B. *Acta Crystallogr.* **1980**, *A36*, 996.
- (15) de Robillard, Q.; Guo, X.; Dingenouts, N.; Ballauf, M. *Macromol. Symp.* **2001**, *164*, 81.
- (16) Guilleaume, B.; Ballauf, M.; Goerigk, G.; Wittman, M.; Rehahn, M. *Colloid Polym. Sci.* **2001**, *279*, 829.
- (17) Goerigk, G.; Schweins, R.; Huber, K.; Ballauff, M. *Europhys. Lett.* **2004**, *66*, 331.
- (18) Zhang, R.; Suter, R. M.; Nagle, J. F. *Phys. Rev. E* **1994**, *50*, 5047.
- (19) Haubold, H.-G.; Gruenhagen, K.; Wagener, M.; Jungbluth, H.; Heer, H.; Pfeil, A.; Rongen, H.; Brandenburg, G.; Moeller, R.; Matzerath, R.; Hiller, P.; Halling, H. *Rev. Sci. Instrum.* **1989**, *60*, 1943.
- (20) Cromer, D. T.; Liberman, D. *J. Chem. Phys.* **1970**, *53*, 1891.
- (21) Cromer, D. T.; Liberman, D. *Acta Crystallogr.* **1981**, *A37*, 267.
- (22) Pabst, G.; Rappolt, M.; Amentisch H.; Laggner, P. *Phys. Rev. E* **2000**, *62*, 4000.
- (23) Pabst, G.; Koschuch, R.; Pozo-Navas, B.; Rappolt, M.; Lohner, K.; Laggner, P. *J. Appl. Crystallogr.* **2003**, *36*, 1378.

[S9]

G. Goerigk, R. Schweins, K. Huber, and M. Ballauff,

The Distribution of Sr²⁺ Counterions around Polyacrylate Chains

Analyzed by Anomalous

Small-Angle X-ray Scattering

Europhys. Lett. 66 (3), pp. 331-337 (2004)

The distribution of Sr^{2+} counterions around polyacrylate chains analyzed by anomalous small-angle X-ray scattering

G. GOERIGK¹(*), R. SCHWEINS², K. HUBER³ and M. BALLAUFF⁴

¹ *Institut für Festkörperforschung, Forschungszentrum Jülich
Postfach 1913, D-52425, Germany*

² *Institut Laue-Langevin, Large Scale Structures Group
B.P. 156, F-38042 Grenoble CEDEX 9, France*

³ *Universität-GH Paderborn, Fachbereich 13 Chemie und Chemietechnik
Warburger Str. 100, D-33098 Paderborn, Germany*

⁴ *Universität Karlsruhe, Polymer-Institut
Kaiserstr. 12/PF 6980, D-76128 Karlsruhe, Germany*

Dedicated to H. B. Stuhmann

(received 18 September 2003; accepted in final form 18 February 2004)

PACS. 07.85.Qe – Synchrotron radiation instrumentation.

PACS. 61.10.Eq – X-ray scattering (including small-angle scattering).

PACS. 82.35.Rs – Polyelectrolytes.

Abstract. – The distribution of Sr counterions around negatively charged sodium polyacrylate chains (NaPA) in aqueous solution was studied by anomalous small-angle X-ray scattering. Different ratios of the concentrations of $\text{SrCl}_2/[\text{NaPA}]$ reveal dramatic changes in the scattering curves. At the lower ratio the scattering curves indicate a coil-like behavior, while at the higher ratio the scattering curves are contracted to smaller q -values, caused by the collapse of the NaPA coil. The form factor of the scattering contribution of the counterions was separated and analyzed. For the scattering curves of the collapsed chains, this analysis agrees with the model of a pearl necklace, consisting of collapsed sphere-like subdomains which are connected by stretched chain segments. An averaged radius of the pearls of 19 nm and a distance between neighbouring pearls close to 60 nm could be established for the collapsed state of the NaPA chains.

Introduction. – The density of charges along a polyelectrolyte chain makes it accessible to a wide variety of conformations. The two most efficient techniques to control changes in polyelectrolyte conformation are: i) the screening of electrostatic interactions among charged polymer segments by adding an inert salt [1]; ii) the extinction of charges on the polyelectrolyte chain by adding specifically interacting counterions [2, 3]. Synthetic polyelectrolytes may therefore be used as simple models for biopolymers, where the role of electric charges is essential for the proper functioning of nucleic acids, numerous enzymes and proteins.

Theoretical understanding of the mechanism underlying the first technique has made significant progress. With increasing electrostatic screening, the shape of the polyelectrolyte gradually changes from a coil to a compact sphere, passing a cascade of transition states. For these transition states, cigar-like or pearl necklace structures are discussed. The latter

(*) Present address: DESY-HASYLAB - Notkestr. 85, D-22603 Hamburg, Germany.
E-mail: guenter.goerigk@desy.de

were predicted in analogy to the Rayleigh instability of oil droplets while being electrically charged [4,5]. Beyond all doubt, the actual shape depends in a subtle way on the counterion concentration and interactions between solvent and chain backbone [4–10]. Although the pearl necklace model has attracted much attention [11–14], direct prove of its existence is still lacking.

The present investigation focuses on the change in size and shape of sodium polyacrylate (NaPA), followed by the addition of alkaline earth cations as an example for technique ii). Alkaline earth cations are known to specifically interact with the anionic carboxylate residues, located on every other carbon atom of the polymer backbone. Formation of complex bonds between the anionic groups and alkaline earth cations neutralizes electric charges and thereby changes the nature of the respective chain segments. As a consequence, solubility of the polyelectrolyte is lowered, which leads to a significant coil shrinking and eventually causes a precipitation of the respective alkaline earth salt [3,14].

The precipitation depends on the concentration of NaPA and of the alkaline earth cations, denoted as M^{2+} . Beyond a threshold concentration $[M^{2+}]_0$, an additional stoichiometric amount of M^{2+} per COO^- function is required to precipitate the polycarboxylate chains. This correlation can be represented in a phase diagram by means of a linear relation of the form $[M^{2+}]_c = a + r_0[\text{NaPA}]_c$ which separates the one-phase regime of a dilute solution from the precipitate, thus acting as a phase boundary [3,14]. Based on light scattering measurements, changes in coil shape and size are expected to be more pronounced the closer one gets to this phase boundary. Although the coils adopt a sphere-like shape prior to precipitation [14], the shape of intermediates along the coil-to-sphere transition is still an unsettled question.

In the present letter, two questions will be addressed: i) the structure of collapsing polyacrylate chains while approaching the phase boundary of strontium polyacrylate (*i.e.* $M^{2+} = \text{Sr}^{2+}$); ii) an evaluation of the potential offered by the technique of anomalous small-angle X-ray scattering (ASAXS) to characterize the conformation of polyelectrolyte coils decorated with specifically interacting counterions.

Anomalous small-angle X-ray scattering enables the structural characterization of the counterion distribution around the macroions by tuning the energy in the vicinity of the absorption edge of the counterion (*i.e.* Sr^{2+}) in question. The distribution of the counterions is not accessible by conventional SAXS measurements, because the scattering contributions of the counterions and the macroions superimpose and cannot be distinguished. The first ASAXS experiments of counterion distributions were reported by Stuhrmann [15] and more recent results are published in [16–21].

ASAXS measurements. – In the case of a dilute solution of negatively charged polymers, which are surrounded by positively charged counterions, the scattering amplitude—neglecting interparticle correlation—writes

$$A(\vec{q}) = \int_{V_p} \Delta\rho_{\text{Poly}}(\vec{r}) \cdot \exp[-i\vec{q}\vec{r}]d^3r + \int_{V_p} \Delta\rho_{\text{Ion}}(\vec{r}) \cdot \exp[-i\vec{q}\vec{r}]d^3r, \quad (1)$$

q is the magnitude of the scattering vector $[= (4\pi/\lambda)\sin\Theta]$, where 2Θ is the scattering angle and λ the X-ray wavelength. $\Delta\rho_{\text{Poly}}$, $\Delta\rho_{\text{Ion}}$ are the excess electron densities of the polyelectrolyte chains and the counterions,

$$\begin{aligned} \Delta\rho_{\text{Poly}}(\vec{r}) &= \Delta f_{\text{Poly}} \cdot u(\vec{r}) = (f_{\text{Poly}} - \rho_m V_{\text{Poly}}) \cdot u(\vec{r}), \\ \Delta\rho_{\text{Ion}}(\vec{r}, E) &= \Delta f_{\text{Ion}}(E) \cdot v(\vec{r}) = ((f_{0,\text{Ion}} - \rho_m V_{\text{Ion}}) + f'_{\text{Ion}}(E) + i f''_{\text{Ion}}(E)) \cdot v(\vec{r}), \end{aligned} \quad (2)$$

calculated from the electron density ρ_m of the solvent and the volumes of the chains V_{Poly} and of the counterions V_{Ion} , while $u(\vec{r})$, $v(\vec{r})$ are the particle densities of the polymer chains

and the counterions, respectively. The molecular scattering factor (number of electrons) of the chain $f_{\text{Poly}}(E) \approx \text{const}$ is nearly energy independent, while the atomic scattering factor of the counterions $f_{\text{Ion}}(E) = f_{0,\text{Ion}} + f'_{\text{Ion}}(E) + i f''_{\text{Ion}}(E)$ shows strong variation with the energy in the vicinity of the absorption edge of the counterion due to the so-called anomalous dispersion corrections $f'_{\text{Ion}}(E)$, $f''_{\text{Ion}}(E)$. Calculating the scattering intensity $I(\vec{q}) = |A(\vec{q})|^2 = A(\vec{q}) \cdot A^*(\vec{q})$ by means of eqs. (1)-(2) and averaging over all orientations of the polymer yields a sum of three contributions: $I(q, E) = |A_{\text{Poly}}(q)|^2 + |A_{\text{mix}}(q, E)|^2 + |A_{\text{Ion}}(q, E)|^2$, with the integrals [15]

$$\begin{aligned} |A_{\text{Poly}}(q)|^2 &= 4\pi \Delta f_{\text{Poly}}^2 \int_{V_p} \int_{V_p} u(\vec{r}) u(\vec{r}') \frac{\sin(q|\vec{r} - \vec{r}'|)}{q|\vec{r} - \vec{r}'|} d^3r d^3r', \\ |A_{\text{mix}}(q, E)|^2 &= 4\pi \cdot 2\Delta f_{\text{Poly}} \cdot (f_{0,\text{Ion}} - \rho_m V_{\text{Ion}} + f'_{\text{Ion}}(E)) \int_{V_p} \int_{V_p} u(\vec{r}) v(\vec{r}') \frac{\sin(q|\vec{r} - \vec{r}'|)}{q|\vec{r} - \vec{r}'|} d^3r d^3r', \\ |A_{\text{Ion}}(q, E)|^2 &= 4\pi \cdot |\Delta f_{\text{Ion}}(E)|^2 \int_{V_p} \int_{V_p} v(\vec{r}) v(\vec{r}') \frac{\sin(q|\vec{r} - \vec{r}'|)}{q|\vec{r} - \vec{r}'|} d^3r d^3r'. \end{aligned} \quad (3)$$

Equation (3) gives the non-resonant scattering of the polymer chains $|A_{\text{Poly}}(q)|^2$, the cross-term or mixed-resonant scattering $|A_{\text{mix}}(q, E)|^2$ originating from the superposition of the scattering amplitudes of the polymer and the counterions and the scattering of the counterions $|A_{\text{Ion}}(q, E)|^2$, which contains the so-called pure-resonant scattering. By measuring the scattering curves at two energies in the vicinity of the absorption edge of the counterions and subtracting the two scattering curves $\Delta I(q, E_1, E_2) = I(q, E_1) - I(q, E_2)$, the non-resonant scattering contribution of the polymer is vanishing:

$$\begin{aligned} \Delta I(q, E_1, E_2) &= 4\pi \cdot 2\Delta f_{\text{Poly}} (f'_{\text{Ion}}(E_1) - f'_{\text{Ion}}(E_2)) \int_{V_p} \int_{V_p} u(\vec{r}) v(\vec{r}') \frac{\sin(q|\vec{r} - \vec{r}'|)}{q|\vec{r} - \vec{r}'|} d^3r d^3r' + \\ &\quad + 4\pi (|\Delta f_{\text{Ion}}(E_1)|^2 - |\Delta f_{\text{Ion}}(E_2)|^2) \int_{V_p} \int_{V_p} v(\vec{r}) v(\vec{r}') \frac{\sin(q|\vec{r} - \vec{r}'|)}{q|\vec{r} - \vec{r}'|} d^3r d^3r'. \end{aligned} \quad (4)$$

Now the scattering function is reduced to the resonant contributions—the so-called separated scattering—but the scattering of the polymer is still present in the cross-term. To overcome this problem, the measurement at a third energy can be performed and when subtracting the separated-scattering curves obtained at the two energies E_1, E_3 from the separated scattering obtained from the two energies E_1, E_2 , the cross-term is vanishing and the form factor $S_{\text{Ion}}(q)$ of the spatial distribution of the counterions remains after normalizing to the energy-dependent anomalous dispersion corrections of the atomic scattering factor of the counterions at the related energies:

$$\begin{aligned} S_{\text{Ion}}(q) &= 4\pi \int_{V_p} \int_{V_p} v(\vec{r}) v(\vec{r}') \frac{\sin(q|\vec{r} - \vec{r}'|)}{q|\vec{r} - \vec{r}'|} d^3r d^3r' = \\ &= \left[\frac{\Delta I_0(q, E_1, E_2)}{f'_{\text{Ion}}(E_1) - f'_{\text{Ion}}(E_2)} - \frac{\Delta I_0(q, E_1, E_3)}{f'_{\text{Ion}}(E_1) - f'_{\text{Ion}}(E_3)} \right] \cdot \frac{1}{F(E_1, E_2, E_3)}, \\ F(E_1, E_2, E_3) &= f'_{\text{Ion}}(E_2) - f'_{\text{Ion}}(E_3) + \frac{f''_{\text{Ion}}(E_1) - f''_{\text{Ion}}(E_2)}{f'_{\text{Ion}}(E_1) - f'_{\text{Ion}}(E_2)} - \frac{f''_{\text{Ion}}(E_1) - f''_{\text{Ion}}(E_3)}{f'_{\text{Ion}}(E_1) - f'_{\text{Ion}}(E_3)}. \end{aligned} \quad (5)$$

Due to eq. (5) ASAXS provides a technique to access directly the scattering of the counterions and the structural information of the counterion distribution surrounding the macroions can be obtained from the analysis of the form factor $S_{\text{Ion}}(q)$. More generally speaking, eq. (5) provides a method which allows to access directly by analytical means the pure-resonant scattering contribution by measuring the small-angle scattering at only three suitable energies.

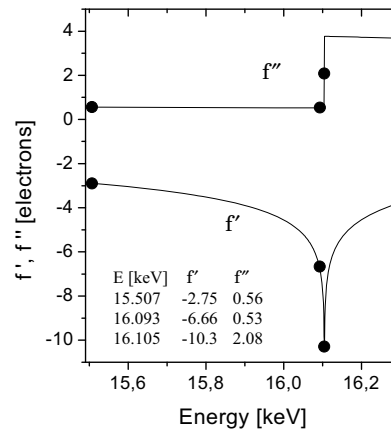


Fig. 1 – Anomalous dispersion corrections obtained by Cromer-Lieberman calculations [24,25]. The values at 16.105 keV result from the convolution with the energy resolution of the JUSIFA beamline.

Experimental. – First, a stock solution of NaPA (supplier: Polysciences, Eppelheim, Germany) was prepared in bidistilled water with 0.007 M NaCl, 0.0015 M SrCl₂ and pH 9. After 3 days, this solution was combined with a SrCl₂ solution with 0.0015 M SrCl₂, pH 9 and 2[Sr²⁺] + [Na⁺] = 0.01 M [14,22]. In order to approach the precipitation limit, several polymer concentrations were produced by diluting with a solution with 1.5 mM SrCl₂, pH 9 and [Sr²⁺] + [Na⁺] = 0.01 M, *i.e.* with a constant concentration of cationic charges. Combined static and dynamic light scattering measurements (ALV 5000E CGS) allowed us to locate the precipitation threshold and to get first information on the shape of the polymer chains in dependence on the ratio of [Sr²⁺]/[NaPA] [22]. Finally, two samples differing in the polymer concentration were chosen: P4KE corresponds to [NaPA] = 3.61 mM, *i.e.* [Sr²⁺]/[NaPA] = 0.42, P4KU2 corresponds to [NaPA] = 3.25 mM, *i.e.* [Sr²⁺]/[NaPA] = 0.46 with P4KU2 lying closer to the borderline of phase separation than P4KE. Compared to coiled chains in Sr²⁺-free solutions, the polyanion dimensions of both samples are significantly shrunken. The two samples as well as the solvent (containing the same amount of Sr²⁺) were filled into capillaries from Hilgenberg GmbH, Malsfeld, Germany. The capillaries are made of borosilicate glass with an inner diameter of 4 mm and a wall thickness of 0.05 mm. The inner diameter of 4 mm is nearly the optimal size for the energy range of the Sr-*K* edge at 16.105 keV. The capillaries were closed with a pipette plug fixed by two-component quick-setting adhesive. ASAXS measurements were performed at the JUSIFA beamline [23] at HASYLAB, DESY, Hamburg in the energy range of the *K* absorption edge of strontium at 16.1046 keV. Measurements were made with a two-dimensional detector at three energies. A *q*-range from about 0.075 to 2.5 nm⁻¹ was covered.

Results. – Figure 1 shows the anomalous dispersion corrections of Sr based on the calculations of Cromer and Liberman [24,25]. The circles represent the X-ray energies, where the SAXS measurements were performed. The table in fig. 1 provides the anomalous dispersion corrections for Sr at the three energies. In the energy range between 16.103 and 16.107 eV, the energy dependence of the anomalous dispersion corrections was convoluted with the energy resolution of the JUSIFA beamline. The value at the energy 16.105 eV in fig. 1 is the result obtained from this convolution. The anomalous dispersion corrections were used in eq. (5) to permit the separation of the form factor of the pure-resonant scattering contribution of the Sr counterions. All scattering curves have been calibrated into absolute units (*i.e.* macroscopic scattering cross-sections in units of cross-section per unit volume cm²/cm³ = cm⁻¹). For all energies the scattering of the solvent was measured with the same statistical accuracy and

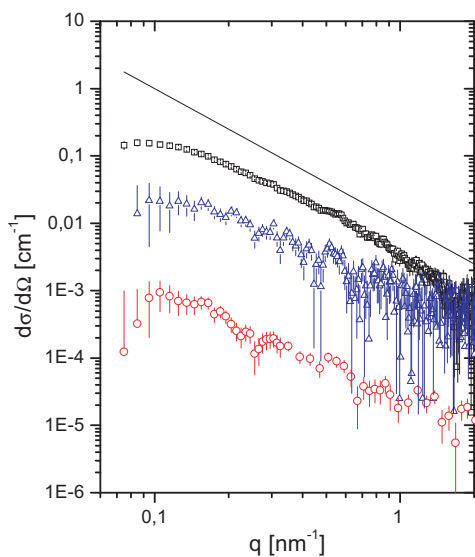


Fig. 2

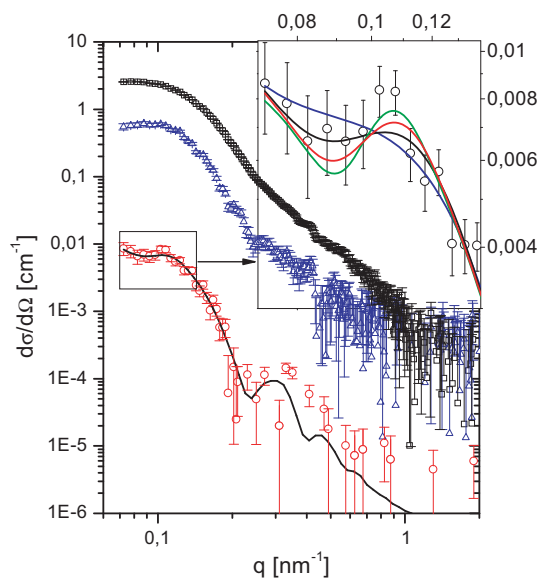


Fig. 3

Fig. 2 – ASAXS measurements of the shrinking NaPA chains ($[\text{NaPA}] = 3.61 \text{ mM}$; $[\text{Sr}^{2+}]/[\text{NaPA}] = 0.41$) at the Sr- K absorption edge at 16.105 keV. The symbols denote: \square total scattering from the polymer and the Sr^{2+} ions; \triangle mixed-resonant curve according to eq. (4); \circ form factor of the distribution of the Sr^{2+} ions; — power law q^{-2} .

Fig. 3 – ASAXS measurements of the shrinking NaPA chains ($[\text{NaPA}] = 3.25 \text{ mM}$; $[\text{Sr}^{2+}]/[\text{NaPA}] = 0.46$) at the Sr- K absorption edge at 16.105 keV. The symbols denote: \square scattering from the polymer and the Sr^{2+} ions; \triangle mixed-resonant curve according to eq. (4); \circ form factor of the Sr^{2+} ions. The solid line is a fitted model function (eq. (6)) with a predefined number of pearls $N = 3$. The inset compares fitted model functions with $N = 2$ (blue), 3 (black), 4 (red) and 5 (green), respectively.

was removed from the scattering curves of the sample before applying eq. (5). In figs. 2 and 3 the scattering curves of P4KE and P4KU2 are shown. The squares show the total-scattering curves comprising both polymer chains and counterions measured at the energy 15.507 keV. The triangles at medium scattering cross-sections show the separated (mainly mixed-resonant) scattering, which corresponds to the superposition of the scattering from the polyacrylates and the Sr counterions. The separated-scattering curves were obtained from measurements at the two energies 15.507 and 16.105 keV and the separation was performed due to eq. (4). The circles represent the form factors of the distributions of the Sr counterions. The separation of the form factors was obtained from measurements at the three energies 15.507, 16.093 and 16.105 keV due to eq. (5). In the case of N scattering curves measured at N different energies $M = N(N - 1)/2$ separated-scattering curves can be obtained and M independent combinations of the M separated-scattering curves can be used in eq. (5) for the calculation of the form factor. The form factors in figs. 2 and 3 represent the averaged curves, which were obtained from the three ($M = 3$) independent separations. The number of q -bins in the Sr^{2+} form factor curves of both samples was reduced in comparison to the mixed-resonant and the total-scattering curves, with the aim to obtain smaller error bars at q -values larger 0.2 nm^{-1} . The procedure was as follows: the cross-section of the form factor curves, which represent the Sr^{2+} counterions, was averaged over neighbouring q -bins. The result gives the cross-section at the center of the averaged q -interval. The error of the averaged cross-section is the averaged squared error calculated from the errors of the single q -bins.

Discussion. – In fig. 2 the scattering curves of NaPA chains at $[\text{NaPA}] = 3.61 \text{ mM}$ (P4KE) obtained from SAXS measurements are shown. The total as well as the separated (mixed-resonant) scattering curve and the form factor of the distribution of Sr counterions follow a power law of $d\sigma/d\Omega \sim q^{-\alpha}$. The exponent α is close to 2 for the three curves, indicating a coil-like behavior [26]. However, it is worth mentioning that the separated curve reveals undulations which points to the occurrence of spherical subdomain formation.

The scattering curves (total, separated and form factor of Sr ion distribution) of the second sample (P4KU2) with a smaller concentration of NaPA ($[\text{NaPA}] = 3.25 \text{ mM}$), but the same SrCl_2 content as P4KE show a different behavior. The total-scattering curve is contracted to smaller q -values and shows several shoulders. This behavior is compatible with the form factor of spherical objects, which is modulated by interspherical scattering contributions. The latter was already suggested by former SANS measurements [27]. This interpretation is strongly confirmed by the separated-scattering curve (triangles) and the separated form factor (circles) of the Sr ion distribution. Both curves exhibit a number of characteristic structures for $q > 0.1 \text{ nm}^{-1}$ with pronounced maxima, minima and shoulders revealing a scattering function, which is strongly influenced by correlation effects between rather monodisperse subdomains within the collapsing chains. Especially the form factor of the spatial distribution of the Sr counterions reveals a correlation maximum at 0.1 nm^{-1} . The solid line in fig. 3 represents a fitted model function to the form factor of the Sr ion distribution. For a counterion-condensation-induced shrinking process (technique i) such a model was first suggested by Rubinstein *et al.* [5] and was confirmed later by computer simulations [7, 8, 10]. The model, denoted as pearl necklace, gives the scattering function of N spheres with radius R and with a distance d between the spheres. For the size distribution of the spheres, a log-normal size distribution $P(R)$ was assumed (eq. (6)):

$$S_{\text{Ion}}(q) = \text{const} \int_0^{\infty} P(R) \cdot \left(\frac{4\pi R^3}{3} \frac{3(\sin(qR) - qR \cos(qR))}{(qR)^3} \right)^2 \cdot \left(N + 2 \sum_{n=1}^{N-1} (N-n) \frac{\sin(nqd)}{nqd} \right) dR,$$

$$P(R) = \frac{1}{\sqrt{2\pi}} \cdot \frac{1}{\sigma R} \cdot \exp \left[- \frac{\ln^2 \frac{R}{R_0}}{2\sigma^2} \right]. \quad (6)$$

In eq. (6), R_0 is the mean radius of the spheres, σ is the second moment of the log-normal size distribution and d is the distance between neighbouring spheres. The first bracket in the integral contains the form factor of a single sphere multiplied by the correlations (second bracket) introduced by the interference of the scattering from the N spheres. An increase of the number of spheres N at constant d i) increases the overall size of the pearl necklace; ii) has small but significant effects in the regime of $0.06 \text{ nm}^{-1} < q < 0.12 \text{ nm}^{-1}$, where a minimum and a maximum occur (inset of fig. 3); iii) does not significantly affect the three fit parameters σ , d and R_0 ; iv) does not affect the scattering curve for $q > 0.14 \text{ nm}^{-1}$. The maximum appears only for $N \geq 3$. Although eq. (6) accounts for a polydispersity, the model is still rather crude due to the assumption of a regular sphere-like structure for the pearls and due to neglect of a polydispersity of the pearl size within each necklace chain, respectively.

In the light of these trends and simplifications, we kept the fit as simple as possible, predefining the number of pearls at $N = 3$. As a result, we found: $R_0 = 19.2(3) \text{ nm}$ for the mean radius of the spheres, $\sigma = 0.088(24)$ for the second moment of the log-normal size distribution, which corresponds to a FWHM in the size distribution of 4 nm and, finally, $d = 60.8(20) \text{ nm}$ for the distance of the spheres. In this interpretation, the fitted model function points into the direction of scattering originating from more than two pearls (dumb-bell).

Conclusions. – From anomalous small-angle X-ray scattering experiments on diluted polyacrylate solution in water with Sr counterions the form factor of the spatial distribution of the Sr counterions was separated. The counterions were found to be located in sphere-like clusters of 19 nm radius which are compatible with collapsed subdomains within the polyacrylate macroions. Assuming a pearl-necklace-like structure an averaged distance of about 60 nm could be established for neighbouring spheres. The distance of the spheres are formed by non-collapsed polyacrylate chain segments. The fitted log-normal size distribution of the spheres revealed a narrow-size distribution with a FWHM value of 4 nm.

* * *

Financial support of the Deutsche Forschungsgemeinschaft, Schwerpunktprogramm “Polyelektrolyte mit definierter Molekülarchitektur” SPP 1009, is gratefully acknowledged.

REFERENCES

- [1] NAGASAWA M., in *Studies in Polymer Science*, Vol. **2** (Elsevier Science Publishers B.V., Amsterdam) 1988, p. 49.
- [2] HUBER K., *J. Phys. Chem.*, **97** (1993) 9825.
- [3] MICHAELI I. J., *Polym. Sci.*, **48** (1960) 291.
- [4] KANTOR Y. and KARDAR M., *Europhys. Lett.*, **27** (1994) 643.
- [5] DOBRYNIN A. V., RUBINSTEIN M. and OBUKHOV S. P., *Macromolecules*, **29** (1996) 2974.
- [6] SOLIS F. J. and OLVERA DE LA CRUZ M., *Macromolecules*, **31** (1998) 5502.
- [7] MICKA U., HOLM CH. and KREMER K., *Langmuir*, **15** (1999) 4033.
- [8] CHODANOWSKI P. and STOLL S., *J. Chem. Phys.*, **111** (1999) 6069.
- [9] LYULIN A. V., DÜNWEIG B., BORISOV O. V. and DARINSKII A. A., *Macromolecules*, **32** (1999) 3264.
- [10] LIMBACH H. J. and HOLM CH., submitted to *J. Phys. Chem. B*.
- [11] ASEYEV V. O., KLENIN S. I., TENHU H., GRILLO I. and GEISSLER E., *Macromolecules*, **34** (2001) 3706.
- [12] LI M.-J., GREEN M. M. and MORAWETZ H., *Macromolecules*, **35** (2002) 4216.
- [13] MINKO S., KIRIY A., GORODYSKA G. and STAMM M., *J. Am. Chem. Soc.*, **124** (2002) 10192.
- [14] SCHWEINS R. and HUBER K., *Eur. Phys. J. E*, **5** (2001) 117.
- [15] STUHRMANN H. B., *Adv. Polym. Sci.*, **67** (1985) 123.
- [16] DE ROBILLIARD Q., GUO X., DINGENOUTS N., BALLAUFF M. and GOERIGK G., *Macromol. Symp.*, **164** (2001) 81.
- [17] GUILLEAUME B., BALLAUFF M., GOERIGK G., WITTEMANN M. and REHAHN M., *Colloid Polym. Sci.*, **279** (2001) 829.
- [18] GUILLEAUME B., BLAUL J., BALLAUFF M., WITTEMANN M., REHAHN M. and GOERIGK G., *Eur. Phys. J. E*, **8** (2002) 299.
- [19] SABBAGH I., DELSANTI M. and LESIEUR P., *Eur. Phys. J. B*, **12** (1999) 253.
- [20] DAS R., MILLS T. T., KWOK L. W., MASKEL G. S., MILLET L. S., DONIACH S., FINKELSTEIN K. D., HERSCHLAG D. and POLLACK L., *Phys. Rev. Lett.*, **90** (2003) 188103-1.
- [21] DINGENOUTS N., BALLAUFF M., PONTONI D., NARAYANAN T. and GOERIGK G., submitted to *Macromolecules* (2003).
- [22] SCHWEINS R., HUBER K., GOERIGK G. and BALLAUFF M., to be published.
- [23] HAUBOLD H.-G., GRUENHAGEN K., WAGENER M., JUNGBLUTH H., HEER H., PFEIL A., RONGEN H., BRANDENBURG G., MOELLER R., MATZERATH R., HILLER P. and HALLING H., *Rev. Sci. Instrum.*, **60** (1989) 1943.
- [24] CROMER D. T. and LIBERMAN D., *J. Chem. Phys.*, **53** (1970) 1891.
- [25] CROMER D. T. and LIBERMAN D., *Acta Crystallogr. A*, **37** (1981) 267.
- [26] RAGNETTI M. and OBERTHÜR R. C., *Colloid Polym. Sci.*, **32** (1986) 264.
- [27] SCHWEINS R., LINDNER P. and HUBER K., *Macromolecules*, **36** (2003) 9564.

Erklärung

Die vorgelegte Zusammenfassung wissenschaftlicher Resultate ging überwiegend aus den wissenschaftlichen Veröffentlichungen [S1-S9] hervor, welche mit Anomaler Röntgen-Kleinwinkelstreuung gewonnen wurden. Diese spezielle Anwendung der Kleinwinkelstreuung unter Einsatz der Synchrotronstrahlung ist ein Arbeitsgebiet, auf dem ich seit fast 30 Jahren wissenschaftlich arbeite und dessen Weiterentwicklung ich maßgeblich beeinflusst habe. Entsprechend waren meine Beiträge in den Publikationen [S1-S9] im Hinblick auf die Kleinwinkelstreuung überwiegend, sofern ich Hauptautor war bzw. unverzichtbar sofern ich als Co-Autor in der Autorenliste auftrete. Meine persönlichen Beiträge zu den einzelnen Publikationen [S1-S9] werden im Folgenden kenntlich gemacht.

In [S1] wurde von mir gezeigt, dass das in den vorangehenden Publikationen verwendete mathematische Verfahren zur direkten Darstellung der Basisstreuungsfunktionen dem Gauß'schen Eliminationsverfahren, angewendet auf ein durch die ASAXS-Messtechnik vorgegebenes lineares Gleichungssystem entspricht. [S1] baut dabei auf den Ergebnissen von [S2] über die Untersuchung der spinodalen Entmischung in ternären Legierungen auf. Die in [S2] untersuchten Legierungen wurden im IFW-Dresden hergestellt und anschließend von mir am JUSIFA-Messstand mit Anomaler Röntgen-Kleinwinkelstreuung untersucht. Die Datenanalyse basiert auf dem von mir für ASAXS entwickelten Zerlegungsverfahren und wurde von mir durchgeführt. In [S3] wurden unter meiner Leitung am JUSIFA-Messstand ASAXS-Messungen nach der von mir entwickelten Zerlegung quantitativ untersucht. Die hochporösen Katalysatorproben wurden an der Universität Budapest hergestellt. In [S4] wurden unter meiner Leitung am JUSIFA-Messstand ASAXS-Messungen an verdünnten chemischen Lösungen der Universität Paderborn nach der von mir entwickelten Zerlegung quantitativ untersucht. In [S5] wurde an multi-lamellaren bio-kompatiblen Membransystemen, die von der Universität Budapest für die Herstellung nano-strukturierter Halbleiterkolloide funktionalisiert wurden, unter meiner Leitung am JUSIFA-Messstand ASAXS-Messungen nach der von mir entwickelten Zerlegung untersucht. In [S6] wurde der von mir entwickelte Zerlegungsalgorithmus erstmals auf eine Halbleiterlegierung angewendet. Die Legierungen wurden vom NREL (National Renewable Energy Laboratory) bzw. an der Colorado School of Mines hergestellt. Die ASAXS Messungen bzw. die nachfolgende Datenanalyse wurden von mir durchgeführt. Die in [S7] mit Ergebnissen der

Lichtstreuung verglichenen ASAXS-Messungen wurden unter meiner Leitung am JUSIFA-Messstand durchgeführt und nach dem von mir entwickelten Zerlegungsverfahren analysiert. Die verdünnten chemischen Lösungen wurden an der Universität Paderborn hergestellt und dort mit Lichtstreuung untersucht. In [S8] wurden unter meiner Leitung am JUSIFA-Messstand ASAXS-Messungen an multi-lamellaren Vesikeln durchgeführt und nach dem von mir entwickelten Zerlegungsverfahren analysiert. Die Vesikelproben wurden an der Universität Budapest hergestellt. In [S9] habe ich erstmals den beschriebenen Zerlegungsalgorithmus auf ASAXS-Messungen, die unter meiner Leitung am JUSIFA-Messstand durchgeführt wurden, auf verdünnte chemische Lösungen mit Sr-Gegenionen angewendet. Diese Publikation hat die nachfolgenden Publikationen [S2-S8] initiiert. Die Proben wurden an der Universität Paderborn präpariert.

Für alle Publikationen [S1-S9] waren neben der Entwicklung eines geeigneten mathematischen Algorithmus meine stetig vorangetriebenen Verbesserungen der Messtechnik am JUSIFA-Messstand mit dem Ziel einer Messgenauigkeit von $\Delta I/I=10^{-3}$ unerlässliche Voraussetzung.

Danksagung

Ich möchte mich herzlich für die spannenden wissenschaftlichen Kooperationen bei allen Wissenschaftlern bedanken, die in den letzten 22 Jahren mit mir am JUSIFA Messtand des Forschungszentrum Jülich im Hamburger Synchrotronstrahlungslabor experimentiert haben. Es ist leider unmöglich alle namentlich an dieser Stelle zu erwähnen. In über 50 wissenschaftlichen Projekten mit ca. 300 teilnehmenden Wissenschaftlern und Studenten wurden bis zu meinem Weggang im Sommer 2007 über 400 Wochen Messzeit vergeben aus denen weit über 300 Publikationen entstanden sind. Diese große Anzahl von wissenschaftlichen Projekten hat es möglich gemacht, einen enormen Erfahrungsschatz für die Methode der Resonanten Röntgen-Kleinwinkelstreuung anzusammeln. Die verschiedenen äußerst unterschiedlichen Systeme, die mit ASAXS untersucht wurden – kristalline und amorphe Legierungen, Keramiken, Magnetische Systeme, Katalysatoren, Halbleiter, Gläser, Polymere, Technische Membranen, Bio-Membranen, Proteine und andere Soft matter Systeme – machten häufig völlig verschiedene Messstrategien erforderlich. Gleichzeitig kehrten aber als Konstanten zwei wesentliche Hauptforderungen immer wieder: Die Messgenauigkeit in den Bereich $\Delta I/I=10^{-3}$ zu treiben mit dem Ziel, den Rein-Resonanten Streubeitrag abzutrennen und geeignete Algorithmen zu verwenden, die eine zuverlässige Matrixinversion erlauben.

Ich möchte deshalb die wissenschaftlichen Kollaborationen namentlich hervorheben, die besonderen Anteil – dokumentiert durch Publikationen - an der Weiterentwicklung von ASAXS zu höherer Genauigkeit mit dem Ziel einer quantitativen Auswertung der Resonant-Invarianten hatten: Die Arbeitsgruppe von Prof. Dr. Klaus Huber von der Universität Paderborn mit umfangreichen Untersuchungen von Gegenionenverteilungen an Polyakrylaten sowie Silberatomen an Farbstoffen, die Arbeitsgruppe von PD Dr. Attila Bota von der Ungarischen Akademie der Wissenschaften mit umfangreichen Untersuchungen an Lipidmembranen, Katalysatoren und komplexen Kolloidsystemen, Prof. Dr. D.L. Williamson von Colorado School of Mines U.S.A. mit der Untersuchung von amorphen Halbleiterlegierungen in der Solarzellenforschung und die Arbeitsgruppe von Dr. N. Mattern vom Leibniz-Institut für Festkörper- und Materialforschung in Dresden mit der Untersuchung der spinodalen Entmischung in ternären Nickel-Niob-Yttrium Legierungen. Besonderer Dank für die langjährige wissenschaftliche Zusammenarbeit und die zahlreichen spannenden wissenschaftlichen Diskussionen geht an Prof. Dr. K. Huber (Universität Paderborn), an PD.

Dr. A. Bota und an Dr. Z. Varga von der Ungarischen Akademie der Wissenschaften sowie an Dr. R. Schweins (heute ILL) für die erstklassigen Präparationen und Untersuchung durch Lichtstreuung der Polyakrylatproben.

Dem Forschungszentrum Jülich insbesondere Dr. H.-G. Haubold und Prof. Dr. W. Schilling vom Institut für Festkörperforschung (IFF) und den zahlreichen Mitarbeitern möchte ich Dank und meine tief empfundene Anerkennung aussprechen für die hohen Verdienste, die es sich um die Entwicklung der ASAXS-Technik durch den Bau des dedizierten ASAXS-Instrumentes *JUSIFA* (*J*uelich's *U*ser-dedicated *S*mall-Angle *S*catter*I*ng *F*acility) erworben hat. Ohne Übertreibung kann man sagen, dass dieser Name weltweit zum Markenzeichen für *ASAXS* geworden ist, wie es durch die Vielzahl der Publikationen und Zitate dokumentiert ist. Während meiner zwanzigjährigen Arbeit im *IFF* ist mir das Institut zur wissenschaftlichen Heimat geworden und wird mir unvergessen bleiben. Dem DESY/HASYLAB möchte ich für die sich über 20 Jahre erstreckende Unterstützung des Messbetriebs, die stetigen Verbesserungen des Strahlstabilisierungssystems bei DORIS und den gelungenen gemeinsamen Instrument-Upgrade von 2006 danken.

Mit besonderem Respekt gehen meine Gedanken zurück zu meinem Doktorvater Prof. Dr. H.B. Stuhmann, einem Urheber der ASAXS Technik, und seinem unversiegbarem Ideenreichtum bei der Entwicklung von Kontrastmethoden zur strukturell-quantitativen Aufklärung komplexer Systeme. Prof. Dr. M. Ballauff vom Helmholtz-Zentrum Berlin und Prof. Dr. K. Huber danke ich für die wohlwollende Unterstützung und die Ermunterung meine wissenschaftlichen Ergebnisse in Form einer Habilitation zusammenzufassen. Schließlich möchte ich besonders meinen Eltern danken, die mir in meiner Jugend ermöglicht haben, eine wissenschaftliche Laufbahn einzuschlagen.